REFERENCE ONLY

UNIVERSITY OF LONDON THESIS

Degree PhD Year 2005 Name of Author NAISBITT S.

COPYRIGHT
This is a thesis accepted for a Higher Degree of the University of London. It is an unpublished typescript and the copyright is held by the author. All persons consulting the thesis must read and abide by the Copyright Declaration below.

COPYRIGHT DECLARATION
I recognise that the copyright of the above-described thesis rests with the author and that no quotation from it or information derived from it may be published without the prior written consent of the author.

LOANS
Theses may not be lent to individuals, but the Senate House Library may lend a copy to approved libraries within the United Kingdom, for consultation solely on the premises of those libraries. Application should be made to: Inter-Library Loans, Senate House Library, Senate House, Malet Street, London WC1E 7HU.

REPRODUCTION
University of London theses may not be reproduced without explicit written permission from the Senate House Library. Enquiries should be addressed to the Theses Section of the Library. Regulations concerning reproduction vary according to the date of acceptance of the thesis and are listed below as guidelines.

A. Before 1962. Permission granted only upon the prior written consent of the author. (The Senate House Library will provide addresses where possible).

B. 1962 - 1974. In many cases the author has agreed to permit copying upon completion of a Copyright Declaration.

C. 1975 - 1988. Most theses may be copied upon completion of a Copyright Declaration.

D. 1989 onwards. Most theses may be copied.

This thesis comes within category D.

☑ This copy has been deposited in the Library of UCL

☐ This copy has been deposited in the Senate House Library, Senate House, Malet Street, London WC1E 7HU.

C:\Documents and Settings\lproctor\Local Settings\Temporary Internet Files\OLK8\Copyright - thesis (2).doc

The Effects of Microstructure on the Gas Sensing Properties of Chromium Titanium Oxide

Simon Carl Naisbitt

This thesis is submitted in partial fulfilment of the requirements
for the Degree of Doctor of Philosophy

August 2005

University College London

UMI Number: U592171

All rights reserved

INFORMATION TO ALL USERS
The quality of this reproduction is dependent upon the quality of the copy submitted.

In the unlikely event that the author did not send a complete manuscript
and there are missing pages, these will be noted. Also, if material had to be removed,
a note will indicate the deletion.

UMI U592171
Published by ProQuest LLC 2013. Copyright in the Dissertation held by the Author.
Microform Edition © ProQuest LLC.
All rights reserved. This work is protected against
unauthorized copying under Title 17, United States Code.

ProQuest LLC
789 East Eisenhower Parkway
P.O. Box 1346
Ann Arbor, MI 48106-1346

Abstract

The general principles relating to construction and operation of semiconducting metal oxide materials as gas sensitive resistors are discussed. The adsorbed oxygen model of sensor response is presented as the origin of the gas sensitivity of the conductivity of these materials. Microstructure is also noted to affect sensor response and various studies, simulations and models from the literature are presented and discussed. Based on a combination of the model developed by Williams *et al.* and the linear form of the empirical equation for sensor response the model that will be used in the present work is developed.

Two batches of sensors made using two chromia raw material powders of differing particle size were obtained from City Technology Ltd. Groups of these sensors were sintered at different temperatures to generate sensors having different microstructures. The different sintering temperatures produced clear gradations in the microstructures of the sensors, observed using scanning electron microscopy. These sensors were then systematically tested to carbon monoxide (CO) and propane at a single operating temperature of 400°C. A further group of sensors created from the batch of sensors made from fine chromia raw material were sintered at a single temperature of 775°C but were operated at temperatures of 350, 400 and 450°C and tested to CO with exposures of 1800 second duration.

The results of all the gas tests were successfully processed so as to obtain solutions to the microstructural model developed for the steady state and transient cases. The trends of the microstructural, sensitivity and time constant parameters with sintering temperature, microstructure, operating temperature and exposure length are successfully discussed with reference to how the model accounts for these trends. The unexpected or unusual results are explained in terms of potential inaccuracies in the model or how it has been applied in this work.

Table of Contents

Table of Abbreviations

AFM	atomic force microscopy
AFT	advanced filter technology, pure chromia layer on CTO
APCVD	atmospheric pressure chemical vapour deposition
BET	Brunauer, Emmett, and Teller (3 scientists responsible for developing a method of measuring surface area)
CTO	chromium titanium oxide or chromium titanate
FIB	focussed ion beam
HDB	heater driver board
LPG	liquefied petroleum gas
MFC	mass flow controller
PEG	poly ethylene glycol
SAED	selected area electron diffraction
SEM	scanning electron microscope
TEM	transmission electron microscope
UCL	University College London
XRD	X-ray diffraction

Table of Figures

Table of Tables

Table of Equations

Acknowledgements

I would like to thank my supervisors Professor David Williams and Professor Ivan Parkin for giving me the opportunity to undertake this work and for their support throughout. I am extremely grateful for the many theoretical and practical discussions I have had with Dr Keith Pratt. The knowledgeable assistance of Dick Waymark, Kevin Reeve, Kevin Lee and Dr Steve Firth with the practical aspects of this work is greatly appreciated. I have most enjoyed working in the Chemistry Department at University College London, and I would like to thank all the friends I have made there for making it so enjoyable. I would especially like to thank my wife, Helen, for her continued support and encouragement.

This project was supported through an Industrial CASE Award from the Engineering and Physical Sciences Research Council and City Technology Limited.

1 An Introduction to Gas Sensing Using Metal Oxide Materials

The detection and discrimination of gases in environments is an important technological aspect of many applications. There are many instances where knowledge of a gas's presence, composition and/or identity is invaluable information. Examples include determination of air/fuel ratios for efficient combustion processes, pollutant identification and/or quantification in environmental control systems, reactant/product quantifications in industrial control processes, odour characterisation using electronic noses and many others besides. One technology that allows detection and quantification of many different gases is that of semiconducting metal oxide gas sensors. A general description of what a semiconducting metal oxide gas sensor is will first be presented. The main section of this introduction is that dealing with how the response of gas sensors, and particularly those made from CTO, has been explained and modelled. Previous work on how sensor response can be affected by microstructure will then be introduced and from this the microstructural model of sensor response that will be used in this work will be explained. Various aspects of using chromium titanate (CTO) as a material for such gas sensors will then be explained.

1.1 Motivation for this Work

The mechanisms governing sensor response are of great interest to those using and developing semiconducting metal oxide gas sensors, as their discovery allows improvements in the understanding of the sensors and how they may be better constructed and implemented. As will be discussed in later sections of this introduction, empirical models of sensor response to gas concentration and other factors exist in the literature. The form of these empirical models has been explained by invoking various mechanisms for the reactions that occur between the gas sensor surface and the species in the atmosphere. These empirical models rarely fit the experimental data obtained perfectly. One inadequacy of these models is deemed to

be that they do not take into account sensor microstructure. Many studies have been recorded which correlate various microstructural features with sensor response. An explanation for these correlations is provided by a description of the particles forming sensor microstructures as having surface layers which are depleted in electrons. The various ways in which different sensor microstructures may affect response through this description have been discussed. A few attempts have been made to simulate the effects of microstructure in terms of sensor response and to compare experimental data with these simulations through response factors and exponents. However, no attempts have been made to apply a microstructural model directly to experimental sensor response data and that is the main aim of this work.

1.2 General Description of Semiconducting Gas Sensors

A sensor is defined as "a device giving a signal for detection or measurement of a physical property to which it responds."[1]

The use of semiconducting metal oxide materials for gas sensors, under particular operating conditions, depends on the sensitivity of their conductivity to the composition of their environment. Put another way, a change in the activity of the various gases in the environment around a gas sensor may cause a corresponding change in the conductivity of the materials from which the sensor is made.

The key aspects of the technology of semiconducting gas sensors mentioned in the statements above are listed below:

1. Metal oxide materials are semiconducting under certain conditions.
2. The conductivity of metal oxides may be dependent on the composition of different species in their environment and the activity of these species in their interactions with the sensor.
3. The sensor must be included in some sort of associated equipment which measures the change in conductivity to provide us with useful information.

The nature of the semiconduction and the interactions between gaseous species and metal oxide materials will be explained in later sections. The last aspect highlighted above is what forms the focus of the remainder of this section.

The construction of semiconducting gas sensors is somewhat determined by the factors mentioned above. Essentially, the following elements are needed:

1. The metal oxide material whose conductivity should be sensitive to the gas(es) of interest, sometimes referred to as the 'target' gas(es).
2. The metal oxide material needs a connection to some associated circuitry which uses the conductivity of the metal oxide to provide a signal which somehow describes the nature of the sensor's environment.
3. The sensor needs to be operated under certain conditions, particularly of temperature, to obtain optimum sensitivity to different gases. Thus a method of controlling these conditions must be employed.

Typical sensors are constructed by depositing the metal oxide material in some fashion over a pair of electrodes which themselves can be made with a connection to the external circuitry which monitors the conductivity of the material. A controllable heater element is commonly incorporated into the design. There are many ways in which this type of design may be constructed. One of the most common and cost-effective methods involves a planar design, illustrated in Figure 1.1 courtesy of City Technology Ltd[2], with the individual components deposited sequentially onto an inert substrate, such as alumina, by a screen-printing method. This is the method that will be used to form the sensors used in this study.

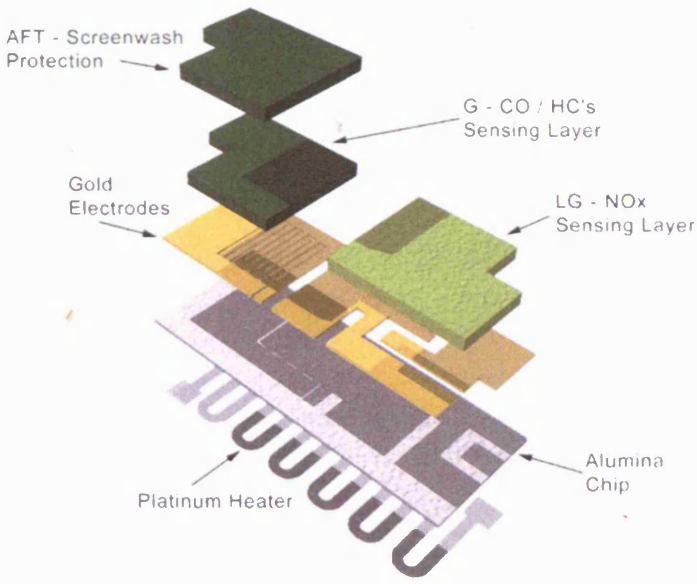

Figure 1.1 Typical planar design of metal oxide gas sensor produced by screen-printing[2]. LG is a tungsten oxide ,WO_3, layer used for sensing nitrogen oxides, NO_x, G is a CTO layer used for sensing carbon monoxide, CO, and hydrocarbons and AFT is a pure chromia layer that is used to prevent alcohols reaching the underlying CTO layer

As mentioned above, metal oxide gas sensors are typically fabricated using a screen-printing process. This process involves the following steps:

1. Obtaining the raw materials; the metal oxide(s) or their precursors
2. Preparing a ceramic powder of the required composition and physical character
3. Mixing this powder with a carrier or vehicle to produce a reproducibly printable ink
4. Depositing this ink onto a substrate prepared with the necessary heater track and electrode structure by the screen printing process
5. Firing (sintering) the sensors to obtain a porous network of sintered ceramic particles
6. Mounting of the sensors in a form that enables their integration into electronic circuits that control the operating conditions of the sensors and allow the monitoring of their conductivity

Each one of these aspects of the fabrication process is partly responsible for determining the characteristics of the sensors' operation as gas sensitive resistors.

1.3 Electrical Conductivity and Semiconductivity in Solids

The property of a metal oxide gas sensor that is commonly measured is that of its resistance, R, measured in ohms, Ω. This is a property that is relatively easy to measure in most circumstances and is governed by the general equation:

$$R = \frac{\rho L}{A}$$

Equation 1.1 for the resistance, R, of a conductor of prismatic form of length, L, and cross-sectional area, A, made from a material of resistivity, ρ

where ρ is the resistivity of the material, measured in Ωm, L is the length of the resistor and A is the cross-sectional area of the resistor. Resistivity is the reciprocal of conductivity, σ, and the resistance is the reciprocal of conductance, G, measured in Ω^{-1}.

$$\rho = \frac{1}{\sigma}$$

Equation 1.2 Resistivity, ρ, is the reciprocal of conductivity, σ

$$R = \frac{1}{G}$$

Equation 1.3 Resistance, R, is the reciprocal of conductance, G

The reciprocal nature of these parameters leads to the alternative form of Equation 1.1 for the conductance of a resistor:

$$G = \frac{\sigma A}{L}$$

Equation 1.4 Conductance, G, as a function of conductivity, σ, cross-sectional area, A, and length, L, of a conductor

The above equations are useful in the general design of a gas sensing element in terms of determining optimum size and shape. Since the application of different gases in the atmosphere around a sensor is unlikely to alter its geometrical parameters of length and cross-sectional area the effect of these gases must be on the materials conductivity. A general introduction to the principles governing conduction

in solid materials, and semiconductivity in particular, is given in the next two sections before the principles and models governing the gas sensitivity of metal oxides' conductivity are introduced.

1.3.1 General Principles of Electronic Conductivity in Solids

Electronic conduction, the transport of charge by the flow of electrons, is a phenomenon that is displayed in a wide range of materials to different extents. Semiconduction is a term that is used to classify materials that, broadly speaking, display a degree of electronic conduction, or conductivity, between that commonly found in metals and that found in insulators. Typical ranges of conductivity(σ) found for materials belonging to these three classes are given in Table 1.1 below.

Table 1.1 Typical conductivity ranges for the three classes of electronic conductors[3]

Material	σ ($ohm^{-1}cm^{-1}$)
Metal	10^{-1} - 10^{5}
Semiconductor	10^{-5} - 10^{2}
Insulator	$<10^{-12}$

The names of these classes can be a little misleading as what is commonly regarded as a metal would be a material composed of one or more of the metallic elements. (i.e. elemental copper or a copper zinc alloy etc) However, any of these class names may be attributed to a material of any composition which falls within the generalised boundaries given in Table 1.1. For example, ReO_2 is a metal oxide material which displays metallic conduction.

However, the value of the conductivity is not the sole determinant of whether a material belongs to one class or another. In fact, this could not be the case as there is a significant overlap, of around 3 orders of magnitude, between materials that display metallic conduction and those that display semiconduction. The origin of this overlap lies in the physical processes which govern conductivity and gives rise to another characteristic type of behaviour in materials. This characteristic is that of the temperature dependence of the conductivities of the different materials. Figure 1.2

shows the markedly different effects temperature has on the conductivity of materials from the different classes.

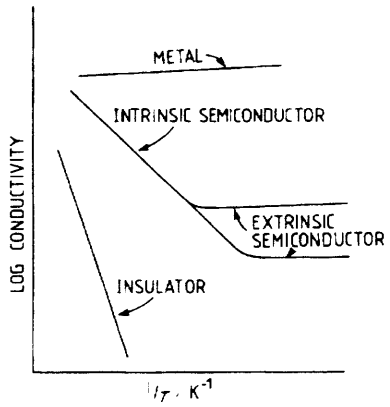

Figure 1.2 Temperature dependence of conductivity of different classes of electronic conductor[3]

This temperature dependence may be related to Equation 1.5 which describes how conductivity, σ, varies with n, the number of charge carriers of charge, e, and μ, their mobility.

$$\sigma = ne\mu$$

Equation 1.5 Conductivity, σ, as a function of number of charge carriers, n, the charge on the carriers, e, and the mobility of the carriers, μ

For metals the conductivity is gradually reduced with increasing temperature. In metals it is known that the concentration or number of electrons in any sample is constant with temperature variation (see section 1.3.2). From Equation 1.5 we can therefore say that the mobility of the electrons responsible for metallic conduction is reduced with increasing temperature. This is explained by the increased temperature causing more phonons, or lattice vibrations, where the atoms in the crystal lattice of the metal vibrate about their mean positions. Electrons travelling through the lattice are more likely to collide with and have their mobility restricted by these phonons when the temperature is higher as there are more of the phonons with higher energy.

For insulators the conductivity gradually increases with increasing temperature. As discussed above, for metals, increasing the temperature leads to higher resistance through the reduced mobility of the conduction electrons caused by lattice vibrations. Since this also occurs in other materials, then from Equation 1.5 it is therefore concluded that the increase in conductivity of insulators with increasing temperature is due to an increase in the number of charge carriers which more than outweighs the decreases due to mobility restriction by phonons.

For semiconductors the conductivity increases with increasing temperature as it does with the insulators. It is concluded that this is due to increased conduction carrier numbers that outweighs the reduction in electron mobility from lattice phonons, as with the case of insulators. However, as mentioned above, the conductivity values of semiconductors tend to be many orders of magnitude higher than that of insulators. Figure 1.2 also displays a transition that occurs in certain semiconducting materials where the gradient of the log conductivity vs 1/T plot changes from one value to another at a specific temperature. This transition is a change from intrinsic to extrinsic semiconduction and is caused by changes in the concentrations of electronic carriers that come from different sources.

1.3.2 Band Theory and Semiconduction

Band theory was developed to explain some of the behaviour of the different electronic conductors that has been described in the previous sections. It has been very useful in this respect and provides a useful picture that can be used to describe the processes that occur. It has also been demonstrated that many of the concepts are experimentally sound.

The bands mentioned in the title of this theory are hypothetical bands or ranges of energy in which the electrons in a solid may or may not reside. The bands have gaps in energy between them, known as band gaps. The actual origin of these bands and band gaps may be explained using a quantum mechanical approach. However, such a detailed understanding is, in the first instance, unnecessary, and only a simplified version will be presented here.

Each atom in a solid has associated with it a set of electrons. This set of electrons is ordered in terms of the energy of each electron. This order is know as the electronic configuration which is divided into shells, subshells and orbitals. Each orbital in an atom is capable of holding one or two electrons only, at a specific energy level. In order to have more than two electrons in an atom there must be more than one orbital. These orbitals are themselves grouped in terms of energy into sub-shells, where the orbitals in the subshells have similar, but not quite the same, energy. Shells are composed of these subshells and again, the different subshells within a shell have almost, but not quite the same energy.

The origin of the bands comes when the individual atoms are arranged in close proximity in a solid crystal. In a solid there are attractive forces, or bonds that keep the atoms together acting against the repulsive forces that tend to keep them apart. There is a balance, or equilibrium between these forces and a crystal may arise. The bonds present originate from the interactions of the electrons in the atoms of neighbouring sites in the crystal. These interactions may have only a short range and highly directional nature as in covalent bonds between nearest neighbours or they may have long range and less directional nature as in the case of metallic bonding.

The valence electrons of the atoms that make up a solid are responsible for the bonding between the atoms. The valence electrons of the atoms are shared (covalent and metallic bonding) or exchanged (ionic bonding) between their neighbours. In these acts of exchange or sharing the electrons cease to be associated only with the single atom from where they originated, and are said to be delocalised. Because the possible states for electrons on neighbouring atoms (e.g. 2s states) may have slightly different energies it appears that, in the crystal, the electrons originating from these states can occupy a range of energies. Similarly, in such proximity as occurs in crystals, electrons originally occupying a 2p state on one atom may have the same energy as an electron occupying a 2s state from the same shell on a neighbouring atom. This means that the bands of possible energy levels for 2s and 2p states of all the atoms in the crystal may overlap to some degree.

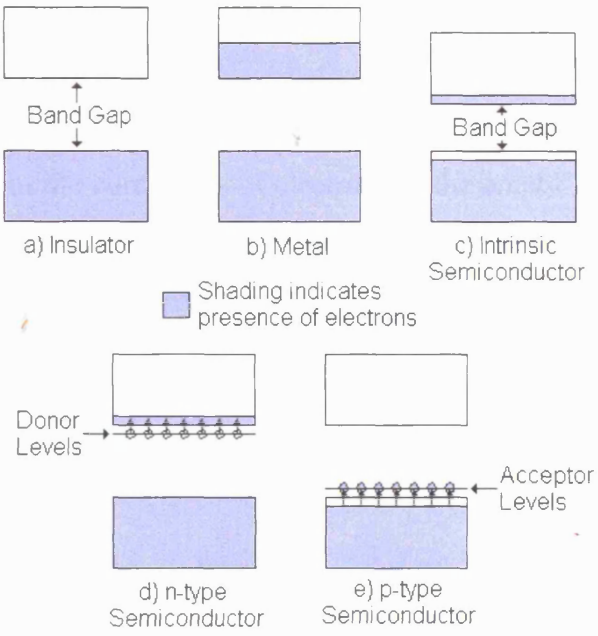

Figure 1.3 Shows schematic energy level diagrams for (a) insulators, (b) metals and (c) intrinsic semiconductors, (d) n-type semiconductors and (e) p-type semiconductors

This model of the different classes of electronic conductor is explained in more detail below:

a) Insulators

The valence band is full. There is a large energy gap between valence band and the next empty band, or the conduction band as it is known. Thus a large amount of energy is required to excite electrons into the conduction band. This accounts for the low concentration of electrons at ambient temperature and hence low conductivity of insulators. It also accounts for the gradual increase in conductivity with increasing temperature as the thermal energy in the lattice may lead to the excitation of electrons into the conduction band with greater frequency.

b) Metals

The valence band is only partly occupied. This may be because an orbital that makes up the valence band is partly filled (i.e. Li 2s1) or that the orbitals that form the valence band overlap and electrons are spread across the two so that neither is full (i.e. Be 2s2, where the 2s orbital is full but overlap occurs between 2s and 2p

orbitals). This accounts for the high conductivity of metals as the electrons are in a band of energy levels in which they can freely move. Also, the concentration of electrons is constant since it would require relatively large amounts of energy to excite electrons from the core shells of electrons to the empty levels of the valence band. The only thing that may result in changes in conductivity is the increased energy available for phonons that impede the passage of electrons as the temperature is increased, thus reducing the conductivity.

c) Intrinsic semiconductor

The valence band is full as with insulators, but there is a smaller gap between the valence and conduction bands than with insulators. This leads to the higher conductivity of semiconductors compared to insulators at ambient temperatures as the number of electrons that are thermally excited from the valence band through the small band gap into the conduction band is greater. In addition, the energy available for such excitations increases with increasing temperature resulting in increasing conductivity.

d) Extrinsic semiconductor

The valence band is full as with insulators and intrinsic semiconductors. However, impurities (of different valence than the atoms in the host lattice) or defects may act as electron donors to the conduction band or electron acceptors from the valence band. These intermediate energy levels lie close to the bands but within the band gap. The energy required to promote electrons to, in the case of acceptor levels just above the valence band, or from, in the case of the donor levels just below the conduction band is relatively low and at ambient temperatures there is sufficient energy available to enable this. Materials may be classified according to which type of these intermediate levels they contain in greater proportion. Those having more donor than acceptor levels are classified as n-type semiconductors where the increased conductivity comes from the extra electrons that are donated to the conduction band to become electronic carriers. Those having more acceptor than donor levels are classified as p-type semiconductors where the increased conductivity comes from the promotion of electrons from the valence band to the

acceptor levels resulting in the formation of electron holes (or vacancies) in the valence band. Electronic conduction may occur in this latter case due to electrons hopping into the hole with the result of leaving another hole from where it came. Essentially this may be considered as the movement of electron holes in the opposite direction to which electrons carry charge.

1.4 Modelling the response of thick film metal oxide gas sensors

The above discussion introduces the general principles of semiconduction that apply to metal oxides used as gas sensors. The principles and models that have been developed to explain how and why the conductivity of semiconducting metal oxide materials are affected by changes in the composition of the gases in the atmosphere are the focus of this section.

1.4.1 Categorising Gas Response of Semiconducting Metal Oxide Materials

The response of semiconducting metal oxide materials is categorised depending on whether their conductivity displays a positive or a negative response on exposure to reducing or oxidising gases, as in Table 1.2[4]. These classifications arise from the changes that occur in the majority electronic charge carrier concentrations as a result of exposure of the metal oxides to gas. In the case of a material classified as n-type, changes in gas concentration affect the concentration of electrons in the conduction band. In the case of a material classified as p-type, changes in gas concentration affect the concentration of holes in the valence band. The specific mechanism proposed to be responsible for these changes in carrier concentration is explained in the following section.

Table 1.2 Classification of semiconducting metal oxides materials as either n-type or p-type according to the signs of their resistance changes to reducing and oxidising gases[4]

Material Classification	Change in Resistance in Response to ...	
	Reducing Gas	Oxidising Gas
n-type	-	+
p-type	+	-

1.4.2 Adsorbed Oxygen Surface Species and Sensor Response

From the above discussion and the fact that the conductivity of certain metal oxide materials is sensitive to the composition of gases in the atmosphere it is possible to determine that the mechanisms governing this property must affect either the number of charge carriers, n, in the materials or their mobility, μ, as per Equation 1.5. Windischmann and Mark[5] proposed a model that accounts for the modulation of the number of conduction carriers in thin film tin oxide, SnO_x, sensors, displaying n-type semiconductivity, on response to carbon monoxide. The model is presented in a general form such that it is applicable to the explanation of the gas responses of a broader spectrum of semiconducting metal oxide materials to different gases.

Figure 1.4 displays a sequence of diagrams that illustrate the generalised reactions that are responsible for the response of n-type materials to reducing gases, as deduced from their testing of tin oxide thin films to carbon monoxide. From the lack of sensitivity of their sensors to CO in atmospheres with low partial pressures of oxygen they deduced that the oxygen forms species at the surface on adsorption that sensitises the sensors to reducing gases. This is the fundamental aspect of this model and from hereon the discussion will be presented in the generalised form so that the responses of the wider field of n-type materials to reducing gases can be explained.

Figure 1.4(a) shows an n-type film having electrons in the conduction band as a result of the presence of shallow donors within the band gap just below the conduction band. Vacant sites, –S( ), exist at the surface of the material where the molecules of a sensitising species, A (such as O_2 in the case of SnO_x films according to Windischmann and Mark[5]), present in the atmosphere can adsorb to form a species, –S(A). Figure 1.4(b) shows the physisorbed species at a surface site and the transfer of an electron from the conduction band to this species. This creates the negatively charged occupied surface species, $-S(A^-)$ (as O_2^- or O^- for SnO_x according to Windischmann and Mark[5]), which is the sensitising species, as shown in Figure 1.4(c). This transfer depletes the bulk material of electrons, resulting in reduced bulk conductivity with respect to the case in low atmospheric concentrations of the sensitising species. The space charge effects of this depletion and the presence of the

negatively charged species at the surface result in the bending of the conduction and valence bands. Also displayed in Figure 1.4(c) is the physisorption of a reducing gas, R (CO as in the study by Windischmann and Mark[5]), at other vacant surface sites to produce another surface species, -S(R), shown in Figure 1.4(d). Figure 1.4(d) also shows a reaction that can occur between the surface species, $-S(A^-)$ and –S(R), that results in the formation of a new, negatively charged species, B- (or CO_2^- as per Windischmann and Mark[5]), and a vacant surface site shown in Figure 1.4(e). The electron causing the negative charge on the surface species, $-S(B^-)$, can then be transferred back to the conduction band in the bulk material. This transfer results in the increased conductivity of the bulk. Finally, Figure 1.4(f) shows the thermal desorption of the neutral product, B (or CO_2 in Windischmann and Mark's[5] example), of the reaction displayed in Figure 1.4(c) leaving another site, -S( ), vacant at the surface.

This model, as set out by Windischmann and Mark[5], can quite easily be modified to explain the change in resistance (as opposed to conductance as above) of p-type semiconducting gas sensor materials to reducing gases. Very similar steps occur in this case, but the physisorbed sensitising species act as new acceptor states, withdrawing electrons from the valence band and leaving behind electron holes in the valence band which contribute to increased conductivity with respect to lower atmospheric concentrations of the sensitising species. Again, this results in band bending as a result of the space charge effects of the accumulation of electron holes in the valence band and negatively charged species at the surface. The physisorption of reducing gases and their reaction with sensitising surface species then occurs in a similar fashion to the description above. When the electron from the negatively charged reaction product, B^-, is transferred back to the valence band, it fills and cancels out an electron hole, resulting in a reduction in the conductivity of the material and an increase in the resistance of the sensor. Thermal desorption of the product, B, can then occur, as above.

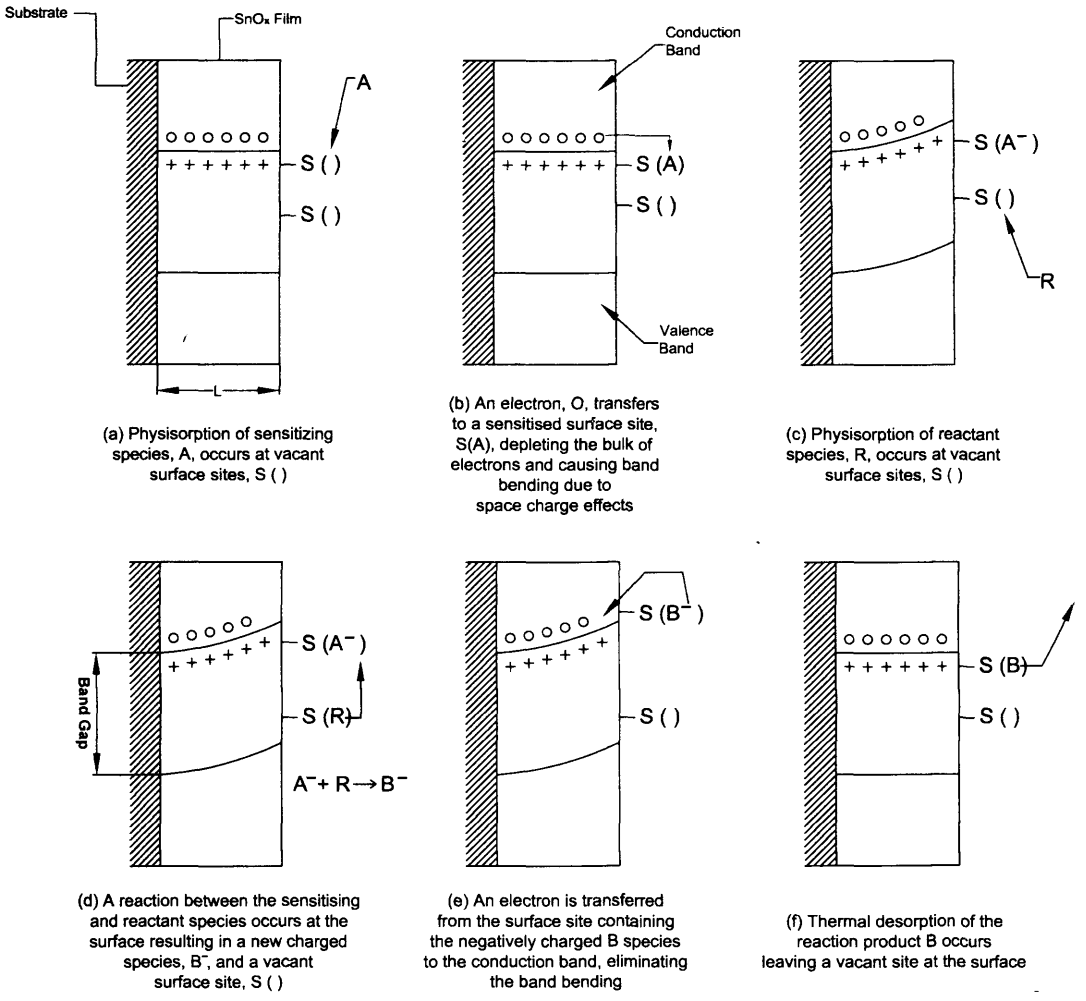

Figure 1.4 Diagram showing the generalised scheme for the response mechanism for tin oxide, SnO_x, thin film of thickness, L, to reducing gases, R, based on the presence of a sensitising species, A, at surface adsorption sites, -S ( ). Electrons in the conduction band are represented by open circles, O, and donor levels just below the conduction band are represented by crosses, +. (Adapted from Windischmann and Mark[5])

Each of the steps in the above scheme can be represented by a chemical reaction. These reactions are presented below in Equation 1.6 to Equation 1.11.

$$S(\ ) + A(gas) \longrightarrow S(A)$$

Equation 1.6 Physisorption of sensitising gas, *A*

$$S(A) + e^{-} \longrightarrow S(A^{-})$$

Equation 1.7 Electron capture by surface species, *S(A)*

$$S(\ ) + R(gas) \longrightarrow S(R)$$

Equation 1.8 Physisorption of reactant gas, *R*

$$S(A^-) + S(R) \longrightarrow S(B^-) + S(\ )$$

Equation 1.9 Reaction between surface species, *S(A⁻)* and *S(R)*, to form a new species, *S(B⁻)*, and a vacant surface site, *S( )*

$$S(B^-) \longrightarrow S(B) + e^-$$

Equation 1.10 Electron release from surface species, *S(B⁻)*

$$S(B) \longrightarrow S(\ ) + B(gas)$$

Equation 1.11 Desorption of product, *B*

Windischmann and Mark[5] reported the sum of the individual reactions Equation 1.8 to Equation 1.11 to give the overall reaction in Equation 1.12 below.

$$R(gas) + S(A^-) \longrightarrow e^- + S(\ ) + B(gas)$$

Equation 1.12 Overall reaction that results in gas response to reducing gases on n-type sensors from the sum of the reaction sequence in Equation 1.8 to Equation 1.11

Equation 1.12 shows that for every reactant gas molecule, R, that reacts at the surface, one electron is released to the conduction band, resulting in the observed increased in the conductivity of the sensors. Windischmann and Mark[5] then go on to formulate an equation that presents the concentration per unit area of surface of electrons in the conduction band, n_{cb}, as a function of the square root of partial pressure of reactant gas, $p_R^{1/2}$, in accordance with their experimental observations on sensors as in Equation 1.13.

$$n_{cb} = \left(\frac{\alpha}{\beta}\right)^{1/2} p_R^{1/2}$$

Equation 1.13 Concentration of electrons in the conduction band, n_{cb}, as a function of the square root of reactant gas partial pressure, $p_R^{1/2}$. α and β are constants of proportionality introduced by Windischmann and Mark[5]

Although Equation 1.13 fits their experimental data of sensor responses to differing CO concentrations, it contradicts the prediction made in Equation 1.12, from their own model, that for every molecule of gas, R, that reacts at the surface, one electron is released to the conduction band. This would predict a linear dependence of the number of electrons in the conduction band, n_{cb}, with the partial pressure of reactant gas, p_R.

Sensor conductance/resistance is often seen to vary with partial pressure of reducing gases in a form similar to that in Equation 1.14[6,7].

$$G = G_0 + A_{gas} p_R^{\beta}$$

Equation 1.14 Conductance, G, of an n-type sensor (or alternatively, resistance of a p-type sensor) having a conductance of G_0 in clean air in response to an atmosphere containing a partial pressure of a reducing gas, p_R. A_{gas} and β for the particular gas in question.

The value of β in this equation is often found to be approximately 0.5. However, this value is found to vary between 0.25 and 1, sometimes even within studies on nominally identical sensors. Williams[7] attempts to reconcile this behaviour through an equation for response that attributes different values of the exponent β to the different oxygen species that have been observed on semiconducting oxides[8]. Thus, for the adsorption and charge transfer to a particular form of the sensitising oxygen species as in Equation 1.15, and for the case of conductance being limited by surface traps, Equation 1.16 shows conductivity as a function of partial pressure of oxygen and reactive gas, R, that reacts with the oxygen at the surface according to Equation 1.17. The variation in the response, i.e. value of exponent β, could therefore be due to the coexistence of these different oxygen species on the surface of sensors with complex variations under differing conditions of oxygen partial pressure and operating temperature.

$$S + e^- + \frac{m}{2} O_2 \underset{K_{-1}}{\overset{K_1}{\rightleftharpoons}} O_m^-$$

Equation 1.15 Surface equilibrium of the adsorption of oxygen species on vacant surface sites, *S*, and charge transfer to these species

$$\sigma = \left(\frac{e\mu N_D h^2}{N_S K_1^0} \right) \left\{ \exp\left[\frac{-(E_S - E_D)}{kT} \right] \right\} \left[p_{O_2}^{-m/2} \left(K_{-1}^0 + K_2^0 p_R{}^m \right) \right]$$

Equation 1.16 the conductivity of a sensor as a function of partial pressure of oxygen, p_{O_2}, and partial pressure of reactive gas, p_R, where the oxygen species vary as displayed in Equation 1.15. *e* is the charge on an electron, μ is the mobility of the majority charge carriers, N_D is the number of ionised donor states, *h* is film thickness, N_S is the number of states, E_S is the activation energy of an electron from a surface state as a result of desorption, E_D is the activation energy for ionisation of a donor as a result of adsorption, *k* is the Boltzmann constant, *T* is the operating temperature of the sensor and the parameters labelled with the character, *K*, are the equilibrium constants from Equation 1.15 and Equation 1.17

$$O_m^- + mR \xrightarrow{K_2} mRO + e^-$$

Equation 1.17 Reaction between the different oxygen species and a reactive gas species, *R*, to produce an oxidised gas, *RO*, and the release of an electron which affects the conductivity of the material

1.4.3 Microstructural Effects on Sensor Response

It is widely known that the microstructural features of a material can greatly affect its physical and functional properties. So it is no surprise that correlations of sensor properties with microstructural features have been widely reported in the field of semiconducting metal oxide gas sensors. A number of studies correlate the magnitude of sensor response with qualitative or quantitative assessments of these microstructural features such as particle size, porosity and/or surface area, as displayed in Table 1.2. Scrutiny of the results of the studies presented in this Table reveals a complex interaction between the effects of different microstructural features on sensor response. There appears to be several instances of disagreement between studies showing correlations of the same sensor properties with the same microstructural features. In most cases this is likely to be a result of a lack of information as some studies only describe the microstructure in terms of a single microstructural feature.

The most consistent correlations between sensor properties and microstructural features occur for the variation of sensor baseline resistance (the resistance of a sensor in an atmosphere of pure air containing only nitrogen and oxygen), response/sensitivity and response time with porosity/density. The effect of porosity is twofold. Firstly, when the material is acting as a resistor, an increase in porosity (which results in a decrease in density) decreases the effective cross-sectional area of the material between the electrodes. This increases the resistance of the material between the electrodes according to Equation 1.1. Thus, the correlation between sensor porosity and baseline resistance is such that an increase in porosity leads to an increase in resistance. Secondly, porosity in a material allows the gases in the atmosphere to penetrate deeper within the material where they can come into contact with the greater surface area that a porous material has to offer. The diffusion occurs with less impedance and occurs more quickly. This means that there is greater potential for interaction between the gases and the material at a greater rate than in denser materials. The greater amount of interaction means that more reactions that affect the resistance can occur, altering the resistance in gas relative to the resistance in clean air by a greater degree. Thus, the correlation between sensor sensitivity and porosity is such that an increase in porosity leads to an increase in sensitivity. The lower impedance to gas diffusion that results from a more porous structure leads to the correlation of lower response times for higher porosity structures.

Table 1.2 Comparison of different studies where sensor properties were correlated with microstructural features

Study	Material	Deposition Method	Sensor Properties Studied			Microstructural Features Correlated				Study Conclusions
			Baseline Resistance	Response	Other	Grain Size	Density/ Porosity	Surface Area	Other	
Nagasawa *et al.*[9]	SnO_2	RF Sputtering		X			SEM (Qualitative)			Dense structure had higher sensitivity to H_2 than open structure
Weber *et al.*[10,11]	SnO_2 with Nb doping	Spin Coating		X	$t_{90\%}$ response	XRD/BET		BET		Increased Nb doping reduced grain size and increased surface area with result of decreased $t_{90\%}$. Maximum response was achieved at intermediate doping levels
Ivaschenko & Kerner[12]	SnO_2	Thin Film Technique			Activation energy of conductivity				Film thickness	Activation energy of conduction decreases with increasing film thickness. Different models for this effect are tested.
Yamazaki *et al.*[13]	SnO_2	DC Sputtering (varying substrate T and discharge gas pressure)	X	X		TEM	Film Density (Calculated from mass and thickness)			Grain size constant with substrate temperature and decreased with increased discharge gas pressure. Film density is highest when substrate temperature is high and discharge gas pressure is low. Sensor resistance is higher for lower density films. Sensitivity shows a maximum at intermediate film densities
Nakatani *et al.*[14]	Fe_2O_3 with Ti, Zr and Sn doping	Co-precipitation and forming of pressed pellets	X	X		TEM&XRD (Qualitative)		BET		Resistance of sensors with varying levels of dopant display minima at around 5 mol% of the oxides of the dopants and increase as purer material compositions are approached. Sensitivities display maxima at around 10 mol% of oxide for Zr and Sn and at 5 mol% oxide for Ti. Effect of dopants is to decrease grain size and increase surface area.
Cosandey *et al.*[15]	SnO_2 and In_2O_3	Not specified		X		Method not specified				Sensitivity increases as particle size is decreased

Table 1.2 Comparison of different studies where sensor properties were correlated with microstructural features

Study	Material	Deposition Method + Variables	Sensor Properties Studied			Microstructural Features Correlated				Study Conclusions
			Baseline Resistance	Response	Other	Grain Size	Density/ Porosity	Surface Area	Other	
Wang *et al.*[16]	Nb_2O_5	Formed on alumina tube, varying calcination temperature	X	X		XRD				Grain size increases with increasing calcination temperature. Baseline increases with calcination temperature. Sensitivity to various gases display maxima at calcination temperatures between 900 and 1000°C
More *et al.*[17]	SnO_2 doped with Cu	Pressed pellets varying sintering temperature	X	X		XRD/SEM				Crystallite size increases with increased sintering temperature. Sensitivity to different species generally increases with increasing sintering temperature and crystallite size with a maximum sensitivity at a sintering temperature of 750°C.
Yamazoe[18]	SnO_2	Varying calcination temperature on pellets	X	X		XRD				Grain size is highly dependent on calcinations temperature. Resistance increases dramatically below a minima at low crystallite size of <10nm and increase gradually above this with increasing crystallite size. Sensitivity increases smoothly with decreasing crystallite size for CO and H_2.
Fliegel *et al.*[19]	SnO_2 doped with Nb, Mn, In and Pd	Manual painting of substrates and variation of sintering temperature and time	X	X		BET		BET		Increasing concentration of all additives results in increased surface area and decreased particle size. Increasing sintering temperature or time decreases surface area. Resistivity generally increases with increasing dopant concentration (except for decrease with Nb). This is due to differing effect of dopant on carrier concentration. Gas sensitivity increases with increasing resistivity.

Table 1.2 Comparison of different studies where sensor properties were correlated with microstructural features

Study	Material	Deposition Method + Variables	Sensor Properties Studied			Microstructural Features Correlated				Study Conclusions
			Baseline Resistance	Response	Other	Grain Size	Density/ Porosity	Surface Area	Other	
Althainz *et al.*[20]	Fe_2O_3	Aerosol deposition of particles from different stages of a cascade impactor and sputtering to different thickness		X	$t_{90\%}$ Response	SEM			Film thickness-SIMS	No significant change in sensitivity for films of different thickness or for granular deposits of different particle size. Sputtered films show increasing response to gases of increasing molecular weight whereas granular films have constant response in the same situation. $t_{90\%}$ increases with film thickness and with particle size. Granular films have shorter $t_{90\%}$.
Yoon *et al.*[21]	ZnO + Corn starch as a fugitive species	Pressed pellets sintered at different temperatures	X	X		SEM	SEM (Qualitative) & Archimedes (Quatitative)			Addition of corn starch inhibited grain growth and decreased sintered density through increased porosity. Higher sintered temperature resulted in grain growth and increased sintered density through reduced porosity. Dense sensors (i.e. those with no starch addition sintered at the highest temperatures) had higher conductivity. Dense sensors have lower sensitivity.
Horrillo *et al.*[22]	SnO_2	RF Sputtering with variation of deposition temperature	X	X		TEM	TEM			At higher deposition temperature more porosity is evident above rough substrate surfaces that is not evident at lower temperatures. Films with higher porosity at higher deposition temperatures have increased baseline resistance and higher gas sensitivities to CO and propanal

Table 1.2 Comparison of different studies where sensor properties were correlated with microstructural features

Study	Material	Deposition Method + Variables	Sensor Properties Studied			Microstructural Features Correlated				Study Conclusions
			Baseline Resistance	Response	Other	Grain Size	Density/ Porosity	Surface Area	Other	
Lee *et al.*[23]	SnO_2	MOCVD for thin films and spin coating of metal organics for thick films		X	Response time	XRD/SEM	SEM(Qualitative)			Thick film sensors had finer crystallite size and higher porosity whereas thin films were dense. Thick films had higher sensitivity to H_2 and CO and responded faster.
Zhang & Liu[24]	SnO_2 doped with CuO	Pressed pellets of sol-gel powders with and without CuO doping that were calcined at different temperatures		X	Response time	SEM(Quantitative)				Increasing sintering temperature and addition of CuO increases particle size. Sensors sintered at lower temperatures had the highest sensitivity to CO_2. Sensitivity to NO was generally higher for CuO doped sensors than pure SnO_2. t90% was shorter with CuO doping.
Kocemba , *et al.*[25]	SnO_2 pure and doped with Al_2O_3, SiO_2 or glass powder	Pellets pressed at different pressures		X	Baseline Stability		Mercury Porosimetry	BET		Effect of increased pressing pressure was an increase in apparent density and a decrease in porosity. With increasing pressure sensitivity decreased and baseline stability increased. Increasing dopant levels increases baseline stability and sensitivity up to approximately 40% dopant. These effects are explained by inhibited grain growth in doped material. Increasing dopant level of these insensitive materials above 40% results in the majority of the material being insensitive to gas.
Bittencourt *et al.*[26]	SnO_2	RF sputtering with varying pressure O_2 compared with drop coating of tin chloride with different evaporation temperatures		X		AFM				Grain diameter for drop coated sensors was approximate twice that of sputtered sensors. Drop coated sensors were much more sensitive to ethanol. Lack of information about porosity and other microstructural features.

Table 1.2 Comparison of different studies where sensor properties were correlated with microstructural features

Study	Material	Deposition Method + Variables	Sensor Properties Studied			Microstructural Features Correlated				Study Conclusions
			Baseline Resistance	Response	Other	Grain Size	Density/ Porosity	Surface Area	Other	
Salehi & Gholizade[27]	SnO_2 doped with varying levels of In	CVD with varying concentrations of $InCl_3$ precursor	X	X			SEM(Qualitative)			Porosity increases with increasing In precursor concentration up to 20wt% $InCl_3$ precursor concentration, after which no change in porosity was observed. Baseline resistance and response to H_2, methanol and CO displayed maxima at 20wt% $InCl_3$.
Ahmad *et al.*[28]	SnO_2 produced by three precipitation methods with varying reactant concentration and another that was commercially sourced	Screen printing followed by sintering for different temperatures and time		X	t90% for response and recovery	XRD/BET		BET		3 SnO2 powders produced by the group had similar particle sizes and surface areas. SnO2 from commercial source had particle size twice that of those produced by group and much decreased surface area. Commercially obtained material consistently had lowest sensitivity to CO and longest response and recovery times. Other SnO_2 powders had high sensitivity to CO and short response and recovery times with exception of that produced from high concentration raw materials which had similar magnitude of response and longer response and recovery times than commercially obtained material. Increasing sintering temperature and time of material produced from dilute raw materials resulted in reduced response whereas other materials displayed no discernible trends with sintering conditions.

Table 1.2 Comparison of different studies where sensor properties were correlated with microstructural features

Study	Material	Deposition Method + Variables	Sensor Properties Studied			Microstructural Features Correlated				Study Conclusions
			Baseline Resistance	Response	Other	Grain Size	Density/ Porosity	Surface Area	Other	
Dolbec *et al.*[29]	SnO_2 doped with ~2at% Pt	Laser ablation at different oxygen pressures		X		XRD/SAED (Qualitative) & TEM (Quatitative)	TEM (Qualitative)			Increasing oxygen pressure during ablation increased crystallite size and porosity. Sensitivity to CO gradually increased from 0 to 100mTorr oxygen pressure and then decreased slightly with increasing pressure. Porosity determined to be key property.
Shoyama & Hashimoto[30]	SnO2	Spin coating $SnCl_2$ with poly ethylene glycol (PEG) additions and different sintering temperatures		X	Response time	SPM/TEM				Particle size was higher for the higher sintering temperature. PEG additions >2wt% resulted in smaller particles. These smaller particles resulted in higher sensitivity to CO and shorter response times.
Ahn *et al.*[31]	SnO_2	Screen printing of powders produced by inert gas condensation method and sintered at different temperatures				SEM/TEM/BET(Quantitative) & XRD (Qualitative)	BET	BET		Particle size increases and surface area decreases with increasing sintering temperature, particularly at the highest temperature of 900°C. Samples generally displayed a bimodal pore structure with fine pores with radius around 10-20nm and coarse pores with radius approximately 80-1000nm. Increasing sintering temperature reduced volume of smaller pores and increased volume of larger pores, particularly at 900°C sintering temperature. Sensitivity to H_2 increased from 500 to 600°C and then decreased significantly thereafter.
Ansari *et al.*[32]	SnO_2	Screen printing of sol-gel derived powders calcined at different temperatures		X		XRD/SEM				Particle size increased with increased calcinations temperature. Sensitivity to H_2 increased steeply as particle size decreased.

Table 1.2 Comparison of different studies where sensor properties were correlated with microstructural features

Study	Material	Deposition Method + Variables	Sensor Properties Studied			Microstructural Features Correlated				Study Conclusions
			Baseline Resistance	Response	Other	Grain Size	Density/ Porosity	Surface Area	Other	
Park & Mackenzie[33]	SnO_2	Solution dip coating, sol-gel process with varying solution concentration and sintering temperature		X	$t_{90\%}$ Response	SEM/TEM	Refractive index method			Film thickness and particle sizes increased with increasing solution concentration when all other conditions remained constant. Increased sintering temperature initially resulted in less porosity up to 400°C but porosity increased afterwards. Sensitivity to ethanol increased with increasing film thickness and a concurrent increase in porosity.
Serventi *et al.*[34]	SnO_2	RF Sputtering with differing substrate temperature		X		SEM/TEM	TEM (Qualitative)			Low deposition temperature structure was porous and granular whilst at high temperature it was compact and columnar with intercolumnar porosity. Sensor deposited on high temperature substrate was twice as sensitive as that deposited at low temperature.
Korotcenkov *et al.*[35]	In_2O_3	Spray pyrolysis with varying temperature of pyrolysis, precursor concentration and volume of sprayed solution			t90% response and recovery	XRD/AFM/ TEM	Refractive index method		Film thickness	Film thickness increased with increasing concentration and volume of the sprayed soloution. Particle size increases with increasing film thickness. Porosity increased with increasing pyrolysis temperature. Sensitivity to ozone decreased with increasing film thickness. Sensitivity to H_2 increased with increasing film thickness. Response and recovery times for ozone increased with increasing film thickness. Response times for CO displayed no variation with grain size but higher porosity films had shorter response times.

Table 1.2 Comparison of different studies where sensor properties were correlated with microstructural features

Study	Material	Deposition Method + Variables	Sensor Properties Studied			Microstructural Features Correlated				Study Conclusions
			Baseline Resistance	Response	Other	Grain Size	Density/ Porosity	Surface Area	Other	
Chabanis *et al.*[36]	CTO	Screen printing of sol-gel powders produced with different composition and stirring conditions		X	Response time	SEM/XRD				Crystallite size was unaffected by stirring conditions. Particle (agglomerate) size decreased with increasing stirring speed. Ethanol sensitivity increased and response time decreased with decreasing particle size.
Shaw *et al.*[37]	CTO	APCVD to varying film thickness		X					Film thickness (SEM)	Ethanol gas response increased with decreasing film thickness

The correlations of sensor properties with particle size are more difficult to interpret. Only three studies published correlations between baseline resistance and particle size[14,16,18]. Wang *et al.*[16] found baseline resistance increased with increasing particle size (brought on as a result of increasing calcination temperature) for n-type Nb_2O_5. No conclusions were made regarding the mechanism for conductance change from these studies. Typically there could be two mechanisms in particular that would act to change conductance with changing particle size. The first is that of a decrease in the number of particle boundaries as particle size increases. The presence of particle boundaries tends to result in increased resistance as they represent incongruity of structure between neighbouring particles. The passage of conduction carriers through the particle boundary defects is typically more difficult than through the unperturbed lattice of the bulk of the material. Thus, with increasing particle size, the number of resistance increasing boundaries becomes less and so the resistance of the material will become less. However, this is not what was found from this study. Another mechanism which may be acting is one that depends on the decreasing surface area with increasing particle size. Since the sensitising species at the surface of the material withdraw electrons from the conduction band in an n-type sensing material, the reduced surface area of materials that have larger particles means there is less potential for these resistance increasing (i.e. conductance decreasing) reactions. Thus, with increasing particle size and decreasing surface area, the resistance decreases. This mechanism also fails to explain the observations of this study and without further experimental evidence on this material it is not possible to determine the mechanisms responsible for the change in resistance observed with calcination temperature.

Fliegel *et al.*[19] found baseline resistance increased or decreased with increasing particle size as a result of changing dopant concentration for n-type SnO_2. The differences in this study were put down to differences in the way that the dopants affected carrier concentrations in the material. Increases in manganese, palladium and, to a lesser extent, indium dopant concentrations all result in decreases in electronic carrier concentration in the material. This effect on carrier concentration would negate, or cloud, the effects of particle size. Increasing niobium concentration affected the carrier concentration to a much lower degree, such that the effects of the dopant on particle size were probably the dominant factor on resistance. This study

concluded that the effect of increasing particle size was a decrease in resistance. This conclusion agrees with the effects of both of the mechanisms of resistance modulation with particle size discussed in the previous paragraph.

Yamazoe[18] presented results of an initial strong decrease of resistance with increasing crystallite size to a minimum followed by a much slighter increase in resistance with further increasing crystallite size. The initial strong decrease observed agrees with the mechanisms discussed above. The mechanism for the slight increase with further increasing crystallite size cannot be determined from the information present. Yamazoe[18] does, however, present a model that accounts for the relatively small variation of resistance at higher crystallite sizes and the change to massive variation at smaller crystallite sizes. This model will be discussed below as it is also used to explain the effects of crystallite size on sensitivity.

The variation of sensitivity with particle size is a much more widely reported correlation than that of the resistance, presumably because this property is of prime importance in gas sensing applications. The majority of the studies report that sensitivity increases as particle size decreases[15,18,23,25,28,30,32,36,37]. These studies are characterised by the variation of a production variable that has been observed to affect only particle size to any significant extent. Thus, calcination/sintering temperature is a variable that has been varied in several of the studies[18,28,30,32], as it is a very simple variable to modulate and it can significantly affect particle size. However, there are just as many studies that present correlations of sensitivity with particle size that do match this simple behaviour[10,11,14,17,16, 20,21,24,29,31,33].

In many of these studies a maximum of sensitivity with decreasing particle size was achieved[10,11,14,16,17,21,31,33]. In most of these cases this is likely to be due to the effects of the dopants used to generate the differences in particle size[10,11,14,16,17]. In the study by Ahn *et al.*[31] a large change in the distribution of porosity is observed as small pores are eliminated with increasing sintering temperature and larger pores increase in size. However, it is not apparent from the data presented whether total porosity is changing and whether this may be a factor in the change of sensitivity. Also apparent from the SEM and TEM micrographs presented by Ahn *et al.*[31] is the fact that the boundaries between particles change from being relatively small contacts or

boundaries to significant necks. This factor may account for the difference in how changing particle size affects sensitivity between this study and the earlier studies. The study by Yoon *et al.*[21] also shows results that display a strong variation in porosity concurrent with the changes in particle size. The decrease in porosity with increasing sintering temperature (and the corresponding decrease in particle size) could, as described above, lead to a reduction in the amount of gas that can interact with a reduced surface area. This effect would lead to a decrease in sensitivity as a result of the decreased porosity which would compound with any decrease in sensitivity with increasing particle size as described in the earlier studies. The decreasing sensitivity with decreasing particle size below this minimum may be a result of a change in the particle boundaries from significant necks to finer boundaries, as with the SEM/TEM results in the study by Ahn *et al.*[31]. Porosity is also a significant factor in explaining the maximum in sensitivity with film thickness observed in the study by Park *et al.*[33]. (Here it will be assumed that, for thin films, film thickness is equivalent to particle size. Thus, a decrease in sensitivity should be correlated with an increase in film thickness as with the decrease in sensitivity with increasing particle size described in the earlier studies.) However, there is a strong initial increase in porosity in this study with increasing film thickness that plateaus as the film reaches a thickness of 40 nm. The sensitivity increases as a direct result of this increase in porosity, negating any effects of the increase in film thickness. With increasing film thickness above 40 nm the porosity remains approximately constant and the effects of increasing film thickness take over and the sensitivity begins to decrease from its maximum value.

A single study presents results displaying the reverse trend of decreasing sensitivity with decreasing particle size[29]. However, an increase in porosity is noted to occur at the same time that the particle size is increasing. This increase in porosity would increase the amount of interaction between a greater surface area as described above. Thus, the sensitivity would be greatly increased. Another study presents results that display no variation of sensitivity with particle size or film thickness[20]. However, there is a lack of any other information about the sensors and so the results of this study are somewhat inconclusive.

The study by Yamazoe[18] presents a model that goes some way to explaining some of these trends. This model is presented in the following section.

1.4.3.1 Space Charge Model of Sensors and Microstructural Effects

The ideas in the model presented by Yamazoe[18] concern a space charge layer that is the result of the charge transfer to the sensitising species in the model presented above in section 1.4.2. This layer is commonly referred to as the depletion layer, and its depth is related to the Debye length. This Debye length changes in response to gases as the number of electrons withdrawn from the material to the surface sensitising species changes. Specifically, this model relates how the distribution of this layer throughout the material varies with particle and neck size. Figure 1.5 displays the three cases of particle geometry that are described by this model. These three cases are defined by the depth of the depletion layer, L, relative to the size (or diameter in this simple model) of the crystallites, D.

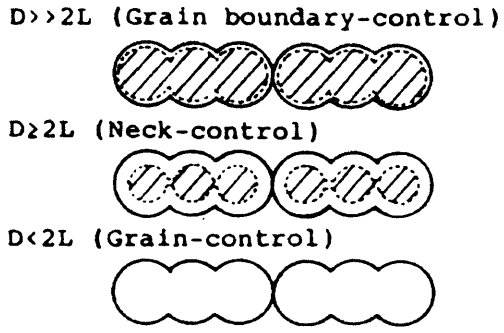

Figure 1.5 Model of sensors whereby the surface layer is depleted of electrons and different grain geometries give rise to differences in which regions contribute most to sensitivity. The model of the microstructure is a relatively simple collection of spherical particles joined predominantly by necks but also by a few grain boundaries. From Yamazoe[18]

In the first case, where D >> 2L, the depletion layer accounts for a relatively small volume of the particles and is restricted to the region closest to the surface in all gas environments. The modulation of the materials conductivity is concentrated at the surface and, in particular, at the grain boundaries with relatively little effect in the other regions. The conductivity in this case is therefore dependent primarily on these grain boundaries and this case is referred to as the "Grain boundary-control" case. This case is used by Yamazoe[18] to explain the lack of variation of sensitivity found

for high crystallite sizes. It may also explain the lack of variance noted for sensitivity with particle size in the study by Althainz *et al.*[20].

In the second case, where $D \geq 2L$, the depletion layer is of a size approaching that of the particle diameters. Thus, when the depth of the depletion layer changes through gas exposure the conductivity of not only the surface and grain boundary regions are affected but the conductivity of the necks between the particles is significantly affected. This occurs because the exposure to gas results in the changing depth of the depletion layer. Thus, the effective cross-sectional area of the necks is significantly affected which carries through to their effective contribution to resistance according to Equation 1.1. Since it is the variation of the resistance of the necks that is most significantly affected this is referred to as the "Neck-controlled" case.

In the final case, where $D < 2L$, the depletion layer engulfs the entire particle. The depth of the depletion layer cannot change in this case. Instead, the concentration of electrons in the whole particle (or grain) changes as a result of the changes in gas concentration and the concentration profile of electrons through the material becomes more or less steep. This is referred to as the "grain-control" case and the structure in this case is predicted to be the most sensitive to gas exposure. Thus, the aim of the sensor designer has been to produce sensors having very small particles. This case was used by Yamazoe[18] to explain the extreme dependence of sensitivity of crystallite size seen for the smallest crystals observed in this study.

The model presented by Yamazoe[18] also explains how various dopants of different valency to the host material may affect gas sensitivity. The example presented in this study is that of doping n-type tin oxide where the tin ions have a valency of 4+ with ions of aluminium of valency 3+ or ions of antimony of valency 5+. The valency of 3+ for the aluminium ions means that in an ionic bond they transfer 3 electrons to the ionic bonding in the surrounding environment. However, each of the tin ions in a perfect tin dioxide lattice would be providing 4 electrons to the surrounding environment in their ionic bonds. This means that when an aluminium ion (Al^{3+}) is substituted for a tin ion (Sn^{4+}) the Al^{3+} ion is not providing enough electrons to satisfy the surrounding environments requirements for ionic bonding. Thus, electrons are more tightly bound to these environments (this defect is an electron hole that acts

as a sink for the electrons from the conduction band). The sensitising reactions that abstract electrons from within the material must therefore probe more deeply for their electrons resulting in an effective increase in the depth of the space charge layer related to the Debye length. This means that when the reactions between a gas and the charged sensitising species at the surface occur, the electrons that are released return to affect the conductivity more deeply within the material than when the material is not doped with aluminium ions. Conversely, the valency of 5+ of the antimony ions means that they contribute 5 electrons to the ionic bonding in their environment. This is more than tin ions in the unperturbed tin dioxide lattice would be providing and the electrons in this environment are less tightly bound (the antimony is acting as another donor state for electrons, in addition to those already present in the tin dioxide that are responsible for this material's n-type conductivity). Therefore, the sensitising reactions do not need to reach as far into the material for the electrons they abstract resulting in a decreased depth of the space charge layer related to the Debye length. When the reactions occur between the sensitised surface species and the reactive gas the electrons are released only to the material nearest the surface and there is a relatively shallow effect on the material's conductivity.

Also presented by Yamazoe[18] are two mechanisms which account for the sensitisation of oxide semiconductors by noble metal additives. Specifically, Yamazoe[18] notes that adding silver and palladium to tin dioxide affects the work function of the oxide whilst the addition of platinum does not. The two mechanisms are termed chemical (as for sensitisation of SnO_2 by Pt) and electronic (as for sensitisation of SnO_2 by Ag or Pd) and they are explained pictorially in Figure 1.6.

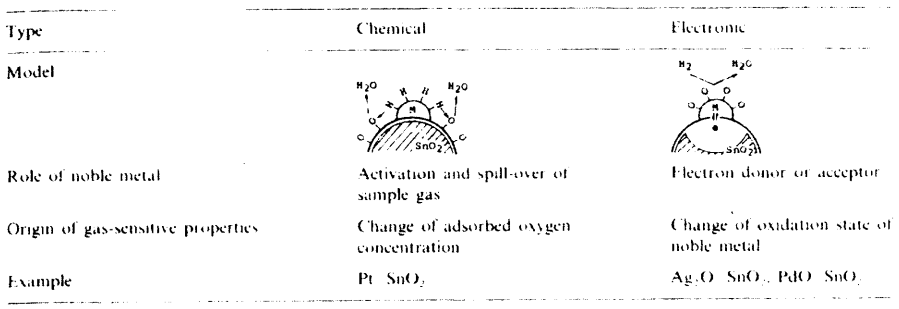

Figure 1.6 Space charge model of metal oxide gas response and sensitisation by noble metal dopants. From Yamazoe[18]

In the chemical mechanism the noble metal is thought to stay in an unoxidised condition in a clean air atmosphere. In this unoxidised condition it does not directly affect the underlying metal oxide's resistance. In an atmosphere containing reactive gas the gas is activated on the noble metal surface from where it spills over to the oxide surface. At the oxide surface it reacts in the same fashion with the sensitising species it would encounter on an undoped metal oxide surface. Thus, the rate of the chemical reactions that result in the gas response is increased and the speed of the gas response is increased.

In the electronic mechanism the noble metal is thought to exist in different oxidation states depending on the composition of the atmosphere. In an atmosphere containing oxygen but not reactive gas the noble metal assumes an oxidised state (e.g. Ag_2O or PdO). In this state a strongly electron depleted space charge region is formed within the underlying metal oxide. In an atmosphere containing reactive gas the oxidation state changes such that the noble metal is now in metallic form (e.g. Ag or Pd). In this state the electrons are returned to the underlying metal oxide and the strongly electron depleted region is saturated with electrons, increasing its conductivity in the case of n-type SnO_2.

This model was used to explain the trends in sensitivity with particle size from experimental data in the observations made by Yamazoe[18]. It is also fitting to attempt to explain the variations of sensitivity with particle size noted in the other studies discussed above in section 1.4.3. The reports by Cosandey *et al.*[15], Lee *et al.*[23], Ahmad *et al.*[28], Shoyama and Hashimoto[30] and Ansari *et al.*[32] concern particles that have very small sizes of less than 20-50 nm. At these low particle sizes changes in particle size are likely to affect the sensitivity according to the grain-control case of the space charge model. This case of the model accounts very well for the significant changes of sensitivity with particle size that are observed in these studies. The changes in particle size in the study by Kocemba *et al.*[25] were achieved through additions of Al_2O_3. As discussed above, when aluminium ions exchange for tin ions in the tin dioxide lattice it increases the Debye length and thereby increases the sensitivity of the material. So, this effect would compound and cloud the effects of decreasing particle size that is achieved as a result of doping with alumina such that it is only possible to say that the increase in sensitivity observed may be a result of

either or both the doping with aluminium ions and the changes in particle size and not one or the other. The study by Chabanis *et al.*[36] reports that crystallite size does not vary for their different preparation methods at approximately 40 nm whilst the size of agglomerates of these crystals varies between 0.7 and 10 μm. As the size of these agglomerates are significantly larger than those in the above studies it may be expected that a different case of the space charge model will be operating. However, the sensitivity of the sensors in this study varies significantly with the range of sizes. This effect is most likely due to a change in the number of grain boundaries that are accessible to gas that occurs when the size of the agglomerates changes as well as the increase in surface area. Thus, it is not just the particle size that is important in the space charge model but also the surface area and the arrangement and distribution of the different microstructural regions and this clearly demonstrates the material's resistance being determined by the grain boundary-control case of the space charge model. The study by Shaw *et al.*[37] reports a slight increase in sensitivity with decreasing film thickness. As this occurs at thicknesses of between 500 and 1500 nm this slight dependence of sensitivity on film thickness could be explained by the operation of the grain boundary or neck-control cases of the space charge model.

The maxima in sensitivity with decreasing particle size in the studies by Weber *et al.*[10,11] and Nakatani *et al.*[14] can be put down to the use of dopants to control particle size. Initially the effects of small concentrations of dopant lead to a significant decrease in the particle size which results in the initial increase in sensitivity accorting to the grain-control case of the space charge model. Further substitutional doping with ions of higher valency than the host (Weber *et al.*[10,11]: Nb^{5+} into SnO_2 where the valency of Sn is 4+. Nakatani *et al.*[14]: Ti^{4+}, Zr^{4+} and Sn^{4+} into Fe_2O_3 where the valency of Fe is 3+) leads to lower sensitivity of the resistance of these n-type materials according to the discussion of dopant effects on the space charge model presented above. As discussed above the studies by Ahn *et al.*[31] and Yoon *et al.*[21] show sensitivity maxima with decreasing particle size whilst Dolbec *et al.*[29] show decreasing sensitivity with decreasing particle size. These unusual variations of sensitivity with particle size are accounted for by the changes in porosity which occur concurrently to the changes in particle size, as discussed above.

Overall the space charge model accounts very well for the variations in sensor properties with changes in microstructure and with changes in material composition. However, the next challenge is to relate not just the ideas to the microstructural changes but to somehow quantify the effects of these microstructural changes in terms of the model on experimental data. Efforts that have been made in this respect will be discussed in the next section.

1.4.3.2 Other Efforts to Model the Effects of Microstructure on Sensor Response

The model described by Yamazoe[18] accounts well for much of the behaviour observed for sensor properties that vary with microstructure. However, in the studies so far discussed it has only be used indirectly to guide the sensor designer towards superior microstructures and compositions, predominantly through very simple changes in processing and manufacture. In order to learn more about the sensor materials it is necessary to modify an existing model or create a new model that can be applied directly to experimental data to provide more detailed information about the mechanisms responsible for changes in sensor properties with microstructure, composition and operating conditions. The research group led by Williams have attempted a more rigorous characterisation of the microstructural effects on sensor properties. This work is discussed below.

The principal work presented by the Williams group is that by Williams and Pratt[38]. This work was based on the simulation of sensor microstructures composed of spherical particles of varying size and randomly distributed on a simple cubic array of elements, typically 60 x 60 x 60 elements on a side. These elements had sides of fixed length equal to the Debye length. Only the conductivity of the material at the surface was assumed to vary with gas composition down to a depth equal to the length. All other material was assumed insensitive to gas. Contacts to electrodes were placed on one opposite pair of faces of the cube and cyclic boundary conditions to the other faces. The conductance or resistance of the cube was then calculated according to an iterative procedure described in the text, both in clean air and in response to gas. The response of the cube was then calculated and plotted for the different gas concentrations and microstructures, particularly in terms of porosity.

The first observation made in this study is that there is an upper limit on the amount of porosity above which a single conductive mass is not achieved. When the individual particles are simply the cubes in a simple cubic array this limit is at 75% porosity. When the particles are formed as spheres composed of groups of these individual cubes randomly distributed on the array this limit is 71% porosity. These figures mean that for a conduction path to exist in a solid it must have less than approximately 70-75% porosity depending on microstructure. Sensitivity was also noted to vary parabolically with porosity, displaying maxima at approximately 40% porosity where the particles were the elementary cubes of the simple cubic array and distributed randomly to approximately 60% porosity where the particles were spherical clusters of these elements randomly distributed on the array. These maxima in sensitivity have been observed in many of the experimental studies discussed above which is an encouraging sign that this simulation is producing results that agree with experimental observations. This effect is explained in this study by the competing effects of response increasing with increasing surface exposed (which experiences a maximum at approximately 25% porosity in this study) and decreasing with decreasing conductivity (which continually decreases with increasing porosity). Finally, this study concluded that the best empirical representation for a p-type sensor was that of a simple series-parallel resistor network, as presented in Figure 1.7, through fitting the simulated data to equations representing this model.

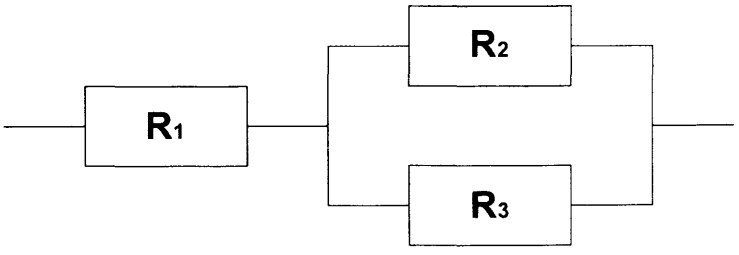

Figure 1.7 Illustration of the simple resistor network which was found as a good empirical fit to the data simulated by Williams and Pratt. Only R_3 was considered as gas sensitive in this study

This model has been used by Williams in a number of studies to relate sensor properties to microstructures[39,40,41,42,43]. The most relevant of these to this present work, is that by Chabanis *et al.*[39]. Both simulated and experimental data are presented by Chabanis *et al.*[39]. The simulated data was generated through the use of

a resistor network as described in Figure 1.7, where one of the resistors in the parallel section is allowed to vary with gas concentration as per Equation 1.18. The response data generated for different values of the three resistors was fitted to the form of Equation 1.14. The values of β obtained were plotted versus the values obtained for α, as shown in the chart reproduced in Figure 1.8. This figure shows that α and β are correlated with one another and that they are highly dependent upon the relative values of the resistors. These resistors can be thought of as representing different regions of the microstructure. As such, R_3 can be thought as representing the gas sensitive surface, R_2 the gas insensitive bulk and R_1 the gas insensitive junctions between particles. It is now possible to interpret the effect of a change in particle size on the values obtained for α and β from this simulated data. A decrease in particle size would lead to more of the material being classified as gas sensitive surface relative to that classified as gas insensitive bulk. With a decrease in particle size the contribution to the resistance of the sensors from the surface would increase relative to that of the bulk. This increased contribution of the surface to the resistance of the sensor as particle size is reduced is represented by an increase in the value of Q, as in Figure 1.8 which shows that β decreases as a result. Experimental data was also obtained for sensors made from CTO powders having different particle sizes, 0.7, 2 and 10 μm. These data showed a decreasing value of β with a decrease in the particle size which confirms the observed trend of the simulated data. This is taken as a good indication of the simple resistor network's validity in terms of representing real sensor responses. However, this approach is still not applying the microstructural model directly to the experimental data, as would be preferable.

$$R_3 = R_3^0\left(1+P\right)$$

Equation 1.18 R_3 from Figure 1.7 as a function of partial pressure of reactant gas. R_3^0 is the clean air baseline resistance of the sensor.

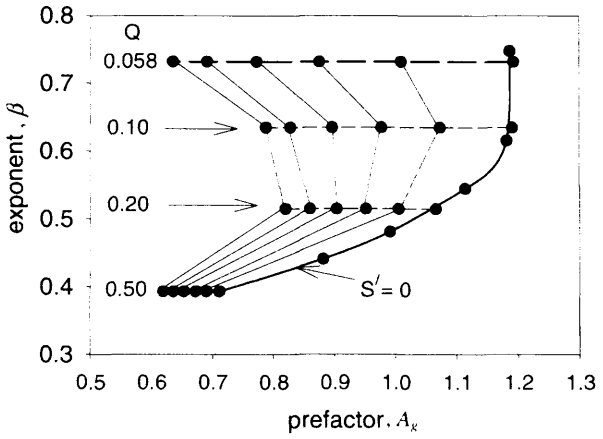

Figure 1.8 response data simulated from the resistor network in Figure 1.7 and fitted to the form of Equation 1.14 yields values of α and β which are plotted in this chart for sensors of different microstructure generated by the varying values of the resistors where $Q=R_3^0/R_2$ and $S'=R_1/R_2$. From Chabanis *et al.*[39]

1.4.4 The Microstructural Model Used in this Study

The present work will attempt to fit experimental response data to equations that represent the microstructure of the sensors as a simple resistor network. This resistor network is similar to that presented by Williams and Pratt[38] and Chabanis *et al.*[39]. However, in this work the different resistors will be attributed directly to the different notional regions of microstructure, the surface, the bulk and the particle boundaries, as presented in Figure 1.9. The total resistance of this simple resistor network can be described by Equation 1.19.

$$R_T = R_{PB} + \frac{1}{\frac{1}{R_S} + \frac{1}{R_B}}$$

Equation 1.19 Total resistance, R_T, of the resistor network shown in Figure 1.9 where R_S is the resistor representing the surface of the particles, R_B is the resistor representing the bulk and R_{PB} is the resistor representing the boundaries between the particles

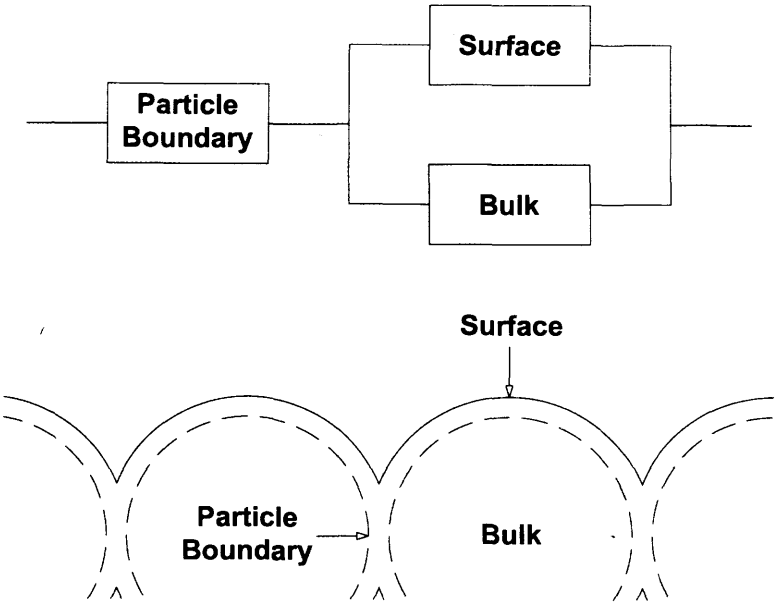

Figure 1.9 The resistor network used in this work and how it related the different resistors to different microstructural regions. The solid line represents the interface between the solid sensor material and the gas whilst the dashed line represents the depth below this interface equal to the Debye length of the material.

It will be assumed that the resistance of the surface and particle boundary regions, which are directly accessible to the gas, will be gas sensitive. The form of the gas response at the gas sensitive regions in the steady state after a step change in the reactive gas concentration will be that given in Equation 1.20. This is the equation that gives a resistance increase for reducing gases (CO, propane etc.) on a p-type material such as CTO. A linear dependence of resistance on gas concentration is likely, as per the discussion by Windischmann and Mark[5], so, β will be assumed to be equal to 1. Therefore, it is postulated that the approximate square root dependence of sensor resistance with gas concentration that is commonly observed for the responses of sensors in experiments is a result of the effects of microstructure. This would account for the variance in the value of β found from fits of the experimental response data to the empirical equation given in Equation 1.14.

$$R_x = R_{x,0}\left(1 + A_{gas}[gas]^{\beta}\right)$$

Equation 1.20 Form for the steady state resistance achieved in a gas concentration, [*gas*], for the gas sensitive microstructural regions (where *x* is *S*, surface, or *PB*, particle boundary) having a clean air starting resistance of $R_{x,0}$. A_{gas} is a constant for a particular gas and sensing material and is hereafter referred to as the sensitivity parameter. β is the response exponent.

Time dependence of Equation 1.20 may be represented for the case of the transient response by Equation 1.21.

$$R_x = R_{x.0}\left(1 + A_{gas}[gas]^{\beta}\left(1 - e^{-t/\tau}\right)\right)$$

Equation 1.21 Time dependent form of Equation 1.20 where t is the time after a step change in concentration of the gas and τ is a time constant

Substituting Equation 1.21 into Equation 1.19 for the gas sensitive regions gives.

$$R_{T,t} = R_{PB,0}\left(1 + A_{gas}[gas]^{\beta}\left(1 - e^{-t/\tau}\right)\right) + \frac{1}{\frac{1}{R_{S,0}\left(1 + A_{Gas}[gas]^{\beta}\left(1 - e^{-t/\tau}\right)\right)} + \frac{1}{R_B}}$$

Equation 1.22 for the resistance, $R_{T,t}$, of a sensor at time, t, after a step change in concentration of gas

The response of a sensor may be calculated at any time, t, after a step change in concentration of gas by dividing by the total response of the sensor in clean air, as in Equation 1.23.

$$\frac{R_{T,t}}{R_{T,0}} = \frac{R_{PB,0}}{R_{T,0}}\left(1 + A_{gas}[gas]^{\beta}\left(1 - e^{-t/\tau}\right)\right) + \frac{1}{\frac{1}{\frac{R_{S,0}}{R_{T,0}}\left(1 + A_{Gas}[gas]^{\beta}\left(1 - e^{-t/\tau}\right)\right)} + \frac{1}{R_B / R_{T,0}}}$$

Equation 1.23 Response of a sensor at time, t, after a step change in concentration of gas

The steady state form of this equation is given in Equation 1.24.

$$\frac{R_{T,t}}{R_{T,0}} = \frac{R_{PB,0}}{R_{T,0}}\left(1 + A_{gas}[gas]^{\beta}\right) + \frac{1}{\frac{1}{\frac{R_{S,0}}{R_{T,0}}\left(1 + A_{Gas}[gas]^{\beta}\right)} + \frac{1}{R_B / R_{T,0}}}$$

Equation 1.24 Form of Equation 1.23 in the steady state case, i.e. at infinite time, t

At zero concentration of gas, i.e. for the clean air baseline resistance, Equation 1.24 simplifies to that in Equation 1.25.

$$\frac{R_{T,t}}{R_{T,0}} = \frac{R_{PB,0}}{R_{T,0}} + \frac{1}{\frac{1}{\frac{R_{S,0}}{R_{T,0}}} + \frac{1}{\frac{R_B}{R_{T,0}}}}$$

Equation 1.25 Form of Equation 1.24 at zero concentration of gas, i.e. the clean air baseline resistance

The main aim for this work is to generate experimental data for sensors that have gradational and/or dramatic differences in their microstructures. The response data obtained for this data will then be subjected to attempts to obtain solutions of this data to Equation 1.24 and Equation 1.23. It is thought that if these attempts are successful then the values of the parameters these solutions yield for $R_{PB,0}/R_{T,0}$, $R_{S,0}/R_{T,0}$ and $R_{B,0}/R_{T,0}$ ought to show clear trends with microstructural features such as particle size. Furthermore, it is thought that A_{gas} and τ should be constants for a particular material tested to a particular gas.

1.5 An Introduction to Chromium Titanate (CTO)

Chromium titanate, chromium titanium oxide, $Cr_{2-x}Ti_xO_3$, or CTO as it is commonly abbreviated, is a metal-oxide material that has proved to be useful in gas sensing applications to detect species including hydrogen (H_2), carbon monoxide (CO), ammonia (NH_3), hydrogen sulphide (H_2S), ethanol and liquefied petroleum gas (LPG).[44,45,46,47,48,49,50,51,52,53,54] Its main beneficial properties over the more commonly used tin dioxide based sensors include superior baseline stability[2,44,47,48] and lower cross-sensitivity to water vapour in the form of humidity.[2,44,47,48,49] The results of the work by Neri *et al.*[55] which claims a high sensitivity to humidity for one of their CTO preparations are likely due to the low 'calcination' temperature of 200°C that was used. This temperature is unlikely to be sufficient for the conversion of their materials to a crystalline form of CTO as is evidenced by their XRD analysis for this material which shows no peaks at all, relating to CTO or otherwise. The high

humidity sensitivity observed for this material is likely to be due to some very different mechanism than that which operates on sensors made of crystalline CTO. Neri *et al.*[55] also calcined samples at the higher temperatures of 400 and 900°C. These samples did display peaks that were attributed to CTO and the sample subjected to 400°C displayed a sensitivity to humidity that appeared to be virtually none existent up to 80% relative humidity (%RH) in agreement with all other works. These beneficial properties of CTO allow devices to be constructed that require more infrequent recalibration and fewer false alarms. As a result the commercialisation of sensors based on the CTO material was initiated by Capteur Sensors Limited, now part of City Technology Limited[2], in the early 1990s.

Phase diagrams have been produced for the Cr_2O_3-TiO_2 system. The range of stoichiometry of $Cr_{2-x}Ti_xO_3$ commonly used to produce CTO sensors is such that $0.05 \leq x \leq 0.2$. In this range of composition the phase diagram obtained by Werner and presented by McHale[56] displayed the phases present above 1300°C were a solid solution of Cr_2O_3 and TiO_2 with the eskolaite structure and an E-Phase of variable composition that existed in all but the lowest concentrations of TiO_2 (below approximately 2 mol% TiO_2, or where $x \sim 0.04$ or below). At these low concentrations of TiO_2 only a solid solution of TiO_2 in Cr_2O_3 with the eskolaite structure was determined to exist. Pownceby *et al.*[57] present ternary phase diagrams for the Fe_2O_3-Cr_2O_3-TiO_2 system which display a solid solution of TiO_2 in Cr_2O_3 in the eskolaite form for the range of stoichiometry commonly used ($0.05 \leq x \leq 0.2$) above 1000°C.

Many studies that have been conducted on CTO materials and have presented x-ray diffraction (XRD) data on their samples to elucidate the structural form of their materials and the phases present.[44,46,47,49,50,51,55,58,59] All of these studies conclude that a solid solution of TiO_2 in Cr_2O_3 exists in the eskolaite structural form as the major phase present for the materials of stoichiometry up to $x = 0.45$. In a few of these studies, particularly those that study CTO compositions that would result in a stoichiometry of $x \geq 0.2$, the presence of small quantities of various second phases was deduced from the presence of a few smaller peaks in the XRD data. McBride and Brydson[59] report the presence of a second E-phase of $Cr_2Ti_2O_7$ in addition to the major α-Cr_2O_3 eskolaite phase in a sample of $Cr_{1.8}Ti_{0.2}O_3$ sintered in air at 1400°C.

Of particular interest in this work are the results from selected area electron diffraction (SAED) tests on the sample of identical composition but sintered in a reducing atmosphere where the conclusion was made that substitution of Ti for Cr in α-Cr_2O_3 occurs and does not affect the structure or the symmetry of the eskolaite unit cell. A two phase structure was also observed by Chabanis *et al.*[46] for samples where $x > 0.2$ and the sintering temperature was 1000°C, with the primary phase consisting of titanium substituted Cr_2O_3 eskolaite structure but the second phase identified by the single peak at $2\theta = 54.8°$ forming the shoulder of a Cr_2O_3 (116) peak was attributed to $CrTiO_3$ through reference to a report by Somiya *et al.*.[60] Jayaraman *et al.*[51] also noted a shoulder on the (116) Cr_2O_3 peak at $2\theta = 54.35°$ in a sample of CTO produced to attain $x = 0.1$ and 0.2 and sintered at 1000°C. This peak was attributed to $CrTiO_3$, as per JCPDS pattern 33-408. In later work[50] they noted the presence of some small peaks at $2\theta = 26.45$ and 28.60° in addition to the (116) Cr_2O_3 shoulder at $2\theta = 54.35°$. In contrast to their earlier work these peaks they attributed to a phase of $Cr_{0.92}Ti_{1.08}O_{3.54}$, as per JCPDS pattern 30-0417. For lower sintering temperatures these peaks were not detected and they concluded the presence of a single phase of titanium substituted Cr_2O_3. Overall, all these studies concur about the presence of the major phase being a solid solution of TiO_2 in Cr_2O_3 having an eskolaite structure. At the higher concentrations of TiO_2 required to achieve CTO compositions where $x \geq 0.2$ the presence of a second phase is detected by XRD, the nature of which is somewhat disputed.

The eskolaite structure noted in the above studies is related to the α-alumina corundum structure. It is composed of oxygen ions (O^{2-}) and chromium ions (Cr^{3+}). As displayed in Figure 1.10, the oxygen ions form close-packed hexagonal layers which stack alternately in the A and B positions. Between each pair of oxygen ion layers there is a layer of chromium ions which occupy two thirds of the octahedral interstices in the C positions, as shown in Figure 1.10. The empty site in each successive chromium ion layer alternates in position between the three possible sites in the C layer in a regular, repeating manner such that the structural unit cell is as shown in Figure 1.11. This unit cell displays another way of viewing the eskolaite crystal structure as face-sharing $\{Cr\}O_6$ octahedra.

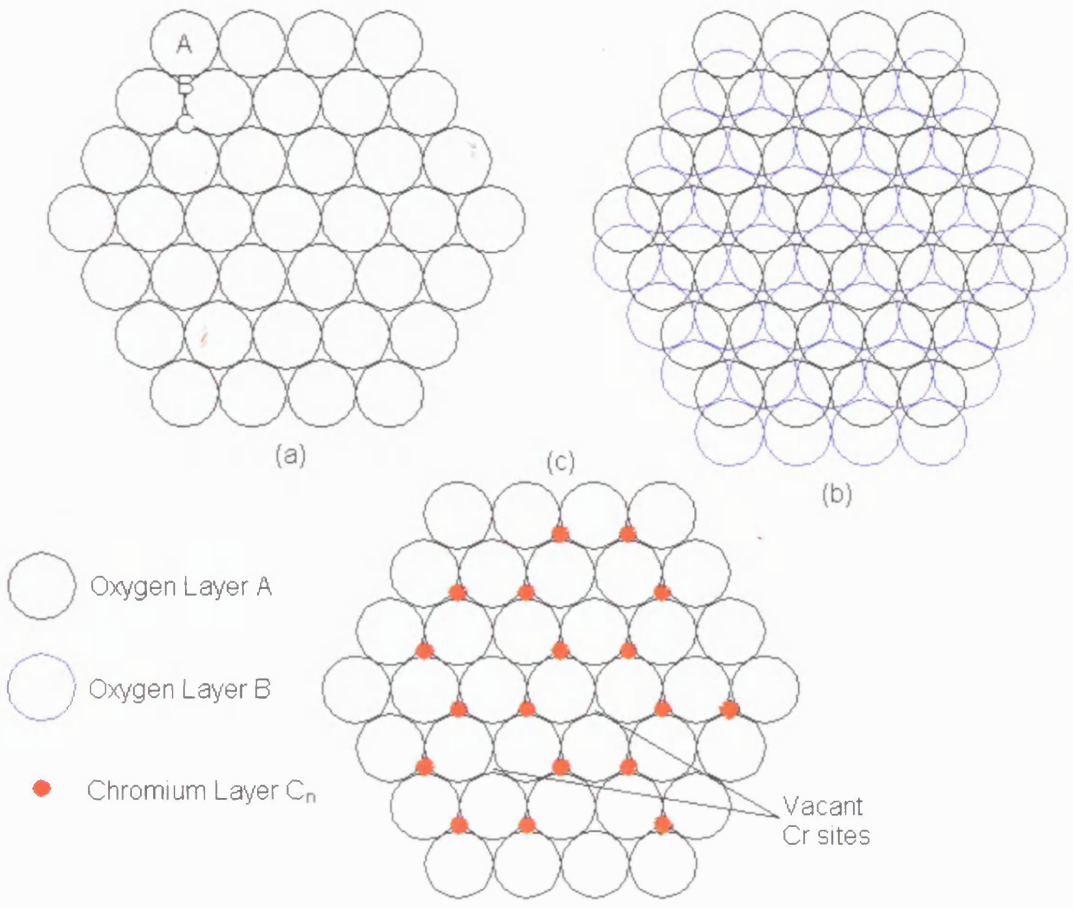

Figure 1.10 crystal structure of eskolaite showing the close packed hexagonal oxygen ions in positions A and B and the chromium ions occupying two thirds of the octahedral sites in layer C

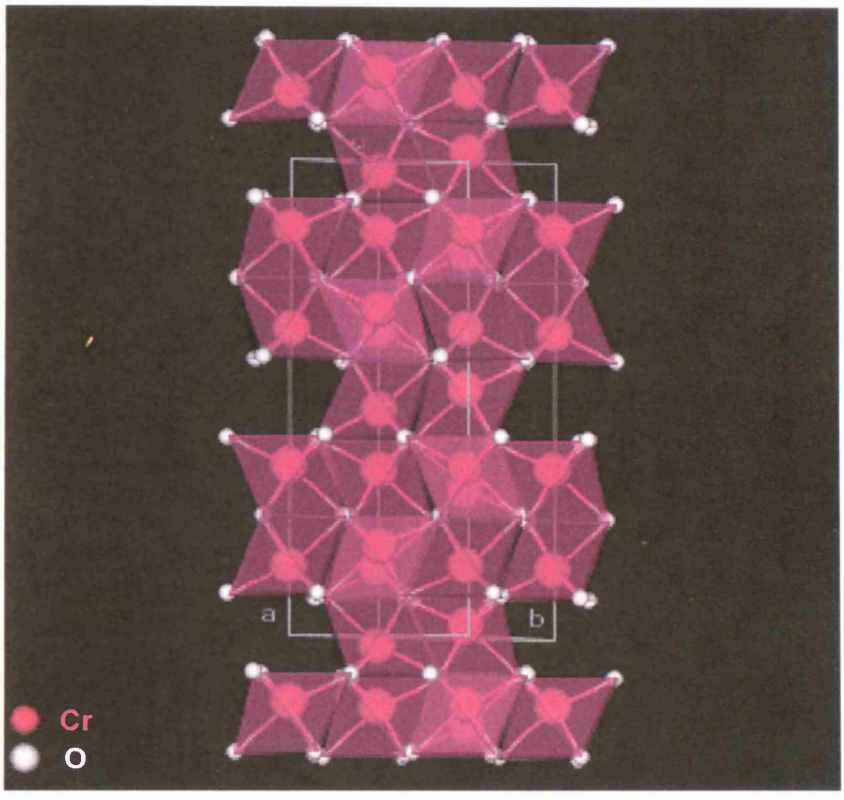

Figure 1.11 crystal structure of eskolaite as $\{Cr\}O_6$ octahedra showing the structural unit cell

X-ray photoelectron spectroscopy (XPS) is another experimental technique that has been widely used in the study of CTO materials.[45,46,47,48,49,53,59] This technique may be used to determine surface composition and the nature of the molecular environment of species at the surface. All of the studies that report measurements of the concentration of the various species find a concentration of titanium at the surface that is greater than the bulk concentration[45,46,47,48,49,59]. This is taken as clear evidence that titanium segregates strongly to the surface of the material. All studies that detail the characterisation of the surface species confirm the existence of Cr^{3+}, Ti^{4+} and O^{2-} species at the surface. McBride and Brydson[59] found no evidence for any alternative oxidation states of these species. However, the group led by Williams have repeatedly shown evidence for small concentrations of a Cr^{6+} species from XPS measurements conducted on CTO material produced by three different methods: CTO derived from solid state mixing and calcination of commercial Cr_2O_3 and TiO_2 powders[45,47], CTO derived from a sol-emulsion-gel process[46] and CTO sensors created by atmospheric pressure chemical vapour deposition[48] (APCVD). It has been suggested[47,58,59] that charge neutrality is preserved around these Ti^{4+} and Cr^{6+} defects by the presence of chromium vacancies, which have an effective negative charge of

3-. Thus, every Cr^{6+} ion present is associated with a single chromium vacancy whilst every Ti^{4+} ion has a share of a third of a chromium vacancy. Furthermore, it is proposed that these chromium vacancies act as acceptor states, accepting electrons from the valence band, and essentially increasing the conductivity of the material above the level which would be attained in defect free material.

Niemeyer *et al.*[47] noted a greater concentration of Cr^{6+} species at the surface of pure chromia than at the surface of CTO and concluded that the titanium ions, which were also strongly segregated to the surface, displaced the Cr^{6+} ions. This displacement reduced the number of acceptor states and thus reduced the conductivity of CTO relative to pure chromia, as was observed experimentally. In addition, these arguments also account for the relatively low sensitivity of pure chromia's conductivity to the presence of reactive gases. The oxygen surface states (from the Windischmann and Mark[5] model above) act as acceptors of electrons from the valence band, leaving behind electron holes which can act as charge carriers. Changing gas concentration affects the concentration of these states at the surface and affects the concentration of charge carriers near the surface. However, because the largest contribution to pure chromia's conductivity comes from the acceptor states associated with the Cr^{6+} ions the effect of changing the oxygen surface state concentration has little overall effect on the material's conductivity.

2 Methods

2.1 Production of the Sensors

Two batches of sensors were obtained from City Technology Limited[2]. The sensors were made using proprietary methods and materials. The sensors within each batch were nominally identical, having been produced from the same material, using the same method at the same time. The two batches were generated from two different CTO materials that were known to have particle sizes that differed by approximately an order of magnitude. Each batch will hereafter be referred to depending on the particle size of the raw material as being produced from fine material or from coarse material. These sensors were taken to UCL where they were split into several small groups. 3 (for the coarse material) or 4 (for the fine material) groups of approximately 3 sensors were created from each batch of sensors. Each of these groups were sintered at a different temperature of either 775, 825, 900 or 1000°C for the groups of sensors made from the fine material or 775, 900 or 1000°C for the groups of sensors made from the coarse material. Another group of sensors was taken from the batch of sensors produced from fine material. These sensors were all fired at 775°C. All firings were carried out in the same Carbolite HTC 1400 furnace using a program that started at a room temperature of approximately 22°C, ramped up to the dwell temperature, as above, at a rate of 15°C per minute, dwelt at this temperature for 60 minutes, before cooling down at a rate of 15°C per minute. Platinum wires of 50μm diameter (Engelhard-Clal) were attached to the contacts on the sensor chip by parallel gap resistance welding. The ends of these wires were then attached to metal pins mounted in a PPS base by a similar welding process.

2.2 Scanning Electron Microscopy (SEM)

SEM was performed on sensor chips after they had been subjected to gas testing. The individual sensor chips were individually mounted onto aluminium stubs using conducting adhesive pads (both from Agar Scientific) so that the surface of the oxide

sensing layer was presented to the beam in the SEM. A layer of gold was deposited over the sensor and the stub to provide a link of high conductivity between the surface being imaged and the stub. This was achieved using an Edwards S150B sputter coater using a pure gold target for 3 minutes at a helium pressure of approximately 0.3 atmospheres and an accelerating voltage of approximately 8.5 kV. Each stub was then mounted in a JEOL 6301F SEM that was fitted with a field emission gun. The working distance used for imaging was always set to 8mm and the accelerating voltage was always set at 15kV. Images were captured and saved as TIFF files using a computer that was interfaced directly to the SEM. Microstructures were generally similar across the entire field of the upper sensor surface and a selection of images of the surface were grabbed in a representative place on this surface at a variety of different magnifications.

SEM was also performed on one of these sensors after they had been subjected to milling by a focussed ion beam. These samples were not recoated with gold before imaging. This process was used to produce several rectangular holes by the raster of an ion beam across the surface as described below. This hole was produced so that the microstructure of the material in cross-section was revealed by looking into it from an angle. This meant that the sample had to be rotated on the stage in the SEM. The angle of rotation used in this instance was 52.8°. All other parameters were as described above.

2.3 Milling Cross-Sections by Focussed Ion Beam (FIB)

Milling of holes in order to obtain partial cross-sections was performed on the sensor made from the coarse CTO material and sintered at 1000°C using a Leo-Zeiss 1540XB. The sample was mounted on an aluminium stub in an identical fashion to that described above for the imaging of the sensors by SEM. This instrument allows the milling of holes in the sample using the FIB and the simultaneous viewing of the results by SEM by using an arrangement of beams and secondary electron detectors as depicted in Figure 2.1. The simultaneous FIB milling and SEM imaging required the instrument to be set up with the help of a qualified technician according to the guidelines of the instrument manufacturer[61].

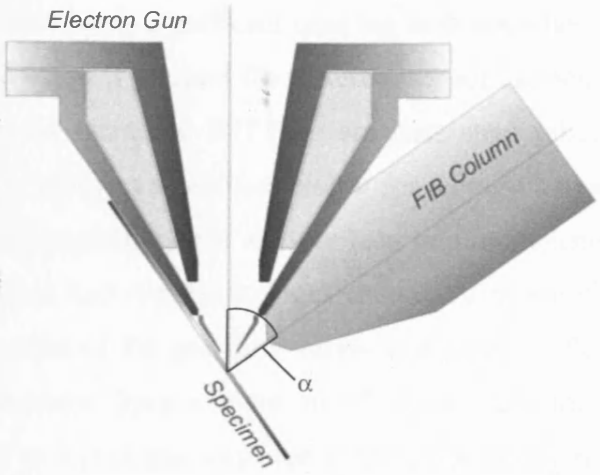

Figure 2.1 Depicting the arrangement of the FIB and the electron beams used in the Leo-Zeiss 1540XB instrument used to produce partial cross-sections. $\alpha \approx 40°$ (Adapted from Gnauck[62])

Three holes were produced that were good enough to be observed later in the SEM as described above. The milling area for each hole is drawn up on screen as a box of particular dimensions. The accuracy of the placement and dimensions of these areas depends upon the calibration of the instrument and how well the cross-beam arrangement is set up by the user. The user then selects a beam current for the FIB and a total time for the milling procedure. The computer controlling the instrument then calculates the appropriate rastering conditions for the FIB to achieve these parameters. The first two holes that were produced were approximately square and were made by two passes of the FIB: the first had an area of approximately 5 by 5 μm and was carried out using a FIB current of 100 pA for a total time of 1200 seconds, the second had an area of approximately 6 by 2 μm and was carried out using a FIB current of 50 pA for 600 seconds. The final hole was made with one pass of the FIB and had an approximate area of 2 by 1 μm. The beam current for this area was 10 pA and the total time for the milling process was 300 seconds.

2.4 Construction and Operation of Apparatus for Gas Testing of Sensors

A special test rig was constructed for the purpose of testing the sensors to step changes in concentration of different gases. A schematic of the entire rig is displayed

in Figure 2.3. As the transient data would be used, a major requirement for the rig was that there should be no significant time lag between when the gas concentration was switched and when it reached the different sensor elements. This was achieved by keeping all pipes (standard PTFE or stainless steel tubing of ¼ inch outside diameter joined by stainless steel Swagelok® connectors) between the gas switching valves and the cell containing the sensors to a minimum length and arranging the sensors in a cell that had symmetrical gas channels cut into it. The cell design and the basic arrangement of the gas flow valves and pipes is illustrated in Figure 2.2. The cell was machined from a block of PTFE as were the sensor holders. This material was used as it is chemically inert to the gases that were tested. Metal sockets were placed in tightly fitting holes drilled through the PTFE sensor holders to allow electronic connections to be made to the sensors.

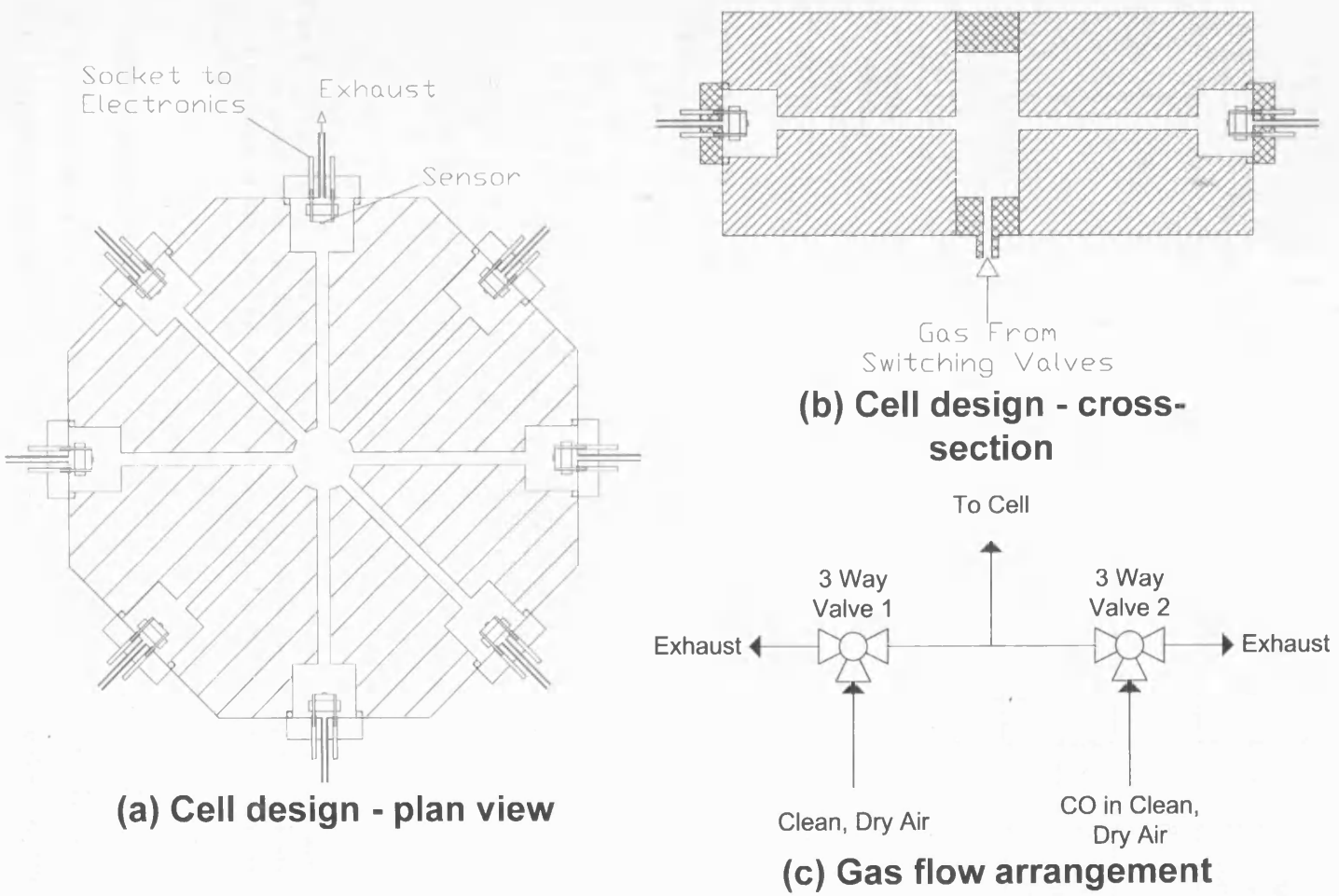

Figure 2.2 Diagrams of cell design in (a) plan view and (b) cross-section and (c) of gas flow arrangement through 3-way valves prior to cell (Drawings not to scale)

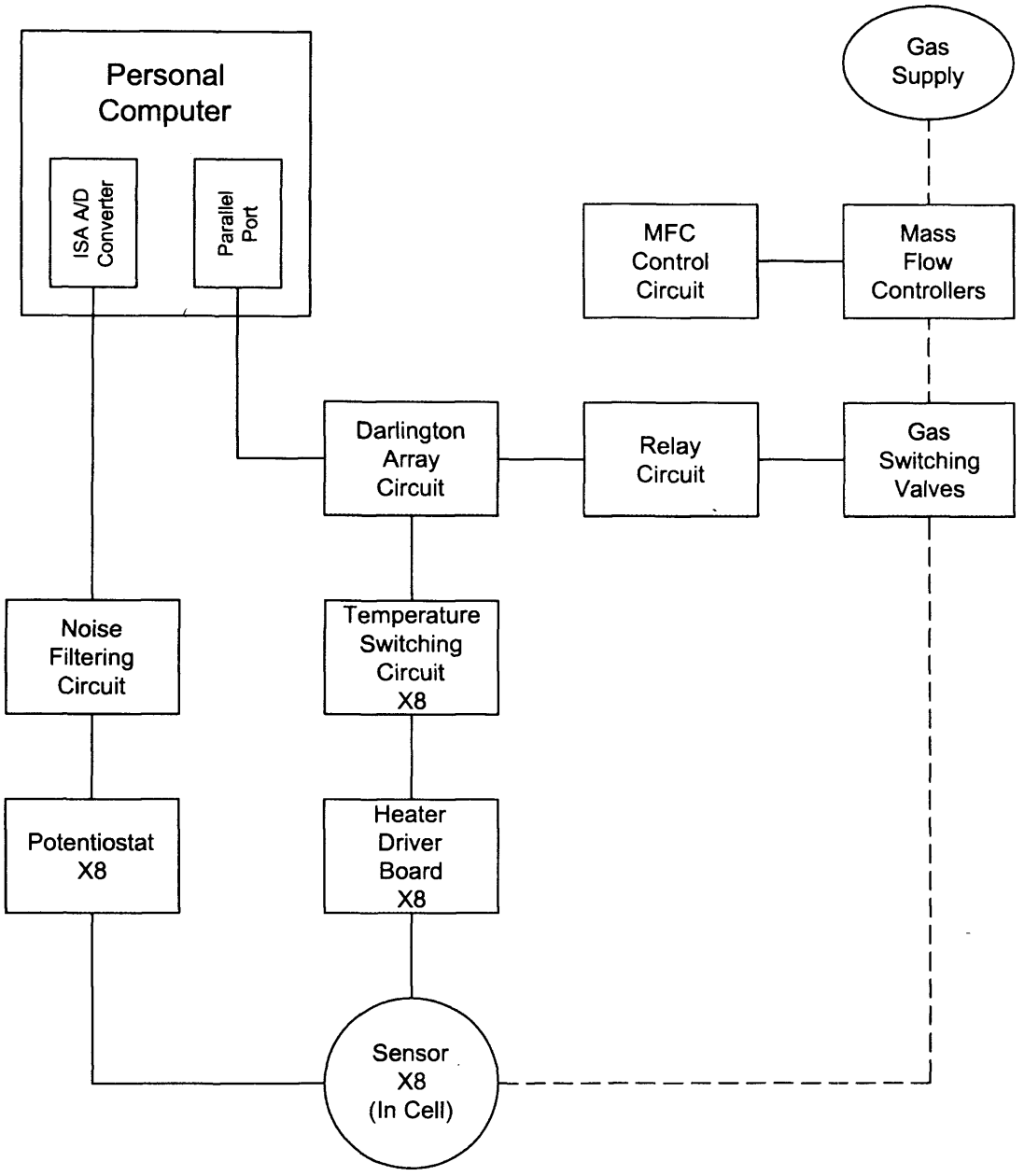

Figure 2.3 Schematic of the apparatus constructed for gas testing sensor. Electronic circuits joined by solid lines, gas flow apparatus joined by dashed lines. Since 8 sensors can be accommodated in the test cell 8 sensor measurement and temperature control circuits are required.

An IBM compatible computer was used to read from or control the majority of the electronic circuits, many of which were custom built at UCL. Those circuits that were bought in were the 12 bit A/D converter (Amplicon Liveline PC27E ISA A/D Converter) and the heater driver boards (Capteur Sensors Ltd, now part of City Technology Ltd., ISS CAP5). The mass flow controllers (Tylan General (UK) Ltd., FC-260, 500 sccm, with Viton or Kalrez seals, calibrated for use in air) and gas

switching valves (RS, 2 of order-code 440-789, rated for operation at 24 V and 0-6 bar, used for air/gas switching and 1 of order code 439-278, rated at 24 V and 0-4.5 bar, used to switch the gas flow on/off to conserve gas supply) were also bought in. To measure sensor conductance two circuits were used: the potentiostat circuit and the noise filtering circuit. The potentiostat circuits' were based on inverting op-amps which provided a voltage that was proportional to the sensors' conductance, and their construction has been documented previously [63] . The constants of proportionality were found for each circuit by measuring resistors having known values. These values were used in the calculation of resistance from the raw data files, as will be described later. The noise filtering circuit comprised two stages: noise filtering followed by attenuation. The noise filtering section of the circuit was based upon the passive twin T circuit[64] that can be tuned to remove noise of a specific frequency, which in this case was 50 Hz. The attenuation section was simply a potential divider that attenuated the voltage to the range that the A/D converter card could read. This circuit had 8 separate sections for each of the sensors.

The Darlington array circuit converted the low power, binary outputs from the PC's parallel ports into signals of sufficient power to control two sets of high power relays. These first set of relays (labelled "Relay Circuit" in Figure 2.3) were used to control the gas switching valves. The second set of relays were incorporated on the temperature switching circuit and were used to switch different resistors into and out of parallel circuit with the resistor labelled "R5" on the heater driver board (HDB) circuit. The values of these resistors were set up individually for each sensor put into each channel so that the sensor temperature could be switched between different values. The HDB circuits were obtained from City Technology Limited. The HDB is essentially a Wheatstone bridge circuit where the platinum base heater track of a sensor is one of the arms. The Wheatstone bridge balances the resistances of the two sides of the bridge and thereby keeps the temperature of the sensor constant. The MFC control circuit controlled the flows of gas through the mass flow controllers. The calibration of this control circuit and the mass flow controllers (MFCs) was checked using a calibrated electrochemical gas sensor from City Technology Limited. Gas flows of varying composition from a carbon monoxide cylinder of known composition (BOC Special Gases ltd.) and an in-house zero air generating system (Peak Scientific ZA180 zero air generator, an AD44L air drying unit and a

compressor) were set up, with a total flow of a constant 1000 cc/min. This provided a calibration curve that was used to provide the correct values to set on the MFC control box to give a flow of the correct composition of gas from the MFCs using a gas cylinder of known composition.

Five sets of tests were carried out as detailed in Table 2.1. These sets of tests were carried out by testing the sensors to a range of gas concentrations between 10 and 10000 ppm. Most of the testing followed the procedure outlined below.

Table 2.1 Summary of testing carried out

Relative Particle Size of Sensor Material	Test Gas	Operating Temperature of Sensors
Coarse	CO	All 400°C
Coarse	propane	All 400°C
Fine	CO	All 400°C
Fine	propane	All 400°C
Fine	CO	Between 350 and 450°C

1. Sensor base heater resistances measured using a Keithley 199 System digital multimeter/scanner at room temperature of approximately 22°C
2. Sensors placed in mountings within cell
3. HDB circuits, now with sensor base heaters in circuit, set so that sensors are operating at the correct temperature
4. Temperature switching circuits set up individually so that the high temperature was for each sensor was 500°C
5. The sensors were left to stabilise for at least 30 minutes
6. Gas flow set up on MFC control box, all valves opened and gases allowed to flow through the equipment before the cell for a period of at least 10 minutes
7. A gas test would be programmed into the computer (see below) and would be initiated

8. The gas programme would be allowed to complete before data was transferred to another computer for data processing
9. Steps 6 through 8 would be repeated for another gas composition

The gas test programme used typically followed the following procedure:

1. 60 seconds in clean air at 500 °C (to speed up recovery from any previous gas exposure)
2. 1800 seconds in clean air at operating temperature (to allow stabilisation of baseline resistance)
3. 600 seconds in test gas concentration at operating temperature
4. 600 seconds in clean air at operating temperature

The only exception to this testing procedure occurred for the tests to CO conducted on the sensors derived from fine CTO material. These tests were conducted without the temperature switching circuits in place. As such the gas test programme was modified, as below:

1. 300 seconds in clean air
2. 300 seconds in test gas concentration
3. 1800 seconds in clean air

Measurements of the voltages received from each of the measuring circuits were logged with experiment time in a data file approximately every fifth of a second after the start of the experiment.

2.5 Data Processing Procedures

The raw data file generated by the computer from each test consisted of a list of the voltages measured by the A/D converter with the time after the experiment was started. These voltages were converted to the resistance of each sensor using the calibration data as described above. This calibration data automatically accounted for the different components used in the potentiostat and attenuation sections of the

resistance measuring circuits. A baseline resistance (the resistance in clean air) was calculated for each sensor as the average of the 20 readings preceding the change from clean air to the test gas concentration. This baseline resistance was used as R_0 to calculate the response (G_t) of the sensors at each time point according to Equation 2.1.

$$G_t = \frac{R_t}{R_0}$$

Equation 2.1 Response (G_t) of a sensor at time, t, having a clean air baseline of R_0 and a resistance at time, t, of R_t

The response achieved at the end of each gas exposure was taken as an approximation to the steady state response. The pseudo steady state responses were collated for each sensor in a separate data file along with the concentration of gas that was tested. These files were then used as the input to a program which performed an automated brute-force search for solutions to Equation 1.24. The programme written in the C programming language by K.F.E. Pratt is documented in the appendix to this thesis. Only the tolerance scaling sections of this code were utilised for the data processed in this work, the autoscaling function was always invoked and the tolerances read in from the data file (`tolminrel` and `tolmaxrel`) were all set to a value of 0.1. This programme returned up to five sets of the parameters of this equation ($R_{PB,0}/R_{T,0}$, $R_{S,0}/R_{T,0}$, $R_{B,0}/R_{T,0}$ and A_{gas}). An average for each parameter was calculated as the values were all very close and this was taken as the steady state solution of the experimental data to Equation 1.24. The transient data obtained for tests to 6 different gas concentrations on each of the sensors was then collated in a single data file for each set of tests. Non-linear least squares regression was then performed on each of the sets of transient data using the XLStatistics package[65]. The values of the parameters representing the different microstructural regions obtained from the steady state solutions were used as constants for these parameters in the regressions to the transient data. Only the parameters A_{gas} and τ were allowed to vary. The values of all these parameters were then collated with the experimental parameters so that graphs could easily be produced. A regression of the pseudo steady state response data was also performed, again using the XLStatistics package[55], to an equation representing the traditional

square root response model of Equation 1.20, where b = ½, rearranged to give Equation 2.2. This allowed the comparison of how well the traditional and microstructural models account for the variation of sensor response with gas concentration.

$$\frac{R_{x,MAX}}{R_{x.0}} = \left(1 + A_{gas}\left[gas\right]^{1/2}\right)$$

Equation 2.2 Traditional square root response model to which non-linear least squares regression of the pseudo steady state response data was carried out for comparison to the microstructural model

3 Microstructural Study by Scanning Electron Microscopy

This chapter deals with the results from scanning electron microscopy (SEM) performed on the raw material powders and manufactured and tested sensors. Samples of chromia raw material powder were obtained from two different sources. These two powders were chosen because of the differences in particle size quoted by their manufacturers, and will, from now on, be referred to as either the coarse chromia raw material and the fine chromia raw material. The titania used in this study came from a single manufacturer. The names of the manufacturers of these powders will not be revealed in this work because of the commercially sensitive nature of this information. Firstly, these powders were observed in the SEM in their as obtained state, the results of which are displayed in section 3.1. Samples of each of the chromia powders was then mixed with titania powder in the correct proportion to obtain the composition of chromium titanate represented by the formula, $Cr_{1.95}Ti_{0.05}O_3$. These powders were then calcined at 1000°C to attempt to obtain a solid solution of the correct composition. These powders were then prepared as inks and screen printed onto sensor substrates. The sensors made from the coarse chromia material were split into 4 groups. One group was kept in the unsintered condition to allow the analysis of the as calcined powder. The other three groups were sintered at 775, 900 or 1000°C. Two sensors sintered at each of the temperatures were made into fully functional sensors and were subjected to gas testing before they were observed in the SEM in section 3.2.1. The sensors made from the fine chromia material were split into 5 groups. Again, one group was kept in the unsintered condition to allow the analysis of the as calcined powder. The other four groups were sintered at 775, 825, 900 or 1000°C. Two sensors sintered at each of the temperatures were made into fully functional sensors and were subjected to gas testing before they were observed in the SEM in section 3.2.2. Finally, in an effort to attempt better methods of obtaining cross-sections, the sensor made from the coarse chromia material and sintered at the temperature of 1000°C was subjected to several FIB milling procedures. The cleanest faces of the milled regions can be observed in the SEM micrographs presented in section 3.2.4.

3.1 SEM of Raw Material Powders

SEM was performed on the raw powders of chromia from both sources and of titania. The SEM micrographs, one low magnification (a) and one high magnification (b), for the coarse chromia material and the fine chromia material and the titania powders are displayed in Figure 3.1, Figure 3.2 and Figure 3.3 respectively. In all cases the individual particles' shapes approximate to spheres. However, slight differences in morphology do appear. For instance, the particles in Figure 3.1 for the coarse chromia material show a degree of crystal facets. Also, the individual particles of both the fine chromia material and the titania, in Figure 3.2 and Figure 3.3 respectively, show some surface roughness or bulges, as though the particles were made up of much smaller particles themselves. The sizes of the larger particles were approximated using image analysis software from these SEM micrographs. The results of these measurements are presented in Table 3.1. The particle sizes for the fine chromia powder and the titania powder are similar at approximately 41 and 53 nm respectively. The approximate size for the coarse chromia powder is significantly larger at 181 nm.

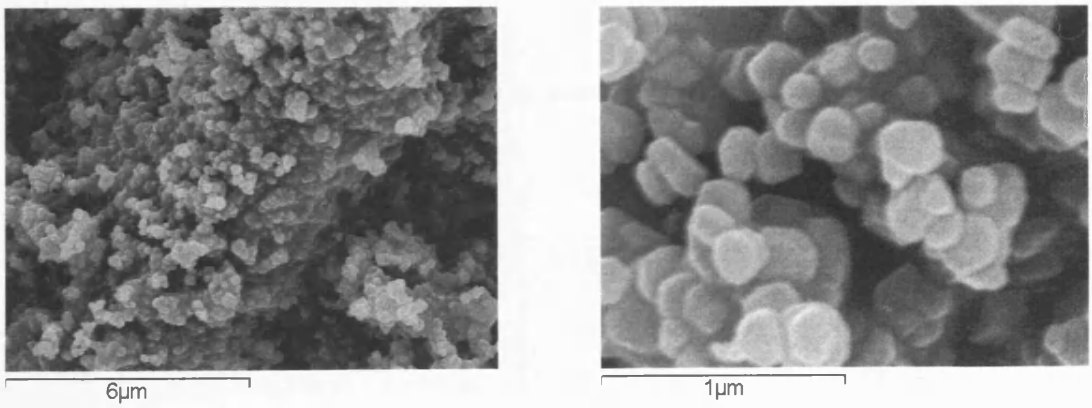

Figure 3.1 SEM micrographs of coarse chromia raw material

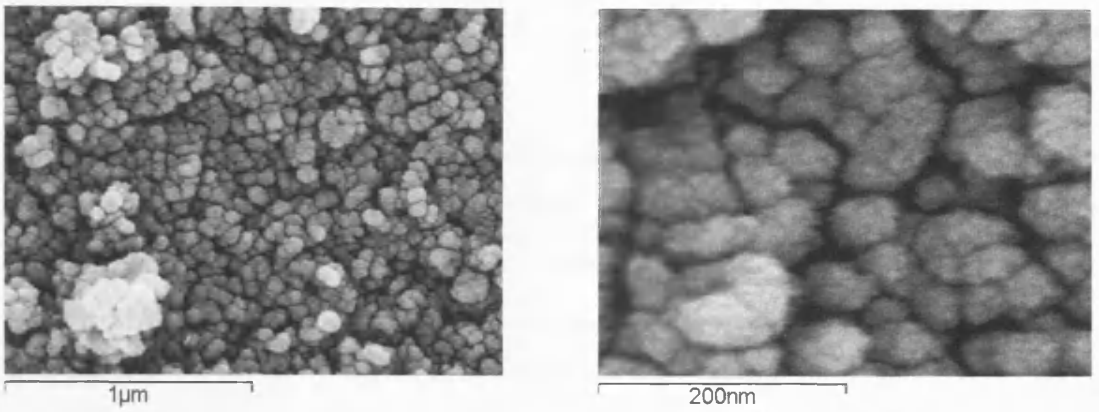

(a) (b)

Figure 3.2 SEM micrographs of fine chromia raw material

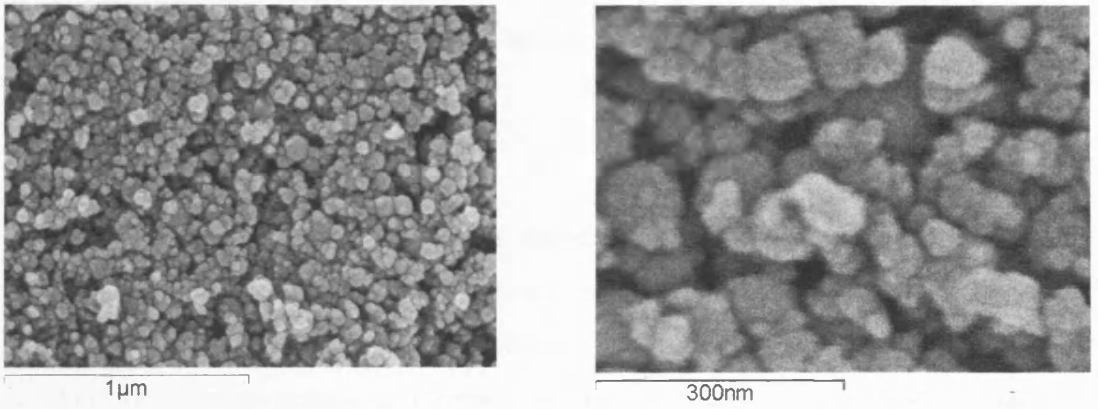

(a) (b)

Figure 3.3 SEM micrographs of the titania raw material

MATERIAL	MEAN PARTICLE SIZE / nm
Coarse Chromia	181
Fine Chromia	41
Titania	53

Table 3.1 Mean particle sizes of raw material powders

3.2 SEM of Gas Sensors

SEM was also performed on sensors produced at the different sintering temperatures from the two different raw materials. Images were taken by viewing the top surfaces of the sensors at a variety of different magnifications. Low, intermediate and high magnification SEM micrographs of the sensors made from the coarse chromia powder are displayed in Figure 3.4, Figure 3.5 and Figure 3.6 respectively. Figure 3.9 and Figure 3.10 display the low and high magnification SEM micrographs obtained for the sensors made from fine chromia powder.

3.2.1 Sensors Made from Coarse Chromia Raw Material

3.2.1.1 Results

The SEM micrographs of the sensors made using the coarse chromia material, in Figure 3.4, Figure 3.5 and Figure 3.6, show the structures of the sensors to be mainly composed of roughly spherical particles. The particles are connected to their neighbours in small groups or clusters. Boundaries between neighbouring particles are of a significant size, approaching the dimensions of the particles themselves. The approximate size of these particles, as measured using image analysis software from these images, increases with sintering temperature, as displayed in Figure 3.7. The approximate sizes of the particles forming the sensors sintered at 1000°C are 50% larger than those of the particles forming the sensors sintered at 775°C.

Another major change, particularly evident in the sensor sintered at 1000°C, is that of reduction of micro-porosity. The SEM micrographs for the unsintered sensor and sensors sintered at the lower temperatures, 775 and 900°C, display structures of particles that have a relatively large number of open pores between them, of approximately 0.5 to 1 μm in size. These SEM micrographs also give the impression that this porosity may be interconnected to a degree that would allow gas to penetrate deep within the structures. The images for the sensor sintered at 1000°C display significantly less porosity on this scale. They also show that the particles are highly interconnected with their neighbours and rather than forming discrete clusters, they

now appear to form a single, massive cluster with the micro-porosity trapped within it. The impression given by these images is that the channels to the depths of the sensor sintered at 1000°C are now fewer and more restrictive to the admission of gas.

The fairly large particles in all the sensors have a rough, rippling surface resembling a cauliflower. In the SEM micrographs taken at the highest magnification, displayed in Figure 3.6, these surface features appear to be much smaller, individual sub-particles that make up the much larger particles described above. Their morphology is approximately spherical and their sizes have been measured and are displayed in Table 3.2. Furthermore, the distribution of the sizes of these smaller sub-particles is displayed in the histogram presented in Figure 3.8. It is somewhat surprising that the mean average size of these small features decreases with increasing sintering temperature since it is more usual for the sizes of features to increase upon sintering. Analysis of the histogram presented in Figure 3.8 indicates that the size of these features measured in the unsintered sensor has a wide, bimodal distribution. With increased sintering temperature the distribution narrows from the top end towards the primary modal bin between 12.5 and 15 nm.

These small features are distributed across the entire surface of the larger particles, described above, that compose the sensors. In addition to the differences in the size of these features there are also differences in how they are joined to their neighbours, their arrangement and the kind of nano-porosity that exists between them and the larger particles that they appear to form. In the unsintered sensor and the sensor sintered at 1000°C the sub-particles seem to be highly bonded to their neighbours in two dimensional plates covering the surfaces of the large particles. There are crevasses in between the plates forming nano-porosity leading into the structure of the large particles. The plates in the sensor sintered at 1000°C appear to be somewhat smaller than those in the unsintered sensor with more crevasses. The sensors sintered at 775 and 900°C give the same impression of forming plates. However, the sub-particles that form the plates appear to be built upon each other in a more three dimensional manner and the nano-porosity that exists between them appears to be greater. This increase in nano-porosity accompanies an increase in surface area of the particles. The boundaries between the large particles that form the

structures appear to be crevasses in the structure possibly extending further into the large particles than the crevasses between the plates of the smaller sub-particles.

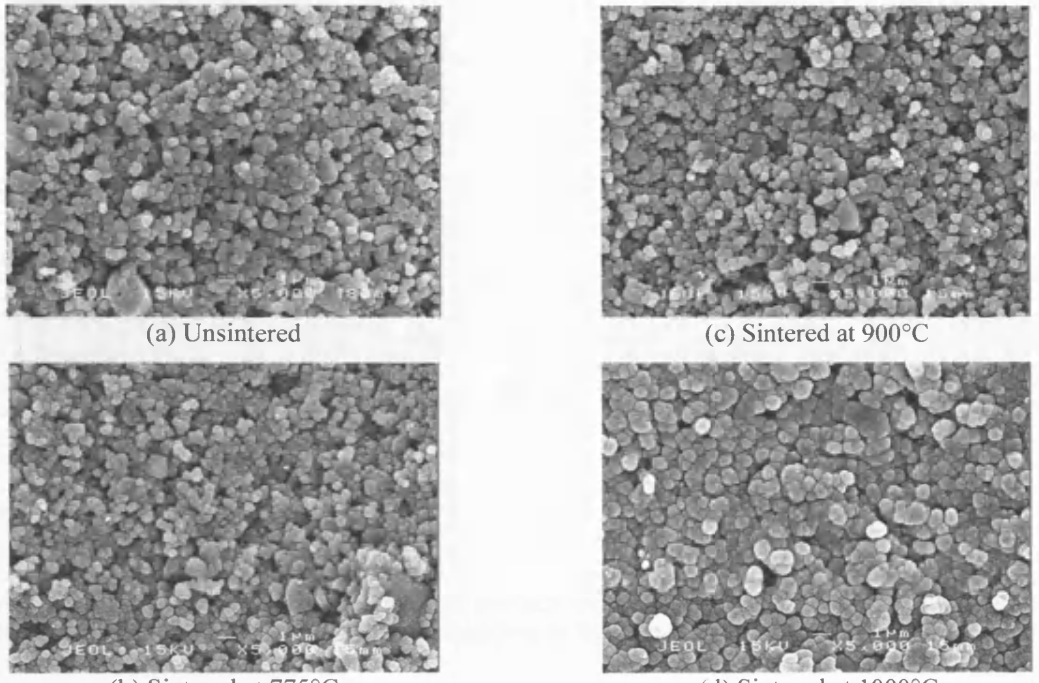

(a) Unsintered (c) Sintered at 900°C

(b) Sintered at 775°C (d) Sintered at 1000°C

Figure 3.4 Low magnification SEM micrographs of sensors made from coarse chromia raw material showing increasing particle size and decreasing micro-porosity with increasing sintering temperature

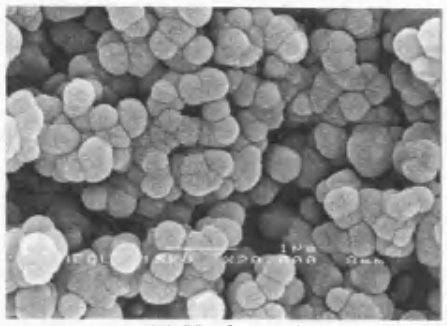

(a) Unsintered

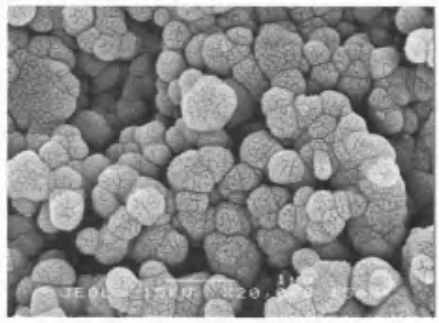

(c) Sintered at 900°C

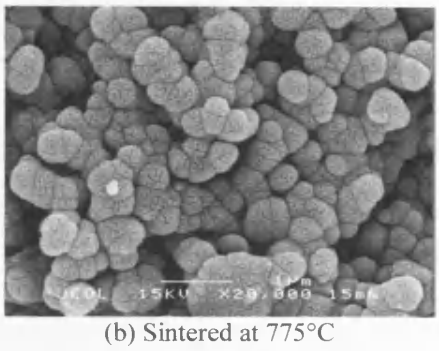

(b) Sintered at 775°C

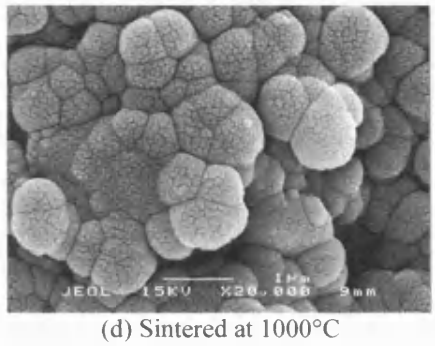

(d) Sintered at 1000°C

Figure 3.5 Intermediate magnification SEM micrographs of sensors made from coarse chromia raw material showing general increase in particle size and degree of particle interconnection with increasing sintering temperature in addition to finer surface features of particles

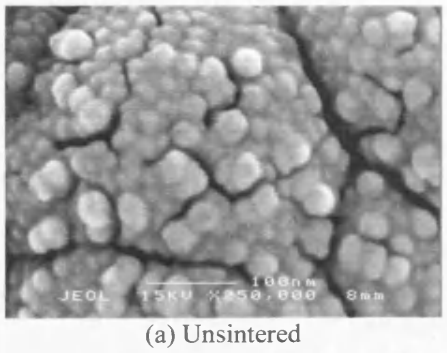

(a) Unsintered

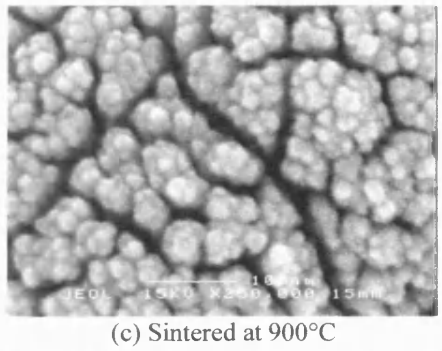

(c) Sintered at 900°C

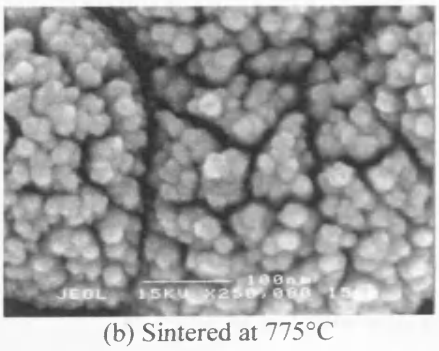

(b) Sintered at 775°C

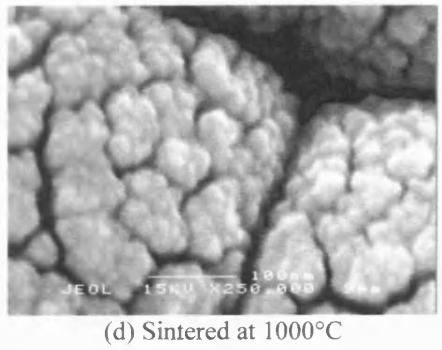

(d) Sintered at 1000°C

Figure 3.6 High magnification SEM micrographs of sensors made from coarse chromia raw material showing surface features of particles and boundaries between particles

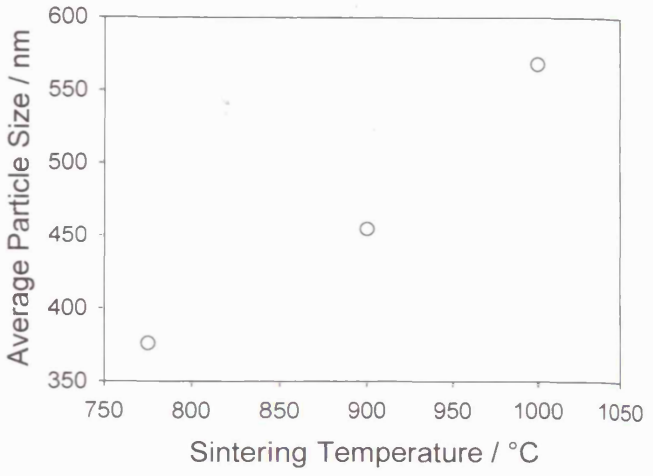

Figure 3.7 Approximate particle size versus sintering temperature for sensors made from coarse chromia. Unsintered particle size was approximately 320 nm.

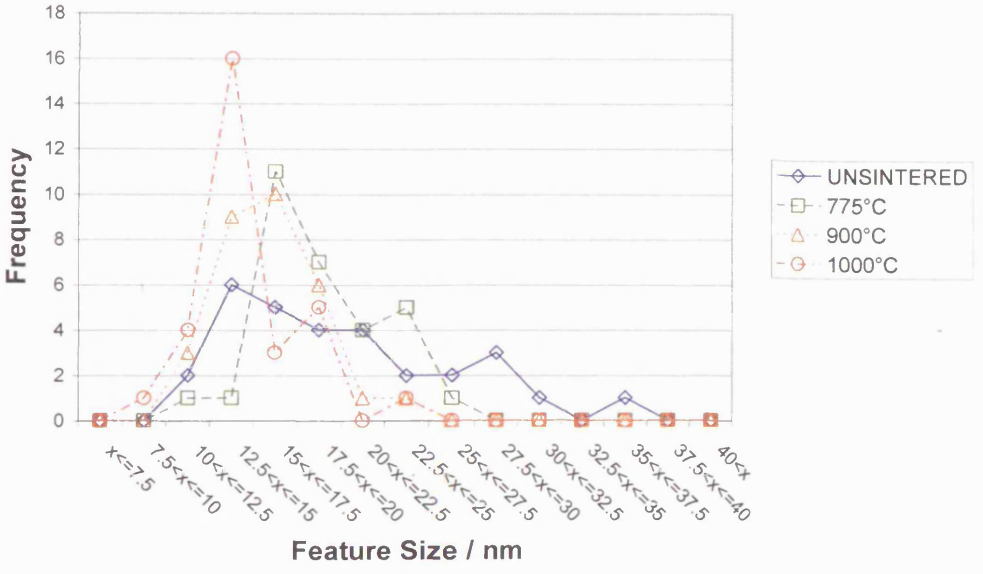

Figure 3.8 Histogram showing the decreasing magnitude and distribution of sizes of particle surface features in sensors sintered at increasing temperatures

Sintering Temperature / °C	Mean Feature Size / nm
Unsintered	20.1
775	18.8
900	15.9
1000	14.6

Table 3.2 Data illustrating decrease in mean average size of surface features with increasing sintering temperature on particles of sensors derived from coarse chromia material

3.2.1.2 Discussion

The parameters in the microstructural model, essentially quantifying the resistors representing the different microstructural regions of the sensors, will be related to the effective dimensions and resistivities of the regions of the microstructure. The effective dimensions of these regions will be related to the microstructures of the sensors and can therefore be related to the observations of the physical features of the microstructures that have been made above.

The size of the large particles in the unsintered sensor is approximately 320 nm. Comparison with the SEM micrographs of the major raw material component, the coarse chromia powder, indicate that the particle size of the chromium titanate powder produced at the powder and ink preparation stage is larger than the raw material by a factor of approximately 1.8. This is due to the fact that mixture of coarse chromia powder and titania powder was calcined at 1000°C for 4 hours in an attempt to produce a homogeneous solid solution of chromium titanate of composition $Cr_{1.95}Ti_{0.05}O_3$. The unsintered sensor's microstructure, in Figure 3.4(a), Figure 3.5(a) and Figure 3.6(a), is indicative of the structures that would have been present in all the other sensors prior to the sintering processes that they were subjected to.

Once the sensors were subjected to their respective sintering stages all displayed an increase in the size of these larger particles. Furthermore, larger increases in particle size were observed for those sensors sintered at higher temperatures. This is a result of the higher rates of diffusion that are obtained at the higher sintering temperatures. Assuming the amount and distribution of material in each of the sensors was nominally identical prior to sintering and in the absence of any other structural changes, changes in particle size will change the proportion of material that is attributed to the different resistors in the model. In particular, the major effect will be on the amount of material attributed to the surface and the bulk resistors. A simple model of sensors composed of ideally spherical particles just touching in a simple cubic array can be used to show that for a fixed volume of material where the surface of the material is assumed to be sensitive to gas to a fixed depth:

a) The lengths of the shortest paths through the bulk and around the surface of the spheres remain constant as the particle size changes
b) The volume of material that is defined as gas sensitive surface decreases and the volume defined as bulk increases as particle size increases
c) The number of particle boundaries will decrease as particle size decreases

From the statements (a) and (b) it is possible to infer that the effective cross-sectional areas of the material defined as surface and as bulk change in the following ways with **INCREASING** particle size:

SURFACE material's effective cross-sectional area **DECREASES** with increasing particle size

BULK material's effective cross-sectional area **INCREASES** with increasing particle size

Since the resistance, R, of a conductor of length, l, and cross-sectional area, A, and composed of a material with resistivity, ρ, is determined by Equation 1.1(restated):

$$R = \frac{\rho l}{A}$$

the resistors representing the surface and bulk will vary inversely to their effective areas with changes in particle size. However, these statements are generalisations of what are the major effects of increases in particle size. They will be affected by other structural changes that may occur as a result of sintering alongside the changes in particle size, particularly those that affect the assumptions made in this rather simplistic model.

As mentioned above, whilst the sensors sintered at 775 and 900°C display a structure composed of spherically shaped particles that are highly interconnected, the interconnection is only to the extent of forming distinct clusters of particles. These clusters have a significant amount of micro-porosity between them. This porosity

appears as though it is very likely to reach within the structure and be connected with further such porosity deeper below the surface of the structure. In the sensor sintered at 1000°C the degree of interconnection between the large particles is so extensive that the structure could be considered as a single mass with micro-porosity trapped within it. Whilst the porosity may still reach the depths of the structure there appears to be much less of it and the degree of interconnection of the porosity below the surface is likely to be much less. Another effect of the increase in interconnection between the particles will be an increase in the effective area of the boundaries. Since this increase in interconnection is extensive its effect is likely to outweigh that from statement (c) above and result in an overall decrease in the contribution to the resistance of the sensor from the particle boundaries as sintering temperature is increased.

This difference in the level of micro-porosity is important for two reasons. First, gases must travel through the porosity in the structure to reach the active surfaces. The level of porosity will therefore determine the ability of gas to enter the structure and react at the surfaces of the sensor. If the gases' ability to get to potentially active surfaces is impeded less gas will reach the potentially active sites and it may get there more slowly. These factors will manifest themselves as reduced response and slower response respectively, in the parameters of the model that account for the sensitivity (sensitivity parameter, A) and speed of response (time constant, τ) to the gases in the atmosphere.

Second, the structure of the solid part of the sensor will also have been affected. Less porosity in a structure means that there is less surface within that structure and therefore less capacity for reactions to occur between gases and the surface of the sensor. In terms of the microstructural model of response this ought to manifest itself as a reduced response through a change in the value of the resistor representing the surface. Since the sensors nominally contained the same amount of material originally and the amount of material that is defined as surface is decreased with less porosity, then the amount of material defined as forming the other parts of the microstructure, the particle boundaries and the bulk, must also be changed. The amount of material defined as particle boundary will be much less since the particles are much larger in size, meaning there are fewer boundaries, and the boundaries are

themselves larger and more continuously bonded, meaning they are now more akin to the separate surface and bulk components of the structure. Again, since the particle boundaries are assumed to contribute to sensor response in the model used in this study, there will be a reinforcing reduction in response from the particle boundaries. Also, if these statements are all true then the proportion of material that is defined as bulk in the model of the sensors must then increase as porosity is decreased.

Another feature of the structures that it is important to consider is that of the fine, rippling features that give the surface the appearance of a cauliflower. As discussed earlier, these features appear to be smaller, spherically shaped particles of around 10 to 30 nm in diameter. They are present in the unsintered sensor so it can be assumed that they are a result of the powder or ink production stages (most probably the calcination step) and that prior to the sintering steps performed all the sensors had these features.

The features also prevail after sintering and, somewhat unusually, their size appears to decrease with increasing sintering temperature. This may be a result of the primary matter transport mechanisms occurring as a result of the sintering temperature. If the dominant mechanism is that of diffusion of matter to particle boundaries from within the bulk of the particles then the particles will merge at the boundary and swell in size[66], thereby stretching the matter at the surfaces of the particles. This stretching of the surface could result in the sub particles being pulled apart to form smaller particles.

In terms of the microstructural model, the main effect of these features will be on the surface resistance. The rough surface increases the amount of nano-porosity near the surface which will then have a much larger surface area than if the surface was smooth. This might also lead to an increase in the predicted sensitivity parameter obtained from the model over what may be expected for smooth particles. There may also be some increase in sensitivity parameter from the decrease in the amount of nano-porosity apparent as sintering temperature is increased. The rough surface will also extend the effective length and increase the effective cross-sectional area of the surface resistor. These effects are likely to cancel each other out to some degree.

3.2.2 Sensors Made from Fine Chromia Raw Material

3.2.2.1 Results

The SEM micrographs of the sensors made from the fine chromia raw material, in Figure 3.9 and Figure 3.10, show that they appear to be composed of approximately spherically shaped clusters of irregularly and quite angularly shaped particles. The approximate sizes of the clusters and the particles that form them were estimated from these SEM micrographs and are plotted versus sintering temperature in Figure 3.11. The sizes of the particles and clusters forming the sensor sintered at 775°C are approximately 48 and 145 nm respectively. These sizes rise to approximately 58 and 225 nm respectively in the sensor sintered at 1000°C. This represents an approximate 20% increase in the size of the particles and a 55% increase in the size of the clusters over the range of sintering temperatures studied.

The clusters are joined together forming a network of solid clusters of material interspersed with porosity of a similar size as the clusters of particles. The images give the impression that this porosity is interconnected and extends within the structure. Although difficult to judge from these images, they also give the impression that the proportion of the volume of the structure that is solid material outweighs that which is porosity. The ratio of solid to porosity could be as much as 3 to 1. Furthermore, the proportion of the structures that is porosity does not seem to be affected to any significant degree by increased sintering temperature. However, the only reliable method of quantifying the amount of this porosity would be to perform image analysis on cross-sections of the sensors. As discussed later, such sections are difficult to prepare.

No significant change in how the particles are joined within the clusters appears to take place with increasing sintering temperature. The particles that form the clusters appear to be separated by fissures. These fissures appear to be relatively deep, possibly extending as far into the clusters as a particle width. These fissures give the solid the overall appearance similar to that which occurs when mud dries and cracks.

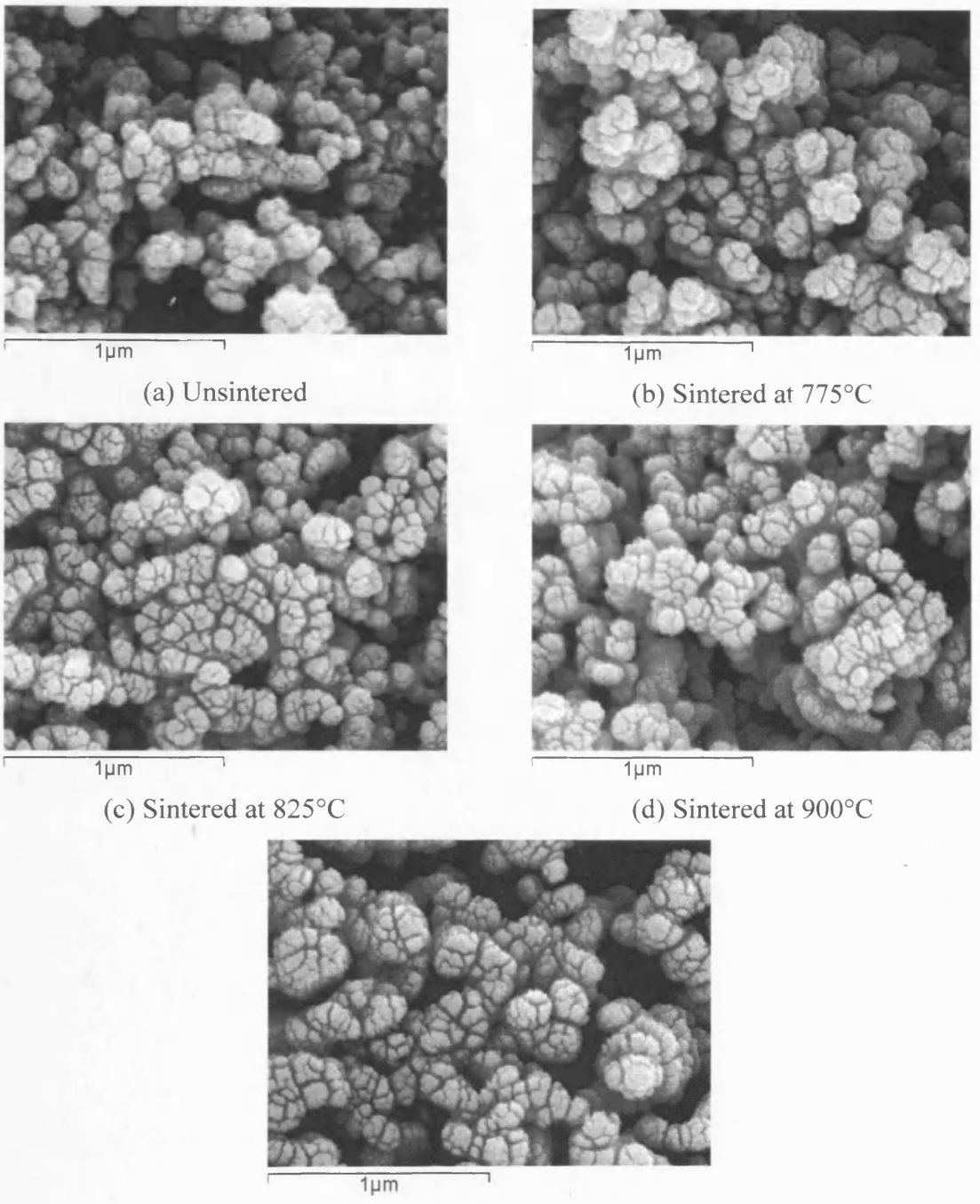

(a) Unsintered

(b) Sintered at 775°C

(c) Sintered at 825°C

(d) Sintered at 900°C

(e) Sintered at 1000°C

Figure 3.9 Low magnification SEM micrographs of sensors made using fine chromia raw material. (a) is unsintered, (b) is sintered at 775°C, (c) is sintered at 825°C, (d) is sintered at 900°C and (e) is sintered at 1000°C

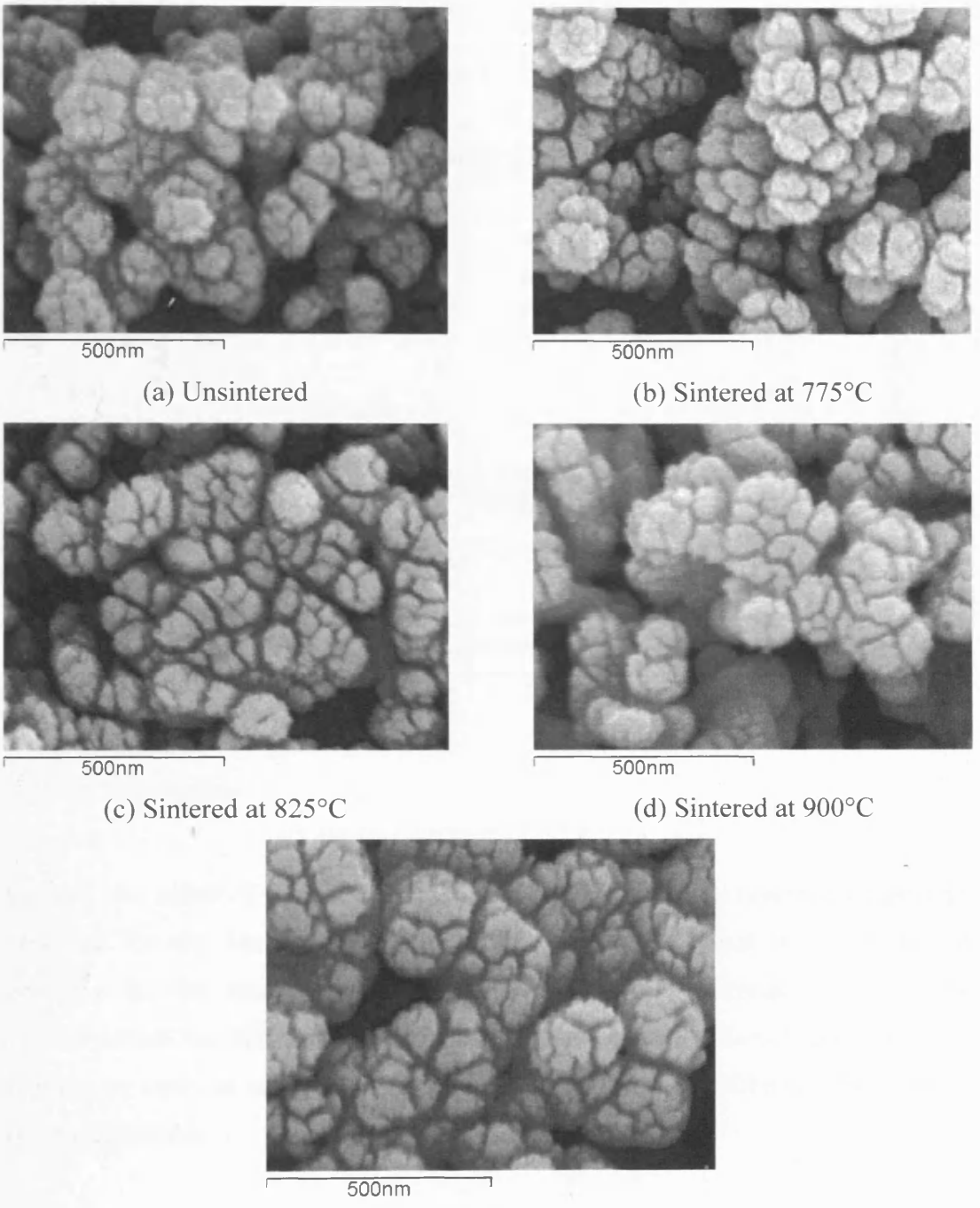

(a) Unsintered

(b) Sintered at 775°C

(c) Sintered at 825°C

(d) Sintered at 900°C

(e) Sintered at 1000°C

Figure 3.10 High magnification SEM micrographs of sensors made using fine chromia raw material. (a) is unsintered, (b) is sintered at 775°C, (c) is sintered at 825°C, (d) is sintered at 900°C and (e) is sintered at 1000°C

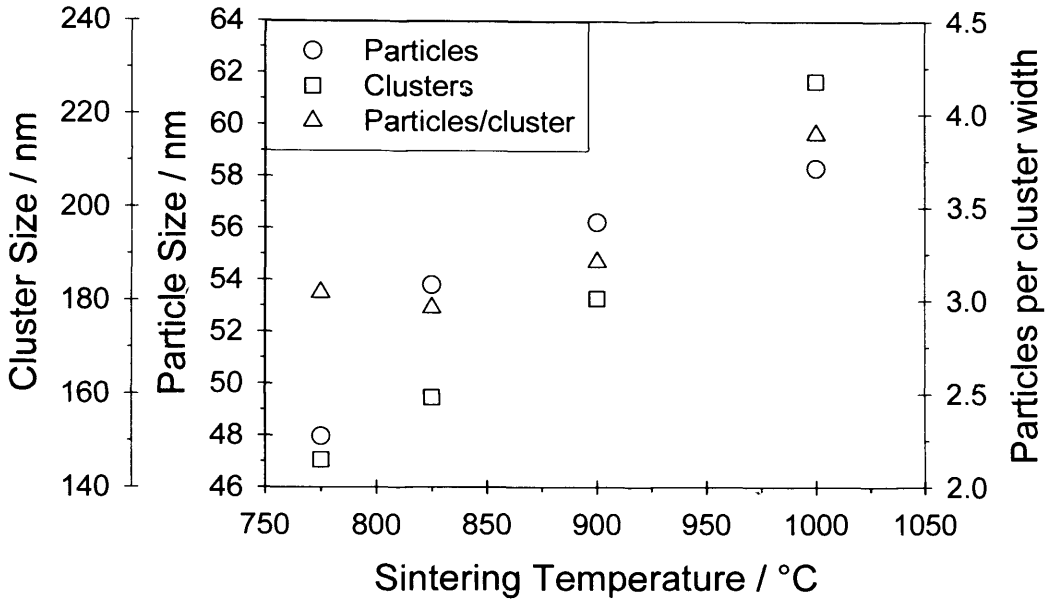

Figure 3.11 Particle and cluster size and particles per cluster width versus sintering temperature for sensors made from fine chromia raw material. In the unsintered sensor, particle size was estimated at 22 nm and cluster size was estimated at 122 nm.

3.2.2.2 Discussion

Overall, the effect of increasing particle size with increasing sintering temperature observed for the sensors derived from fine chromia material is similar to that observed for the sensors derived from coarse chromia material. Therefore, the overall effects on the different resistors representing the different microstructural regions are likely to be similar for both materials. The major differences between the two materials are:

(a) the sizes of the features observed for the sensors derived from fine chromia material are approximately a quarter of those observed for the sensors derived from coarse chromia material

(b) the particle boundaries appear to be less extensive and integrated for the sensors derived from fine material than those derived from coarse material

(c) it does not appear that porosity decreases to any significant degree in the sensors derived from fine chromia material, even at the highest sintering

temperature, whereas this was particularly evident for the sensors derived from coarse chromia material

(d) the fissures that exist between the particles seem to have a depth equivalent to a third of the width of the clusters, whereas the fissures between the surface ripples observed in the sensors derived from coarse chromia material are inferred to have a depth of approximately a twentieth of the size of the large particles.

The much smaller features observed for the sensors derived from fine chromia material will have a variety of effects on different aspects of sensor performance. The smaller particle size will mean that the proportion of material that is classified as surface ought to be higher for the sensors derived from fine chromia material than for the coarse chromia material. In direct relation the proportion of material that is bulk ought to be decreased for the fine material compared to the coarse material. This ought to mean that the resistance of the surface for the fine material will be lower than for the coarse material and that of the bulk will be higher. The effect on the particle boundaries will be complicated by the specific differences observed in their other characteristics and will be discussed below.

Overall, the porosity in the sensors derived from fine chromia material is much smaller than that observed for the sensors derived from coarse chromia material. This smaller porosity is likely to offer more restriction to the passage of gas through the structures and will likely lead to a reduced sensitivity parameter (A) and reduced speed of response (τ) for the fine material compared to the coarse material. The fact that the degree of porosity does not appear to change with sintering temperature for the fine material is likely to mean that the sensitivity parameter (A) and the speed of response (τ) will not vary as much as it is predicted to with the coarse material.

The situation with the particle boundaries is difficult to interpret. On the one hand the seeming lack of integration between neighbouring particles across boundaries observed in the sensors derived from fine chromia material compared to that observed for the sensors derived from coarse chromia material is likely to mean that the resistance of the boundaries observed for the coarser material is significantly lower. This is because the integration between particles will be related to the

effective cross-sectional area of the resistor representing the particle boundaries. Another factor is that because the particles are much smaller in the sensors derived from finer material there will be a greatly increased number of boundaries. This will potentially affect both the effective cross-sectional area and the effective length of the resistor representing the boundaries. The presence of the fissures increases the effective surface area of the sensors over what would be present without them.

3.2.3 Mechanically Polished Cross-Sections

In view of the fact that the porosity of these devices is important in determining the ability of gas to access the structure cross-sectional observation of microstructure is highly desirable. Mechanical polishing of these ceramic devices has been attempted before with limited success in describing features on a macro to microscopic level[67]. The sensors produced for this study were limited to those that were produced for gas testing. This meant that SEM could only be commenced once gas testing was completed. Furthermore, since it is a destructive process, once mechanical polishing of the sensors takes place they can only be subjected to other forms of analysis with great difficulty. The mechanical polishing and SEM observation of sensors as similar as possible to those described above was performed in order to get an idea of what information would be obtained whilst preserving the valuable, original sensors. The SEM micrographs obtained from this process are displayed below in Figure 3.12 and Figure 3.13.

These SEM micrographs show that the overall structures within the sensors, the substrate, electrode and sensing layers, can quite easily be discerned at low magnification. At higher magnification it is apparent that the cross-section is not a simple flat surface as would be obtained in the section of a metal sample. It appears that because the particles of diamond in the polishing media are of similar size to the particles in the structures being polished the polishing process occurs through the structure's particles being stripped out rather than sheared through. This means that it will not be possible to quantify the level of porosity in the structures using classical techniques on sections prepared by this method. The structure revealed in the sensor derived from coarse chromia material does appear to have a significant

amount of micro-porosity that is likely to be interconnected. Much less micro-porosity is evident in the structure of the sensor derived from fine chromia material. These results are not reliably indicative of what would be observed in the structures of the sensors observed in previous sections due to different processing conditions. Also, it is possible that a large degree of the surfaces being observed are covered by the materials used to mount the samples.

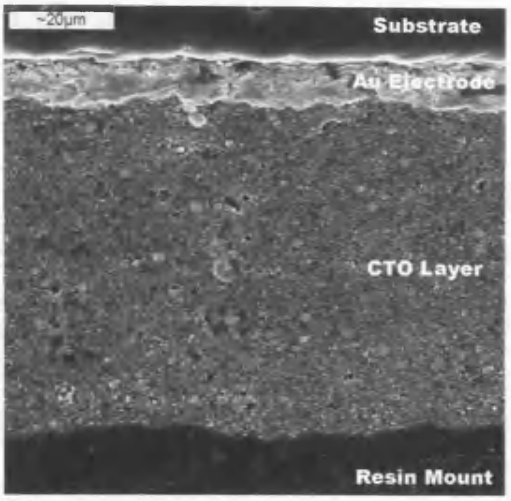

(a)

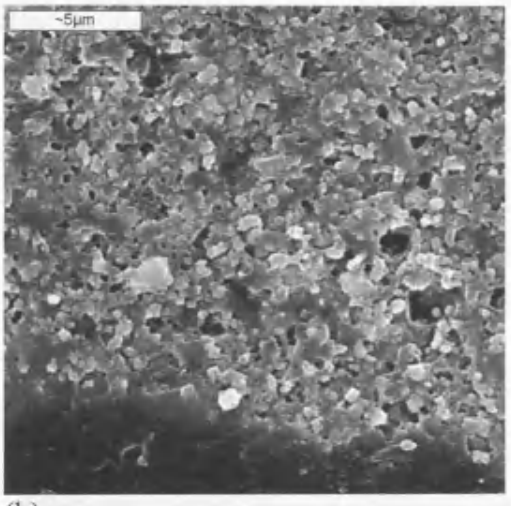

(b)

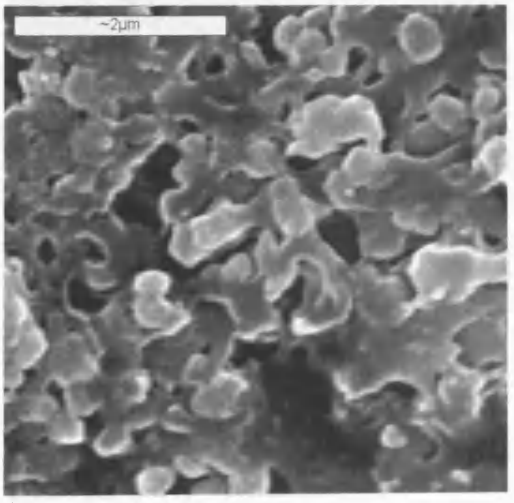

(c)

Figure 3.12 Cross-sectional SEM micrographs of sensor derived from coarse chromia material at different magnifications

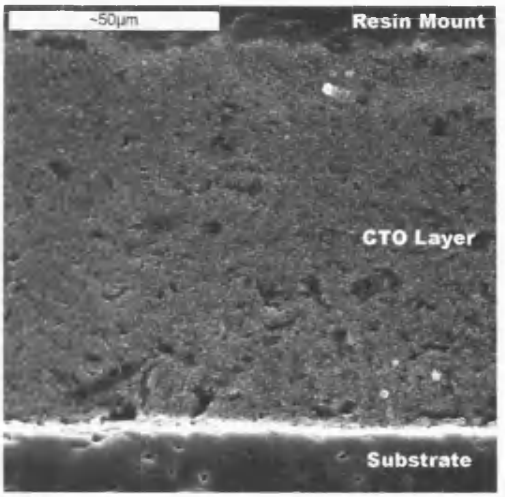

(a)

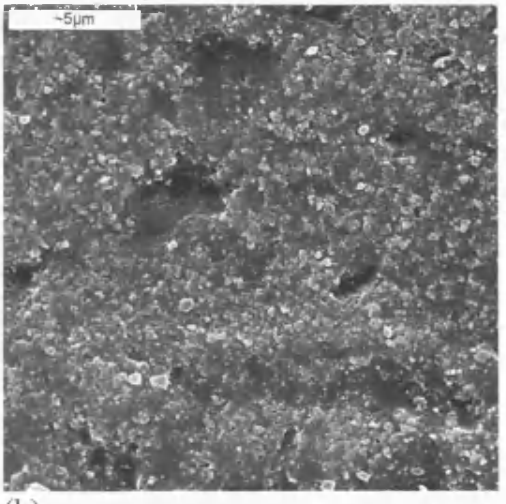

(b)

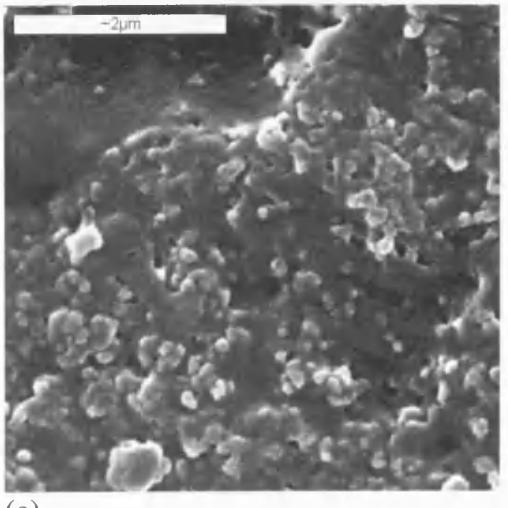

(c)

Figure 3.13 Cross-sectional SEM micrographs of sensor derived from fine chromia material at different magnifications

3.2.4 Cross-sections Produced by Focussed Ion Beam (FIB) Milling

Due to the lack of success in observing cross-sections prepared by mechanical polishing, other techniques for producing cross-sections were investigated. One such technique that appeared to show particular promise was that of ion beam milling. Different equipment is available for this process[68,69]. The JEOL cross-section polisher (SM-09010) would seem to offer the ideal method of producing a cross-section of an entire sensor. Unfortunately the use of such an instrument could not be secured for this work. However, the use of a Leo-Zeiss 1540XB focussed ion beam (FIB) and field emission gun, scanning electron microscope (FEGSEM) was kindly provided by the London Centre for Nanotechnology[70]. Only very small sections can be milled in reasonable lengths of time using this method. Typically, it takes approximately and hour to mill a volume of approximately 125 μm^3.

Three regions were successfully milled on the sensor made using coarse chromia material and sintered at 1000°C. The SEM micrographs of the two largest milled regions are presented in Figure 3.14 and Figure 3.15 whilst Figure 3.16 presents the smallest milled region.

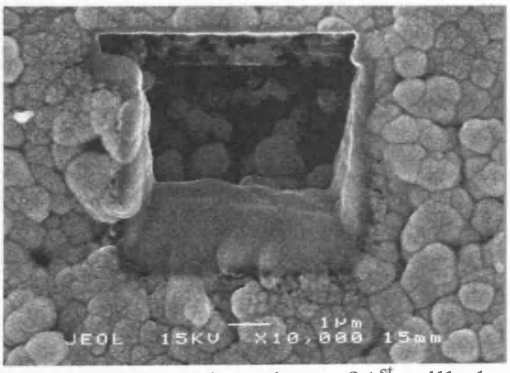

(a) Showing plan view of 1st milled area

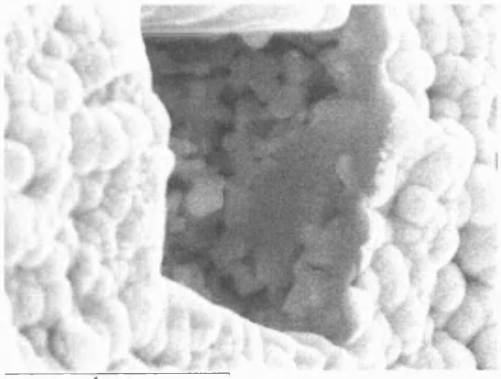

(b)Showing cleanest cross-section obtained

Figure 3.14 SEM micrographs of 1st large area produced by FIB milling of sensor derived from coarse chromia material sintered at 1000°C

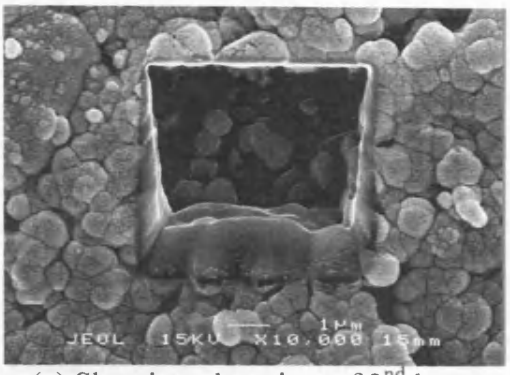

(a) Showing plan view of 2nd large milled area

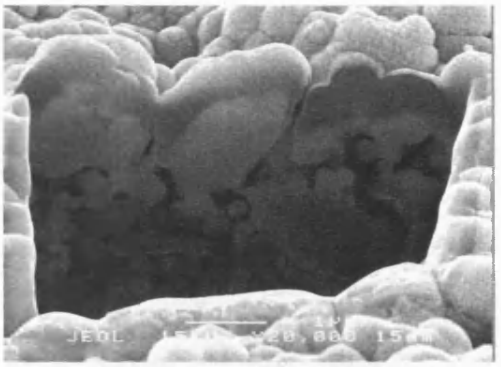

(b) Showing overview of cleanest cross-section

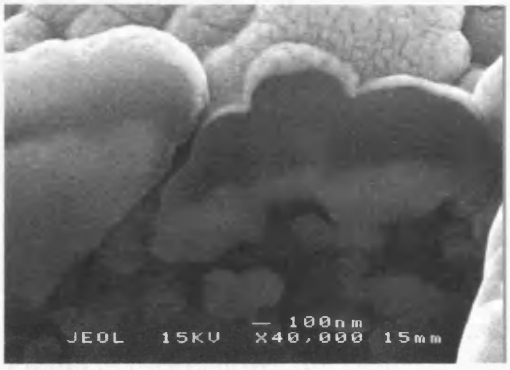

(c) Showing detail of cleanest cross-section near specimen surface

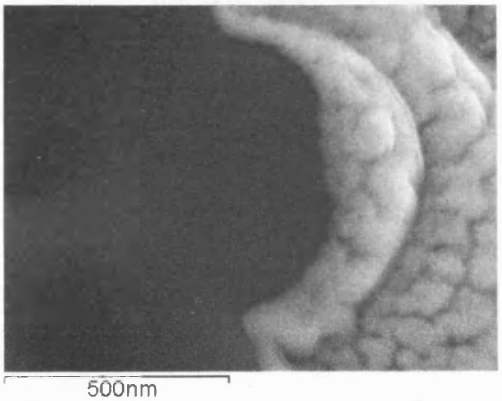

(d) Showing fine detail of cleanest cross-section near specimen surface

Figure 3.15 SEM micrographs of 2nd large area produced by FIB milling of sensor derived from coarse chromia material sintered at 1000°C

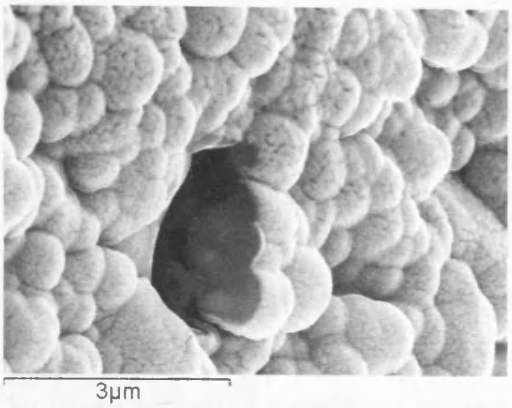

(a) Showing overview of smallest milled area

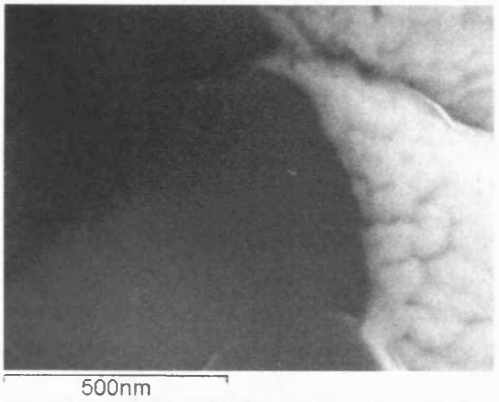

(b) Showing fine detail of smallest milled area nearest specimen surface

Figure 3.16 SEM micrographs of smallest area produced by FIB milling of sensor derived from coarse chromia material sintered at 1000°C

3.2.4.1 Results

Figure 3.14(a) shows the plan view of the first large area milled using the focussed ion beam (FIB). The section is a pit of approximately square shape. The pit is surrounded by material similar to that observed in the original SEM micrographs of the material in Figure 3.4, Figure 3.5 and Figure 3.6. The process of using two FIB milling stages to create the bulk of the pit and then a good quality cross-sectional surface to view is evident in the thin, off-centre extension to the pit that it as the top of the pit in the picture. Also apparent is that the surfaces that were milled first are now smooth in appearance and do not show the structure of the underlying material. This is likely to be a result of the FIB scanning progressively away from the first surfaces milled. Some material that was milled away later is then redeposited on these first surfaces, essentially covering them up.

When the sample is rotated in the SEM it is possible to view the cleanest milled surface in the side of the pit as shown in Figure 3.14(b). The contrast in this image is exceptionally high. There are two reasons for this contrast. The first is that the original top surfaces of the sensor were coated in gold. Far more image forming secondary electrons are produced when the electron beam interacts with these regions. Another factor is that because the surface of interest is within the pit it is more likely that the secondary electrons formed by the interaction of the primary

electron beam with the surface will be absorbed in the pit and will not reach the detector.

The structure of the profile that has been revealed can be divided into two distinct regions. The first is a dense 'skin' on the surface where the particles have merged to become a single mass with very little porosity apparent. The second is the underlying material that is composed of generally fairly small, equiaxed particles separated by a large proportion of porosity. Also apparent, just below the surface in the underlying material, is a more massive, elongated particle that is approximately 3 times as wide and 10 times as long as the surrounding particles.

Figure 3.15(a) shows a very similar plan view of the second large milled pit as observed for the previous one. Figure 3.15(b) shows the overview of the cleanest milled surface. This surface displays a similar profile as noted for the first milled region above. The structure is again shown to be formed of two distinct regions. The dense surface region seems here to be formed of more distinct massive particles and contains a few small channels of porosity through the skin. The underlying structure again seems to be mostly composed of fine, equiaxed particles separated by a large proportion of porosity. There is a solitary massive and elongated particle evident in this region similar to that noted in the first milled region. There also appears to be some smaller elongated particles of a similar size to the majority of the particles in this underlying structure.

Also evident in these images, and particularly in Figure 3.15(c), is that the upper surface skin appears to be composed of a much darker layer at the very surface with a much lighter layer below. This image also shows the rippled surface of the material that was also noted above. It shows this rippling in profile through a particle. The rippling is shown at higher magnification in Figure 3.15(d). The troughs of these ripples do not appear to extend very far into the bulk of this surface, certainly no more than the peak to peak distance of the ripples.

Figure 3.16(a) shows an overview of the cleanest surface produced on the third, and smallest, milled area on this sample. This section shows only the continuous skin on the surface of the sensor and none of the underlying structure. Part of this surface is

shown at much higher magnification, close to the surface of the sensor in Figure 3.16(b). Again it shows the troughs of the rippled surface do not extend throughout the bulk.

3.2.4.2 Discussion

The fact that these structures display two distinct regions of microstructure in cross-section is of great interest. The pre-sintering microstructure seen on the top surface of the sensor in Figure 3.4(a), Figure 3.5(a) and Figure 3.6(a) displays a relatively fine structure composed of equiaxed particles. These features and their size are somewhat akin to those observed in the second microstructural regions below the surface of the sensor in Figure 3.14(b) and Figure 3.15(b). The fact that the particles below the surface do not appear to have undergone any significant changes upon sintering is initially very surprising. From viewing only the top surface of the sensors and observing the significant changes that occur here upon sintering one might expect this to be typical of the structure throughout the bulk of the sensor. However, sintering only appears to have occurred at the very surface of the sensor resulting in a dense skin of material that encapsulates the inner material that is relatively unaffected by sintering.

By looking at the top surface SEM micrographs of the sensors sintered at the lower temperatures of 775 and 900°C in Figure 3.4(b+c), Figure 3.5(b+c) and Figure 3.6(b+c), it appears that this dense surface skin develops gradually. As the particles in the surface layer coarsen the amount of porosity is gradually decreased and it becomes trapped, as observed above. This means that it will be more difficult for gases to penetrate the surface skin for the sensors sintered at higher temperatures. This is likely to affect the sensitivity parameter (A) and the speed of response (τ) of the whole structure.

Another effect of these two distinct microstructural regions will be that the simple microstructural model will not accurately represent the real microstructure. The model used in this study assumes the microstructure is simply a collection of three resistors. It is thought that such a simple model may also represent a reasonable

approximation of microstructures composed of homogenous arrangements of equiaxed particles and could be used to provide information about simple changes in the properties of these structures such as particle size where the caveats apply. However, the presence of the two regions having distinct microstructure means that the structures for these sensors may be represented better by a more complicated model.

Such a model would have to account for the different proportions of the resistors that would represent the different microstructural regions and also the complications of gas access to the different regions that would arise because of the change in the porosity of the surface skin. Such a model may be represented by a resistor network such as that given in Figure 3.17. The changes in porosity could be represented by manipulations to the sensitivity parameter (A) and time constant (τ) that represent the different concentrations of gas that would reach the different regions at different times. However, with the added complexity of such a model the clarity and simplicity of understanding microstructures would be lost. Despite this possible complication, the simple model may be used on tests for these sensors. The results will require more interpretation than would be necessary if the structures were homogenous collections of equiaxed particles as will be discussed later.

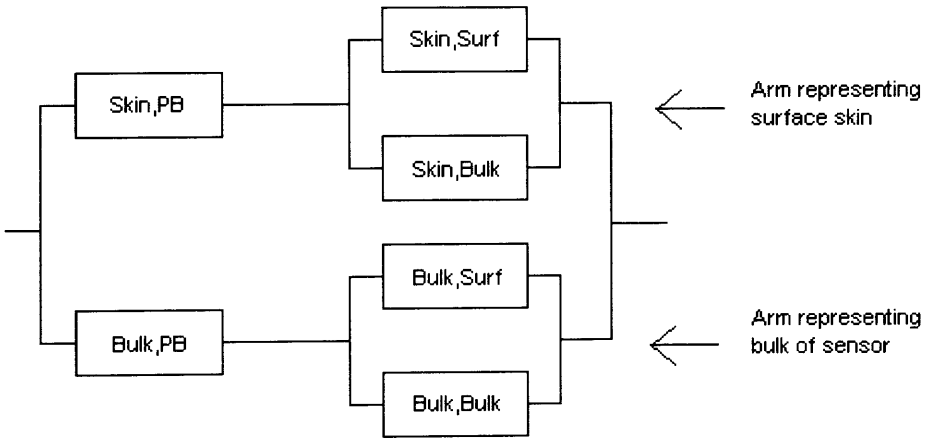

Figure 3.17 Diagram of resistor network that may better represent sensors having a microstructure composed of two different distinct regions as observed in FIB milled cross-sections for sensor derived from coarse chromia material sintered at 1000°C

3.3 Conclusions

The main requirement for this study was that of sensors having different microstructures. This requirement has been met through the variation of two experimental parameters: raw material source and sensor sintering temperature. The particle size of the coarse chromia raw material has been approximated, from these SEM micrographs, to be almost four and a half times greater than that of the fine chromia raw material. In the sensors that have been kept unsintered after screen printing, the size of the chromium titanate particles they contain is also show to be significant different between the sensors derived from the two sources of raw chromia material: again, the coarser particles are approximately four times the size of the finer particles. The sensors derived from both raw material sources appear to show clear trends in their particle size with increasing sintering temperature that have been approximated from the SEM micrographs. In the following chapter the results of gas testing and data processing to obtain solutions to the microstructural model will be interpreted in terms of these differences in microstructure that have been observed. Highly important aspects of the microstructure such as porosity and surface area have not been successfully described or quantified in this study due to complications in preparing suitable samples. This may complicate later discussions. Attempts to generate suitable samples for analysis of porosity appear to indicate that a skin of material at the surface of the sensors derived from coarse chromia material undergoes large degrees of sintering whilst the bulk of the material, below the surface, remains relatively unaffected. Because this structure is more complicated than a homogenous, equiaxed collection of particles the interpretation of the results from the solutions to the simple model is likely to be complicated.

4 Gas Tests on Sensors Derived From Coarse Chromia

Batches of sensors having different initial microstructures by virtue of their particle sizes were obtained from City Technology Ltd. These batches of sensors were split into several groups. These groups of sensors were sintered at different temperatures in order to obtain microstructures that displayed clear trends in the magnitude and distribution of their features. This chapter details the results of gas testing and the subsequent data processing that was carried out on the batch of sensors that were derived from chromia material having a coarse particle size. The main aim of these tests was to investigate whether the microstructural model developed in section 1.4.4 could be applied to sensor response to generate solutions to this model. A further, vital aim was to investigate whether the parameters obtained from these solutions displayed any trends with sintering temperature and microstructural features. It was also of interest to investigate the effects that testing to different gases would have. This forms the basis of the two subsections of this chapter, section 4.1 and 4.2, which respectively deal with the CO and propane test performed on these sensors derived from the coarse chromia material.

The type of results presented for each set of tests is identical. The response transients are shown first to illustrate the shape of the transients and how close they are to reaching the steady state. The pseudo steady state response data is then shown plotted versus gas concentration. In these plots the solutions that are obtained to both the traditional square root model and the microstructural model are plotted to show how well the solutions fit the experimental data. From each solution of the data to the microstructural model the values of the parameters representing the different microstructural regions are obtained. The parameters found for the different sensors can then be compared by plotting them versus the properties that are being controlled: i.e. sintering temperature or operating temperature. These plots show how the contribution to resistance from each of the different regions changes with sintering temperature or operating temperature. If the microstructural model is valid then it ought to be possible to explain why the trends in the parameters with sintering temperature and operating temperature are observed by relating them to how the

changes in microstructure and operating temperature are likely to affect different parameters. After the steady state solutions are presented the solutions to the transient data are presented. In these transient regressions the microstructural parameters obtained from the steady state solutions are taken as constants. Only the sensitivity parameter, A, and time constant, τ, are allowed to vary. The values of these parameters are then displayed in bar charts for the different sensors and gas concentrations. As with the results from the steady state solutions, an explanation of the changes that occur in the transient parameters in terms of the microstructure or operating temperature can then be attempted. Finally, each response transient is plotted with all the different solutions obtained for the different gas concentrations of that particular sensor to show how the different values of the transient parameters obtained affect the solutions.

4.1 Response to Carbon Monoxide

4.1.1 Gas Exposure Transients

The response versus time plots for the CO gas exposures on sensors derived from coarse chromia material are displayed in Figure 4.1. At the end of these 600 second exposures the responses are good approximations to the steady state response. However, the degree to which this is the case does vary. It is particularly notable that the responses to 4600 ppm CO for the sensors sintered at 775°C in Figure 4.1(a+b) have reached the plateau in response which defines the steady state and that their responses would not change significantly with a more prolonged exposure to gas than was conducted here. The other transients presented in Figure 4.1 for lower concentrations and sensors sintered at higher temperatures show responses that rise more gradually towards their steady state values and have plateaued to different extents. The elbow between the initial rise and the plateau region of the response curves also heads towards longer and longer times with decreasing CO concentration and increasing sintering temperature. Another significant observation is that the magnitude of the responses to different concentrations is decreased for the sensors sintered at higher temperatures.

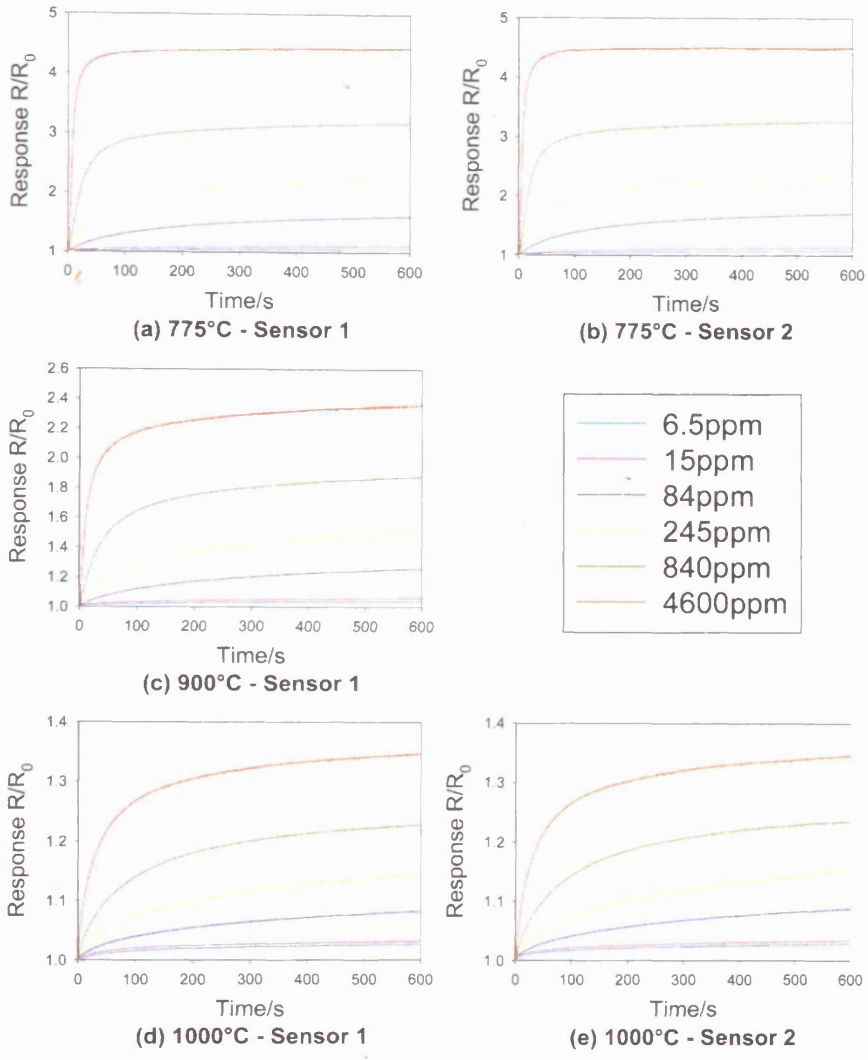

Figure 4.1 Response versus time plots for the gas exposures to different CO concentrations on sensors derived from coarse chromia material sintered at 775 (a+b), 900 (c) and 1000°C (d+e). These plots show the steady state is most closely approached in sensors sintered at lower temperatures tested to the highest gas concentrations. It is also evident that the magnitude of responses for the sensors sintered at lower temperatures is higher than for those sintered at higher temperatures.

4.1.2 Solutions to the Model – Steady State Gas Response

The first thing to note about the results for the sensors prepared from coarse chromia material when tested to varying concentrations of CO shown in Figure 4.2 is that sensors sintered at high temperature have a decreased response. The solid lines in Figure 4.2 represent the solutions for the set of data to the steady state form of the microstructural model given in Equation 1.24. These lines are shown to pass most

closely to the experimental data points for sensors sintered at lower temperatures. This indicates that the degree to which the solution obtained for the microstructural model fits the experimental data decreases with increasing sintering temperature. In comparison with the solutions of the data to the traditional square root model, represented by the dotted lines in the charts in Figure 4.2, the solutions to the microstructural model appear to pass more closely to the data points. The solutions to the microstructural model can therefore be said to represent a better fit to the experimental data than the solutions to the traditional square root model. The degree to which the solutions to the traditional model fit the data is not observed to be significantly dependent on the sintering temperature.

Figure 4.3 above shows the different microstructural parameters obtained from the solutions to the microstructural model plotted versus sintering temperature. For the sintering temperatures of 775 and 1000°C there are two sensors and the values of the parameters obtained are shown to be reasonably close. Only one sensor sintered at a temperature of 900°C was tested. All the parameters display a clear trend with increasing sintering temperature: $R_{PB,0}/R_{T,0}$, $R_{B,0}/R_{T,0}$ and the steady state value of A show a clear decreasing trend, whilst $R_{S,0}/R_{T,0}$ shows a clear increasing trend with increasing sintering temperature.

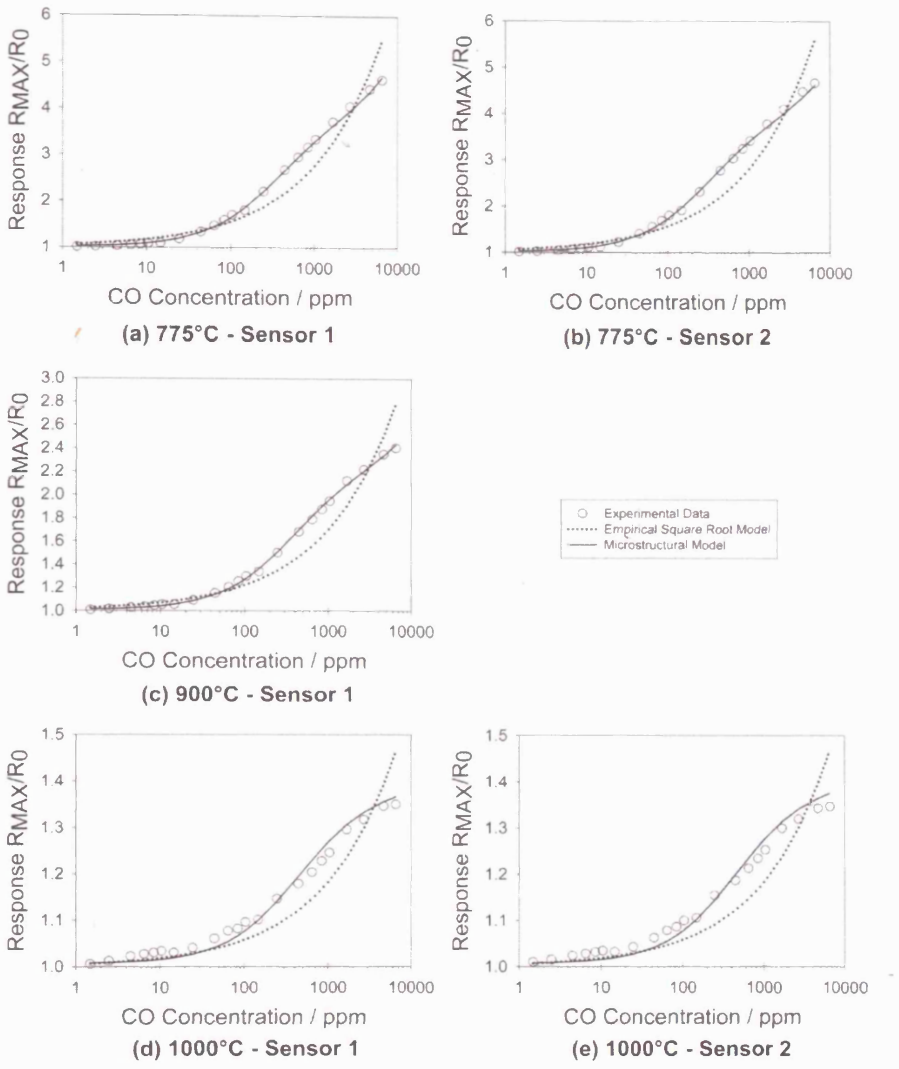

Figure 4.2 Plots of response versus carbon monoxide concentration for sensors sintered at 775°C (a+b), 900°C (c) and 1000°C (d+e). Magnitude of response decreases with increasing sintering temperature. Solutions obtained for the microstructural model are shown to have much better fit to the experimental data than for the empirical square root model. As sintering temperature is increased the degree to which the obtained solution to the microstructural model fits the data is observed to decrease. The degree to which the solutions to the traditional model fit the data is not significantly affected by sintering temperature.

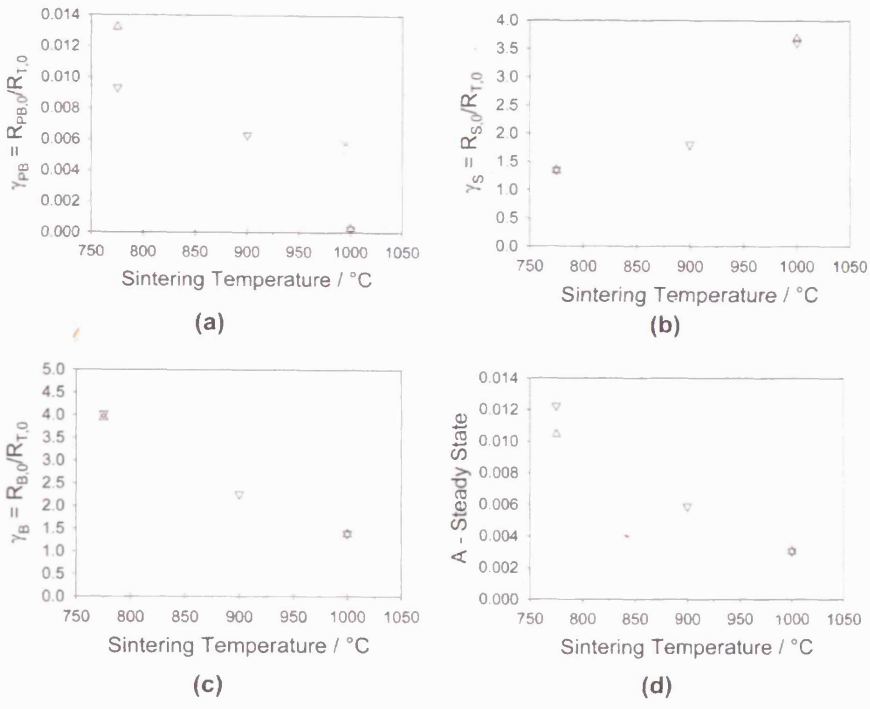

Figure 4.3 The microstructural parameters of the solutions of the experimental data to the microstructural model are plotted versus sintering temperature. The variations of the parameters that occurs with sintering temperature may be explained by microstructural observations and reassessing assumptions.

4.1.3 Solutions to the Model – Transient Gas Response

For each sensor the response transients for 6 gas concentrations are subjected to non-linear least squares regression to the transient form of the microstructural model. The microstructural parameters obtained above from the steady state treatment of the response data are fed into the equation representing the model as constants. Only the sensitivity parameter, A, and the time constant, τ, are allowed to vary. Assuming the regression process converges properly, a solution is obtained for each sensor and for each of the 6 gas response transients. The parameters A and τ are plotted for each sensor and gas concentration below in Figure 4.4 and Figure 4.5 respectively.

Where there are two sensors that have been sintered at the same temperature, 775 and 1000°C, the values of both A and τ are found to be almost identical at each concentration. In most cases there is no variation of the value of the parameters with concentration. The average values of the sensitivity parameter, A, obtained from the transient regressions for the different concentrations in Figure 4.4 display a

decreasing trend with increasing sintering temperature. This trend and the actual values follow closely those that were obtained for this parameter from the steady state data presented in Figure 4.3(d). The value of the time constant, τ, appears to be invariant for both sintering temperature and gas concentration at a value of approximately 200.

Two exceptions to the statement of constant values of A and τ with gas concentration are apparent in these data. For both sensors sintered at 775 °C the value of A is constant, as stated, but the value of τ displays a decreasing trend with increasing gas concentration. For both sensors sintered at 1000 °C this situation is reversed, with the value of A displaying a decreasing trend with increasing gas concentration and the value of τ remaining constant.

It is interesting to see what these different solutions look like when plotted with the transients used to generate them. For each sensor, in Figure 4.6, Figure 4.7, Figure 4.8, Figure 4.9 and Figure 4.10, the experimental response data for each concentration is plotted versus time in a different chart, (a) to (f), as the black lines. The coloured lines represent the different solutions obtained for all the concentrations tested for the particular sensor in question. As would be expected, the solution obtained for a particular concentration fits the experimental transient data for that concentration best, whilst the solutions obtained for other concentrations do not fit so well. The degree to which this is true varies between sensors. For instance, all the solutions obtained for the sensor sintered at 900 °C fit the experimental transient data for all the different concentrations quite well. However, for the sensors sintered at 775 and 1000°C only the solution for the particular concentration in question fits the data particularly well and all others are very poor fits.

It is interesting to note that for the sensors sintered at 775°C, whose value of the time constant, τ, varies with gas concentration, the apparent speed of response (the speed with which the transient response approaches the steady state) shows an increasing trend with increasing gas concentration and this is the exact opposite of that for the sensors sintered at 1000 °C where the sensitivity parameter, A, varies with gas concentration. Another key observation is that none of the response transients obtained for the solutions to the transient response data at the start of the gas

exposures (i.e. when time of exposure is 0 seconds) starts at 1. All these responses should start at a response of 1 at this time since R_0/R_0 should be equal to 1.

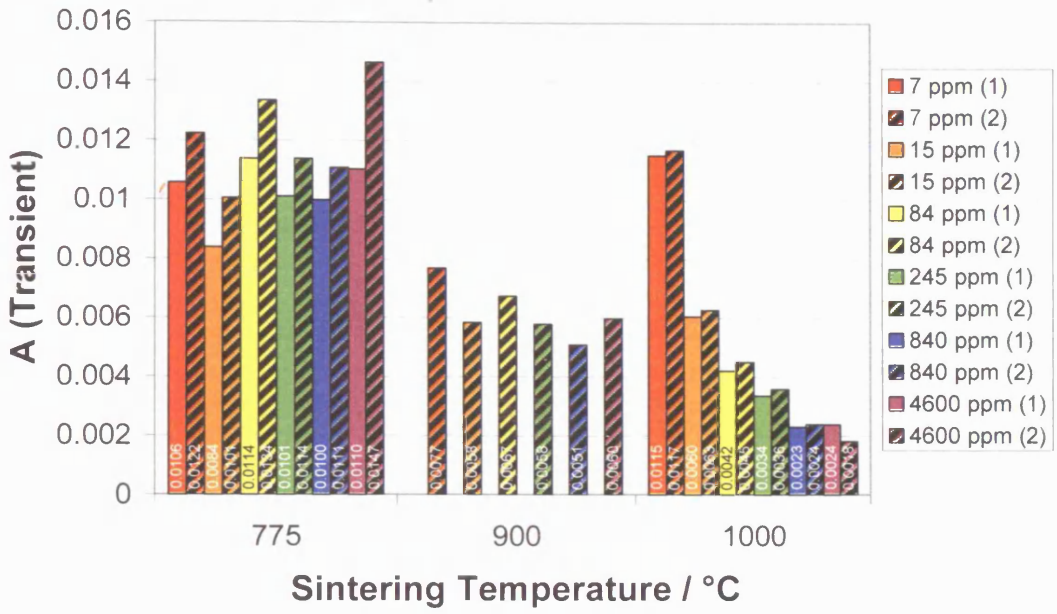

Figure 4.4 Bar chart showing the different values of A obtained from non-linear least squares regression of transient data from sensors sintered at different temperatures and tested to different concentrations of CO

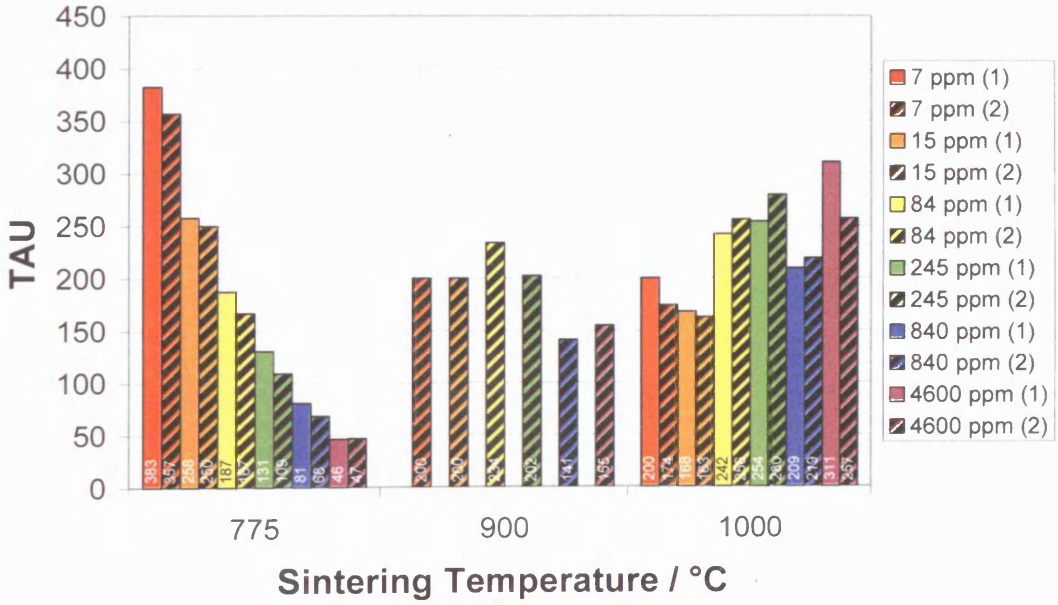

Figure 4.5 Bar chart showing the different values of τ obtained from non-linear least squares regression of transient data from sensors sintered at different temperatures and tested to different concentrations of CO

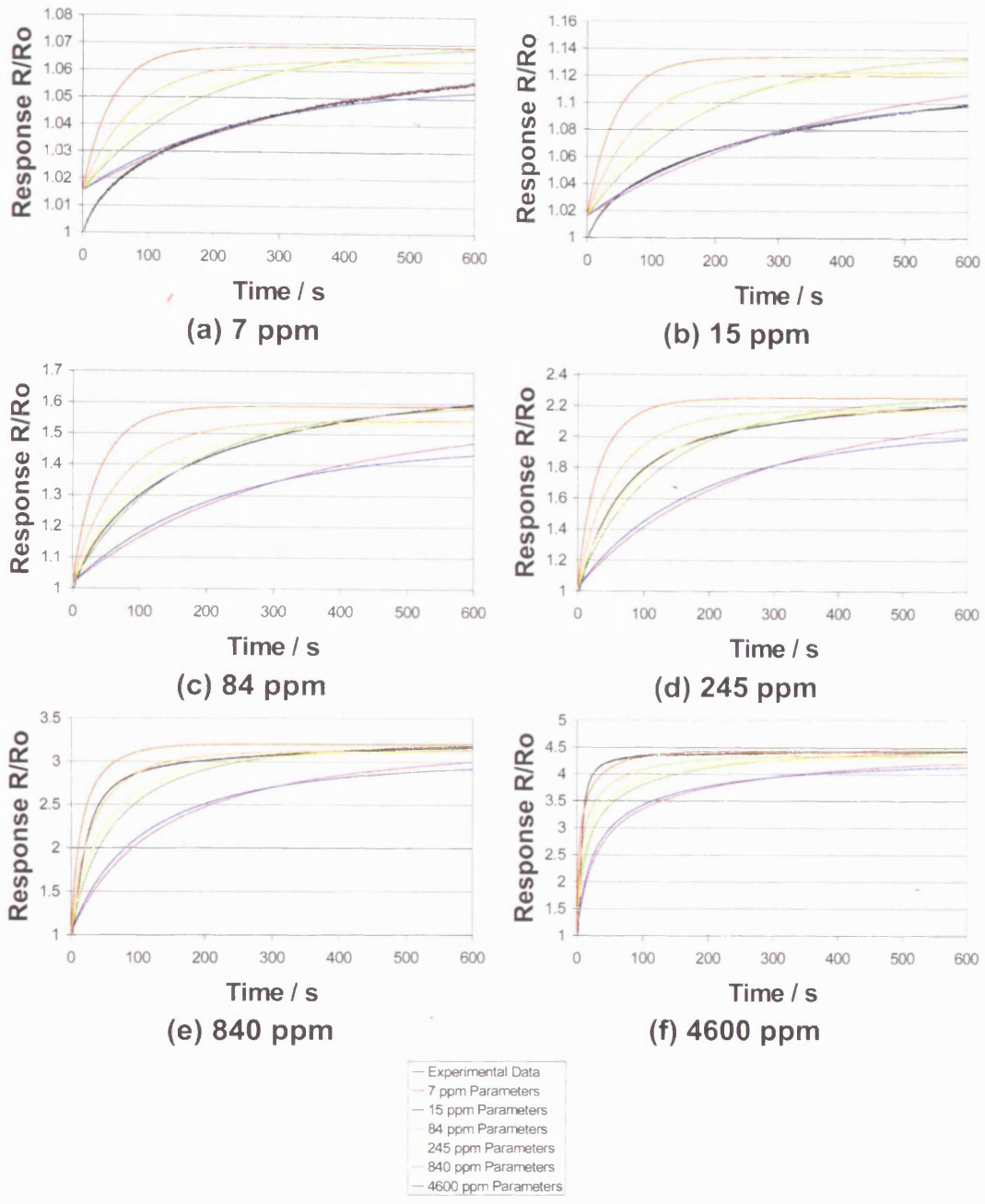

Figure 4.6 Coarse chromia sensor, sintered at 775°C, sensor number 1, tested to CO. Charts (a) to (f) show the experimental response transient for the particular concentration indicated as the black lines and the simulated transients of the regression solutions of all concentrations as the coloured lines. The observations made from these data are: (1) Response of solutions at t=0 is not equal to 1 as it should be (this is because the steady state solution is slightly inaccurate); (2) The solution obtained for a particular concentration fits the experimental transient for that concentration very well; (3) In this case, for an experimental transient for a particular concentration the solutions obtained for other concentrations do NOT fit particularly well

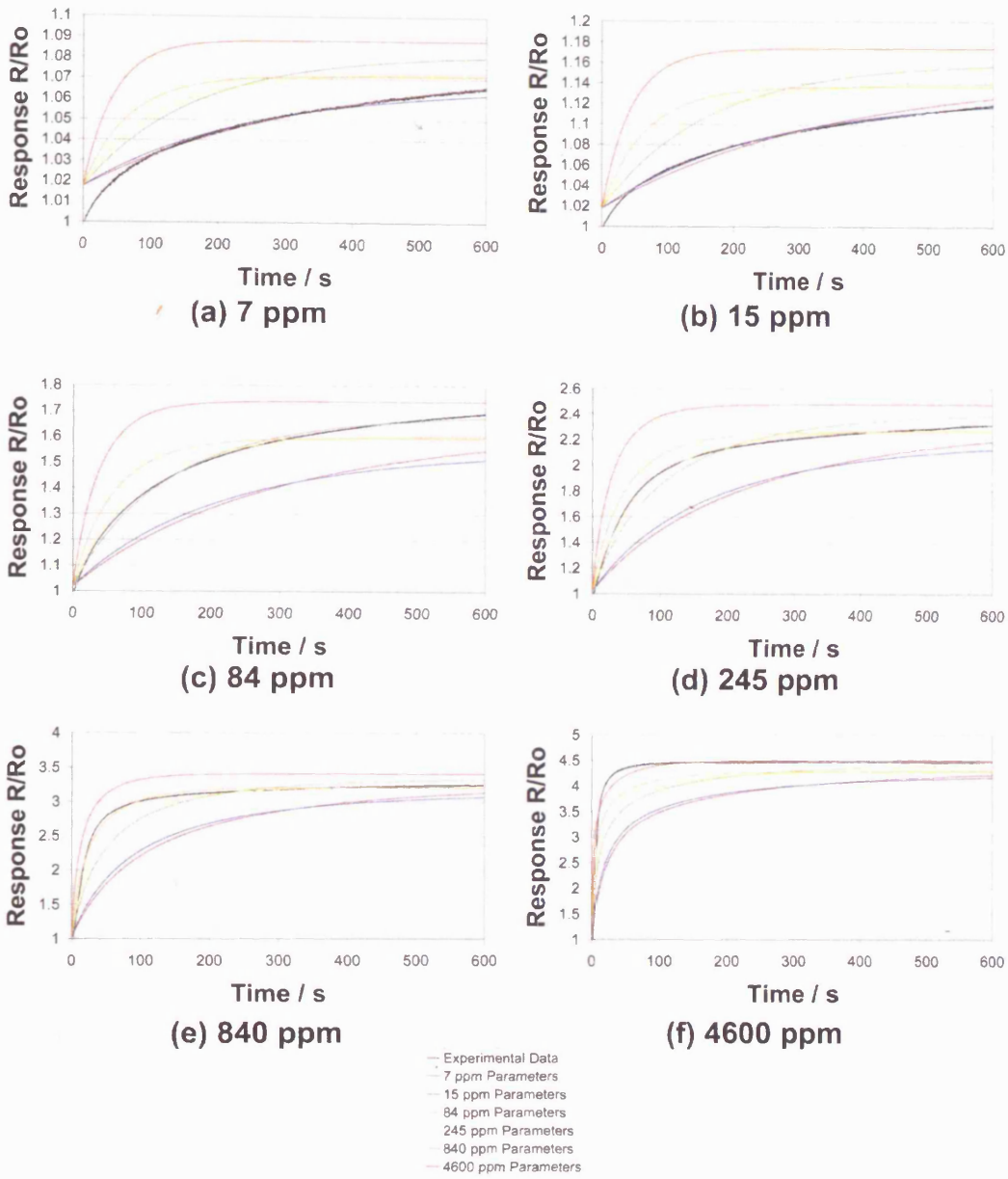

Figure 4.7 Coarse chromia sensor, sintered at 775°C, sensor number 2, tested to CO. Charts (a) to (f) show the experimental response transient for the particular concentration indicated as the black lines and the simulated transients of the regression solutions of all concentrations as the coloured lines. The observations made from these data are: (1) Response of solutions at t=0 is not equal to 1 as it should be (this is because the steady state solution is slightly inaccurate); (2) The solution obtained for a particular concentration fits the experimental transient for that concentration very well; (3) In this case, for an experimental transient for a particular concentration the solutions obtained for other concentrations do NOT fit particularly well

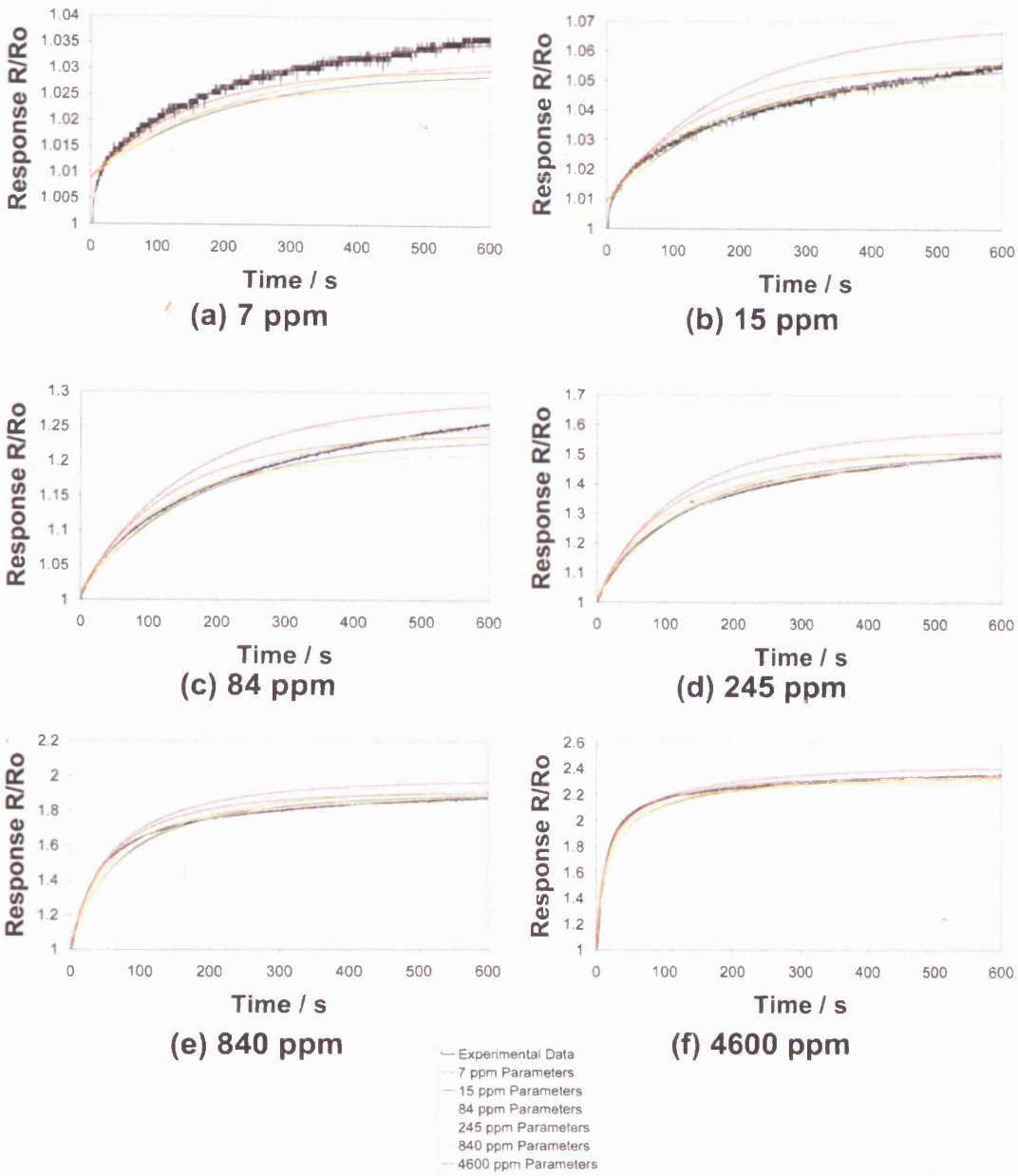

Figure 4.8 Coarse chromia sensor, sintered at 900°C, sensor number 1, tested to CO. Chart (a) to (f) show the experimental response transient for the particular concentration indicated as the black lines and the simulated transients of the regression solutions of all concentrations as the coloured lines. The observations made from these data are: (1) Response of solutions at t=0 is not equal to 1 as it should be (this is because the steady state solution is slightly inaccurate); (2) The solution obtained for a particular concentration fits the experimental transient for that concentration very well; (3) In this case, for an experimental transient for a particular concentration the solutions obtained for other concentrations DO fit well

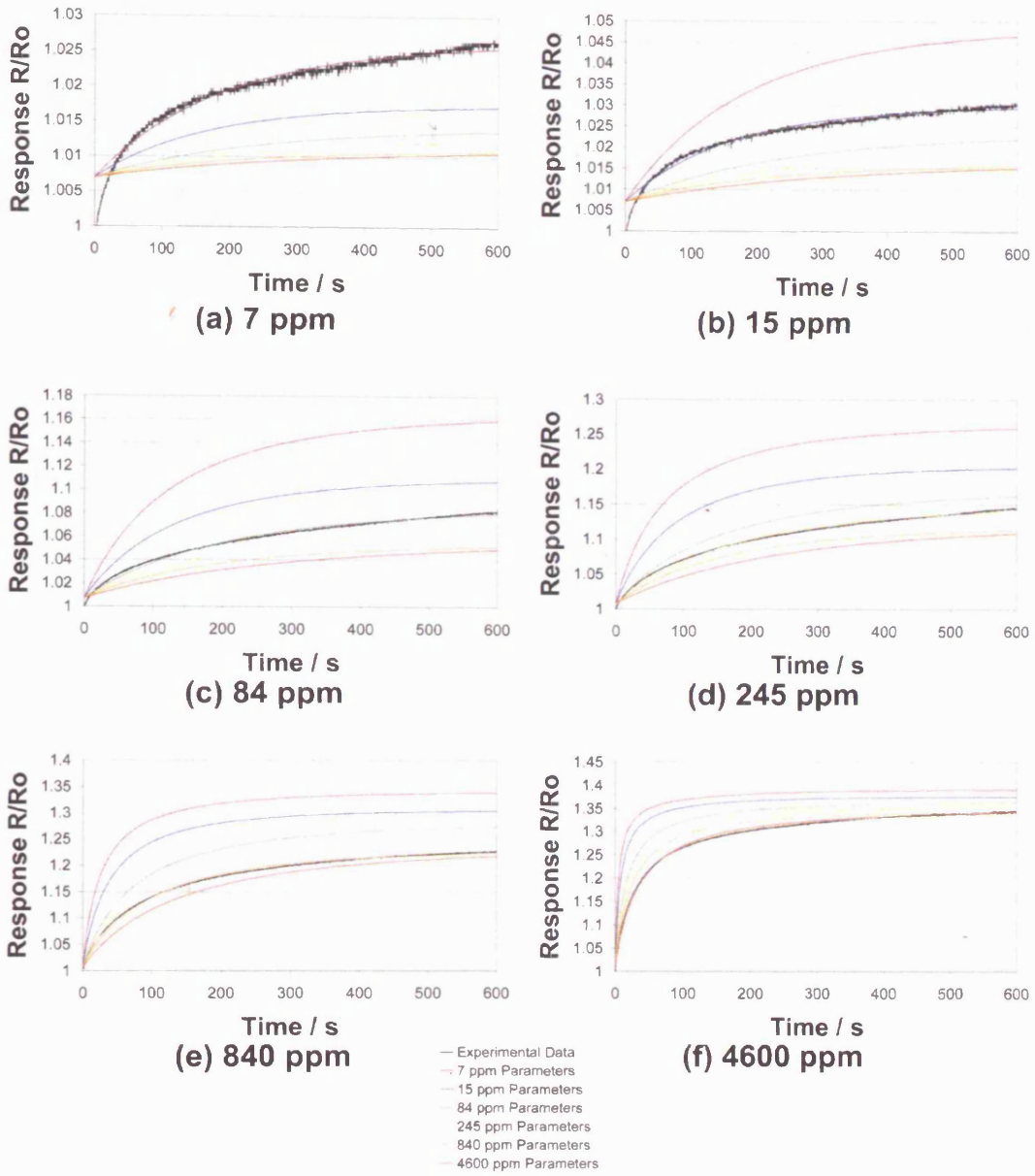

Figure 4.9 Coarse chromia sensor, sintered at 1000°C, sensor number 1, tested to CO. Chart (a) to (f) show the experimental response transient for the particular concentration indicated as the black lines and the simulated transients of the regression solutions of all concentrations as the coloured lines. The observations made from these data are: (1) Response of solutions at t=0 is not equal to 1 as it should be (this is because the steady state solution is slightly inaccurate); (2) The solution obtained for a particular concentration fits the experimental transient for that concentration very well; (3) In this case, for an experimental transient for a particular concentration the solutions obtained for other concentrations do NOT fit particularly well

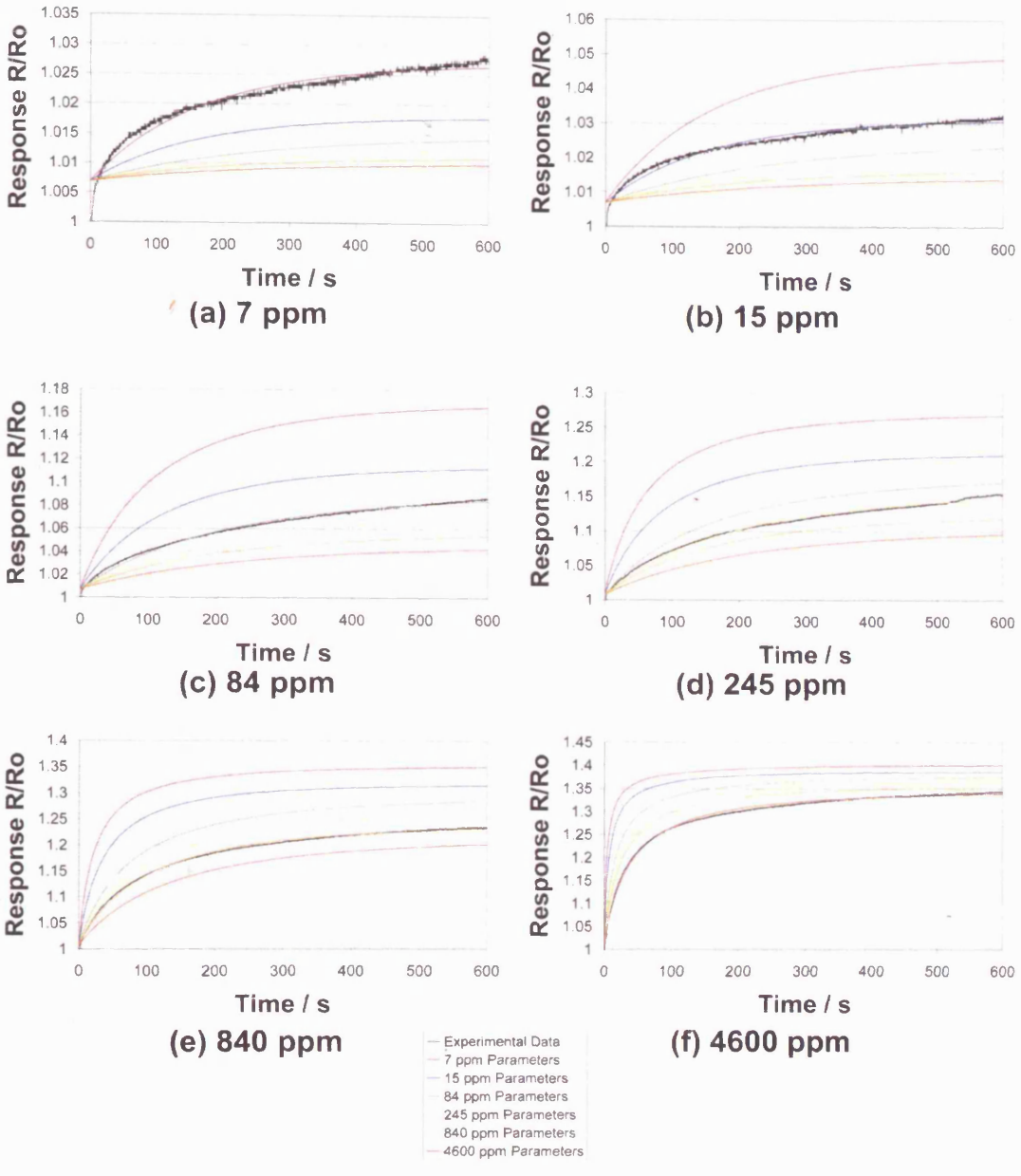

Figure 4.10 Coarse chromia sensor, sintered at 1000°C, sensor number 1, tested to CO. Chart (a) to (f) show the experimental response transient for the particular concentration indicated as the black lines and the simulated transients of the regression solutions of all concentrations as the coloured lines. The observations made from these data are: (1) Response of solutions at t=0 is not equal to 1 as it should be (this is because the steady state solution is slightly inaccurate); (2) The solution obtained for a particular concentration fits the experimental transient for that concentration very well; (3) In this case, for an experimental transient for a particular concentration the solutions obtained for other concentrations do NOT fit particularly well

4.1.4 Discussion

The transients presented in Figure 4.1 show the primary data from which all the following results are derived. The nature of the methods used and the assumptions made in using the microstructural model to analyse sensor responses may be highly dependent on the character of these primary results. Of particular importance is the fact that the methods used to generate the primary solutions of the data to the microstructural model rely on the pseudo steady state data derived from these response transients. In most cases the response achieved by the end of the experiments can only be said to be a rough approximation of the true steady state value. Because the assumptions used to generate the model rely on the data being true steady state data there will likely be some inaccuracy in the values obtained for the different parameters of the model in the later stages of data processing.

These inaccuracies may manifest themselves in different ways depending upon how the integrity of the approximations vary with the different experimental variables and how solutions to the model are derived from the data. For instance, the varying integrity of the approximations of the steady state responses with sintering temperature observed for these CO tests will likely mean that there is some inaccuracy of the values of the parameters obtained for the solutions to the microstructural model. This may mean that the microstructural and/or sensitivity parameters obtained from the solutions to the microstructural model are slightly inaccurate and may display trends with sintering temperature that are unexpected, amplified or attenuated as a direct result of these inaccuracies.

The variations noted in all these tests for the integrity of the approximations with gas concentration is likely to be another major factor in the accuracy of the solutions obtained to the microstructural model. In terms of the way that the solutions have been processed there will be two major effects of these variations with gas concentration. The first is that there will be an overall inaccuracy in the solutions obtained to microstructural model from the pseudo steady state data. Secondly, because of the inaccuracy of these initial solutions which are then used as constants for the microstructural parameters in the regressions of the transients, the solutions

for the sensitivity parameter and time constant obtained from these regressions will not only be slightly inaccurate but may also display some unexpected variation with gas concentration. The inaccuracy of the values of the parameters obtained will likely decrease with increasing gas concentration as the responses are seen to approach the true steady state case more closely under these circumstances and the initial approximation of the maximum response achieved as the steady state response becomes more valid.

One of the clearest indications that the microstructural model of sensor response is superior to the traditional square root model is displayed in Figure 4.2. The lines plotted for the solutions to the microstructural model clearly fit the experimental data far better than those plotted for the solutions to the traditional square root model. It has also been noted that the degree to which the solution to the microstructural model fits the data does decrease with increasing sintering temperature. The variation in the validity of the pseudo steady state response with sintering temperature noted in the transients displayed in Figure 4.1 could be an indication that this method of approximating the steady state response may indeed lead to some inaccuracy in the solutions obtained to the microstructural model.

Clear trends with sintering temperature have been noted for the parameters of the solutions to the microstructural model. If the microstructural model is an accurate description of how sensor response varies with microstructure and all the assumptions that have been made in its formation are valid then it ought to be possible to explain the trends that occur in the microstructural parameters with sintering temperature through the variations that have been observed in the microstructures of the sensors in chapter 3.

One of the effects of sintering that has been noted in the microstructural study of the sensors made from coarse chromia material in section 3.2.1 above is that of increasing interconnection between neighbouring particles. With increasing sintering temperature and, therefore, driving force for diffusion, the degree of interconnection between particles has generally been found to increase. This effect is deemed, in this case, to outweigh that of increasing particle size leading to a decrease in number of particle boundaries. Overall therefore, the effect of increased interconnection

between particles will be to increase the effective cross-sectional area of the boundaries. As discussed above, because resistance is inversely proportional to cross-sectional area, such an increase would lead to a decrease in the resistance of the particle boundaries and an overall decrease in their contribution to the resistance of the sensor. Thus, the observation of a decrease in the value of the particle boundary parameter with increasing sintering temperature displayed in Figure 4.3 can be related directly to the microstructural observations of increased particle interconnection.

Increasing particle size is the other major effect of increasing sintering temperature noted in the microstructural study of the sensors made from coarse chromia material in section 3.2.1 above. As discussed above, increasing particle size changes the proportion of the material present that is classified as surface and bulk. This changes the effective cross-sectional areas of these regions and therefore their contribution to the resistance of the sensors. Thus, it was inferred that with increasing sintering temperature:

1) the decreased effective cross-sectional area of the surface would lead to an increase in the contribution to resistance from the surface
2) the increased effective cross-sectional area of the bulk would lead to a decrease in the contribution to resistance from the bulk

Both of these statements are actually realised in the trends of the parameters representing the surface and the bulk obtained from the solutions to the microstructural model with increasing sintering temperature displayed in Figure 4.3. This means that all the trends in the parameters representing the microstructure of the sensors with sintering can be successfully explained in terms of the changes in microstructure that were described in chapter 3.

The sensitivity parameter, A, obtained from these solutions is also found to be dependent on sintering temperature. This result was somewhat unexpected as it was thought that most variation in response ought to be due to the microstructural changes that occur upon sintering and would be taken into account by variations in the microstructural parameters, such as those that have been observed above. There

are several possible explanations for why the value of the sensitivity parameter, A, would vary with sintering temperature. The first is related to the possibility of titanium surface segregation that has been observed previously for CTO[45,46,47,48,49,59]. The different sintering temperatures used to produce the different microstructures of the sensors may also result in different levels of titanium surface segregation. If so, this would be a change in the surface of the sensors with sintering temperature and the activity of the sites responsible for mediating gas response are likely to be affected to some degree by these differences. The sensitivity of the sensors would thus be affected to different degrees with sintering temperature, with a corresponding variation of the sensitivity parameter, A.

A second possible explanation could be that the decrease in the porosity of the surface skin layer that is observed with increasing sintering temperature leads to more restricted progress of the gas through this layer to the internal surfaces of the sensors. This would mean that the concentration in the depths of the sensors with the lower porosity skin would effectively be lower than those with a highly porous skin and there would also be some sort of delay, or lengthening, in the response. These effects could result in the reduced value of sensitivity parameter at higher sintering temperatures, but would also likely result in higher values of the time constant, τ, that will be obtained from the regressions to the transient data.

Another alternative explanation could lie in variation of the validity of the pseudo steady state responses with sintering temperature that was observed in the response transients in Figure 4.1. Such a variation would mean that the solution obtained to the microstructural model would be inaccurate. This inaccuracy would manifest itself in the parameters obtained from the solutions. It may be that this variation in the sensitivity parameter is simply the manifestation of this inaccuracy. Yet another possible explanation could lie in the different regions of the microstructure noted at the surface and in the bulk in the cross-sections of a sensor produced by FIB milling. The microstructural model essentially assumes the microstructures of sensors to be a homogenous, evenly sized, equiaxed arrangement of particles. Such a perfect situation is highly unlikely and has not been observed in the microstructures. It is possible that these differences cannot solely be accommodated in the values of the microstructural parameters and that the value of the sensitivity parameter is changing

in response. Of course, any or all of these possible explanations could be acting to produce this unexpected variation of sensitivity parameter, A, with sintering temperature.

The fact that the average values of the sensitivity parameter, A, obtained from the regressions of the transient data to the microstructural model at different concentrations follow the same trend with increasing sintering temperature and at similar values as was found in the solutions of the steady state data is a positive indication that the microstructural model can be used to describe sensor response in a repeatable manner. This also means that the same factors that resulted in the variation of the sensitivity parameter with sintering temperature for the steady state data has affected the values found for the transient data. Because the value of the time constant, τ, does not vary significantly with sintering temperature, the explanation of decreased surface skin porosity leading to reduced penetration of gas and delayed response appears to be unsubstantiated. The other two explanations for the effect remain as possibilities.

It is highly interesting to note the trends of the parameters obtained from the transient regressions with sintering temperature and gas concentration. For the sensors sintered at 775 °C the value of the sensitivity parameter, A, is constant with increasing gas concentration whilst the value of the time constant, τ, decreases. For the sensors sintered at 1000 °C this situation is reversed and the value of the sensitivity parameter, A, decreases with increasing gas concentration whilst that of the time constant, τ, is constant. The sensor sintered at 900 °C bucks both these trends and the values of both the sensitivity parameter and the time constant are constant with gas concentration.

These differences in how the transient parameters vary with gas concentration also appear to affect how the solutions to the transient data fit the experimental transient data as displayed in Figure 4.6, Figure 4.7, Figure 4.8, Figure 4.9 and Figure 4.10. Each of these figures represents the transient response data for a single sensor sintered at a particular temperature. Each of the charts, (a) to (f), within these figures has the experimental response data plotted versus time as the black line. Each coloured line represents a solution obtained to a transient for a particular gas

concentration on the particular sensor in question. All the solutions are plotted on each chart to allow comparison of how well the different solutions fit all the experimental data to see whether these variations have a significant effect. Where one of the transient parameters of the model, A or τ, is noted to vary with gas concentration in Figure 4.4 or Figure 4.5 (i.e. for the sensors sintered at 775 or 1000°C), the transients representing the solution to the experimental data for each concentration fit only that particular response transient well and do not fit the response transient for the other gas concentrations well at all. In contrast, for the sensor sintered at 900°C where the transient parameters are not noted to vary with gas concentration all solutions fit all the experimental data to a much better degree. Even so, the solution for the particular concentration in question fits much better than those obtained for other concentrations.

A major factor that may result in the variations of the sensitivity parameter, A, with sintering temperature and also in the value of both the sensitivity parameter and the time constant, τ, with gas concentration in certain circumstances is that the transient responses for all sensors and gas concentrations are not observed to start at a response equal to 1. This is a result of the parameters that are obtained from the steady state solutions of the model for each sensor not being strictly valid. Equation 1.25 represents how the transient form of the model simplifies at time of gas exposure equal to zero. The values of response at zero time for all the sensors tested here are displayed in Table 4.1. All values are found not to be equal to 1 as they should. This fact may also be observed in Figure 4.6 to Figure 4.10, and in particular in the charts for the lowest concentration, (a), where the responses at zero time start at higher values than 1, whereas the experimental data starts from much closer to the correct value. This means that none of the solutions obtained to the microstructural model for either the steady state or the transient cases are valid in the strictest sense. However, they are extremely close to being valid and it is likely the repeatability and the general success of applying the microstructural observations to the trends in values obtained for the parameters of the solutions to the model attest to the superiority of this model in describing sensor response over the traditional square root model.

Table 4.1 Showing the values of response at t=0 for the sensors made from coarse chromia material tested to CO. These values should equal 1 but are found to be inaccurate for all sensors.

SENSOR	Response at t=0
775°C-1	1.0153
775°C-2	1.0174
900°C-1	1.0088
1000°C-1	1.0069
1000°C-2	1.0069

4.1.5 Conclusions

Overall, the microstructural model has been successfully applied to the experimental data. The solutions obtained to the microstructural model fit the experimental data much better than those obtained to the traditional square root model. The trends in the value of the microstructural parameters obtained from the solutions with sintering temperature have been successfully explained in terms of the observations made of the sensor microstructures in chapter 3. The unexpected variations of the sensitivity parameter, A, with sintering temperature in the steady state case and of the sensitivity parameter and time constant, τ, with gas concentration in the transient case are most likely a result of the steady state solutions being invalid in the strictest sense as their predicted baselines are not equal to 1. However, these solutions are likely to be close to the true solutions as is evidenced by how closely the solutions to the microstructural model fit both the steady state and the transient data and the ability of the microstructural observations to accommodate for the changes in the parameters obtained from these solutions. The effects of the varying degree of accuracy of the pseudo steady state responses with sintering temperature and of the possible effects of differing titanium surface segregation with sintering temperature are likely to be other factors contributing to these unexpected results.

4.2 Response to Propane

4.2.1 Gas Exposure Transients

Figure 4.11 displays the response transients for the gas exposures to propane on the sensors derived from coarse chromia material. The responses at the end of the 600 second gas exposures to propane continued to rise slowly for all the preparation conditions and gas concentrations studied. In contrast to the CO results, the propane results showed no condition that reached a steady state in the observation time. The magnitude of the responses again shows a heavy dependence on sintering temperature, with reduced magnitudes for sensors sintered at higher temperatures.

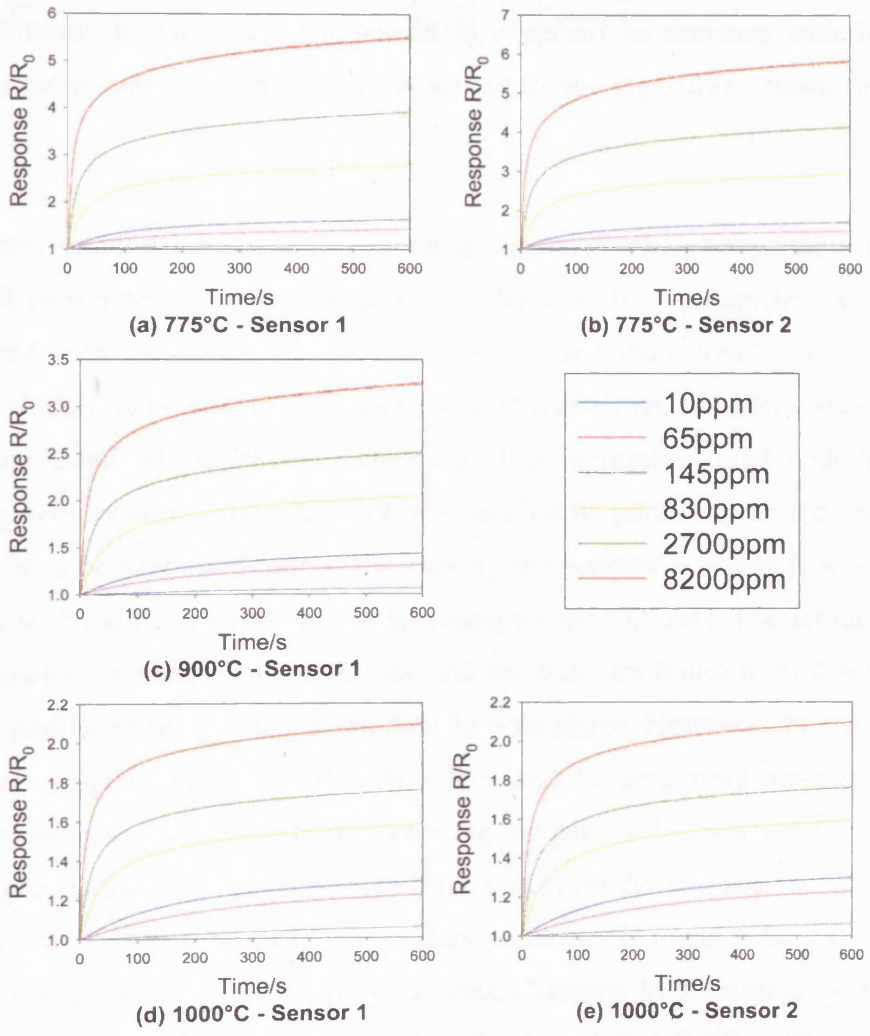

Figure 4.11 Response versus time plots for the gas exposures to different propane concentrations on sensors derived from coarse chromia material sintered at 775 (a+b), 900 (c) and 1000°C (d+e). The extent to which the steady state is approached did not seem to be affected by sintering temperature for these propane tests, in contrast to the results for the CO tests. The magnitude of the response decreased with increasing sintering temperature.

4.2.2 Solutions to the Model – Steady State Gas Response

As with the tests performed on these same sensors to CO above, the magnitude of the response of the sensors to propane is shown to decrease with increasing sintering temperature in Figure 4.12. The decrease in the degree of fit to the experimental data of the solution to the microstructural model observed with increasing sintering temperature for the CO tests above is not observed to the same extent in these results for propane. However, the effect may just be discerned. The solutions obtained to the traditional square root model for these propane tests display a better degree of fit to the experimental data than the CO tests for the same sensors. The degree of fit of these solutions to the traditional model is observed to decrease with increasing sintering temperature which was not observed to any significant extent for the CO tests.

The microstructural parameters are plotted versus sintering temperature in Figure 4.13. All parameters with the exception of the sensitivity parameter, A, display a clear trend with increasing sintering temperature and these trends are the same as was previously observed for the CO tests: $R_{PB,0}/R_{T,0}$ and $R_{B,0}/R_{T,0}$ show a clear decreasing trend whilst $R_{S,0}/R_{T,0}$ shows a clear increasing trend with increasing sintering temperature. The value of the sensitivity parameter found from these propane tests remains constant with sintering temperature whereas it was found to decrease with increasing sintering temperature for the CO tests. The actual values of the parameters representing the surface and the bulk are found from these propane tests are similar to those found from the CO tests above. However, the values of the parameters representing the particle boundary and the sensitivity parameter display some differences. The parameter representing the particle boundary is found to have much higher values (by approximately three times) for the propane tests than for the CO tests. The value of the particle boundary parameter is found to be less dependent on sintering temperature for the propane tests, changing by a factor of only three or four as opposed the factor of greater than fourteen found for the CO tests. As the value of sensitivity parameter for propane is constant with sintering temperature it displays variance from the values found for CO although the average value found for CO is similar to the average value found for propane.

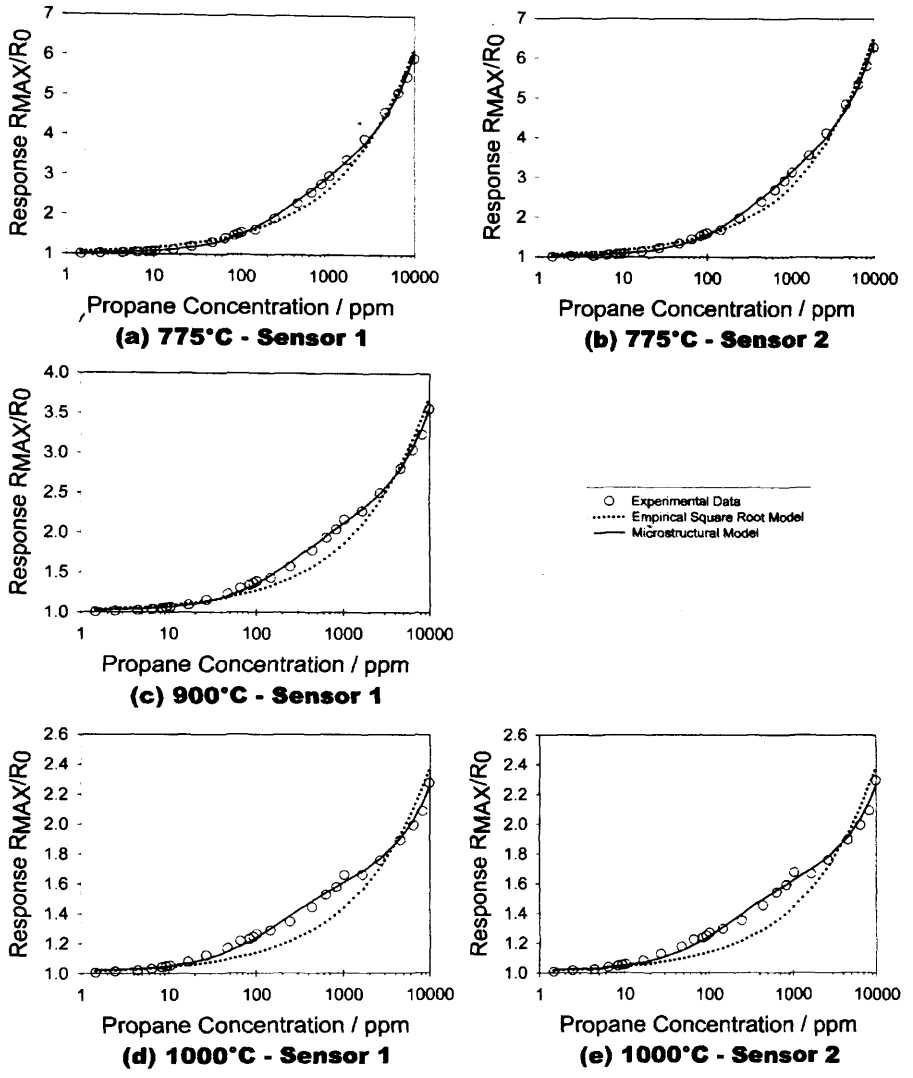

Figure 4.12 Plots of response versus propane concentration for sensors sintered at 775°C (a+b), 900°C (c) and 1000°C (d+e). As with the CO tests on these sensors above, the magnitude of the responses are observed to decrease with increasing sintering temperature. Solutions obtained for the microstructural model are shown to have a better fit to the experimental data than for the traditional model. The solutions for the traditional model for these propane tests fit the experimental data better than for CO presented earlier and the degree of fit is also much more dependent upon sintering temperature.

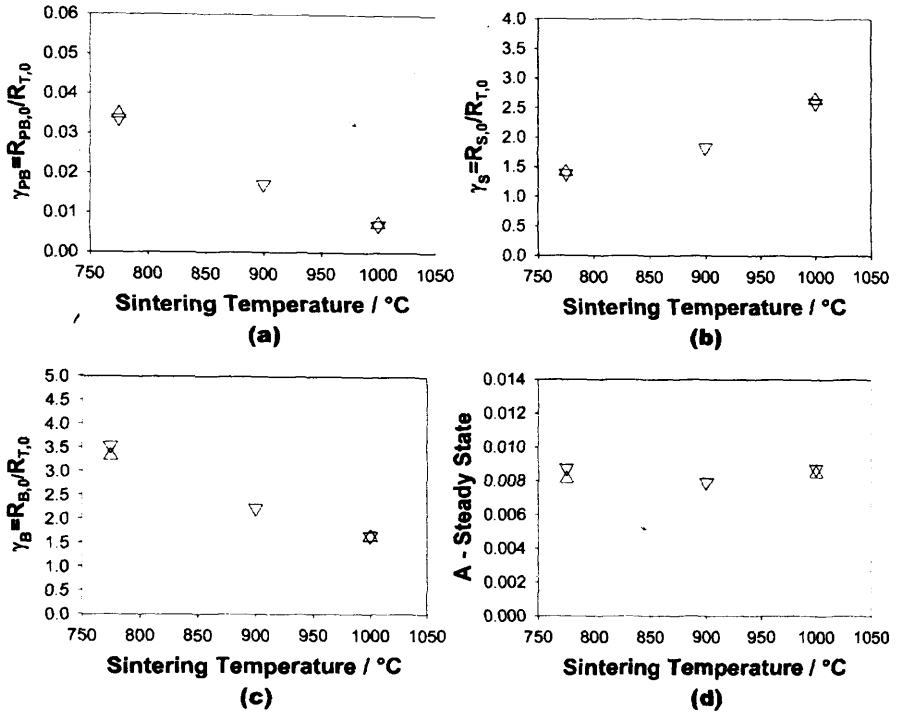

Figure 4.13 The microstructural parameters of the solutions of the experimental data to the microstructural model are plotted versus sintering temperature. The variations with sintering temperature may be explained by microstructural observations and reassessing assumptions.

4.2.3 Solutions to the Model – Transient Gas Response

The sensitivity parameter, A, and the time constant, τ, are plotted for the different sensors and gas concentrations in Figure 4.14 and Figure 4.15 respectively. Some of the values found for these parameters for some sensors, particularly at low concentrations, were vastly different from others for the same sensor and were allowed to go off the scale presented here to show the other values on a more sensible scale. The numbers shown at the base of the bars is the value for that particular bar, so that the information is preserved. Also noted for the values of the parameters A and τ in Figure 4.14 and Figure 4.15 is the fact that the values generally appear to display some dependence on gas concentration. This dependence seems to decrease with increasing concentration such that the values for the higher concentrations are more similar. This is even the case where the out of range data discussed above is excluded.

With the exception of the values for the lower concentrations that differ greatly from the other values for the reasons explained above, the values obtained for the

sensitivity parameter, A, for the different sintering temperatures are, on average, approximately the same. The values obtained for the time constant, τ, do appear to display an increasing trend with sintering temperature, although the values at the highest concentration are approximately the same.

Figure 4.16, Figure 4.17, Figure 4.18, Figure 4.19 and Figure 4.20 show, for the different sensors, the experimental response data for each concentration tested plotted versus time in a different chart, (a) to (f), as the black lines. Each of the coloured lines represents the solution obtained to the experimental response data for the sensor in question and the different concentrations. The solution obtained for a particular concentration fits the experimental data for that concentration best, whilst it does not fit the data for other concentrations as well. There is not so much variation in how well the solutions obtained for different concentrations fits the data between sensors tested to propane here as was observed for the same sensors tested to CO above. However, the solutions obtained for the low concentration tests on the sensors sintered at 775 and 900°C are particularly poor fits to the data for other concentrations. This is not so much the case for the solutions obtained to low concentrations for the sensors sintered at 1000°C.

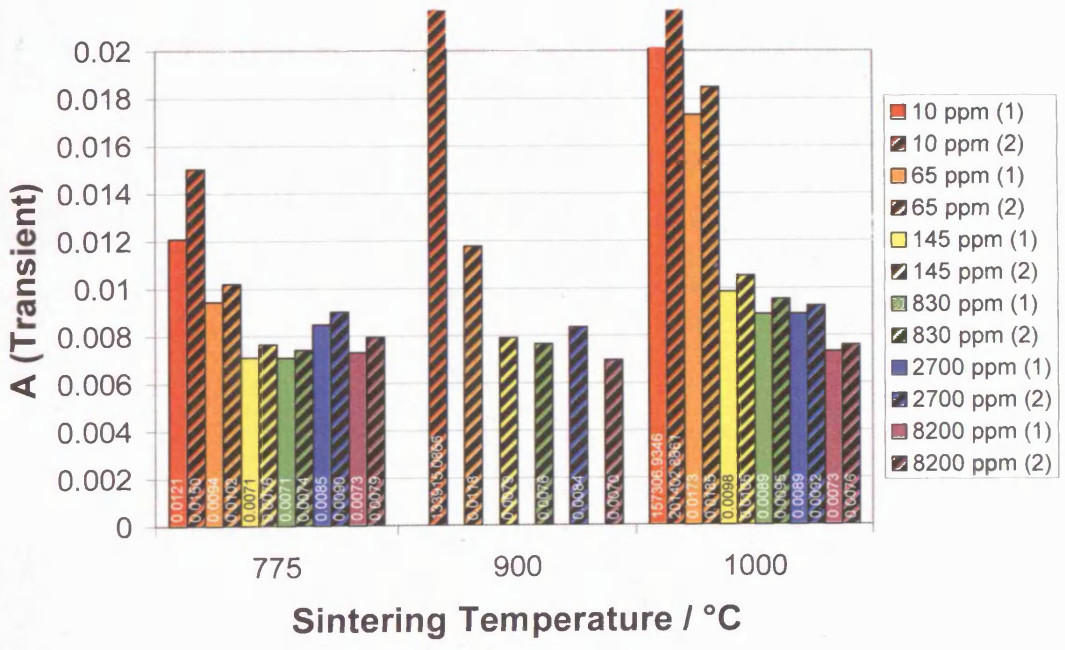

Figure 4.14 Bar chart showing the different values of A obtained from non-linear least squares regression of transient data from sensors sintered at different temperatures and tested to different concentrations of propane

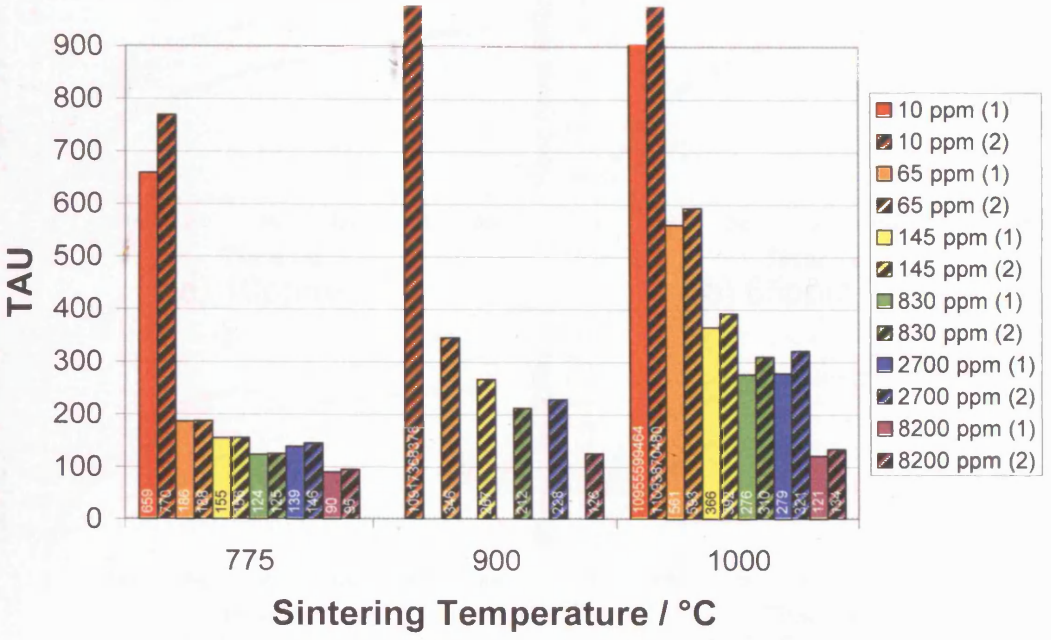

Figure 4.15 Bar chart showing the different values of τ obtained from non-linear least squares regression of transient data from sensors sintered at different temperatures and tested to different concentrations of propane

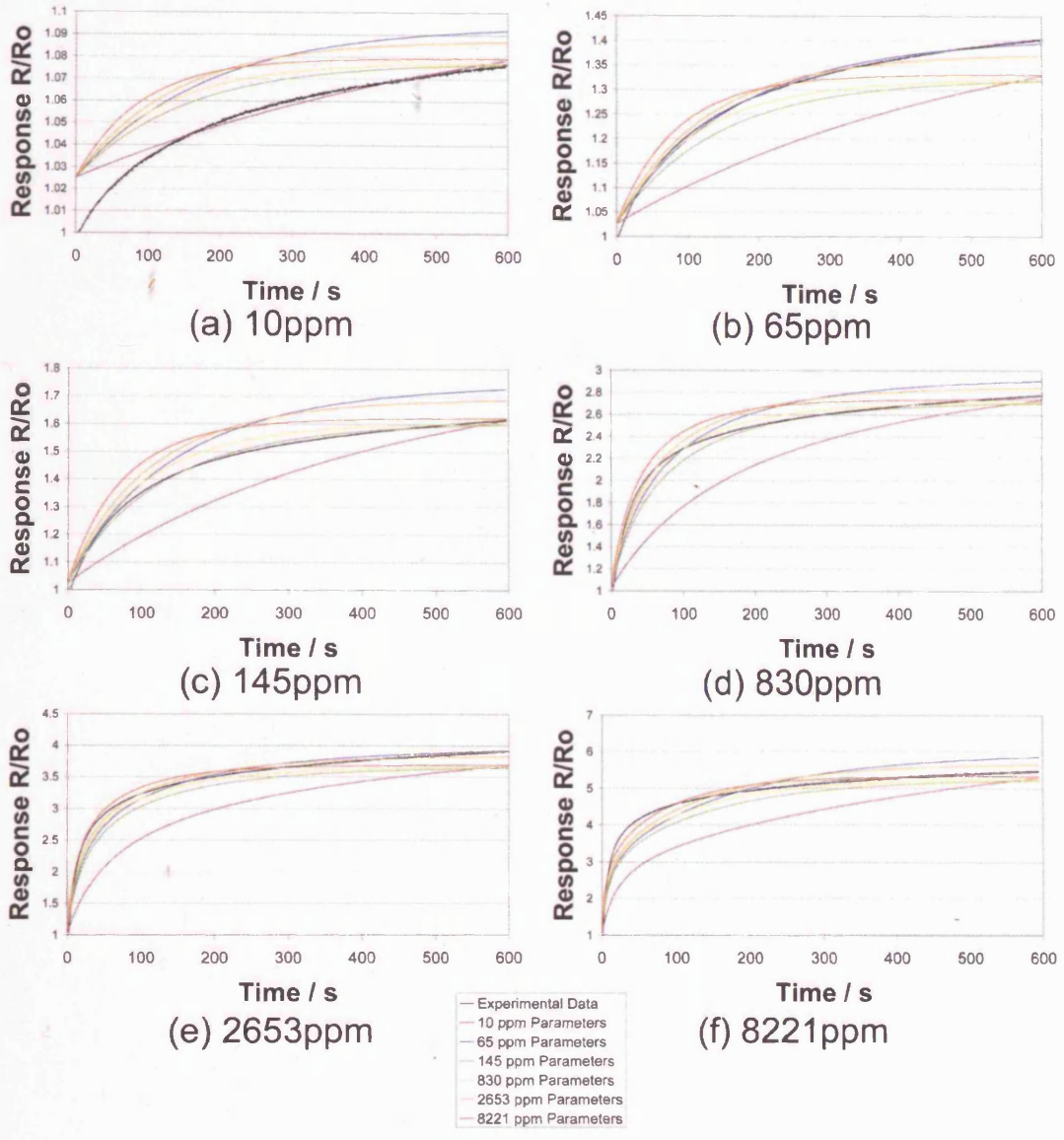

Figure 4.16 Coarse chromia sensor, sintered at 775°C, sensor number 1, tested to propane. Chart (a) to (f) show the experimental response transient for the particular concentration indicated as the black lines and the simulated transients of the regression solutions of all concentrations as the coloured lines. The observations made from these data are: (1) Response of solutions at t=0 is not equal to 1 as it should be (this is because the steady state solution is slightly inaccurate); (2) The solution obtained for a particular concentration fits the experimental transient for that concentration very well; (3) In this case, for an experimental transient for a particular concentration the solutions obtained for other concentrations do NOT fit particularly well; (4) the variation in fit between the solutions for different concentrations is generally less than was observed for the CO data

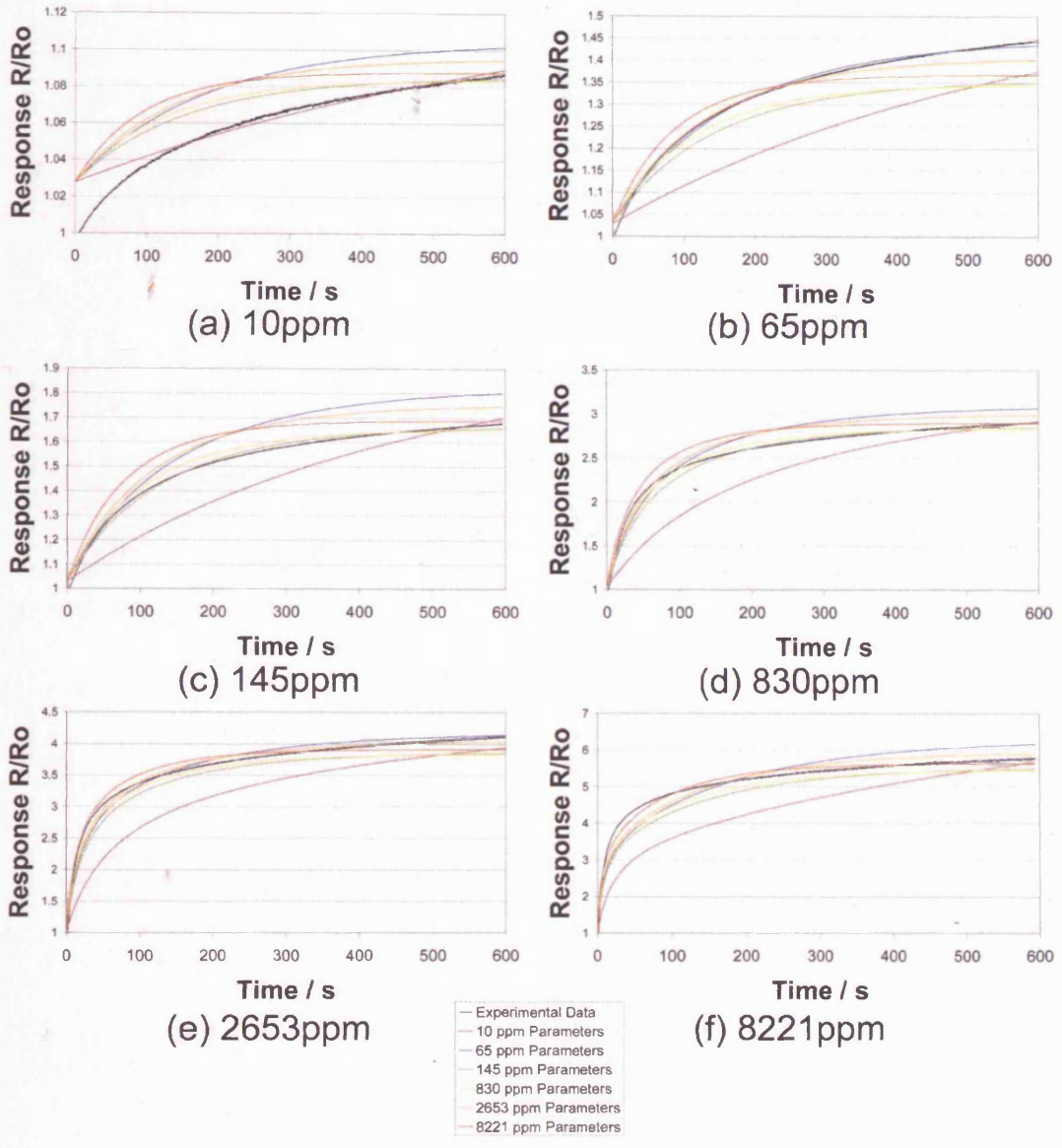

Figure 4.17 Coarse chromia sensor, sintered at 775°C, sensor number 2, tested to propane. Chart (a) to (f) show the experimental response transient for the particular concentration indicated as the black lines and the simulated transients of the regression solutions of all concentrations as the coloured lines. The observations made from these data are: (1) Response of solutions at t=0 is not equal to 1 as it should be (this is because the steady state solution is slightly inaccurate); (2) The solution obtained for a particular concentration fits the experimental transient for that concentration very well; (3) In this case, for an experimental transient for a particular concentration the solutions obtained for other concentrations do NOT fit particularly well; (4) the variation in fit between the solutions for different concentrations is generally less than was observed for the CO data

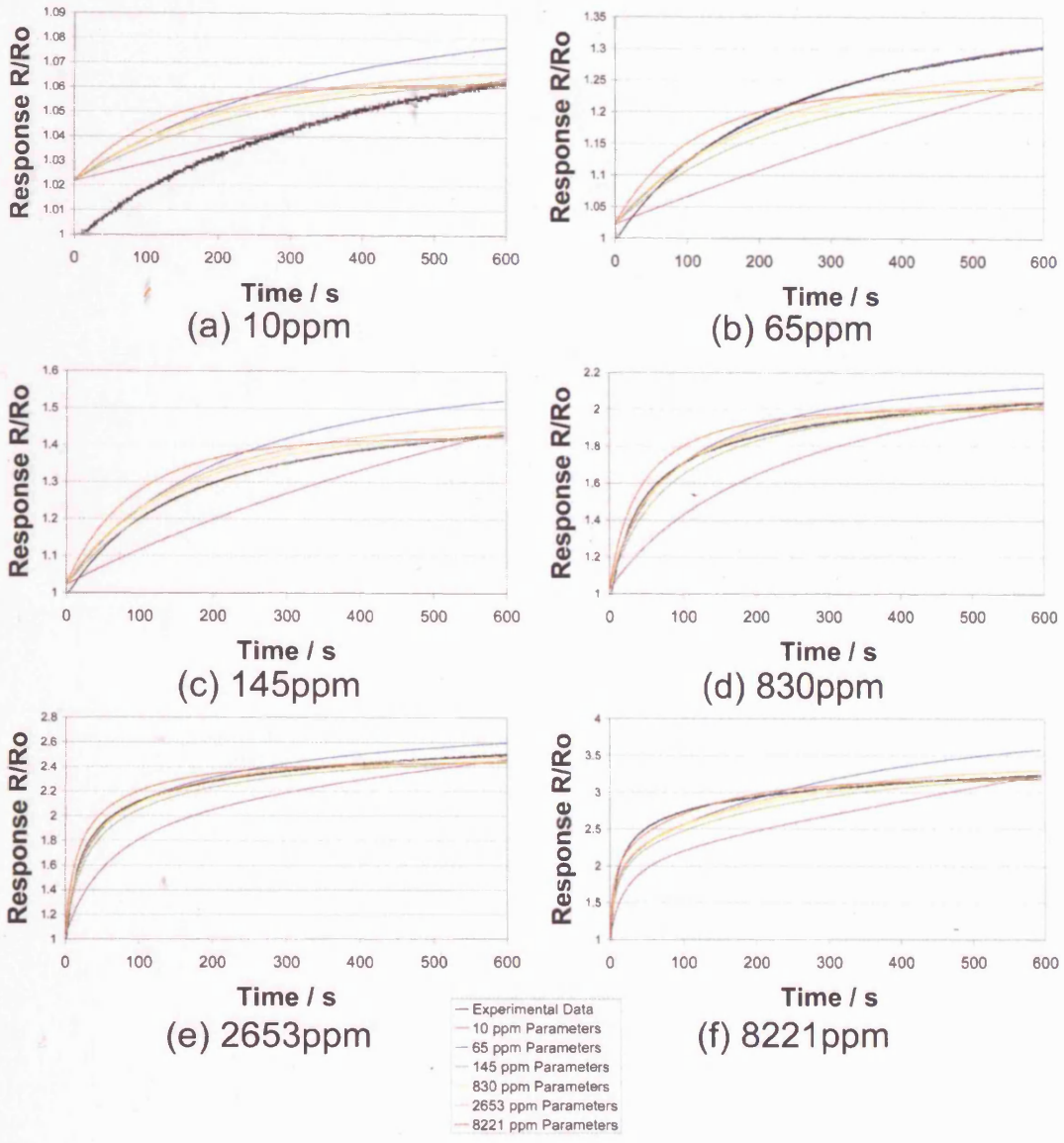

Figure 4.18 Coarse chromia sensor, sintered at 900°C, sensor number 1, tested to propane. Chart (a) to (f) show the experimental response transient for the particular concentration indicated as the black lines and the simulated transients of the regression solutions of all concentrations as the coloured lines. The observations made from these data are: (1) Response of solutions at t=0 is not equal to 1 as it should be (this is because the steady state solution is slightly inaccurate); (2) The solution obtained for a particular concentration fits the experimental transient for that concentration very well; (3) In this case, for an experimental transient for a particular concentration the solutions obtained for other concentrations do NOT fit particularly well; (4) the variation in fit between the solutions for different concentrations is generally less than was observed for the CO data

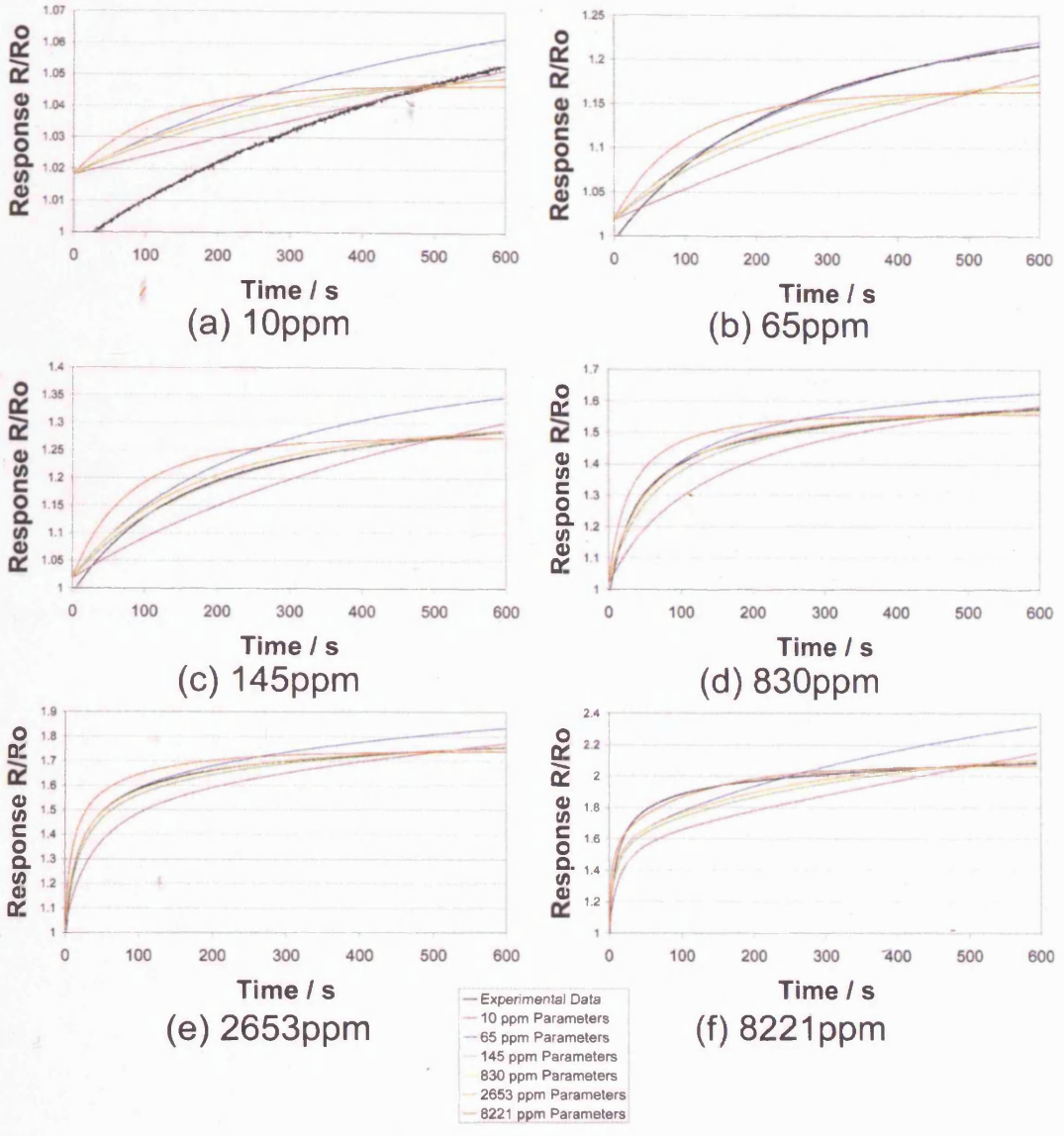

Figure 4.19 Coarse chromia sensor, sintered at 1000°C, sensor number 1, tested to propane. Chart (a) to (f) show the experimental response transient for the particular concentration indicated as the black lines and the simulated transients of the regression solutions of all concentrations as the coloured lines. The observations made from these data are: (1) Response of solutions at t=0 is not equal to 1 as it should be (this is because the steady state solution is slightly inaccurate); (2) The solution obtained for a particular concentration fits the experimental transient for that concentration very well; (3) In this case, for an experimental transient for a particular concentration the solutions obtained for other concentrations do NOT fit particularly well; (4) the variation in fit between the solutions for different concentrations is generally less than was observed for the CO data

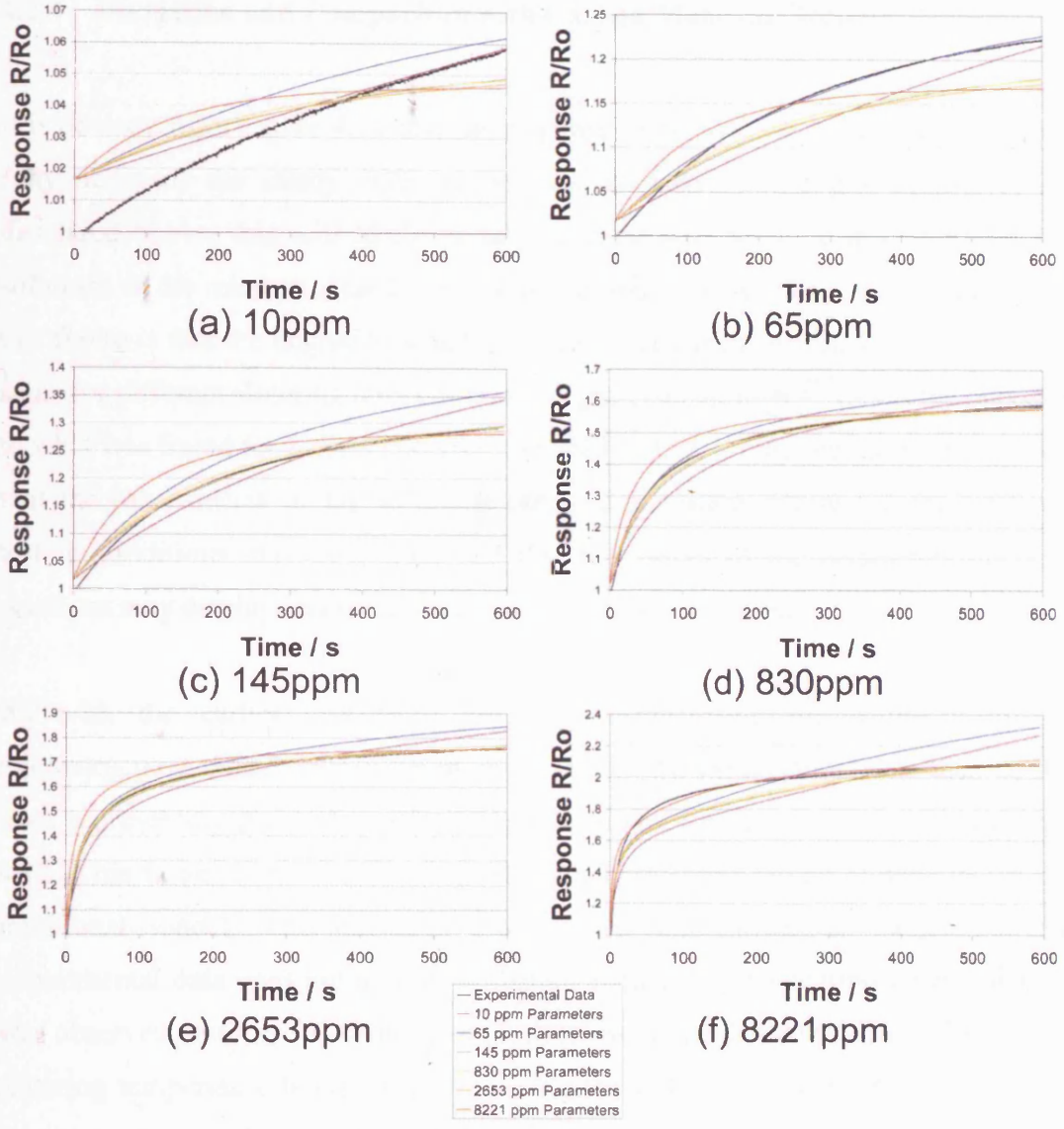

Figure 4.20 Coarse chromia sensor, sintered at 1000°C, sensor number 2, tested to propane. Chart (a) to (f) show the experimental response transient for the particular concentration indicated as the black lines and the simulated transients of the regression solutions of all concentrations as the coloured lines. The observations made from these data are: (1) Response of solutions at t=0 is not equal to 1 as it should be (this is because the steady state solution is slightly inaccurate); (2) The solution obtained for a particular concentration fits the experimental transient for that concentration very well; (3) In this case, for an experimental transient for a particular concentration the solutions obtained for other concentrations do NOT fit particularly well; (4) the variation in fit between the solutions for different concentrations is generally less than was observed for the CO data

4.2.4 Discussion and Comparison with Carbon Monoxide Results

It is obvious from Figure 4.11 that the response to propane on these sensors has not fully achieved the steady state in the time allowed for the gas exposures. As discussed above, this will likely mean that there will be some inaccuracy in the solutions to the microstructural model that are obtained. Another thing to note from this figure is that the degree to which the steady state is approached seems to be the same for different sintering temperatures and gas concentrations. This is the opposite to what was found for these same sensors tested to CO. It may therefore be expected that the inaccuracies of the solutions obtained for these different processing and testing conditions may be similar and that the values of the parameters of these solutions may display less or no variation with these conditions.

As with the earlier CO tests, the lines representing the solutions to the microstructural model pass much more closely to the experimental data than do the lines representing the traditional square root model for the propane tests in Figure 4.12. This is another indication that the microstructural model is superior to the traditional model. The degree to which the microstructural model fits the experimental data does not appear to change as much with sintering temperature as was observed with the CO tests. A slight decrease in the degree of fit with increasing sintering temperature is just perceptible. For the CO tests on these sensors where a large variation in the accuracy of the pseudo steady state has been noted, a large variation is observed in how well the solution obtained to the microstructural model fits the experimental data. Conversely, for the propane tests, a small variation in the degree of accuracy of the pseudo steady state response was noted and has resulted in little variation of how well the solution to the microstructural model fits the experimental data. It can therefore be concluded that there is a link between how accurate the pseudo steady state response is and how well the solution to the microstructural model fits the experimental data. Another aspect of these results is that the solution to the traditional square root model fits the data better for propane than for CO for sensors sintered at lower temperatures. At 1000°C the degree of fit of the traditional model is as poor as it was for the CO tests. Although the traditional

model solution is better at the lower sintering temperatures for the propane than it was for the CO, the solution to the microstructural model is still superior in all cases.

The trends for the microstructural parameters found from the propane testing in Figure 4.13 are the same as those that were observed for the CO testing in Figure 4.3. The reasons for these trends remain the same and this is an encouraging sign that the microstructural model provides repeatable and meaningful results. However, it is of prime importance to compare the actual values of the different parameters that are obtained from the solutions. Such a comparison may be made from the above figures but is more easily made below in Figure 4.21. This figure shows that whilst the parameters representing the bulk and surface are approximately the same for the two different gases tested, the value found for the parameter representing the particle boundaries is found to be much higher for the propane than for the CO. It also shows that for propane the value for the sensitivity parameter, A, is found to be constant but in the same range of values found for CO. The large difference between the values of particle boundary parameter for CO and propane is quite a surprising result as it was thought that the parameters representing the microstructure would be independent of the chemistry of response. One possible explanation for this effect could be that the response transients for the propane tests in Figure 4.11 were noted to be of a different shape and to generally be further away from the steady state response than the CO tests shown in Figure 4.1. This means the data used as the response in the generation of the solutions to the microstructural model were further away from the steady state for propane than they were for CO. This inaccuracy could have been transferred to the values of the parameters obtained from these solutions and specifically to the value of the parameter representing the particle boundaries.

The sensitivity parameter, A, and the time constant, τ, are plotted for the different sensors and gas concentrations in Figure 4.14 and Figure 4.15 respectively. Some of the values found for these parameters for some sensors, particularly at low concentrations, were vastly different from others for the same sensor and were allowed to go off the scale presented here to show the other values on a more sensible scale. The reason these out of scale values exist can be observed in the plots of the experimental transient response data with the plots of the response transients representing the solutions to the transient data presented in Figure 4.16, Figure 4.17,

Figure 4.18, Figure 4.19 and Figure 4.20 for different concentrations in the charts, (a) to (f), that compose these figures. The plots for the low concentrations in the charts, (a), in the figures show that the steady state solutions are, again, not strictly valid since the responses at the start of the gas exposures are not equal to 1, as they should be, and are slightly higher. The regression process attempts to fit a line from this invalid intercept across the data. The best fit solution obtained can be seen to be somewhat 'stretched' and rather linear for the data for the lower concentrations where the maximum response attained in these cases is not much higher than the incorrect baseline predicted from the steady state solutions. The values of the parameters representing the sensitivity parameter, A, and the time constant, τ, are therefore 'stretched' to accommodate these inaccuracies as far as possible resulting in the wildly out of range values observed at lower concentrations.

Also noted for the values of the parameters A and τ in Figure 4.14 and Figure 4.15 is the fact that the values generally appear to display some dependence on gas concentration. This dependence seems to decrease with increasing concentration such that the values for the higher concentrations are more similar. This is even the case where the out of range data discussed above is excluded. One of the most important factors leading to this behaviour is probably the discrepancy between the baseline obtained for the steady state solution and the true baseline obtained for the data, as discussed above. As the gas concentration is increased the magnitude of the response increases such that the response becomes increasingly larger than the offset baseline from the steady state solution. This has a big effect on how well the solutions obtained fit the experimental transient data as the error in the baseline has much less effect at higher concentrations when the response is larger.

With the exception of the values for the lower concentrations that differ greatly from the other values for the reasons explained above, the values obtained for the sensitivity parameter, A, for the different sintering temperatures are, on average, approximately the same. The values obtained for the time constant, τ, do appear to display an increasing trend with sintering temperature, although the values at the highest concentration are approximately the same. This may also be a result of the discrepancy between the baseline predicted from the steady state solution to the model and the true experimental baseline. As the sintering temperature is increased

the magnitude of response is decreased across the range of concentrations tested. As with the dependence of the values of the parameters obtained from the transient data with gas concentration, the lower responses for high sintering temperatures will be closer to the offset baseline and therefore more affected by it. The higher responses for the sensors sintered at lower temperatures will not be so affected. These differences are accounted for in the values of the parameters obtained from the solutions and they therefore display variations with these experimental parameters.

In comparison with the results obtained for these same sensors to CO, the values for both sensitivity parameter, A, and the time constant, τ, are remarkably similar. The average value for A found from the transient data is slightly lower for the CO than for the propane. This was also observed for the value found from the steady state data. This is likely to be part of the difference in the response to the two different gases. Another difference between the parameters found for the two gases is that the value of the time constant, τ, for the propane increases with increasing sintering temperature whilst it remains constant with sintering temperature for CO. In addition to the explanation for this observation based on the effects of the baseline predicted from the steady state solution presented above, this observation may also be explained by possible differences in titanium surface segregation induced by increasing sintering temperature. Such changes could lead to changes in the magnitude and speed of response that could be different for different gases.

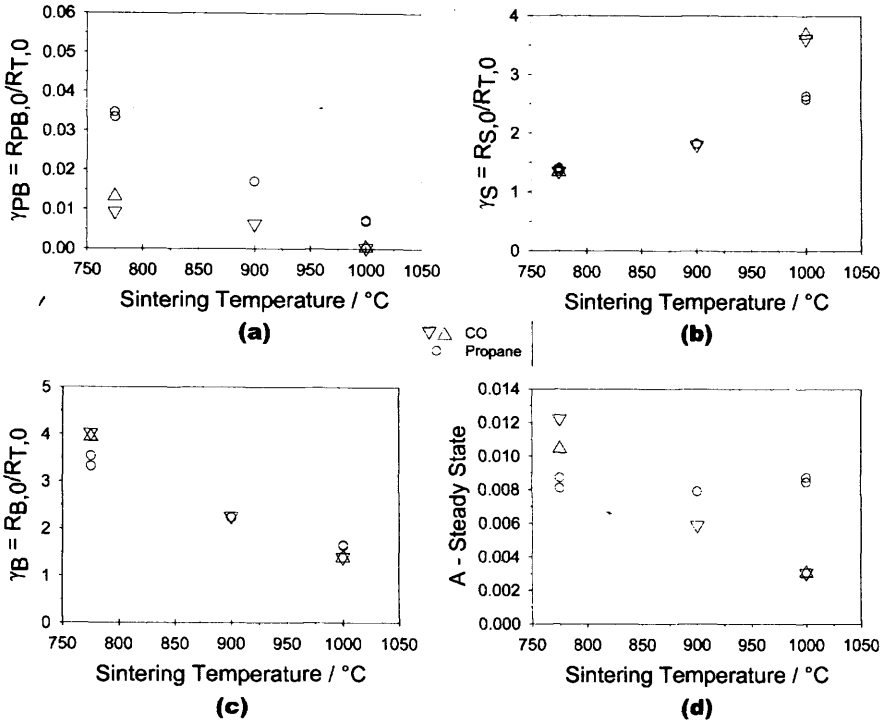

Figure 4.21 Comparison of parameters obtained from CO and propane tests on sensors constructed from coarse grained material. The parameters representing the surface and the bulk are similar for the two gases as expected. The parameter representing the particle boundaries is somewhat higher for propane than for CO which was unexpected as it was thought changes to chemistry would be accounted for in the sensitivity parameter. This could be due to differences in the accuracy of the pseudo steady state responses as discussed in the text. The sensitivity parameter, A, is constant for propane and varies for CO with sintering temperature. These effects could also be due to changes in the accuracy of the pseudo steady state responses.

4.2.5 Conclusions

As for results of the CO tests on these sensors presented above, the propane tests have also shown the microstructural model can be successfully applied to the experimental response data. The solutions obtained fit the experimental data better than the solutions obtained to the traditional square root model. The trends in the parameters of the solutions with sintering temperature have been explained with reference to the changes in microstructure observed in section 3.2.1. The differences between the values of sensitivity parameter, A, obtained from the steady state data and the sensitivity parameter and the time constant, τ, obtained from the transient data for the different gases may be explained by the different nature of the chemical reactions that occur on the surface when different gases are tested. The difference between the values of the particle boundary parameters obtained for the CO and

propane tests could be explained by the fact the differences in the degree to which the steady state has been approached in the tests to the different gases. This difference could, it is thought, lead to slight inaccuracies in the validity of the steady state solutions which could, in turn, be translated to the particle boundary parameter. The fact that the steady state solutions predict an incorrect baseline is deemed to have a significant impact on the transient solutions, and the values of the parameters so obtained, particularly at the lower concentrations where the maximum response is not much greater than the offset baseline intercept.

5 Gas Tests on Sensors Derived From Fine Chromia

As mentioned at the head of the previous chapter, two batches of sensors were obtained from City Technology Ltd. These two batches were chosen because of the substantial differences in the particle sizes of the chromia raw materials from which they were made[67]. It was thought that the difference in initial particle size may produce great differences in the microstructures of finished sensors. This has indeed been demonstrated by the study of the sensor microstructures presented here in chapter 3. This chapter proceeds in an identical format to the previous one to allow a direct comparison of the sensors derived from the materials of differing initial particle size. A primary aim of performing these tests was to illustrate whether solutions to the microstructural model could be obtained in a similar manner to those obtained for the sensors derived from the other starting chromia material. Of prime importance was the investigation of whether there were any significant differences between the solutions obtained to the microstructural model for the sensors made from the two different materials, as may be expected from the differences in microstructure observed in chapter 3.

5.1 Response to Carbon Monoxide

5.1.1 Gas Exposure Transients

The transients for the CO tests performed on sensors derived from fine chromia material are displayed in Figure 5.1. The trends that are observed for the integrity of the approximations to the steady state case and for the magnitudes of the responses are identical to those observed for the CO tests performed on the sensors derived from coarse chromia material. That is to say, the approximations to the steady state case tend to be poorer as sintering temperature is increased and/or gas concentration is reduced whilst the magnitudes of the responses decrease with increasing sintering temperature. These CO responses appear to have approached the steady state to a lesser degree than the CO responses on sensors derived from coarse chromia material. The amount of difference between the degree to which the steady state is

approached with changing sintering temperature is less for these tests on sensors derived from fine chromia material than it was for the sensors derived from coarse chromia material. Comparisons between the magnitudes of the responses to CO for the different sensors will be left for the following chapter, where the transient data are fitted to the behaviour expected from the microstructural model.

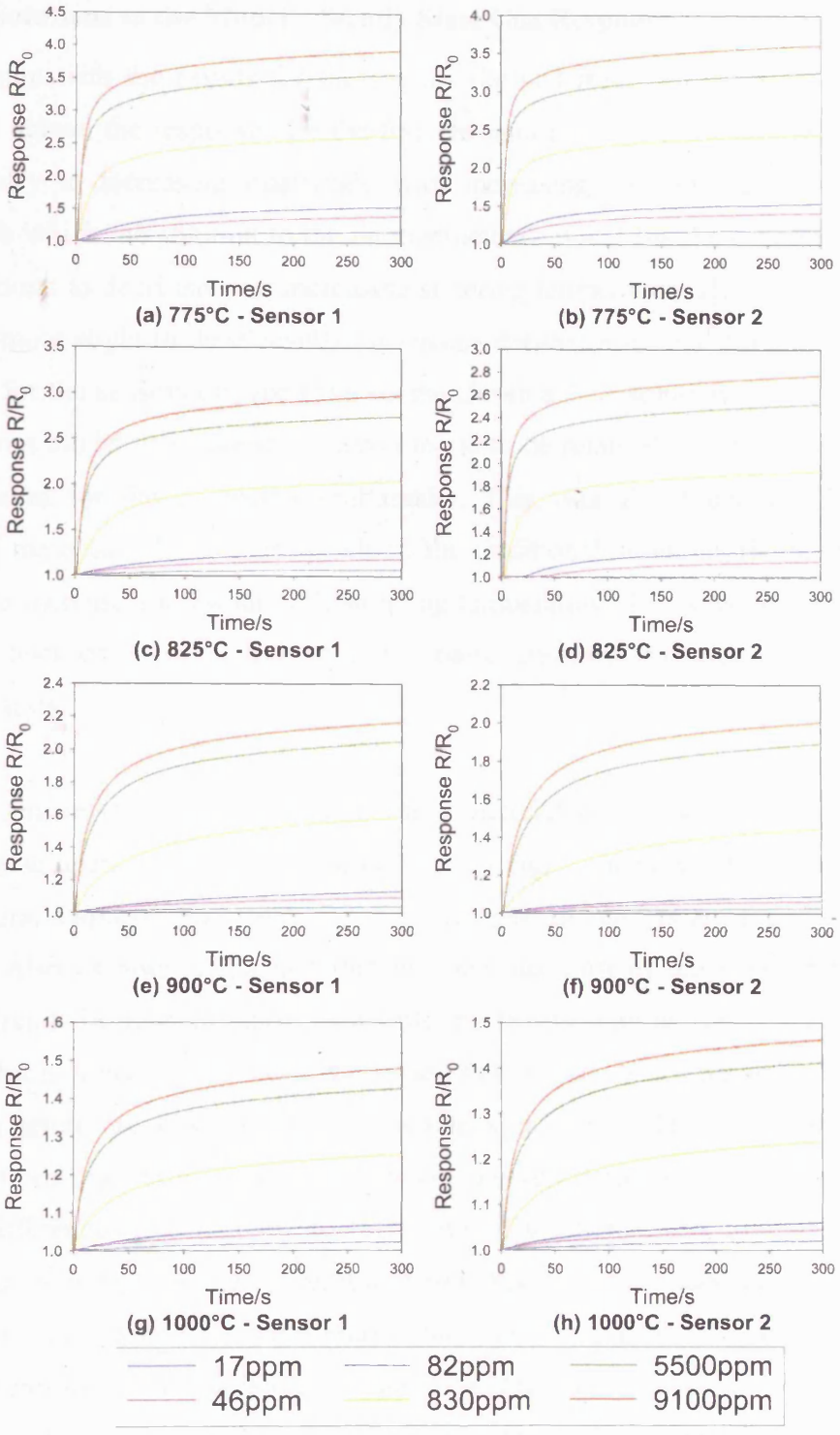

Figure 5.1 Response versus time plots for the gas exposures to different CO concentrations on sensors derived from fine chromia material sintered at 775 (a+b), 825 (c+d), 900 (e+f) and 1000°C (g+h). In common with the previous observations for the CO tests with coarse chromia derived material, the steady state is approached more closely for sensors sintered at lower temperatures tested to higher concentrations of CO. The magnitude of responses is greatest for sensors sintered at the lowest temperatures.

5.1.2 Solutions to the Model – Steady State Gas Response

In common with the results for the sensors derived from coarse chromia material reported above, the responses for the fine chromia material to CO shown in Figure 5.2 display a decreasing magnitude with increasing sintering temperature. The degree to which the solution to the microstructural model fits the experimental data is also found to decrease with increasing sintering temperature. However, this effect appears more slight in these results for sensors derived from fine chromia compared to those for the sensors derived from coarse chromia. The solutions to the traditional square root model of response are again found to be relatively poor compared to the those found for the microstructural model. This was also found for the coarse chromia material. The degree to which the traditional solutions fit the data does appear to increase somewhat with sintering temperature. This was not observed for the CO tests on sensors derived from coarse chromia, but was found for their propane tests.

For the sensors derived from fine chromia material two sensors produced at each sintering temperature were available for testing. Generally, the values of the parameters, displayed in Figure 5.3, for each pair of sensors are found to be very similar. Also of note is the fact that not only do most of the parameters display similar trends in their variation with sintering temperature as was observed for the coarse chromia material tested to the same gas but their values are also very similar. All parameters are observed to vary within similar boundaries for these sensors derived from fine chromia as for the sensors derived from coarse chromia. The only major differences apparent in the behaviour of the parameters found for the two materials are in the parameters representing the particle boundary and the bulk. The values of the parameter representing the bulk found for the lower sintering temperatures of 775 and 900°C are found at slightly lower values for sensors derived from fine chromia than for coarse chromia material. The values for the parameter representing the particle boundary appears to be approximately constant for the sintering temperatures of 775, 825 and 900°C before decreasing at 1000°C. The values of this parameter are also slightly lower for sensors derived from fine chromia than for coarse chromia material at low sintering temperatures whilst being much higher for sensors derived from fine chromia at the higher sintering temperaturtes.

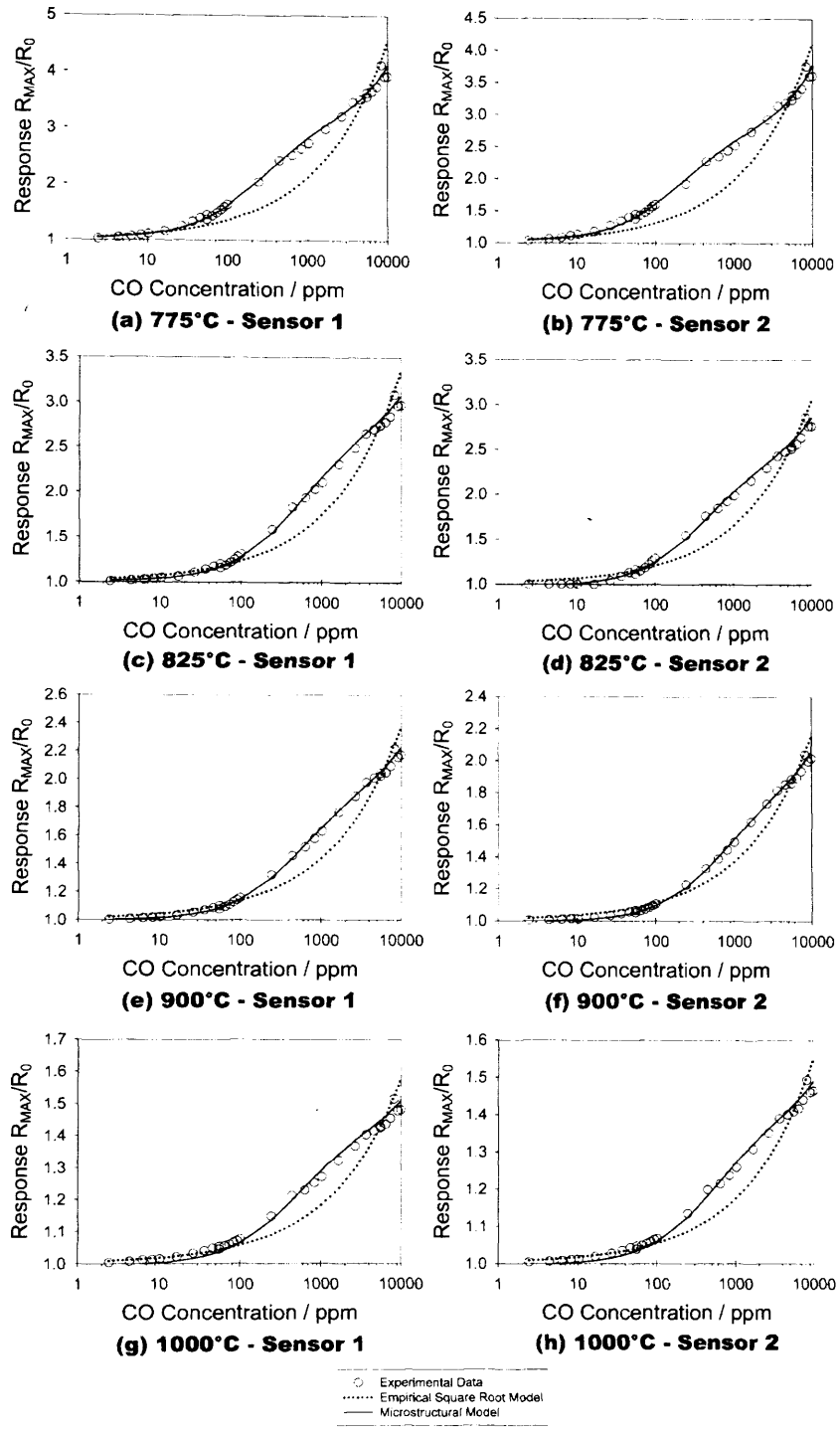

Figure 5.2 Plots of response versus carbon monoxide concentration for sensors sintered at 775°C (a+b), 825°C (c+d), 900°C (e+f) and 1000°C (d+e). Magnitude of response is observed to decrease with increasing sintering temperature as with the tests performed on sensors derived from coarse chromia. Solutions obtained for the microstructural model are shown to have much better fit to the experimental data than those obtained for the traditional model. There appears to be a slight decrease in the degree to which the solutions to the microstructural model fit the data for these CO tests but this effect is perceived to be less for this material than for the sensors derived from coarse chromia. Conversely, the degree to which the solutions to the traditional model are observed to fit the experimental data increases with increasing sintering temperature.

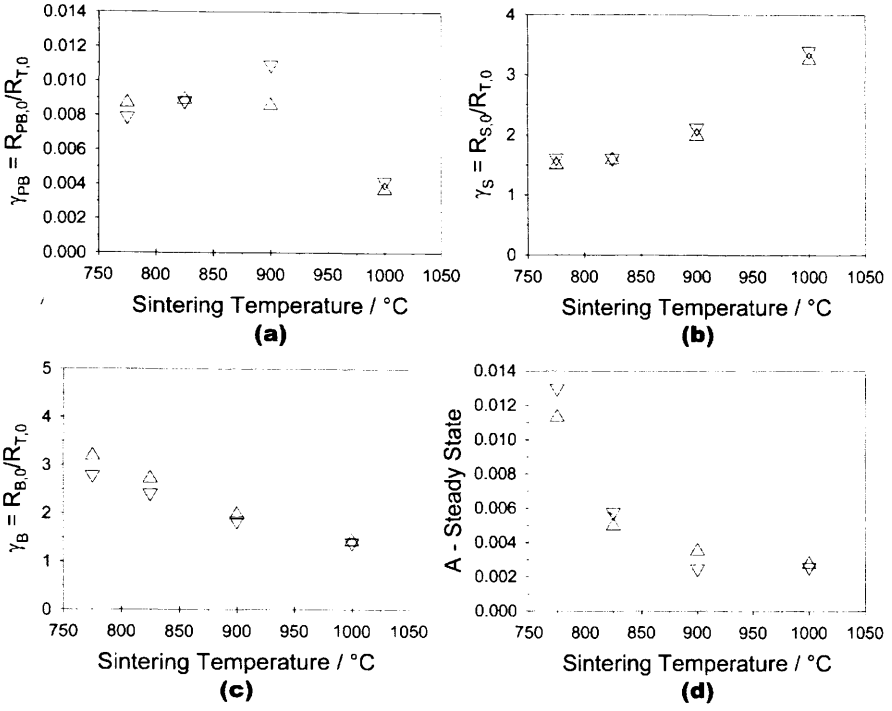

Figure 5.3 The microstructural parameters of the solutions of the experimental data to the microstructural model are plotted versus sintering temperature. The variations with sintering temperature may be explained by microstructural observations and reassessing assumptions.

5.1.3 Solutions to the Model – Transient Gas Response

The sensitivity parameter, A, and the time constant, τ, of the solutions obtained to the microstructural model from the regressions of the transient data are plotted in Figure 5.4 and Figure 5.5 respectively for the different sensors and gas concentrations of CO. The value for the sensitivity parameter, A, displays a clear decreasing trend with increasing sintering temperature in common with the trend observed for the value of the same parameter obtained from the steady state data. Furthermore, the values of the sensitivity parameter obtained from the steady state data and the transient data are nearly identical at each sintering temperature. The agreement between the values of the sensitivity parameter obtained for the different sensors is very good. The only result that shows significant variation between sensors is observed for the two sensors sintered at 825°C and tested to the lowest concentration, where the second sensor displays a much lower value of the sensitivity parameter than the other similar sensor. The sensitivity parameter also

displays a slight decreasing trend with increasing concentration, although this effect is relatively small.

The values of the time constant, τ, display a lot more variation between the sensors sintered at the same temperature. There doesn't appear to be any clear trends in the values with either sintering temperature or gas concentration. The average values in both cases are approximately equal across the ranges of values tested. As with the values of the sensitivity parameter discussed above, there is a significant difference between the values of the time constant obtained for the sensors sintered at 825 °C and tested to the lowest concentration of CO. This difference is such that the value for the first sensor appears to be fairly reasonable, around where it might be expected, but the value for the second sensor is negative. Such negative values don't really make sense in the context of the model governing sensor response and it is of interest to determine what happened during the regression procedure to result in this value. This will be discussed below.

The response transients of the experimental data are shown, as the black lines, together with the transients representing the solutions obtained for all different concentrations, as the coloured lines, for the sensors sintered at different temperatures in Figure 5.6, Figure 5.7, Figure 5.8, Figure 5.9, Figure 5.10, Figure 5.11, Figure 5.12 and Figure 5.13. As with the data obtained for the sensors derived from coarse chromia material, the solution obtained for a particular gas concentration fits the experimental transient response data obtained for that particular concentration best, but does not fit the transient obtained for other concentrations quite so well. This effect generally lessens at increased concentration such that, at the highest concentration tested here, 9097 ppm, the transients representing the solutions to all different concentrations are all fairly good fits to the experimental data. The amount of variation in this degree of fit with gas concentration is also different for the different sensors. For both sensors sintered at 775°C, shown in Figure 5.6 and Figure 5.7, the first sensor sintered at 825°C, shown in Figure 5.8, and the first sensor sintered at 900°C, shown in Figure 5.10, the solutions obtained at all concentrations fit all the experimental data at all concentrations particularly well. For all other sensors the solutions obtained at different gas concentrations than that at which the experimental data was generated fit the experimental data very poorly,

particularly at the lower gas concentrations. Also of note in these results is the fact that the baseline predicted from the steady state solutions, as represented by the point at which the lines representing the solutions to the transient data meet at the y-axis at the start of the gas exposure, is offset from where it ought to be, at a value of 1, in every case, in common with the results obtained on the sensors made from coarse chromia material. However, in contrast to these earlier results, the offset baselines observed for these tests are in some cases greater than 1 and in other cases less than 1.

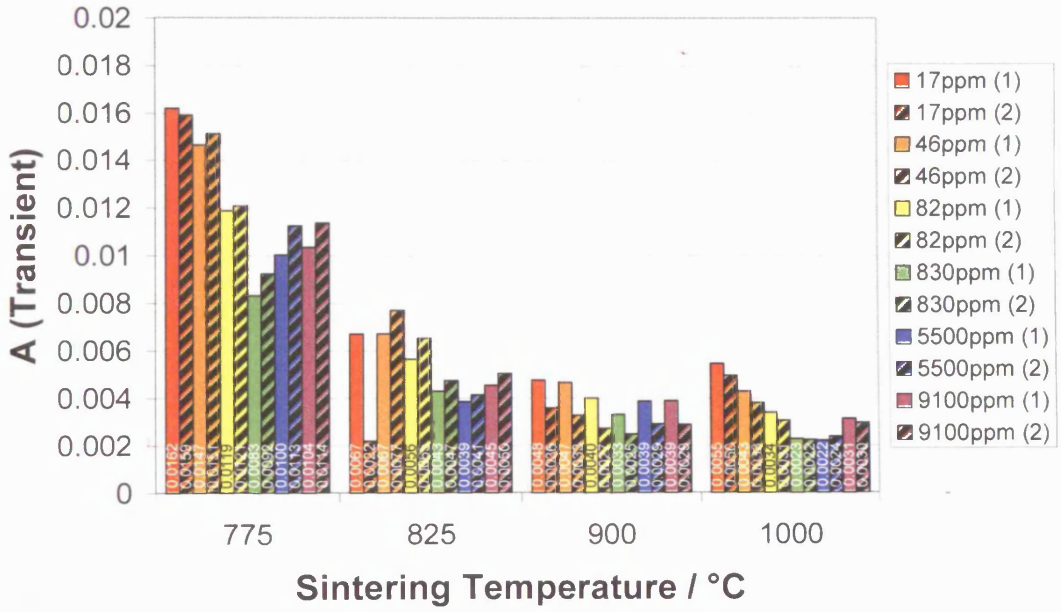

Figure 5.4 Bar chart showing the different values of A obtained from non-linear least squares regression of transient data from sensors sintered at different temperatures and tested to different concentrations of CO

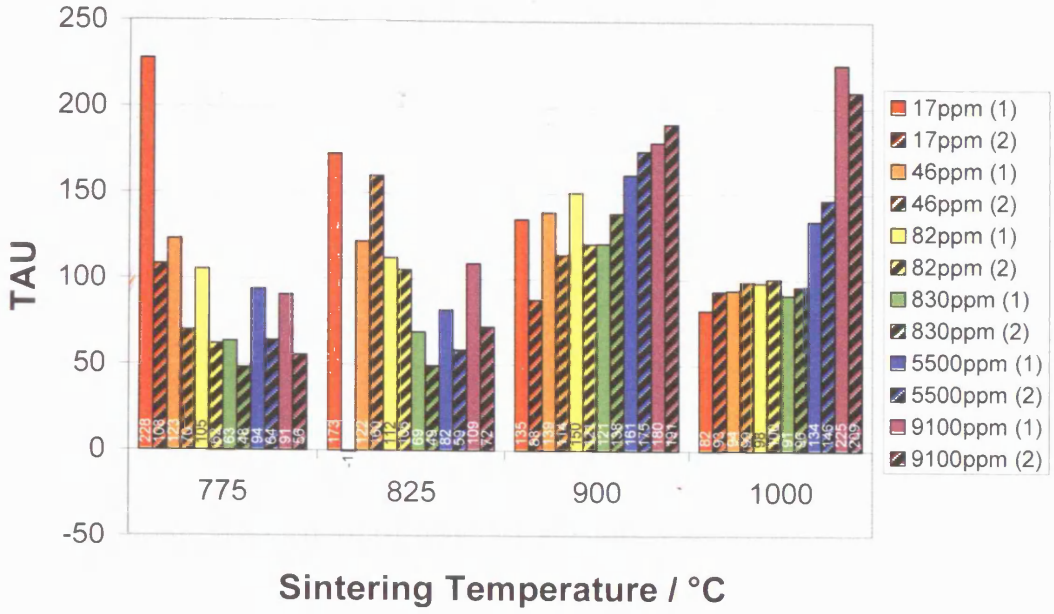

Figure 5.5 Bar chart showing the different values of τ obtained from non-linear least squares regression of transient data from sensors sintered at different temperatures and tested to different concentrations of CO

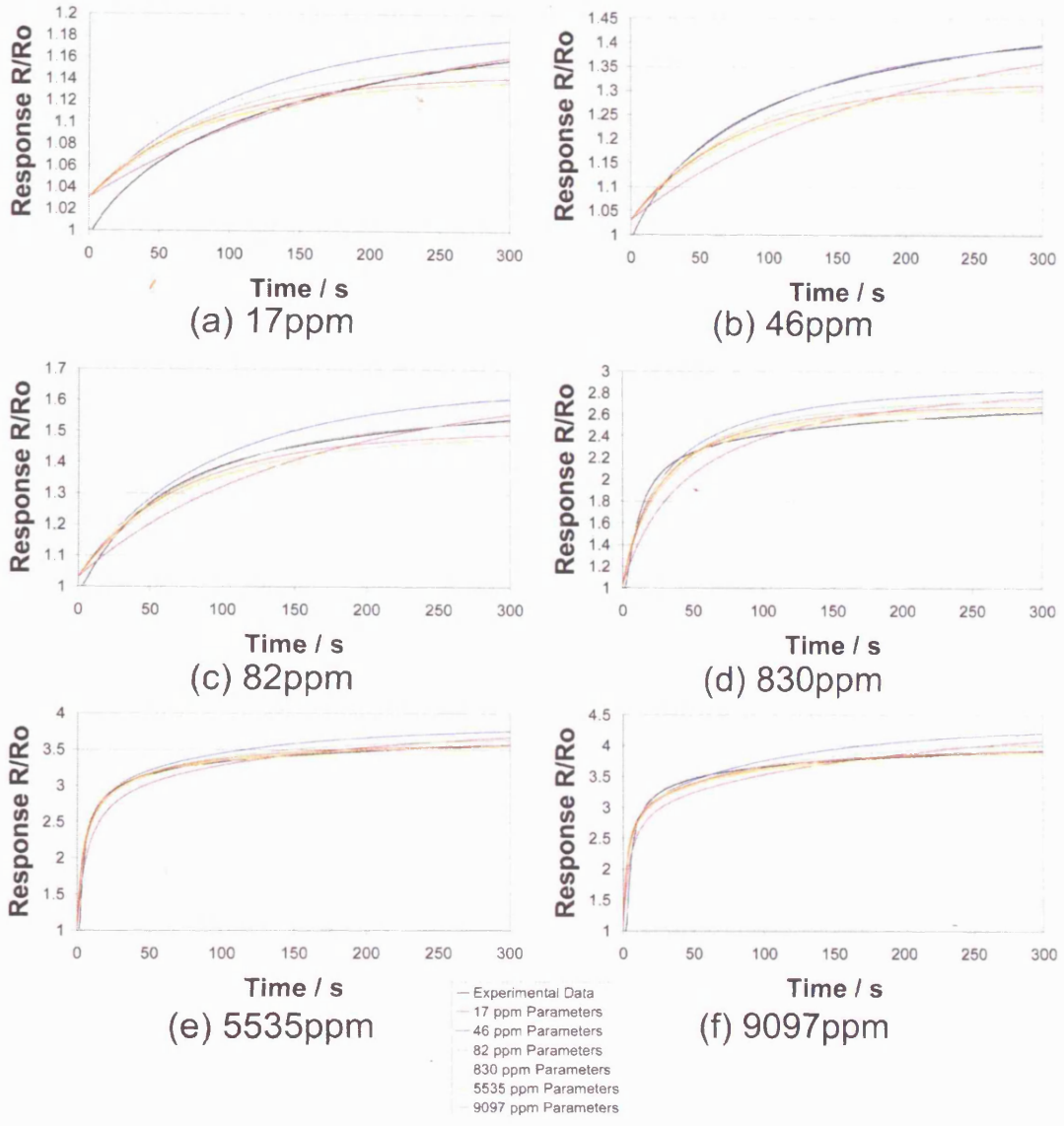

Figure 5.6 Fine chromia sensor, sintered at 775°C, sensor number 1, tested to CO. Chart (a) to (f) show the experimental response transient for the particular concentration indicated as the black lines and the simulated transients of the regression solutions of all concentrations as the coloured lines. The observations made from these data are: (1) Response of solutions at t=0 is not equal to 1 as it should be (this is because the steady state solution is slightly inaccurate); (2) The solution obtained for a particular concentration fits the experimental transient for that concentration very well; (3) In this case, for an experimental transient for a particular concentration the solutions obtained for other concentrations DO fit well, particularly at high concentrations

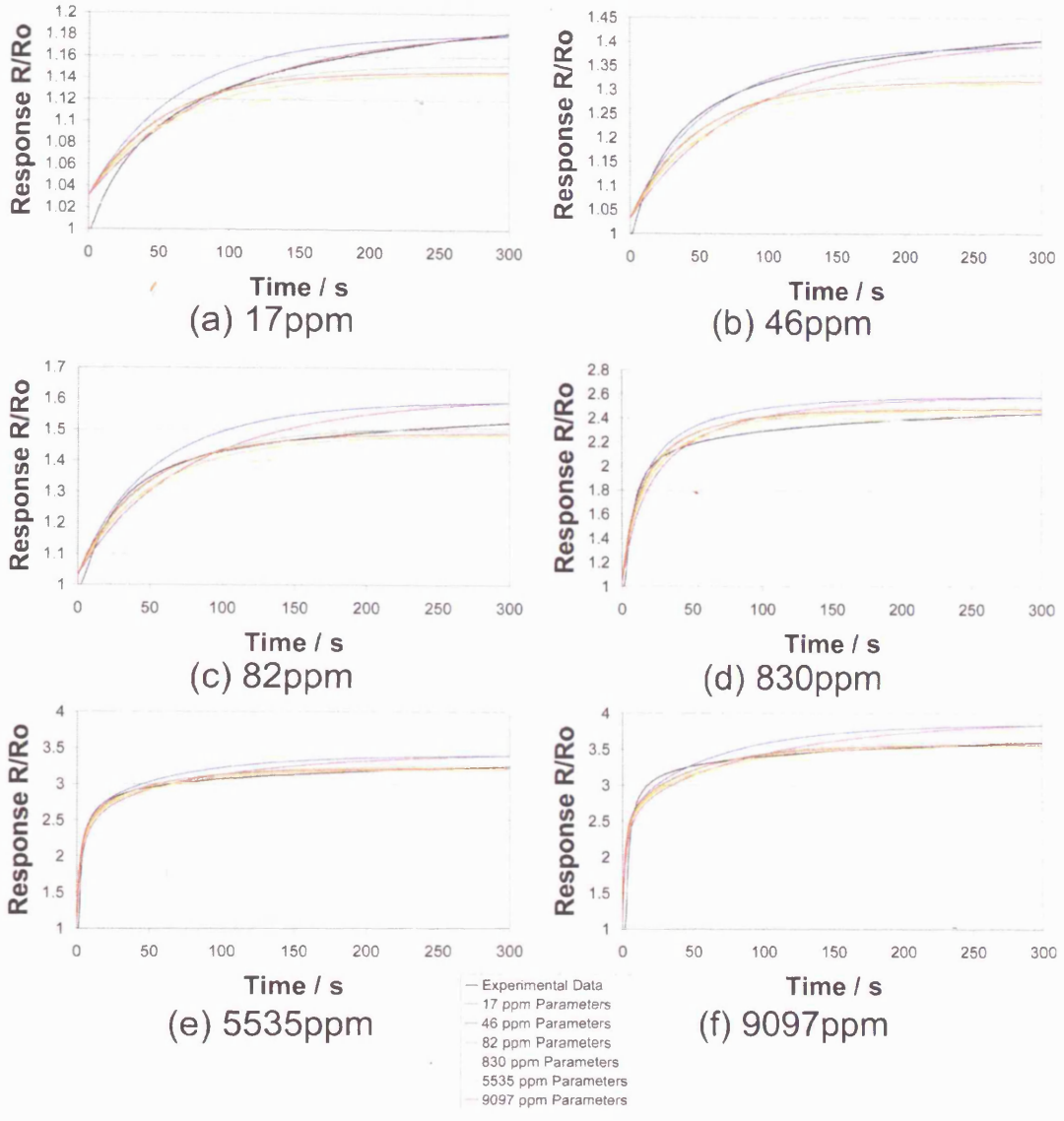

Figure 5.7 Fine chromia sensor, sintered at 775°C, sensor number 2, tested to CO. Chart (a) to (f) show the experimental response transient for the particular concentration indicated as the black lines and the simulated transients of the regression solutions of all concentrations as the coloured lines. The observations made from these data are: (1) Response of solutions at t=0 is not equal to 1 as it should be (this is because the steady state solution is slightly inaccurate); (2) The solution obtained for a particular concentration fits the experimental transient for that concentration very well; (3) In this case, for an experimental transient for a particular concentration the solutions obtained for other concentrations DO fit well, particularly at high concentrations

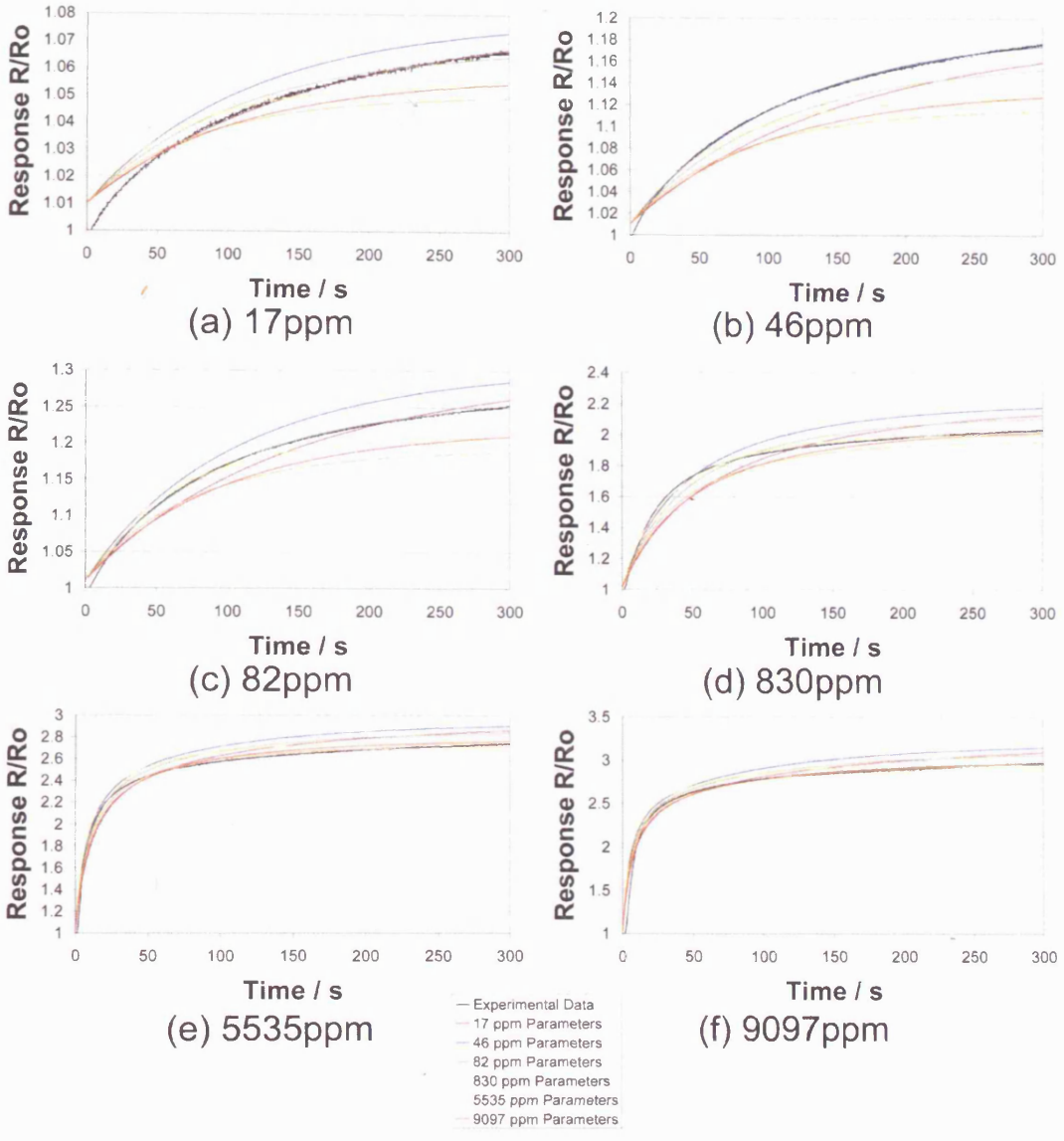

Figure 5.8 Fine chromia sensor, sintered at 825°C, sensor number 1, tested to CO. Chart (a) to (f) show the experimental response transient for the particular concentration indicated as the black lines and the simulated transients of the regression solutions of all concentrations as the coloured lines. The observations made from these data are: (1) Response of solutions at t=0 is not equal to 1 as it should be (this is because the steady state solution is slightly inaccurate); (2) The solution obtained for a particular concentration fits the experimental transient for that concentration very well; (3) In this case, for an experimental transient for a particular concentration the solutions obtained for other concentrations DO fit well, particularly at high concentrations

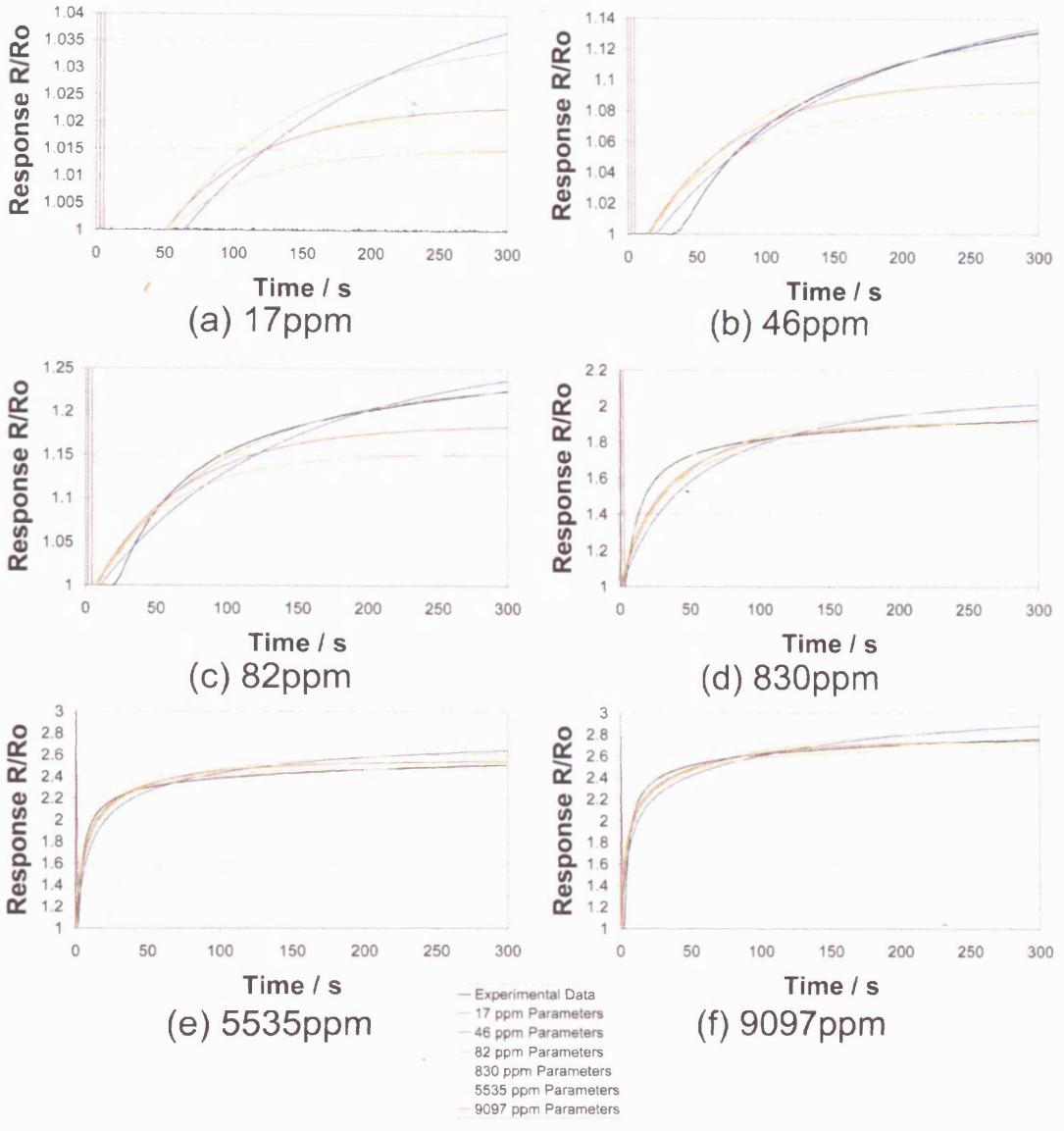

Figure 5.9 Fine chromia sensor, sintered at 825°C, sensor number 2, tested to CO. Chart (a) to (f) show the experimental response transient for the particular concentration indicated as the black lines and the simulated transients of the regression solutions of all concentrations as the coloured lines. The observations made from these data are: (1) Response of solutions at t=0 is not equal to 1 as it should be (this is because the steady state solution is slightly inaccurate); (2) The solution obtained for a particular concentration fits the experimental transient for that concentration very well; (3) In this case, for an experimental transient for a particular concentration the solutions obtained for other concentrations DO fit well, particularly at high concentrations

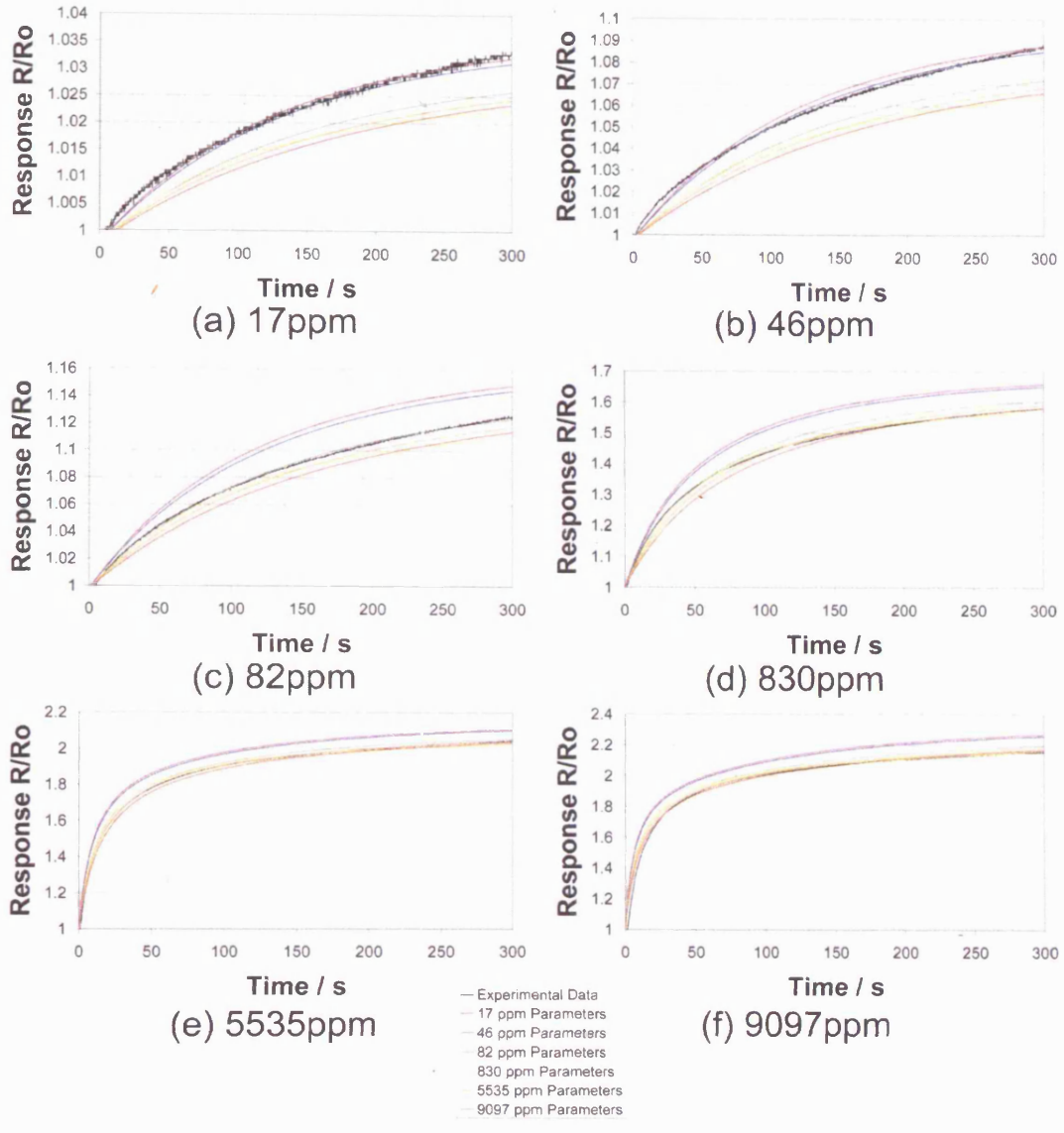

Figure 5.10 Fine chromia sensor, sintered at 900°C, sensor number 1, tested to CO. Chart (a) to (f) show the experimental response transient for the particular concentration indicated as the black lines and the simulated transients of the regression solutions of all concentrations as the coloured lines. The observations made from these data are: (1) Response of solutions at t=0 is not equal to 1 as it should be (this is because the steady state solution is slightly inaccurate); (2) The solution obtained for a particular concentration fits the experimental transient for that concentration very well; (3) In this case, for an experimental transient for a particular concentration the solutions obtained for other concentrations DO fit well, particularly at high concentrations

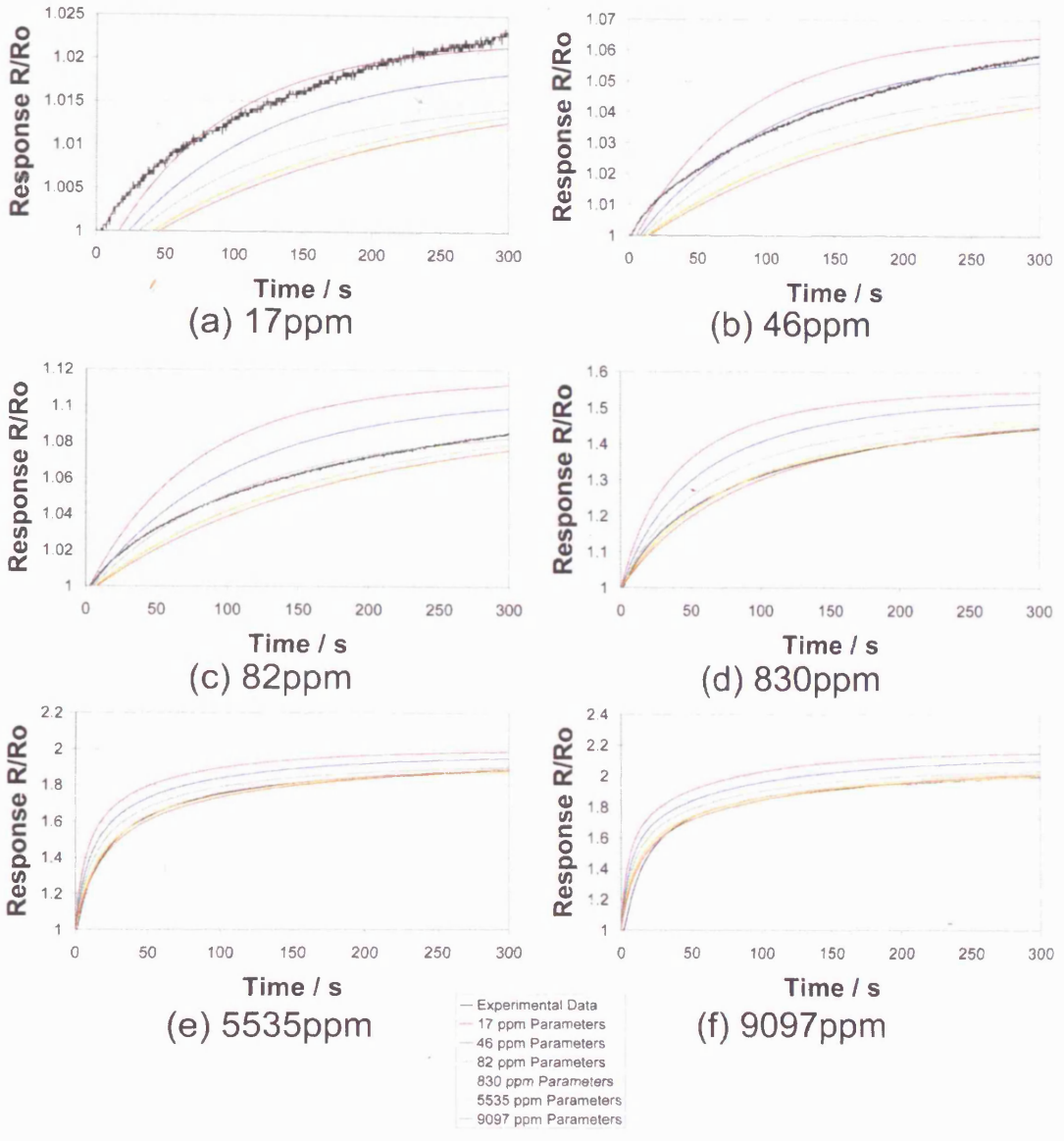

Figure 5.11 Fine chromia sensor, sintered at 900°C, sensor number 2, tested to CO. Chart (a) to (f) show the experimental response transient for the particular concentration indicated as the black lines and the simulated transients of the regression solutions of all concentrations as the coloured lines. The observations made from these data are: (1) Response of solutions at t=0 is not equal to 1 as it should be (this is because the steady state solution is slightly inaccurate); (2) The solution obtained for a particular concentration fits the experimental transient for that concentration very well; (3) In this case, for an experimental transient for a particular concentration the solutions obtained for other concentrations do NOT fit well, but the fit gets better at higher gas concentrations

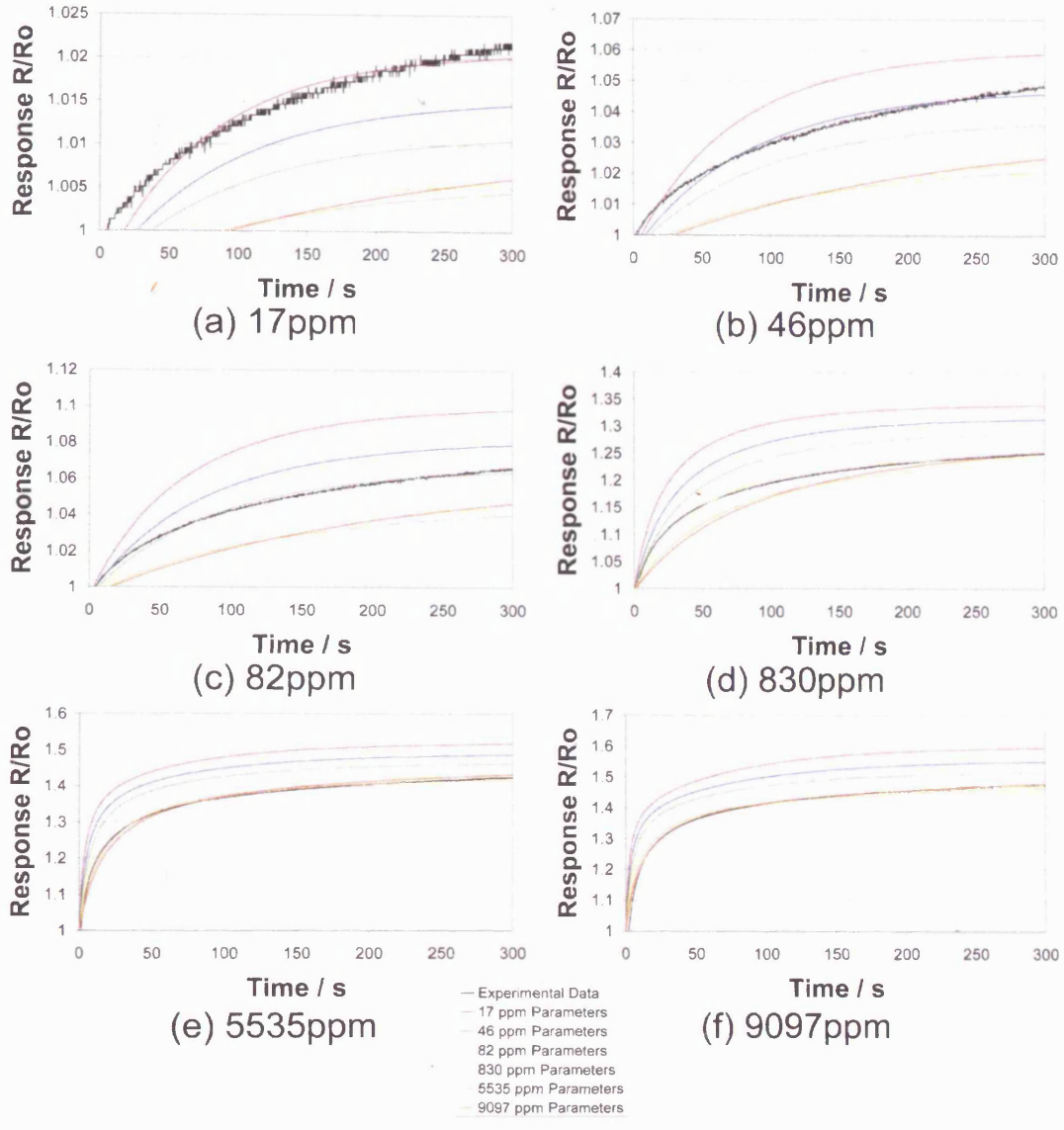

Figure 5.12 Fine chromia sensor, sintered at 1000°C, sensor number 1, tested to CO. Chart (a) to (f) show the experimental response transient for the particular concentration indicated as the black lines and the simulated transients of the regression solutions of all concentrations as the coloured lines. The observations made from these data are: (1) Response of solutions at t=0 is not equal to 1 as it should be (this is because the steady state solution is slightly inaccurate); (2) The solution obtained for a particular concentration fits the experimental transient for that concentration very well; (3) In this case, for an experimental transient for a particular concentration the solutions obtained for other concentrations do NOT fit well, but the fit gets better at higher gas concentrations

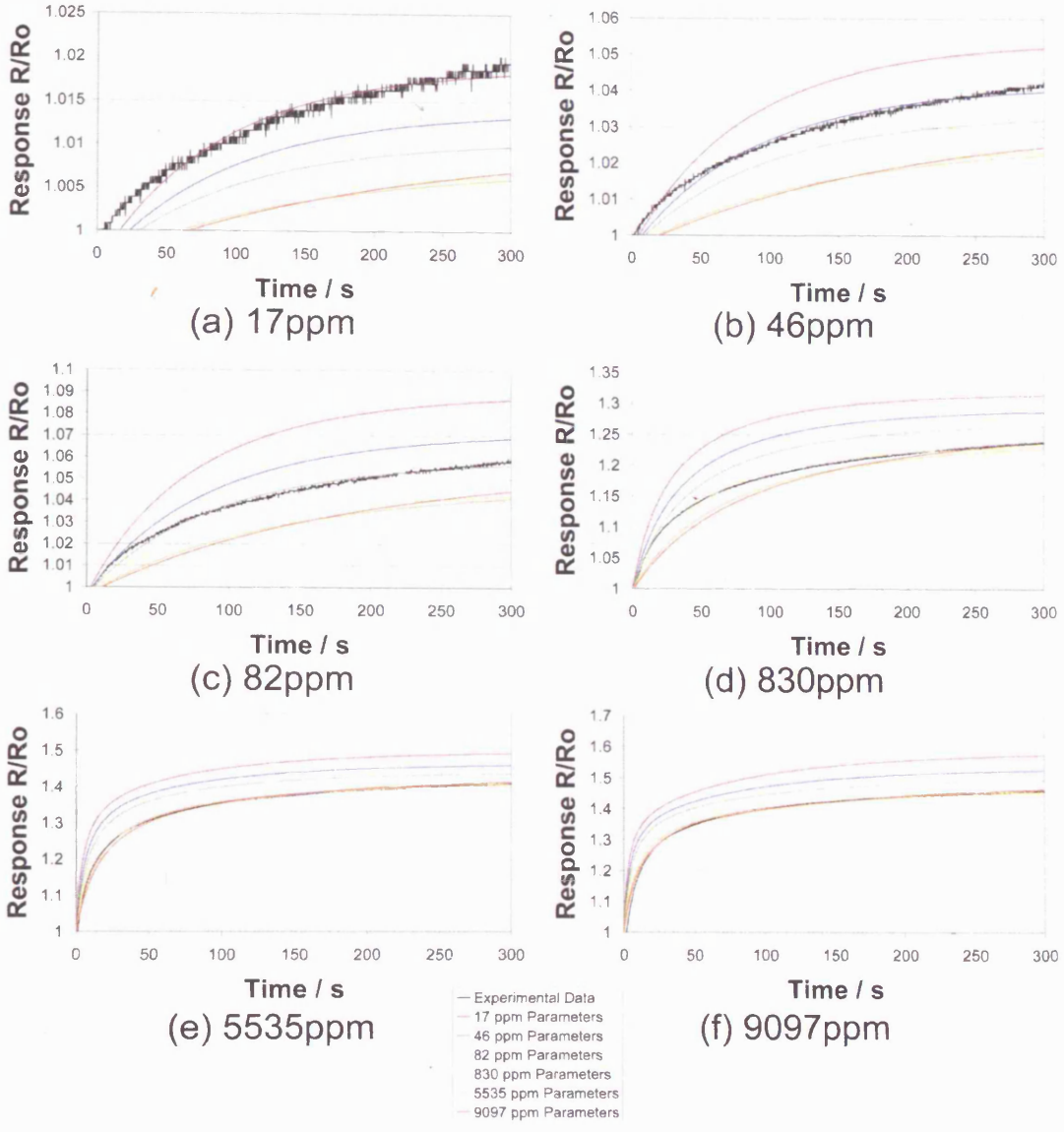

Figure 5.13 Fine chromia sensor, sintered at 1000°C, sensor number 2, tested to CO. Chart (a) to (f) show the experimental response transient for the particular concentration indicated as the black lines and the simulated transients of the regression solutions of all concentrations as the coloured lines. The observations made from these data are: (1) Response of solutions at t=0 is not equal to 1 as it should be (this is because the steady state solution is slightly inaccurate); (2) The solution obtained for a particular concentration fits the experimental transient for that concentration very well; (3) In this case, for an experimental transient for a particular concentration the solutions obtained for other concentrations do NOT fit well, but the fit gets better at higher gas concentrations

5.1.4 Discussion and Comparison with Carbon Monoxide Results on Sensors Derived From Coarse Chromia Material

As with the CO tests on sensors derived from coarse chromia material the transients in Figure 5.2 for CO tests on sensors derived from fine chromia material show the steady state is most closely reached in tests to high CO concentration on sensors sintered at the lowest temperatures. As the sintering temperature is increased or the gas concentration is decreased the degree of deviation from the steady state is increased. The degree to which the steady state is approached for these tests on sensors derived from fine chromia appears less than for the sensors derived from coarse chromia. The shorter gas exposure time for these tests on sensors derived from fine chromia is probably mostly responsible for this difference. The degree of inaccuracy in the solutions to the microstructural model for the fine chromia material may be greater as a result.

The superiority of the solutions to the microstructural model over those to the traditional square root model are confirmed again in Figure 5.2. It is surprising that these solutions appear to fit the experimental data to an almost equal degree over the range of sintering temperatures tested here since a fairly large variation was observed for the CO tests on sensors derived from coarse chromia material. This is especially so because of the fact that the gas exposure times for sensors derived from fine chromia material were much shorter and the inaccuracy of the solutions was expected to be greater as a result. A slight decrease in the degree of fit is observed for the sensors sintered at the highest temperature. This lower than expected variation could be because there is a much weaker variation in how closely the steady state response is approached with sintering temperature for sensors derived from fine chromia as was observed for the tests on sensors derived from coarse chromia. The solutions to the traditional square root model do appear to vary in how closely they fit the experimental data being extremely poor fits at 775°C and getting better for the higher sintering temperatures.

The trends in the values of the parameters obtained from the solutions to the microstructural model with sintering temperature are identical to those observed for

the CO tests on the sensors derived from coarse chromia material. The magnitudes of the values may be compared in the charts above in Figure 4.3 and Figure 5.3 or, in a more direct way, in Figure 5.14, below. On the whole it is remarkable how close the values from the two different materials appear as the particle size observed for the sensors derived from coarse chromia is between 5 and almost 10 times greater than that in the sensors derived from fine chromia. The value of the parameter representing the particle boundaries is higher for sensors derived from fine chromia material at the higher sintering temperatures. This means that the particle boundaries contribute more towards sensor resistance for the finer material. This may be a result of a higher effective length or lower cross sectional area of the particle boundary resistor for sensors derived from fine chromia. The length could be increased higher due to the greater number of boundaries in the finer material although this factor is also likely to impact upon the effective cross sectional area of the resistor with the opposite effect on resistance. The overriding factor is likely to be the much more integrated boundaries evident for the coarse chromia material having higher effective cross sectional area and therefore lower resistance.

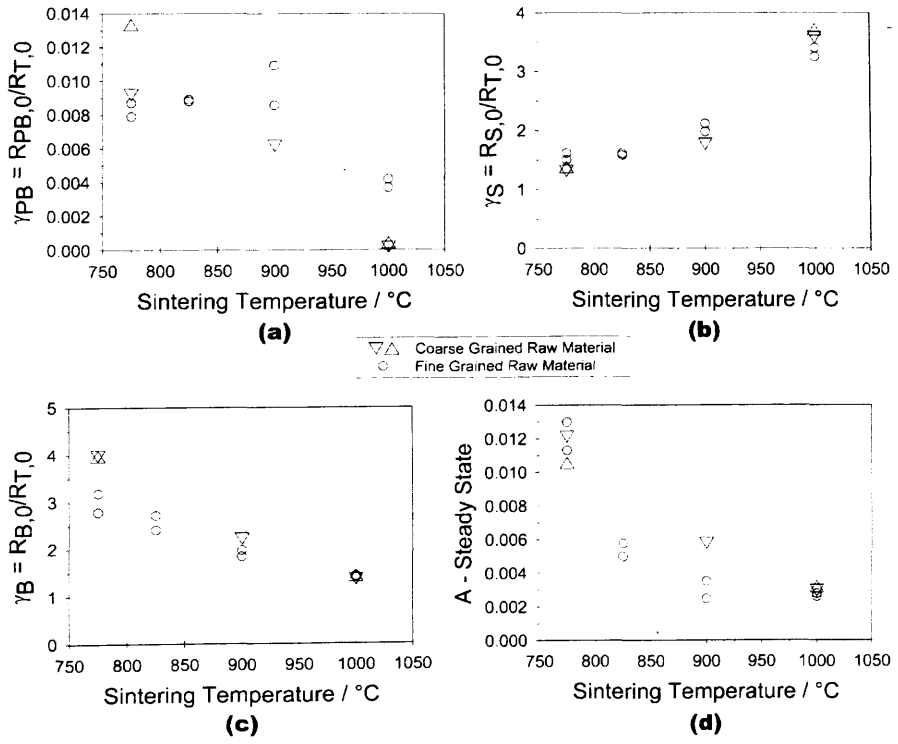

Figure 5.14 Comparison of parameters obtained from the solutions to the microstructural model from the CO tests for sensors derived from coarse and fine grained chromia raw material

The value of the surface parameter, A, is approximately the same for both materials. The sensors made from the coarse chromia material perhaps have a slightly lower value overall. This slightly lower value for sensors derived from coarse chromia seems to suggest that the larger particles lead to a decreased contribution of the surface to the resistance. This observation is surprising as it directly contradicts that evident in the increasing trends of the surface parameter with increasing sintering temperature and hence particle size. The similarity between the values found for sensors made from the two materials is also somewhat surprising as the difference in particle size between the sensors made of the two materials may suggest that quite large difference in this parameter would be expected. However, the value of the surface parameter must always be considered along with the bulk parameter due to their resistors being in parallel in the equivalent circuit. The value of the bulk parameter is higher for the coarser material. This result is again contradictory to that noted in the decreasing trends of the bulk parameter with increasing particle size as a result of increasing sintering temperature.

There are several possible explanations for these apparently contradictory observations. They are the result either of some microstructural or compositional difference that has not been accounted for yet or of some aspect of the model or its application. Although particle size is a very important factor that can be quantified and applied to the understanding of these results relatively easily, there are likely to be other microstructural differences that are not so easily applied. One such difference between the two materials is the nature and quantity of material at the surface of the sensor. Although sensors made of both materials display microstructures formed of clusters of smaller particles they are larger and more closely spherical for the coarse chromia material. The clusters appear much more fractured for the sensors composed of fine chromia material and appear to have a more tortuous surface. This tortuosity could lead to an increase in the effective length of the resistor representing the surface in the fine chromia material. Such an increase could account for the higher contribution to resistance from the surface relative to the bulk than expected solely from a consideration of particle size.

Another possible explanation could be that the porosity in the sensors made from the two different materials is different in quantity, form and distribution. Such changes

could heavily affect the amount of material that is exposed to the atmosphere and can therefore be defined as surface. Unfortunately, the porosity of the sensors has not been studied to the extent to allow judgements of how it may affect these parameters due to the complications in obtaining good samples for such analysis noted above. So porosity remains a possible reason for these irregularities.

Material composition is another aspect of the sensors that could differ between these sensors accounting for these contradictions. It has been assumed that the composition of the materials is simply that of the correct stoichiometric proportions of chromia and titania that results in $Cr_{1.95}Ti_{0.05}O_3$. However, there are two aspects of material that are likely to cause differences between the sensors made from the two different raw materials. The first is that the raw materials themselves will have different compositions with different impurities and defects as a result of the different processes used to create them. The second is the widely reported effect of titanium segregation[45,46,47,48,49,59]. Because diffusion depends not only on temperature but also on surface curvature, there may well be differing degrees of surface segregation of titanium in the sensors made from the different materials. Although the effects of material composition are expected to be accommodated mainly in the value of the sensitivity parameter, A, there could also be an effect on the values of the resistors representing the different microstructural regions.

Although the above microstructural and compositional factors could account for the above contradictory results, other possible explanations could lie in the formation and the application of the microstructural model. For instance, the assumption of a linear response model may be incorrect or the fundamental arrangement of the resistors in the equivalent circuit may be inadequate to explain the variations that occur due to these changes. There is a high probability that the simple model used in this study will never be able to explain all the variations that could possibly be experienced through microstructural changes since it is a gross simplification of reality. A much better model may be a more complicated arrangement of a much larger number of resistor elements. However, the beauty and simplicity of understanding of the present model would be lost and many of the aspects of microstructure that have not been described are most likely to explain the contradictions, as discussed above.

In terms of the application of the model used in this study there is one aspect in particular that could result in the introduction of errors. Such errors could account for the above irregularities. This aspect of the method used to apply the model is the estimation of final response achieved in the gas exposures as the steady state value of response. This estimation was shown to be most valid, in the CO tests, for the sensors derived from coarse chromia material sintered at the lowest temperatures and least valid overall for the sensors derived from fine chromia. This could mean that the data used to generate the solutions to the microstructural model was more inaccurate for the sensors derived from fine chromia and there is the possibility that the values of the parameters for this material are somewhat 'skewed' with respect to their true values.

The similarity between the values and trends observed for the sensitivity parameter, A, obtained from the transient data and the steady state data is an encouraging indication of the validity of both forms of the model, as is the repeatability of the values between different sensors sintered at the same temperature and tested at the same time. The lack of such repeatability for the values of the time constant, τ, may be of some concern, but the values are generally of around the same magnitude across the whole range of tests and they don't display any clear trends with either sintering temperature or gas concentration. The major outlying result in sensor repeatability is found for the sensors sintered at 825°C tested to the lowest gas concentration. Here, for the second of the two sensors, the value of the sensitivity parameter, A, was significantly below the value that was expected, and was achieved for the first sensor, and the value of the time constant, τ, was negative, which is theoretically nonsense. The spurious nature of these results may be traced to the apparent lack of any experimental response data for this gas concentration on this sensor. This result should therefore be ignored. The average values obtained for the sensitivity parameter, A, from the transient solutions to the model for each of these sensors derived from fine chromia material and tested to CO are generally at slightly lower values than those that were obtained for the sensors derived from coarse chromia material. This was also observed for the values of the sensitivity parameter obtained from the steady state data. This is a good indication of the compatibility between the two forms of the model.

The fact that the fit of the solution for a particular concentration fits the transient experimental data for that concentration very well whilst it does not fit the data for other concentrations quite so well is of no surprise considering the method used to generate these results. As with the earlier observations for sensors constructed from coarse chromia material and tested to CO, the fit of the different solutions to the experimental transient data tends to improve as concentration is increased. As discussed earlier, this is likely to be due to the difference between the real baseline and the offset baseline becoming relatively more insignificant in comparison to the increasing magnitude of the response that is achieved with increasing concentration. The differing values of the baseline predicted from the steady state solution, being both greater and less than 1, is an interesting observation. This factor is of great importance in how well these transient solutions fit the experimental data. Control of this factor should be established in the generation of new solutions so that the parameters obtained should result in a fixed baseline of 1.

5.1.5 Conclusions

The microstructural model has again been successfully applied to the experimental data. The solutions obtained to this model fit the experimental data much better than those obtained to the traditional square root model. The trends in the values of the microstructural parameters obtained from the solutions with sintering temperature have been successfully explained in terms of the observations made of sensor microstructures in chapter 3. Essentially, the conclusions for the CO testing performed on the sensors made from fine chromia raw material in terms of the effects of sintering temperature match those made for the CO testing performed on the sensors made from coarse chromia raw material in section 4.1.5. It is surprising how close the values for the parameters found for the two materials are. The differences between the values found for the parameters from the different materials are also contradictory to the trends that are observed in the parameters with sintering temperature in terms of the microstructural observations that have been made. No definitive reasons can be given for these effects. However, it is likely that there are aspects of the microstructure and composition of the sensors, particularly in terms of

porosity, surface area and surface segregation of titania, that have not been analysed in this study that may account for them. There may also be aspects of the data processing, testing procedures and the model itself that could account for these observations. In particular, the estimation of maximum response achieved during these experiments as the steady state response may have varying validity for these results in particular as the length of the gas exposures used for these sensors made from fine chromia material are half the length of those for the sensors made from coarse chromia material in section 4.1.

5.2 Response to Propane

5.2.1 Gas Exposure Transients

For the propane tests conducted on the sensors derived from fine chromia material the response transients are presented in Figure 5.15. The sensors derived from fine chromia material show a clearly greater magnitude of response towards propane than towards CO which stands in contrast to the behaviour of the sensors derived from coarse chromia material. In contrast to the behaviour observed with CO, and just as observed for sensors derived from coarse chromia material, the response transient to propane did not approach the steady state any more rapidly as the sintering temperature of the devices was decreased. The trend of increasing integrity of the approximation of the final response achieved in the exposure as the steady state response with increasing gas concentration is again shown to exist as with all previous tests. Also, the integrity of this approximation does not appear to vary significantly with sintering temperature of the sensors for these propane tests. This is the same observation that was made for propane tests on sensors derived from coarse chromia material.

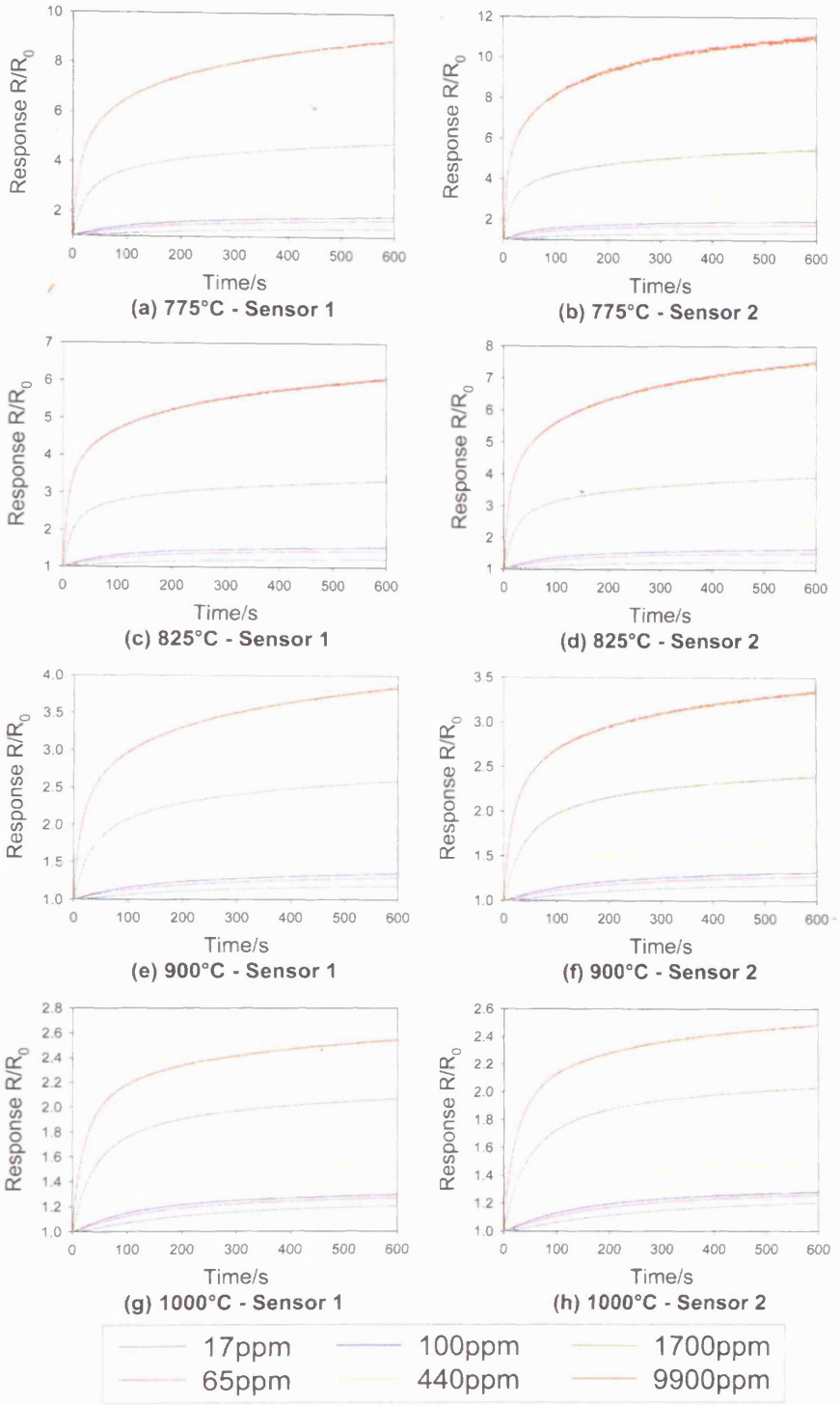

Figure 5.15 Response versus time plots for the gas exposures to different propane concentrations on sensors derived from fine chromia material sintered at 775 (a+b), 825 (c+d), 900 (e+f) and 1000°C (g+h). These plots show the steady state is approached most closely in the tests to the highest concentrations of propane. The degree to which the steady state is approached does not appear to be significantly affected by sintering temperature in common with the earlier observation made for propane tests for sensors derived from coarse chromia material. The magnitude of responses decreases with increasing sintering temperature as with all other cases observed so far.

5.2.2 Solutions to the Model – Steady State Gas Response

The responses for the sensors derived from fine chromia tested to propane displayed in Figure 5.16 show the now familiar trend of decreasing magnitude with increasing sintering temperature. The lines plotted for both the microstructural model and the traditional square root model show increasing variance from the experimental data with increasing sintering temperature as has been noted above in all tests but those for sensors derived from coarse chromia tested to CO. As with the propane tests for sensors derived from coarse chromia the solutions to the traditional square root model are much better than was observed for CO for these propane tests on sensors derived from fine chromia. The solutions obtained for the microstructural model also represent excellent fits to the experimental data. It is impossible in this case to form a conclusion of which model better represents the response data. This was not the case with the results for the propane tests on sensors derived from coarse chromia where the microstructural model was clearly better at representing the variation of response with concentration than the traditional square root model.

The trends in the parameters representing the different microstructural regions with increasing sintering temperature displayed in Figure 5.17 are the same as those previously noted for all the other tests above: $R_{PB,0}/R_{T,0}$ and $R_{B,0}/R_{T,0}$ decrease whilst $R_{S,0}/R_{T,0}$ increases with increasing sintering temperature. The parameter representing the particle boundary is found to be approximately 3 times greater for propane than for CO for these sensors derived from fine chromia as was also found for sensors derived from coarse chromia. The magnitudes of the parameter representing the surface are similar for both CO and propane. As with the earlier comparison of CO and propane for the sensors derived from coarse chromia, the magnitude of the parameter representing the bulk is somewhat lower for CO than is displayed in these results for propane. The value of the sensitivity parameter, A, could generally be described as displaying a decreasing trend with increasing sintering temperature as observed for the CO tests on both materials. However, the range over which this change occurs is relatively narrow and it could equally be considered that the value is relatively constant with sintering temperature as was observed for the propane tests for the sensors derived from coarse chromia. In comparing these results with the propane results from sensors derived from coarse chromia, the same trends are

displayed in both and the magnitudes of the parameters found for sensors derived from fine chromia appear to be slightly higher than for sensors derived from coarse chromia.

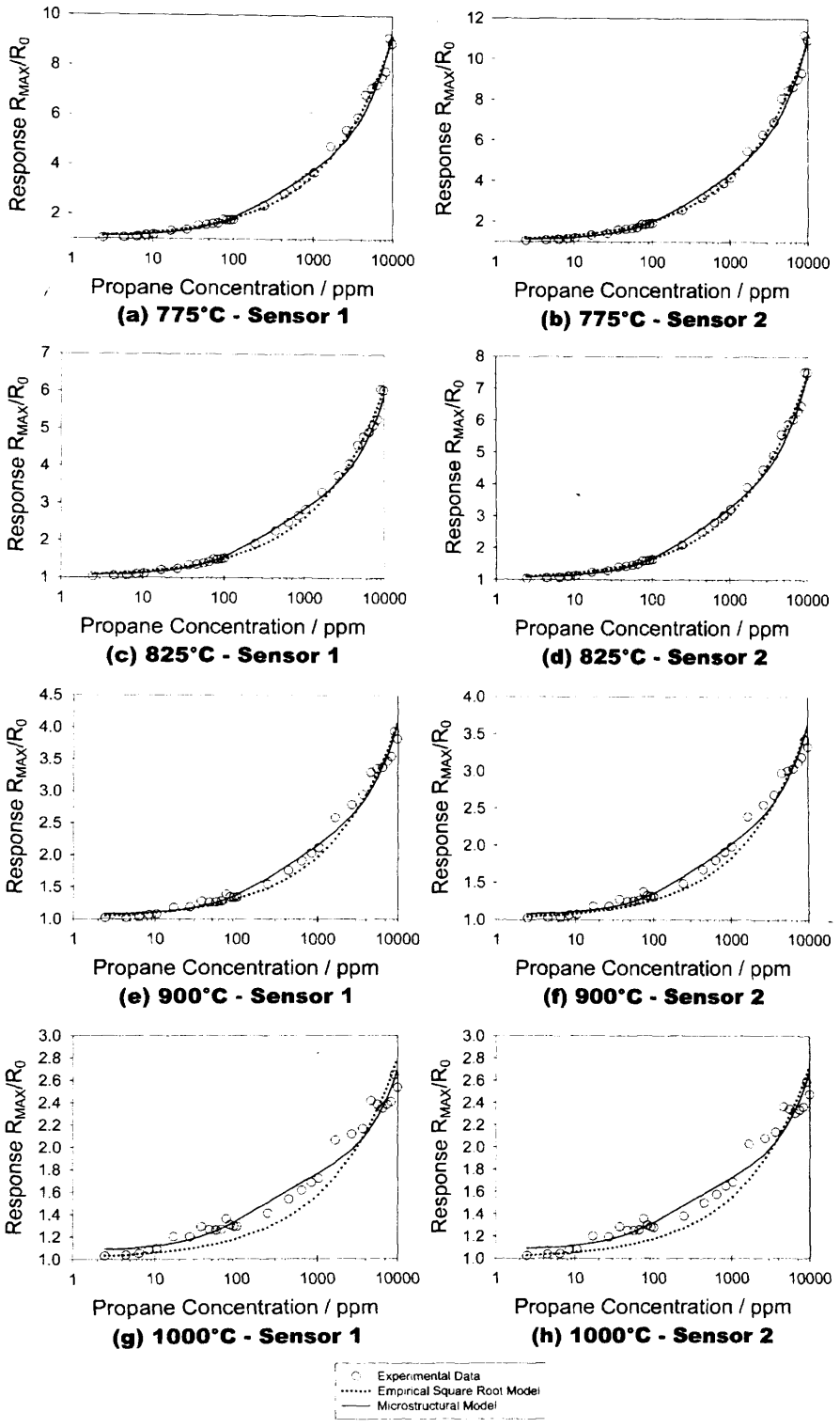

Figure 5.16 Plots of response versus propane concentration for sensors sintered at 775°C (a+b), 825°C (c+d), 900°C (e+f) and 1000°C (d+e). As noted for all other tests the magnitude of the response decreases with increasing sintering temperature. Generally, solutions obtained for the microstructural model are shown to have a better fit to the experimental data than for the empirical square root model although the degree of fit to both solutions is close at the lower sintering temperatures. The degree of fit to both models decreases with increasing sintering temperature. The degree of fit of the empirical square root model is observed to be better for the propane than for the CO tests with this material as was also the case for the sensors derived from coarse chromia.

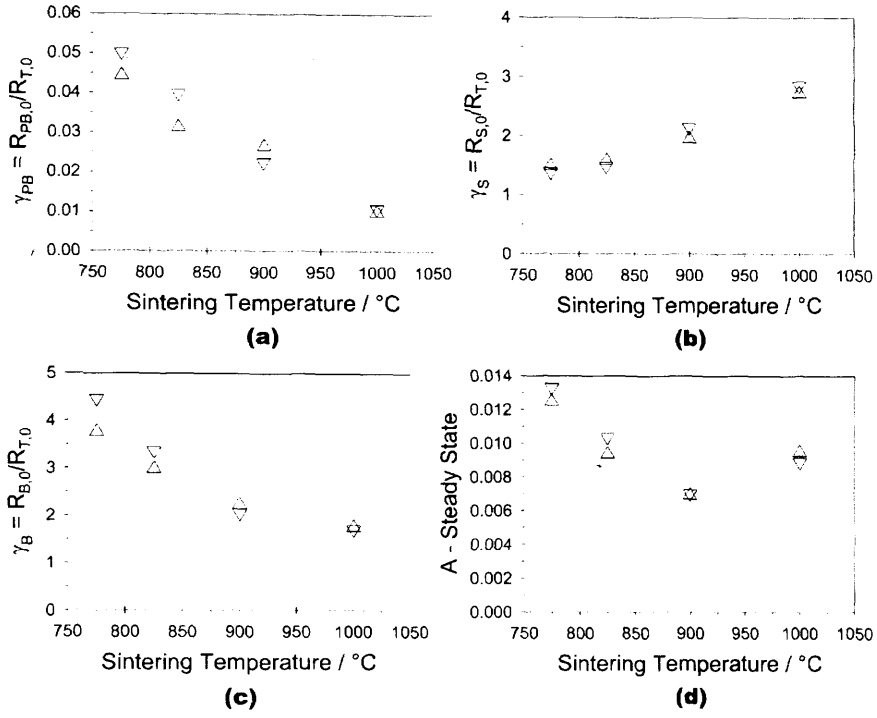

Figure 5.17 The microstructural parameters of the solutions of the experimental data to the microstructural model are plotted versus sintering temperature. The variations with sintering temperature may be explained by microstructural observations and reassessing assumptions.

5.2.3 Solutions to the Model – Transient Gas Response

The bar charts in Figure 5.18 and Figure 5.19 show the values of the sensitivity parameter, A, and the time constant, τ, respectively obtained for the sensors sintered at different temperatures and tested to different concentrations. Again, there are values that have been allowed to go off scale to preserve the illustration of trends in the more 'sensible' values. Disregarding the results for the lower concentrations, which are generally those that are off the scale, the average values of the sensitivity parameter, A, show a slight decreasing trend with increasing sintering temperature. This trend and the values are similar to those that were observed for the value of the sensitivity parameter obtained from the steady state solutions. The value of the time constant, τ, displays an increasing trend with increasing sintering temperature and a decreasing trend with increasing concentration.

The plots of the experimental transient data, as the black lines, and the solutions to the model obtained at the different concentrations, the coloured lines, are displayed

in Figure 5.20, Figure 5.21, Figure 5.22, Figure 5.23, Figure 5.24, Figure 5.25, Figure 5.26 and Figure 5.27 for the sensors sintered at the different temperatures. As with all other tests that have been conducted, the solution obtained for a particular solution fits the experimental data for that concentration very well and does not fit the experimental data for other concentrations quite as well. An increase in the degree of fit of the different solutions with increasing concentration is not so evident in these results as was noted for the CO results or the results from the sensors derived from coarse chromia material. The fit of all the solutions obtained to the experimental response transients for the different concentrations tested is better for the sensors sintered at 775 and 825°C than for the sensors sintered at higher temperatures.

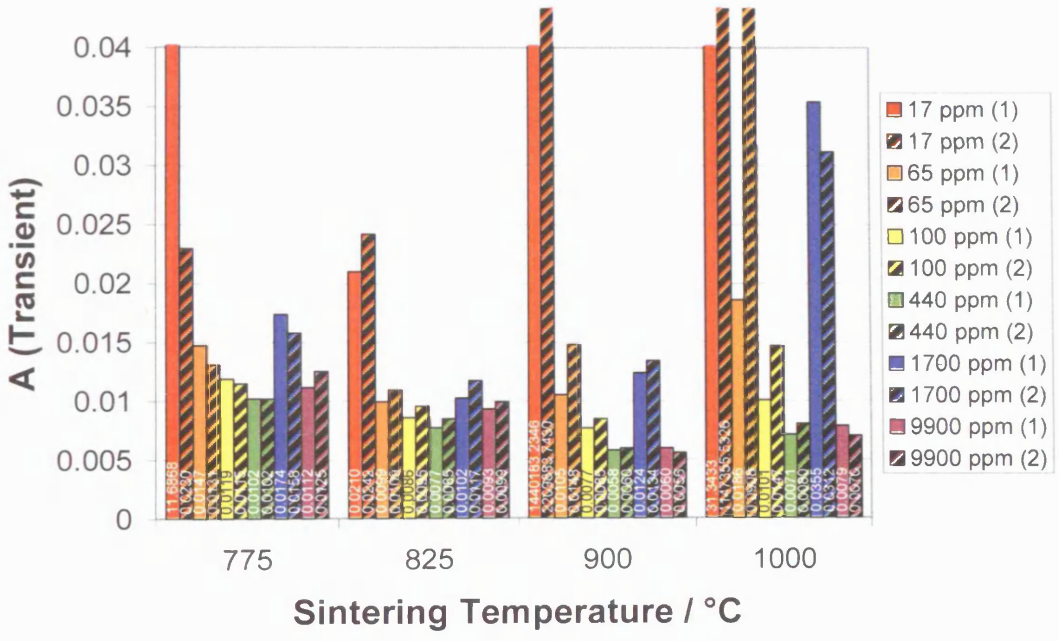

Figure 5.18 Bar chart showing the different values of A obtained from non-linear least squares regression of transient data from sensors sintered at different temperatures and tested to different concentrations of propane

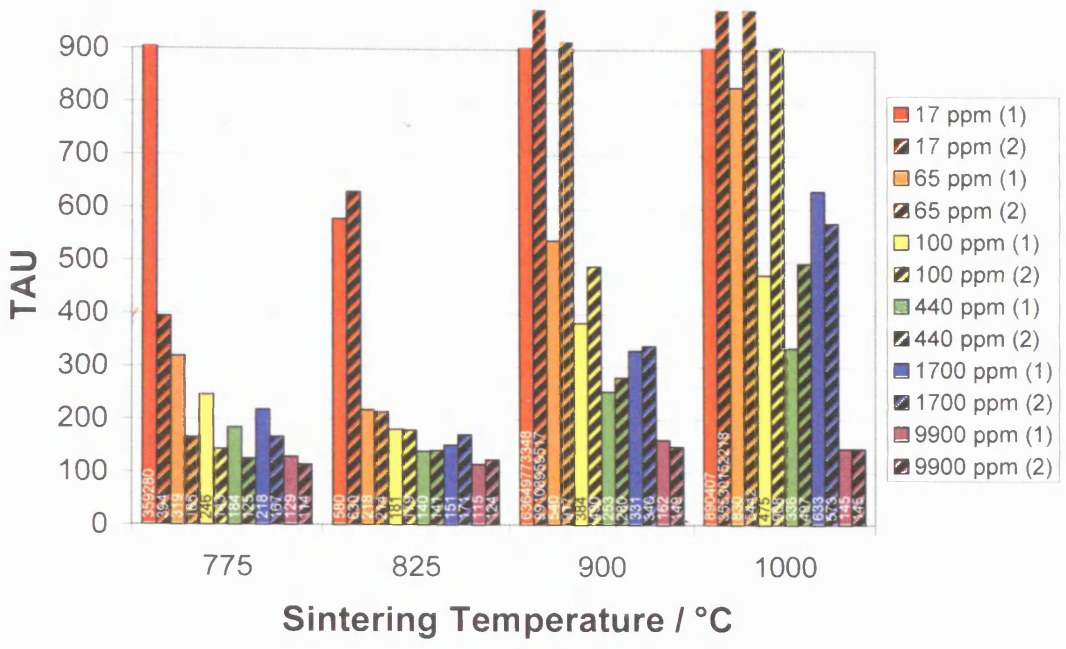

Figure 5.19 Bar chart showing the different values of τ obtained from non-linear least squares regression of transient data from sensors sintered at different temperatures and tested to different concentrations of propane

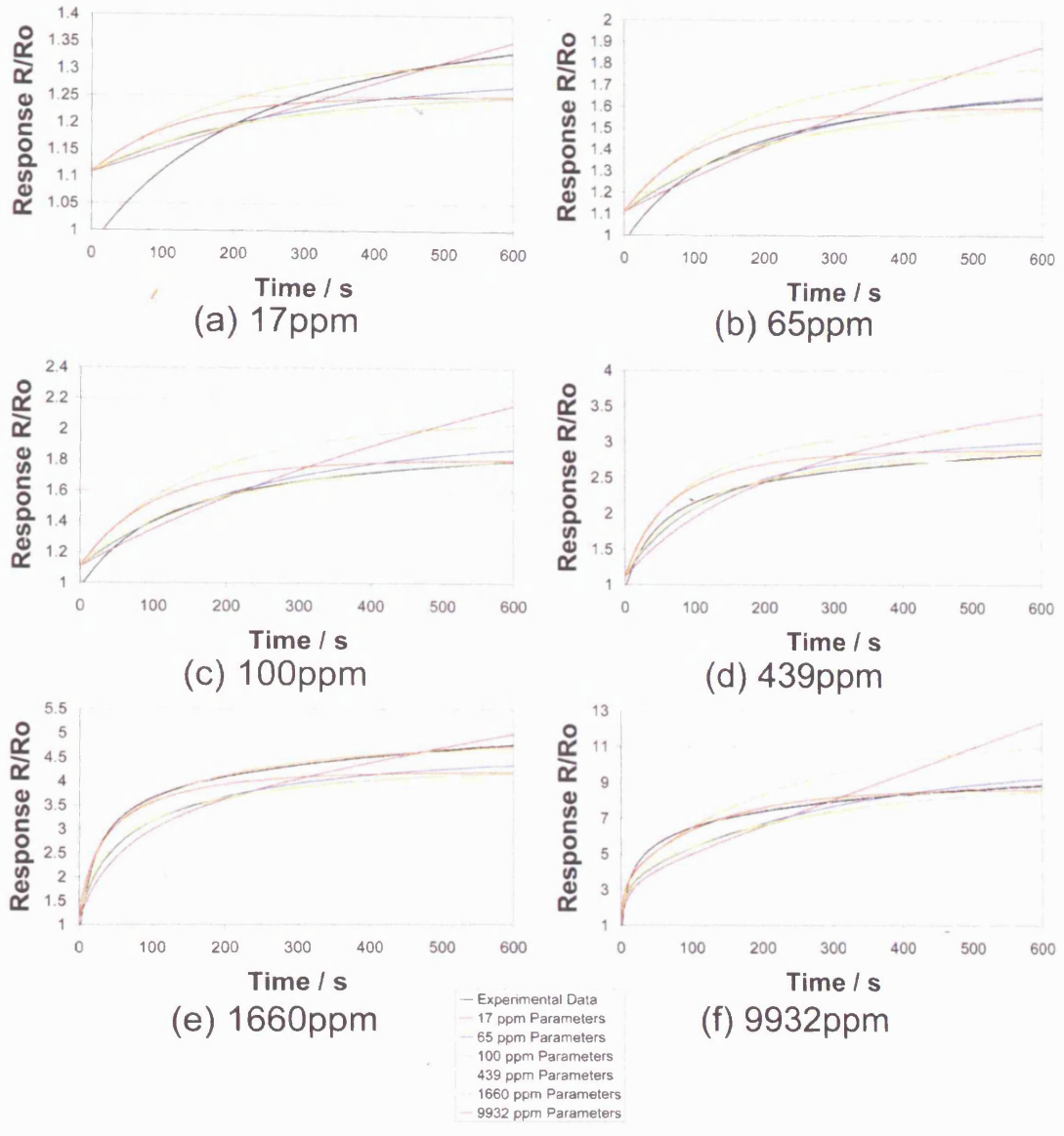

Figure 5.20 Fine chromia sensor, sintered at 775°C, sensor number 1, tested to propane. Chart (a) to (f) show the experimental response transient for the particular concentration indicated as the black lines and the simulated transients of the regression solutions of all concentrations as the coloured lines. The observations made from these data are: (1) Response of solutions at t=0 is not equal to 1 as it should be (this is because the steady state solution is slightly inaccurate); (2) The solution obtained for a particular concentration fits the experimental transient for that concentration very well; (3) In this case, for an experimental transient for a particular concentration the solutions obtained for other concentrations do NOT fit well, and the degree of fit does not appear to change with gas concentration

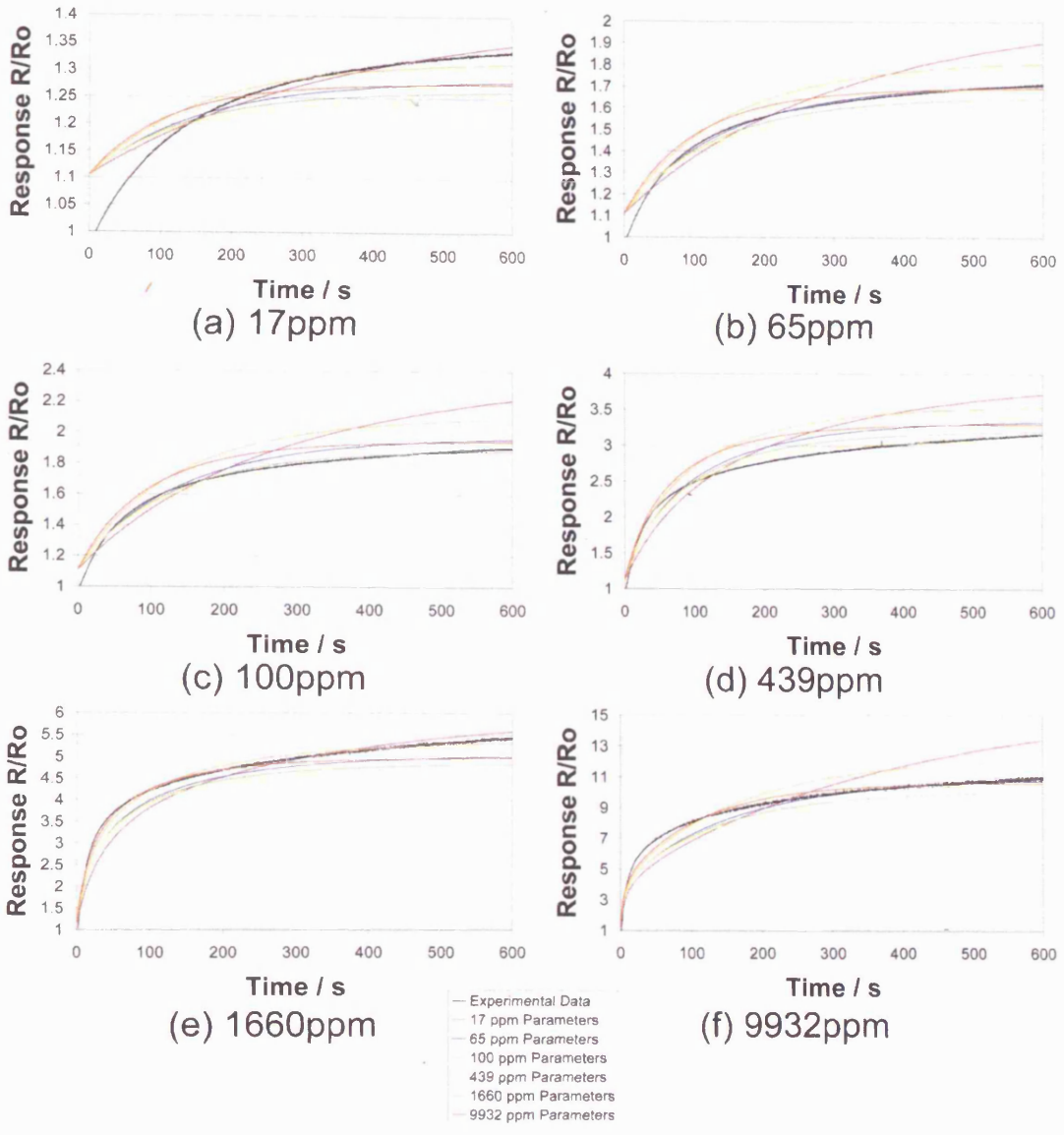

Figure 5.21 Fine chromia sensor, sintered at 775°C, sensor number 2, tested to propane. Chart (a) to (f) show the experimental response transient for the particular concentration indicated as the black lines and the simulated transients of the regression solutions of all concentrations as the coloured lines. The observations made from these data are: (1) Response of solutions at t=0 is not equal to 1 as it should be (this is because the steady state solution is slightly inaccurate); (2) The solution obtained for a particular concentration fits the experimental transient for that concentration very well; (3) In this case, for an experimental transient for a particular concentration the solutions obtained for other concentrations do NOT fit well, and the degree of fit does not appear to change with gas concentration

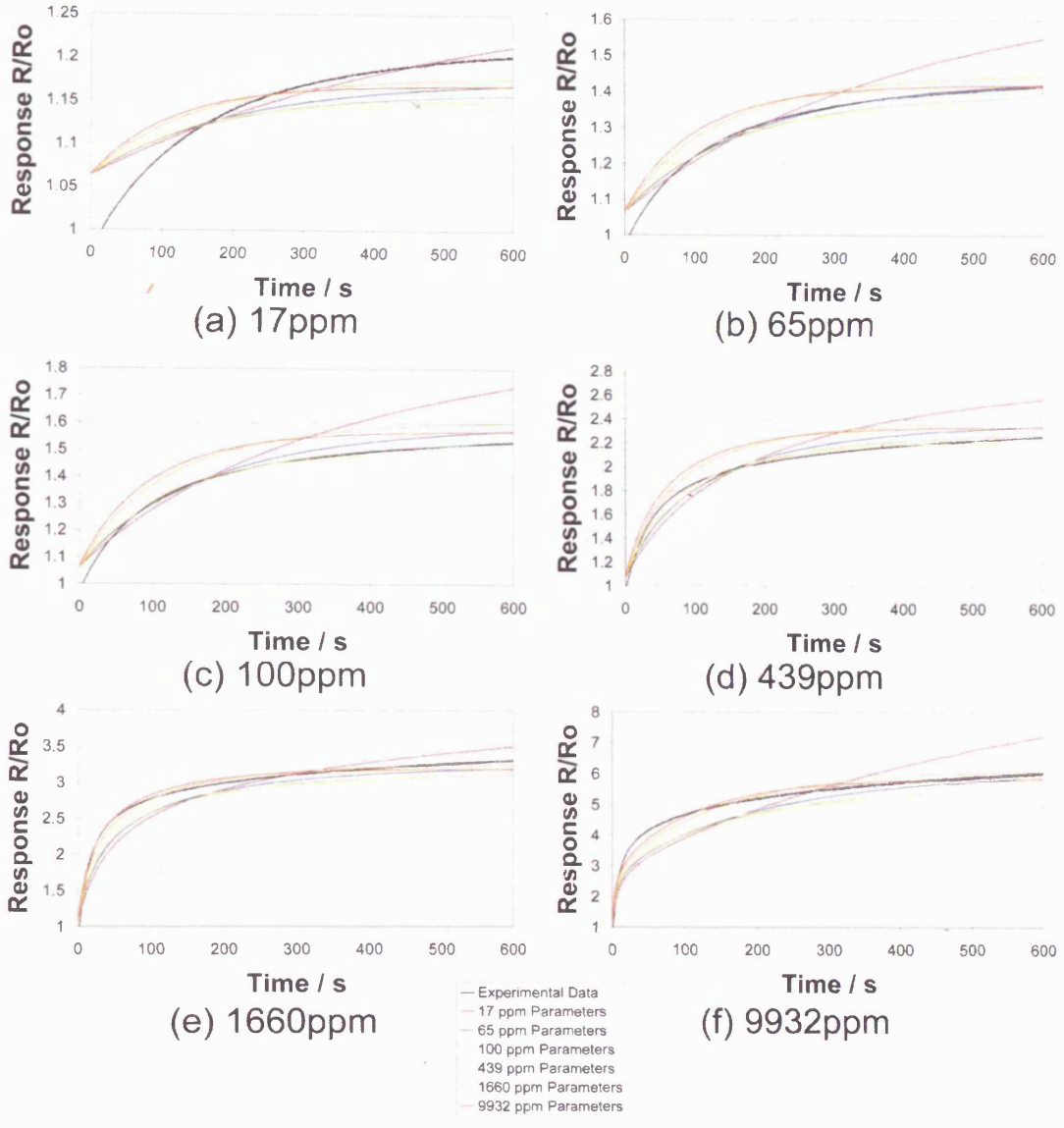

Figure 5.22 Fine chromia sensor, sintered at 825°C, sensor number 1, tested to propane. Chart (a) to (f) show the experimental response transient for the particular concentration indicated as the black lines and the simulated transients of the regression solutions of all concentrations as the coloured lines. The observations made from these data are: (1) Response of solutions at t=0 is not equal to 1 as it should be (this is because the steady state solution is slightly inaccurate); (2) The solution obtained for a particular concentration fits the experimental transient for that concentration very well; (3) In this case, for an experimental transient for a particular concentration the solutions obtained for other concentrations do NOT fit well, and the degree of fit does not appear to change with gas concentration

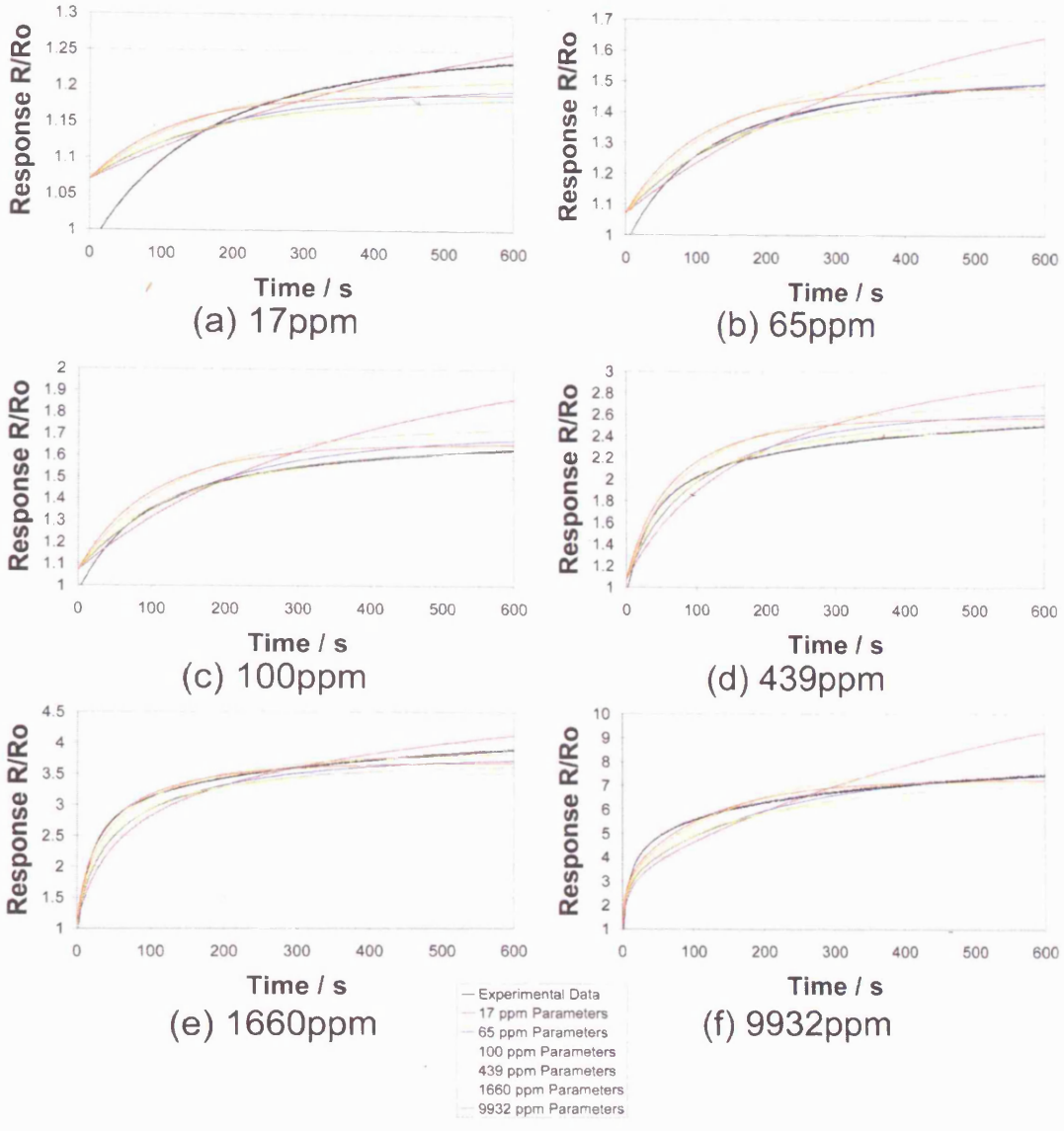

Figure 5.23 Fine chromia sensor, sintered at 825°C, sensor number 2, tested to propane. Chart (a) to (f) show the experimental response transient for the particular concentration indicated as the black lines and the simulated transients of the regression solutions of all concentrations as the coloured lines. The observations made from these data are: (1) Response of solutions at t=0 is not equal to 1 as it should be (this is because the steady state solution is slightly inaccurate); (2) The solution obtained for a particular concentration fits the experimental transient for that concentration very well; (3) In this case, for an experimental transient for a particular concentration the solutions obtained for other concentrations do NOT fit well, and the degree of fit does not appear to change with gas concentration

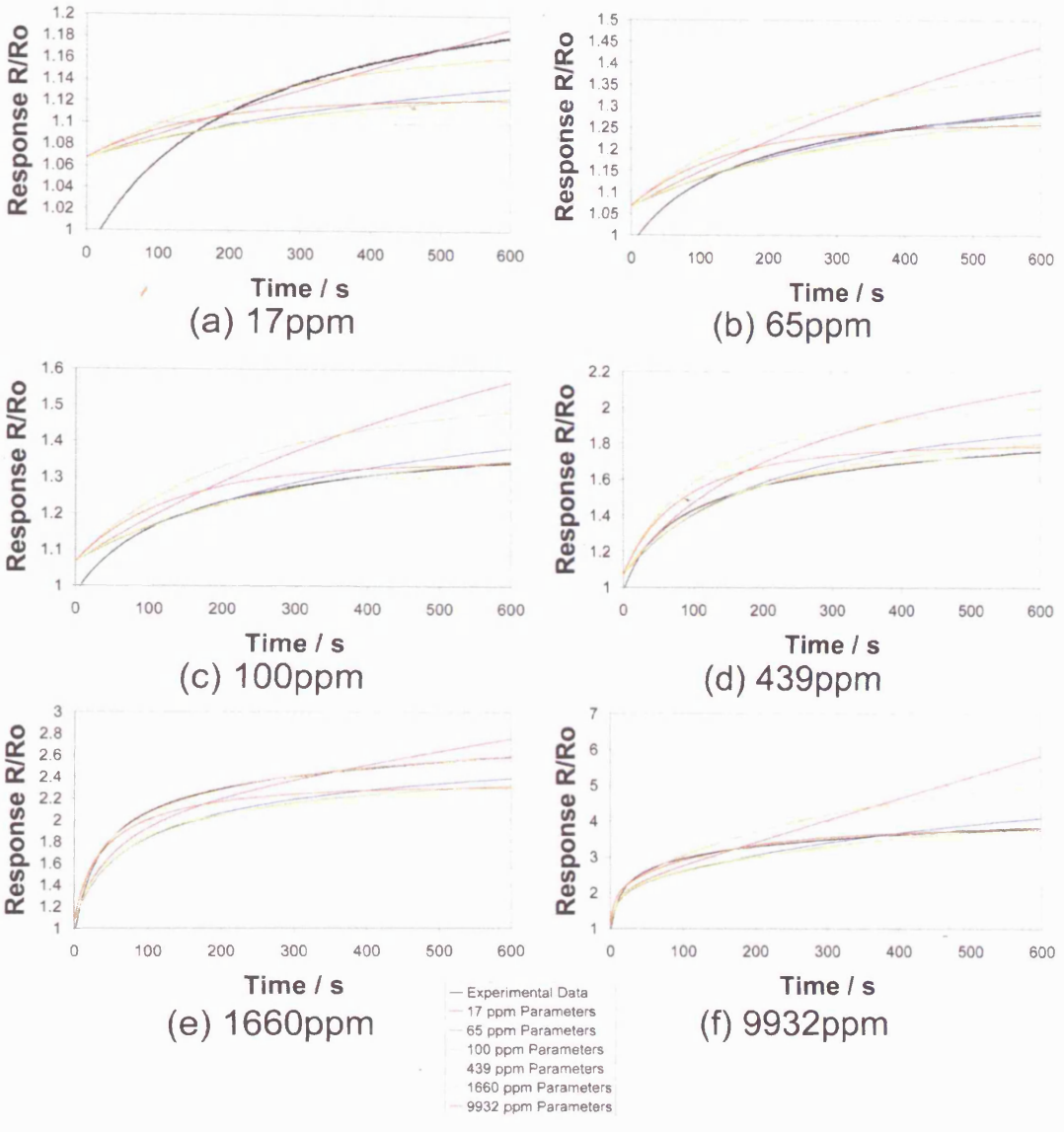

Figure 5.24 Fine chromia sensor, sintered at 900°C, sensor number 1, tested to propane. Chart (a) to (f) show the experimental response transient for the particular concentration indicated as the black lines and the simulated transients of the regression solutions of all concentrations as the coloured lines. The observations made from these data are: (1) Response of solutions at t=0 is not equal to 1 as it should be (this is because the steady state solution is slightly inaccurate); (2) The solution obtained for a particular concentration fits the experimental transient for that concentration very well; (3) In this case, for an experimental transient for a particular concentration the solutions obtained for other concentrations do NOT fit well, and the degree of fit does not appear to change with gas concentration

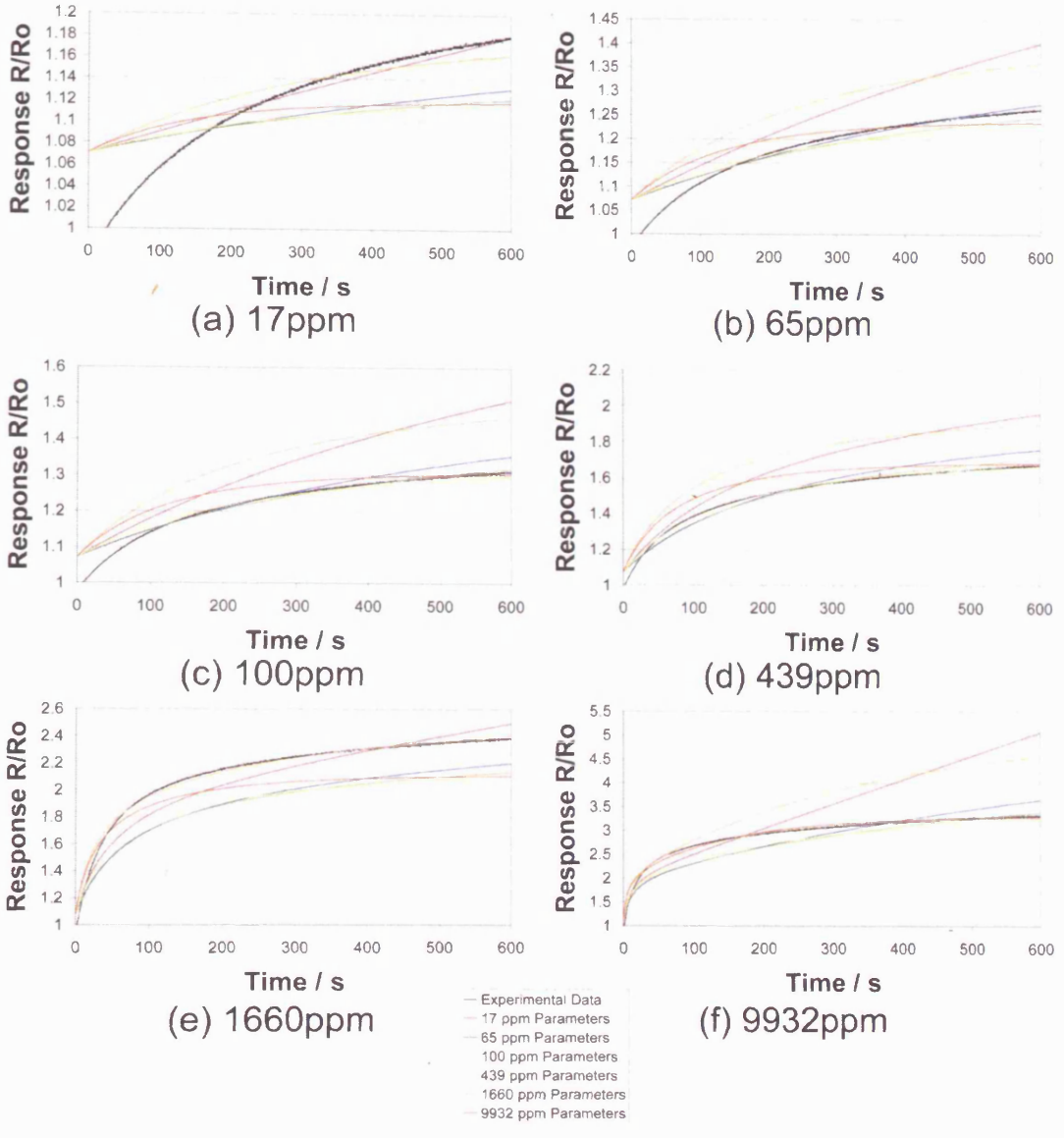

Figure 5.25 Fine chromia sensor, sintered at 900°C, sensor number 2, tested to propane. Chart (a) to (f) show the experimental response transient for the particular concentration indicated as the black lines and the simulated transients of the regression solutions of all concentrations as the coloured lines. The observations made from these data are: (1) Response of solutions at t=0 is not equal to 1 as it should be (this is because the steady state solution is slightly inaccurate); (2) The solution obtained for a particular concentration fits the experimental transient for that concentration very well; (3) In this case, for an experimental transient for a particular concentration the solutions obtained for other concentrations do NOT fit well, and the degree of fit does not appear to change with gas concentration

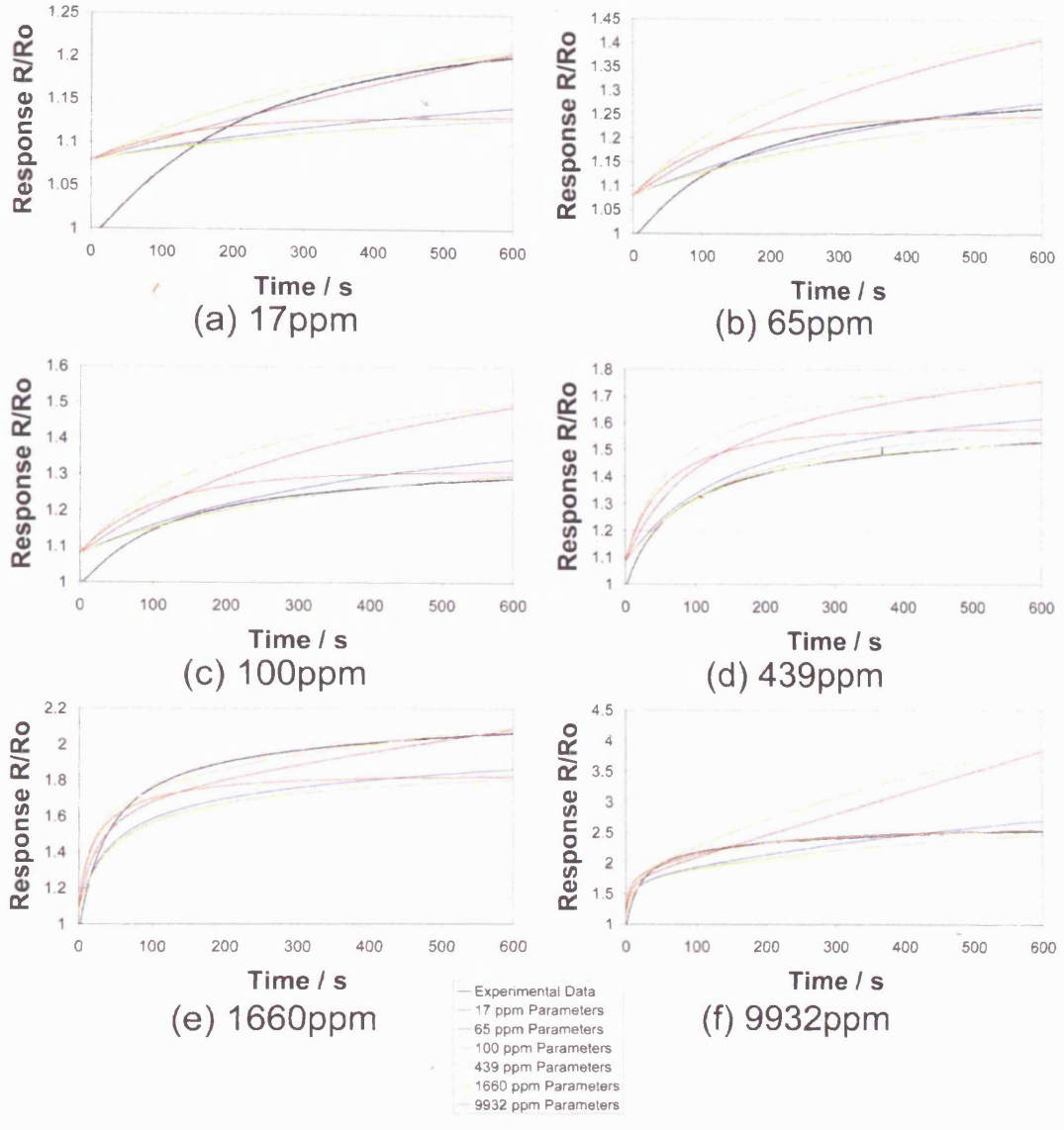

Figure 5.26 Fine chromia sensor, sintered at 1000°C, sensor number 1, tested to propane. Chart (a) to (f) show the experimental response transient for the particular concentration indicated as the black lines and the simulated transients of the regression solutions of all concentrations as the coloured lines. The observations made from these data are: (1) Response of solutions at t=0 is not equal to 1 as it should be (this is because the steady state solution is slightly inaccurate); (2) The solution obtained for a particular concentration fits the experimental transient for that concentration very well; (3) In this case, for an experimental transient for a particular concentration the solutions obtained for other concentrations do NOT fit well, and the degree of fit does not appear to change with gas concentration

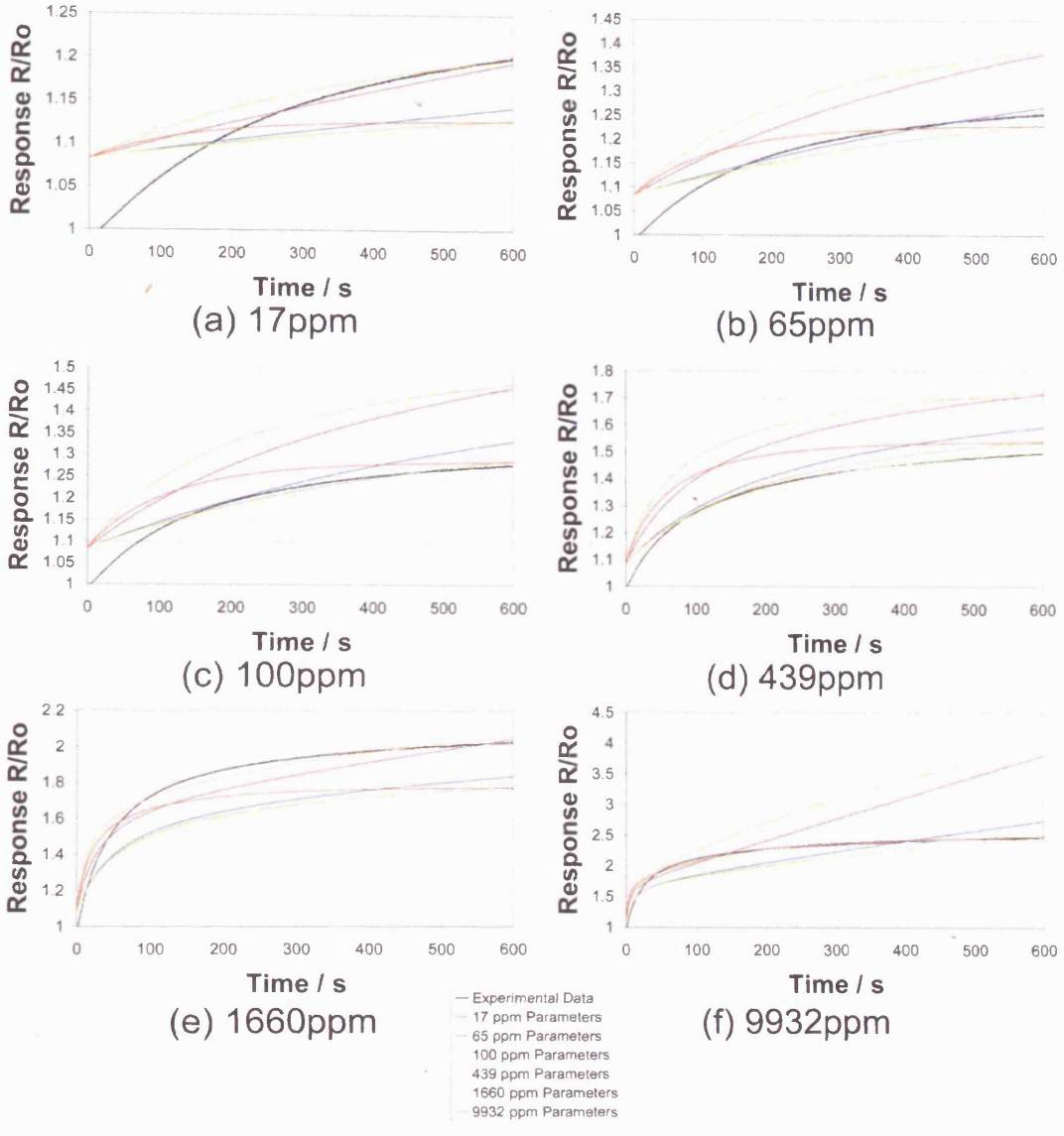

Figure 5.27 Fine chromia sensor, sintered at 1000°C, sensor number 2, tested to propane. Chart (a) to (f) show the experimental response transient for the particular concentration indicated as the black lines and the simulated transients of the regression solutions of all concentrations as the coloured lines. The observations made from these data are: (1) Response of solutions at t=0 is not equal to 1 as it should be (this is because the steady state solution is slightly inaccurate); (2) The solution obtained for a particular concentration fits the experimental transient for that concentration very well; (3) In this case, for an experimental transient for a particular concentration the solutions obtained for other concentrations do NOT fit well, and the degree of fit does not appear to change with gas concentration

5.2.4 Discussion and Comparison with Carbon Monoxide Results and Results from Sensor Derived From Coarse Chromia Material

As with the comparison between the propane and CO results for sensors derived from coarse chromia material, the transients for sensors derived from fine chromia show the same patterns and differences for the two gases. The lack of difference in degree of accuracy of the pseudo steady state response with sintering temperature may again result in less/no apparent variations of the values of the parameters of the solutions with sintering temperature. Because the responses are obviously not as near the steady state solution as they could be, there will likely be inaccuracy in the solutions obtained. They may also be less accurate than those for the CO as the responses are generally further away from the steady state even though the gas exposures for the CO tests were only half the length of these propane tests. For this reason there may be less difference between the CO and propane in these tests on sensors derived from fine chromia compared to those for the coarse chromia material as the CO tests were shorter and appear to be further away from the steady state response.

The plots of response versus propane concentration in Figure 5.16 showed the solutions from both the traditional square root model and the microstructural model fit the experimental data to roughly the same degree for each sensor tested. The degree of fit for both solutions deteriorates somewhat at the higher sintering temperatures, more so than was evident in the tests to propane on sensors made from coarse chromia material. It also appears worse at higher temperatures when compared to the responses from the CO tests on sensors made from fine chromia material. These effects may be due to the increase in experimental variation that is evident in these responses to propane on sensors sintered at higher temperatures. The fact that the solution to the traditional model is better for the propane responses than the CO responses is noted again for this fine chromia material as it was for the coarse chromia material.

There are two comparisons to be made for the parameters of the solutions to the microstructural model obtained for these fine chromia sensors tested to propane. The

first is the comparison between how the fine chromia sensors respond to CO and propane. For ease of comparison the parameters obtained from both gases are plotted versus sintering temperature in Figure 5.28. The trends in the microstructural parameters with increasing sintering temperature are the same for CO and propane. The value of the sensitivity parameter also appears to decrease slightly with increasing sintering temperature for propane as with CO. However, from the form of this variation and its magnitude it could be argued that the value of the sensitivity parameter is almost constant. The reasons for these trends are the same as discussed above. The actual values of the parameters representing the surface are very similar for both gases. The parameter representing the bulk is fairly similar for the two gases, although for the propane it is slightly higher. These observations tend to agree with the thought that the microstructural parameters should be invariant of chemistry of response. However, the parameter representing the particle boundaries is much higher for propane than for CO. As for the earlier comparison between CO and propane for the sensors made from coarse chromia material, this could be due to the difference in the degree to which the steady state response is approached in the responses to CO and propane. There may also be a contribution to these differences in a similar manner from the shorter gas exposure used for the CO tests. The actual values for the sensitivity parameter are slightly higher overall for propane than CO which may be expected from the noted higher sensitivity to propane than CO. On the whole these observations are the same as was noted in the comparison between CO and propane response for the sensors made from coarse chromia material.

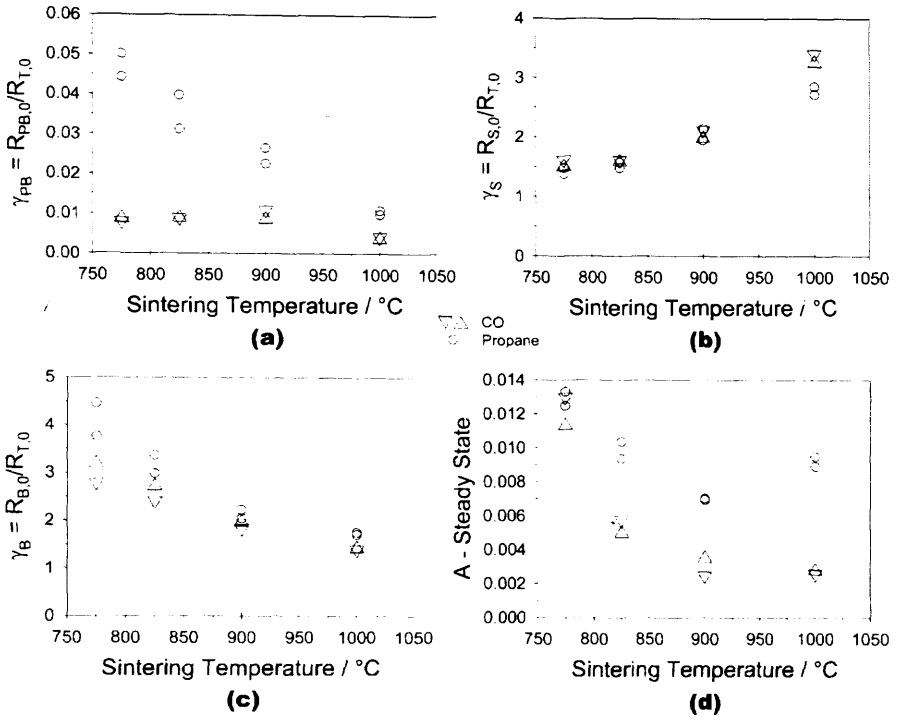

Figure 5.28 Comparison of parameters obtained from CO and propane tests on sensors constructed from fine grained raw material

The second comparison to be made is between the propane tests on sensors made from fine chromia material with those made from coarse chromia material. For ease of comparison the parameters obtained from the solutions to the microstructural model for these tests are plotted in Figure 5.29. As with the comparison above of the parameters obtained from the CO tests on sensors derived from fine chromia and coarse chromia, it is remarkable how close the values are considering the significant differences in particle size. In fact, the only significant difference between the parameters obtained for fine chromia and coarse chromia sensors in the propane tests occurs in the value for the parameter representing the particle boundaries which is higher for the finer fine chromia material than the coarse chromia. As discussed above for the CO results this is most likely to be due to the much greater integration between neighbouring particle that was observed for coarse chromia sensors resulting in an increase in the effective cross sectional area of the particle boundaries and their decreased contribution to resistance in this material.

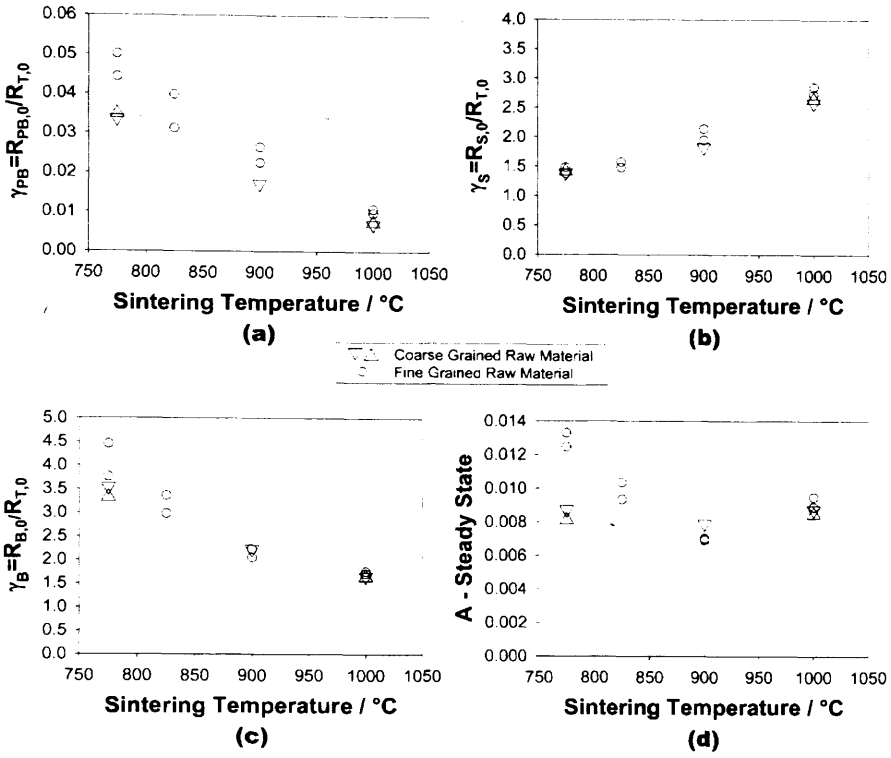

Figure 5.29 Comparison of parameters obtained from the solutions to the microstructural model from the propane tests for sensors derived from coarse and fine grained chromia raw material

The fact that the values and trends with sintering temperature of the sensitivity parameter, A, found from the transient data match those obtained from the steady state data means the two methods results corroborate again. The slight decreasing trend of the sensitivity parameter with increasing sintering temperature could be deemed not particularly significant compared to the changes in the parameter that have been observed in other situations. As with the similarly stable value found for the tests to propane on sensors derived from coarse chromia material this could identify a difference that occurs between different gases tested. This stable value for propane on sensors derived from fine chromia material could be a result of the same reasons that were given for the results on this other material. The apparent decreasing trend with increasing concentration may in part be due to the offset in the baseline predicted by the steady state solutions from its proper value. This offset gradually becomes more and more insignificant compared to the magnitude of the response at higher concentrations. The degree of variation of the obtained solution from the 'true' solution therefore could become less and the parameter's value could stabilise at higher concentrations, as is observed. The trend in the value of the time

constant, τ, with concentration and with increasing sintering temperature is also likely to be due to the same baseline offset factor.

5.2.5 Conclusions

The trends in the values of the microstructural parameters with sintering temperature are identical to those observed for the CO tests on these sensors and for the sensors made from coarse chromia material. Again, these trends can be related to the microstructural changes that result from the different sintering conditions. Similar observations are made of the trends in the values of the parameter in the comparison between CO and propane results in the cases of sensors made from the two materials. The comparison between the propane results for the two materials shows similarities to the comparison made between the CO results for the two materials.

6 Effect of Different Operating Temperatures and Lengths of Gas Exposure on Response of Sensors Derived From Fine Chromia Material to Carbon Monoxide

This chapter details the results of tests on nominally identical sensors produced from the same batch of sensors that was used to produce the sensors whose results are presented in chapter 5. These sensors were all sintered at 775°C but were operated at three different temperatures, 350, 400 and 450°C, with gas exposures of 1800 second duration. These tests were performed to investigate the effects of sensor temperature on response and how the microstructural model accounts for these changes. It was also envisioned that the sensor response could be calculated from the response data obtained at different times to see what was the effect of gas exposure length on the solutions obtained to the microstructural model and the parameters representing the microstructure and response of the sensors.

6.1 Gas Exposure Transients

To show the effect of the length of the gas exposure, tests were performed with a gas exposure of 1800 seconds. The transients presented in Figure 6.1 are taken from the first 600 seconds of these responses. The transients presented in Figure 6.2 display all data obtained in the 1800 second exposures. The magnitude of the responses decreases with increasing temperature. The degree to which the steady state response is approached is seen to vary quite dramatically in these results. The responses of the sensors operated at the low temperature of 350°C are obviously quite far from approaching the steady state. Those for the sensors operated at 450°C appear as though the steady state response has been attained. The responses on the sensor operated at 400 °C are intermediate between these extremes.

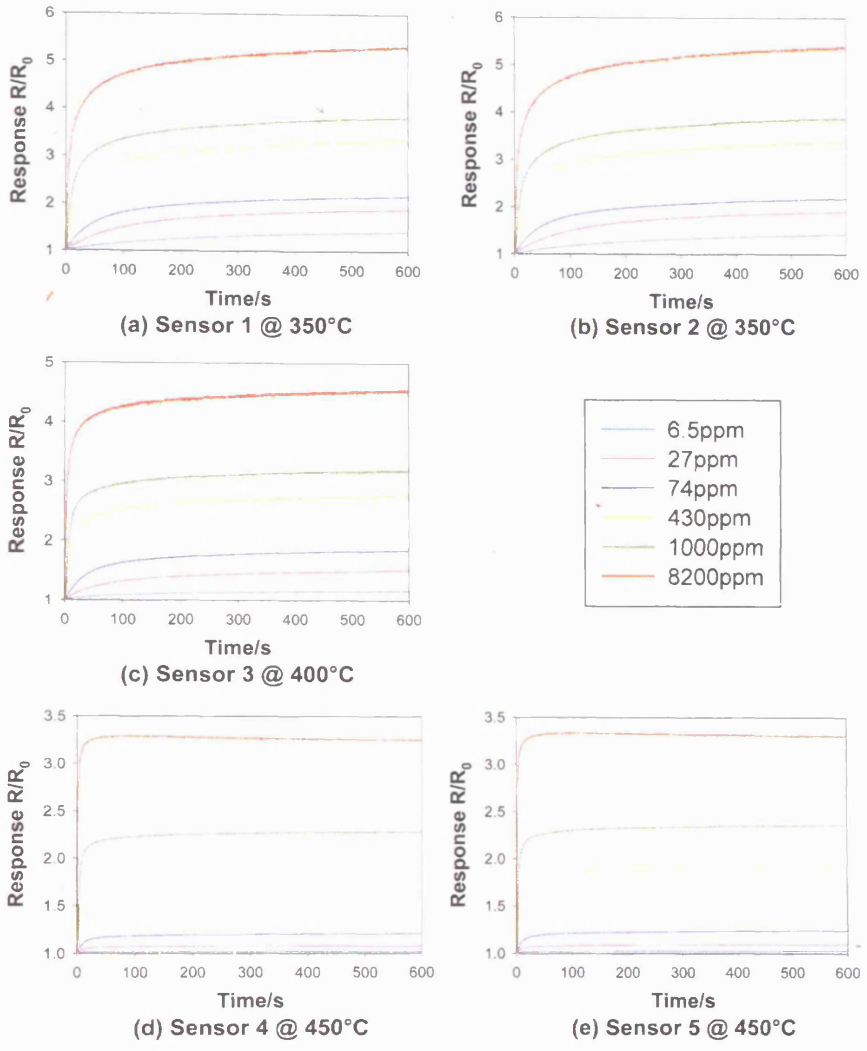

Figure 6.1 Response versus time plots to 600 seconds for CO tests on sensors made from fine chromia material sintered at 775°C and operated at different temperatures. The degree to which the steady state response is approached increases with increased operating temperature. The responses at an operating temperature of 450°C appear particularly close to the steady state. The magnitude of response is decreased with increasing operating temperature.

The response transients to 1800 seconds in Figure 6.2 are, by nature, very similar to those above for the 600 second exposures in Figure 6.1. The same trends with operating temperature are observed. The responses at 1800 seconds approach the steady state only slightly more closely than those for the 600 second exposures.

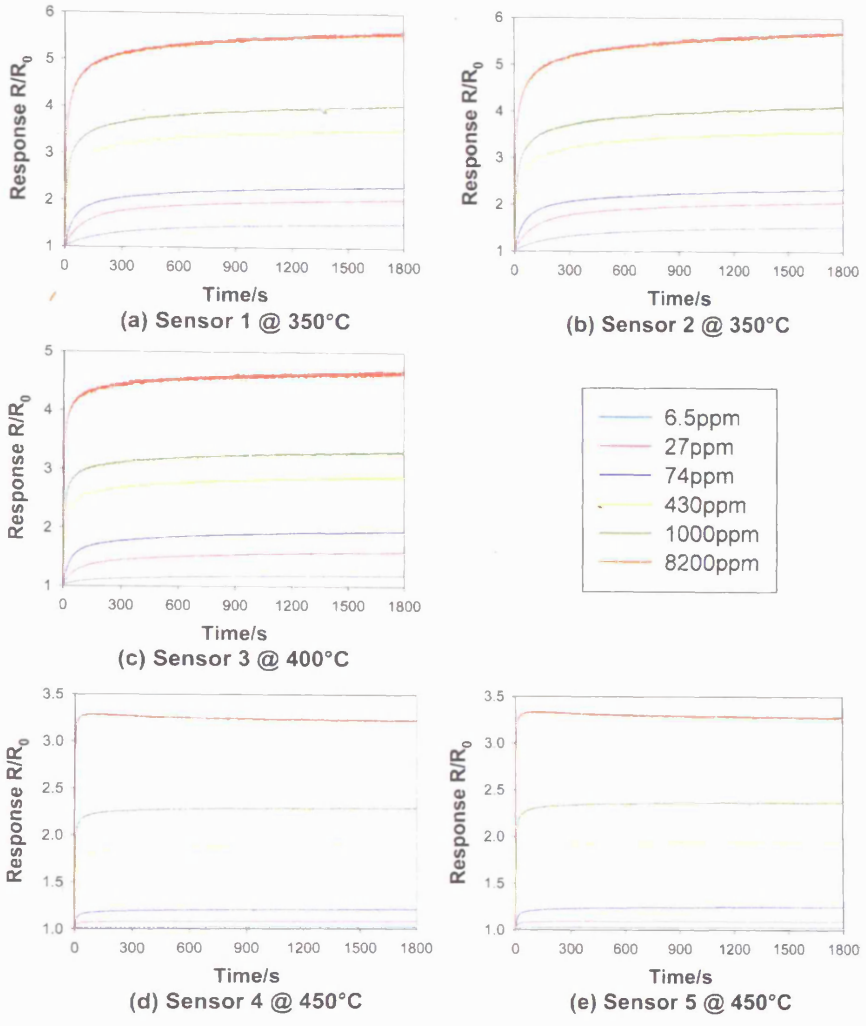

Figure 6.2 Response versus time plots to 1800 seconds for CO tests on sensors made from fine chromia material sintered at 775°C and operated at different temperatures. These are the same responses as in Figure 6.1. The magnitude of response decreases with increasing operating temperature. The degree to which the steady state response is approached increases with increasing operating temperature. There is only a slight increase in the degree to which the steady state response is approached in the extended gas exposures here compared with the shorter 600 second exposures above.

6.2 Solutions to the Model – Steady State Gas Response

Figure 6.3 shows plots of the experimental response data for gas exposures of 600 and 1800 second duration. At the lower operating temperature of 350°C there is quite a large gap between the responses at 600 seconds and those at 1800 seconds. For the sensors operated at higher temperatures this gap diminishes until at 450 °C the data appears to overlap. The fit of the solutions to the traditional square root model of response to the experimental data are poor compared to those for the

microstructural model. The fit of the solutions to the microstructural model to the experimental data are very good at the highest operating temperature of 450 °C and dimishes only slightly for the sensors operated at lower temperatures. As may be expected from the noted differences in the experimental data for the different gas exposure times, the solutions to the microstructural model for the different exposure times are slightly different in each case according to how the responses themselves vary.

The values of the microstructural parameters displayed in Figure 6.4 show very little variation with operating temperature. The values for the different gas exposure times are also very similar. The value of the sensitivity parameter, A, is shown in the same diagram to be highly dependent on operating temperature. The value of sensitivity parameter is noticeably higher for the exposure to 1800 seconds, particularly for sensors operated at the lower temperatures of 350 and 400°C. In comparison to the earlier CO tests on sensors derived from fine chromia material, shown in Figure 5.3, the values of the parameters for the sensor operated here at 400°C are approximately the same as those in the earlier tests.

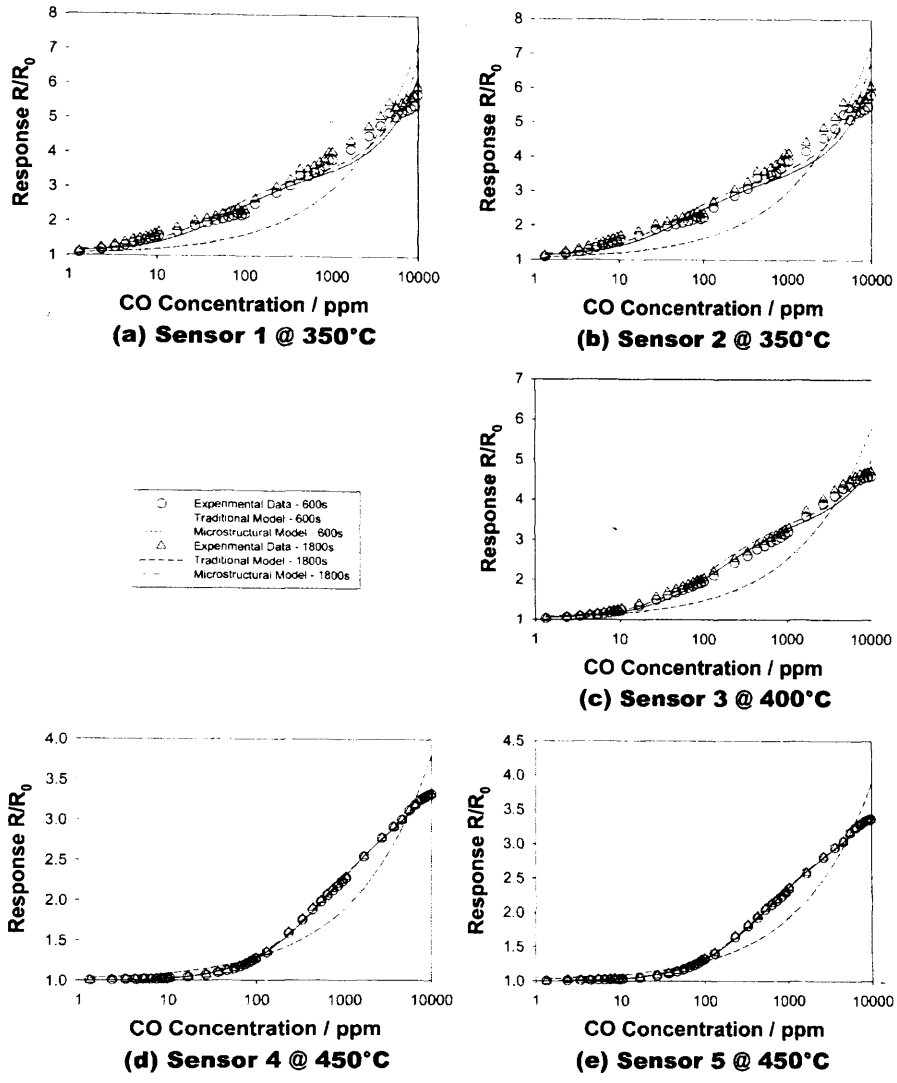

Figure 6.3 Response plotted versus CO concentration for CO tests on sensors made from fine chromia material sintered at 775°C and operated at different temperatures. The responses obtained from both lengths of gas exposure are plotted as circles (600 second exposure) and triangles (1800 second exposure). The large difference between the two sets of experimental data for the sensor operated at 350°C is an indication that these responses are quite far away from the steady state. The points for the responses for the sensors operated at higher temperatures, particularly at 450°C, are virtually on top of one another indicating the steady state has practically been achieved. The solutions to the traditional square root model represent fairly poor fits to the experimental data. The fits to the microstructural model are excellent in comparison to the traditional model. The degree to which the solutions to the microstructural model fit the experimental data increases with increasing operating temperature. The solutions to the microstructural model for the different lengths of exposure are quite far apart for sensors operated at low temperatures, 350 and 400°C, and are practically identical for those operated at high temperature, 500°C.

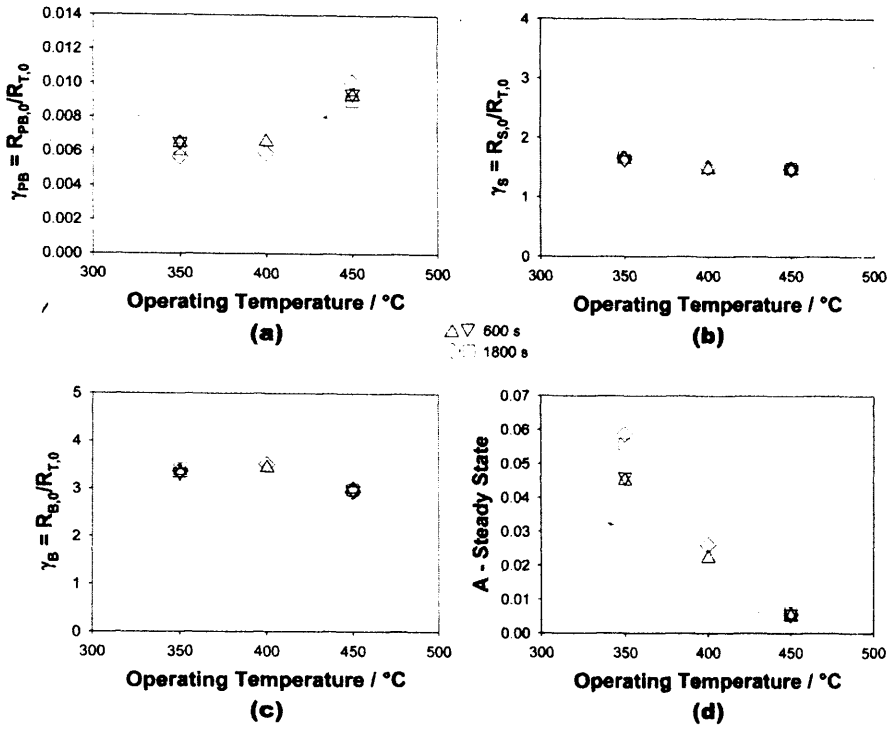

Figure 6.4 Parameters obtained from the solutions to the microstructural model for gas exposure times of 600 and 1800 seconds plotted versus operating temperature for CO tests on sensors made from fine chromia material sintered at 775°C and operated at different temperatures. With the exception of chart (d) for the sensitivity parameter, A, these charts are plotted with similar scales on the ordinate axis as was used for the CO tests on fine chromia material sintered at different temperatures presented in Figure 5.3 for ease of comparison. Generally, the values of the parameters for the sensor operated here at 400°C are the same as those in Figure 5.3 for the sensor sintered at 775°C. Furthermore, the values of the microstructural parameters here are relatively constant with operating temperature. The value for the sensitivity parameter, A, is heavily dependent on operating temperature showing a strong decreasing trend with increasing operating temperature. This is consistent with the observed decrease in magnitude of response with increasing operating temperature noted in Figure 6.1, Figure 6.2 and Figure 6.3. The values of the parameters obtained for the different lengths of gas exposure are very similar with the largest differences noted in the value of the sensitivity parameter.

6.3 Solutions to the Model – Transient Gas Response

The charts of the values of the sensitivity parameter, A, and the time constant, τ, for the 600 second exposure to CO on these sensors derived from fine chromia material and operated at different temperatures are displayed in Figure 6.5 and Figure 6.6. The value of the sensitivity parameter, A, is proved to be repeatable between different sensors and also to show a strong decreasing trend with increasing operating temperature. The sensors operated at 400 and 450°C do not show any clear trend in their values of the sensitivity parameter with concentration and the values

are essentially constant. The value of the sensitivity parameter, A, obtained for the sensors operated at 350°C could either be interpreted as displaying a decreasing trend with increasing concentration or a fairly constant value with sintering temperature if the significant variability between the values obtained is taken into account. The value of the time constant, τ, is also proved to be repeatable between different sensors and also to show a strong decreasing trend with increasing operating temperature. The value of the time constant, τ, obtained for the sensors operated at 350°C show either a decreasing trend with increasing concentration or a constant value taking into account the variability between values. The value of the time constant, τ, obtained for the sensor operated at 400°C appears to display a clear decreasing trend with increasing sintering temperature. The value of the time constant, τ, obtained for the sensors operated at 450°C display a humped dependence on concentration, at first increasing and then decreasing with increasing concentration. The charts of the values of the sensitivity parameter, A, and the time constant, τ, for the longer 1800 second exposure to CO on these sensors derived from fine chromia material and operated at different temperatures are displayed in Figure 6.7 and Figure 6.8. These essentially display the same trends of the values with the different conditions. However, the magnitudes of the values obtained for the sensitivity parameter, A, are generally the same for the two lengths of exposure whilst the values obtained for the time constant, τ, are generally slightly higher for the exposures of 1800 seconds length.

The plots of the experimental transient data to 600 seconds, as the black lines, and the solutions to the model obtained at the different concentrations, the coloured lines, are displayed in Figure 6.9, Figure 6.10, Figure 6.11, Figure 6.12 and Figure 6.13 for the sensors operated at different temperatures. The plots of the experimental transient data to 1800 seconds, as the black lines, and the solutions to the model obtained at the different concentrations, the coloured lines, are displayed in Figure 6.14, Figure 6.15, Figure 6.16, Figure 6.17 and Figure 6.18 for the sensors operated at different temperatures. As with all other tests that have been conducted, the solution obtained for a particular solution fits the experimental data for that concentration very well and does not fit the experimental data for other concentrations quite as well. Generally, the degree to which the other solutions fit the data for a particular concentration increases with increased concentration and with increased operating

temperature. Again, all the baselines predicted from the solutions to the steady state data are offset from their proper positions.

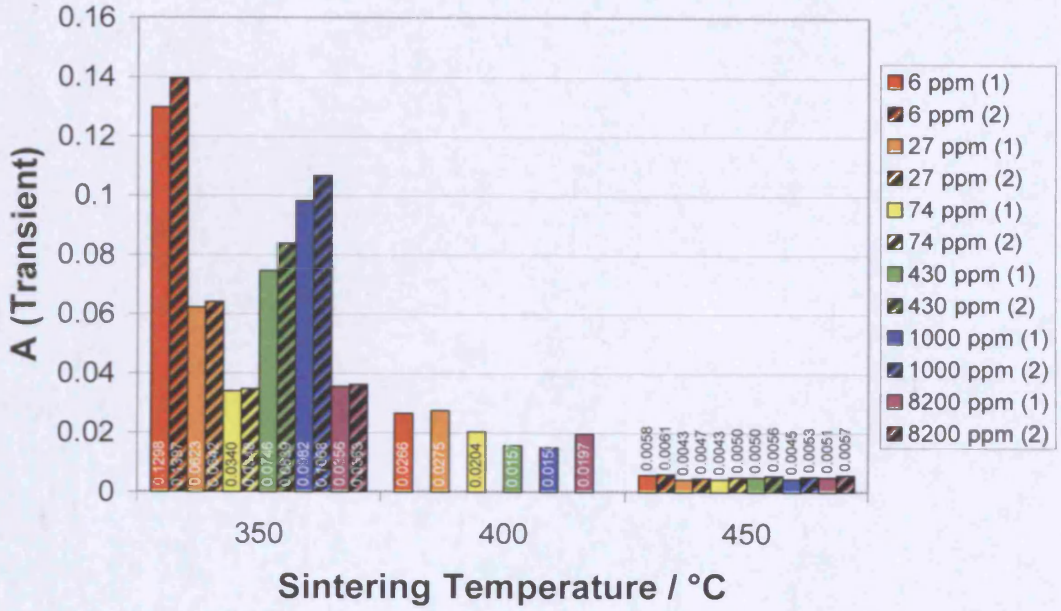

Figure 6.5 Bar chart of the sensitivity parameter, A, obtained at different gas concentrations from the solutions of the transient data over 600 seconds to the microstructural model for CO tests on sensors made from fine chromia material sintered at 775°C

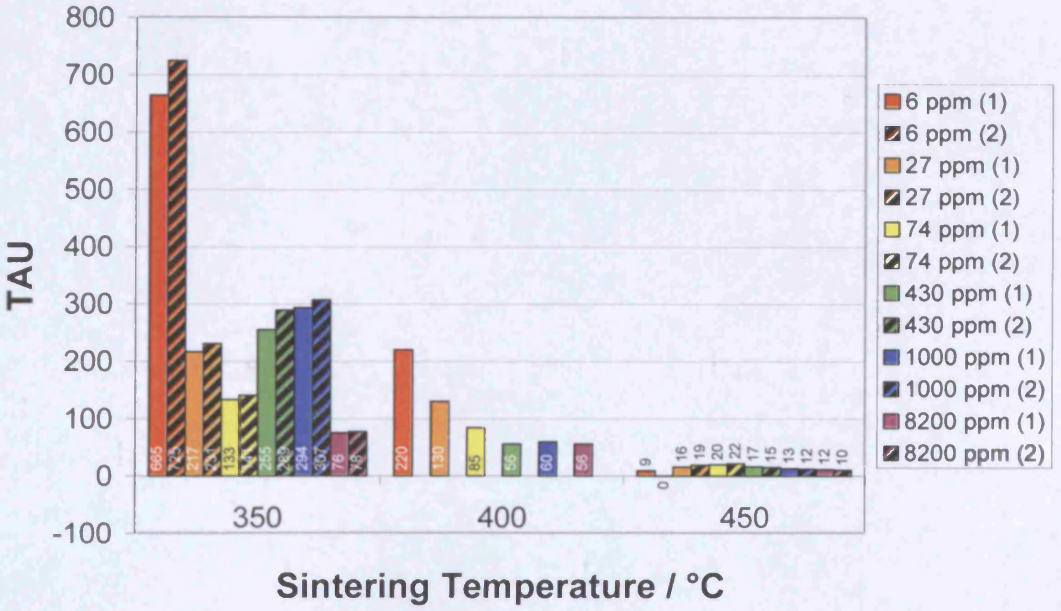

Figure 6.6 Bar chart of the time constant, τ, obtained at different gas concentrations from the solutions of the transient data over 600 seconds to the microstructural model for CO tests on sensors made from fine chromia material sintered at 775°C

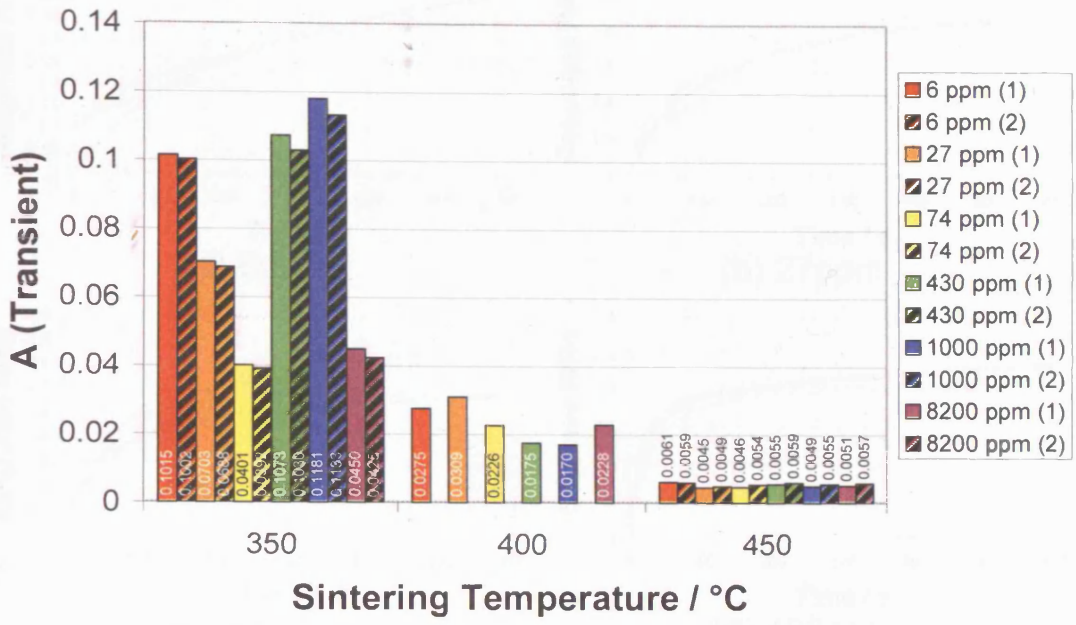

Figure 6.7 Bar chart of the sensitivity parameter, A, obtained at different gas concentrations from the solutions of the transient data over 1800 seconds to the microstructural model for CO tests on sensors made from fine chromia material sintered at 775°C

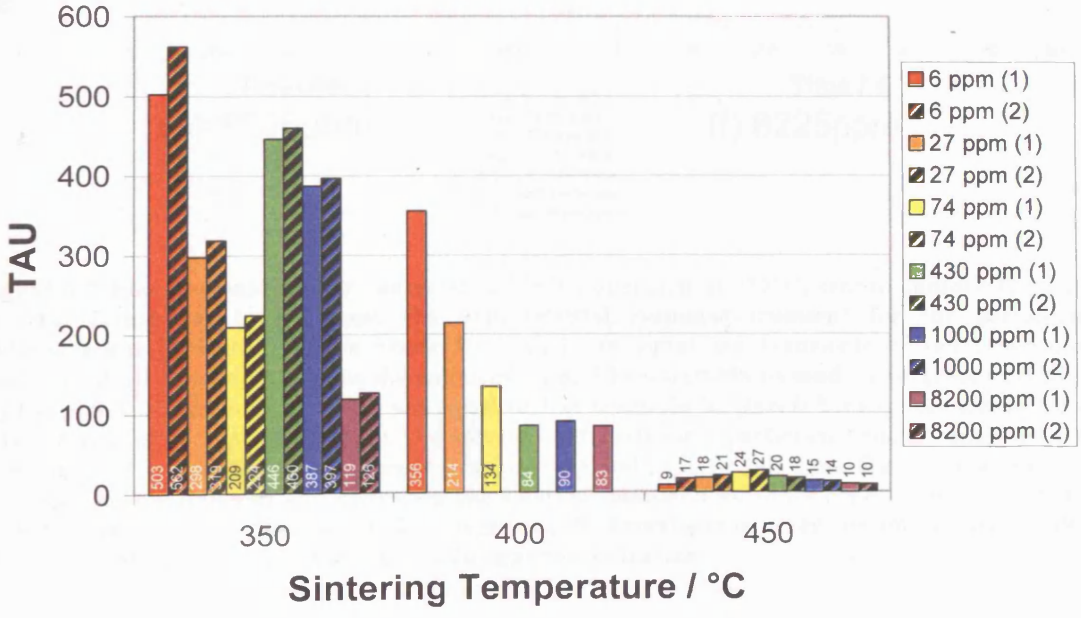

Figure 6.8 Bar chart of the time constant, τ, obtained at different gas concentrations from the solutions of the transient data over 600 seconds to the microstructural model for CO tests on sensors made from fine chromia material sintered at 775°C

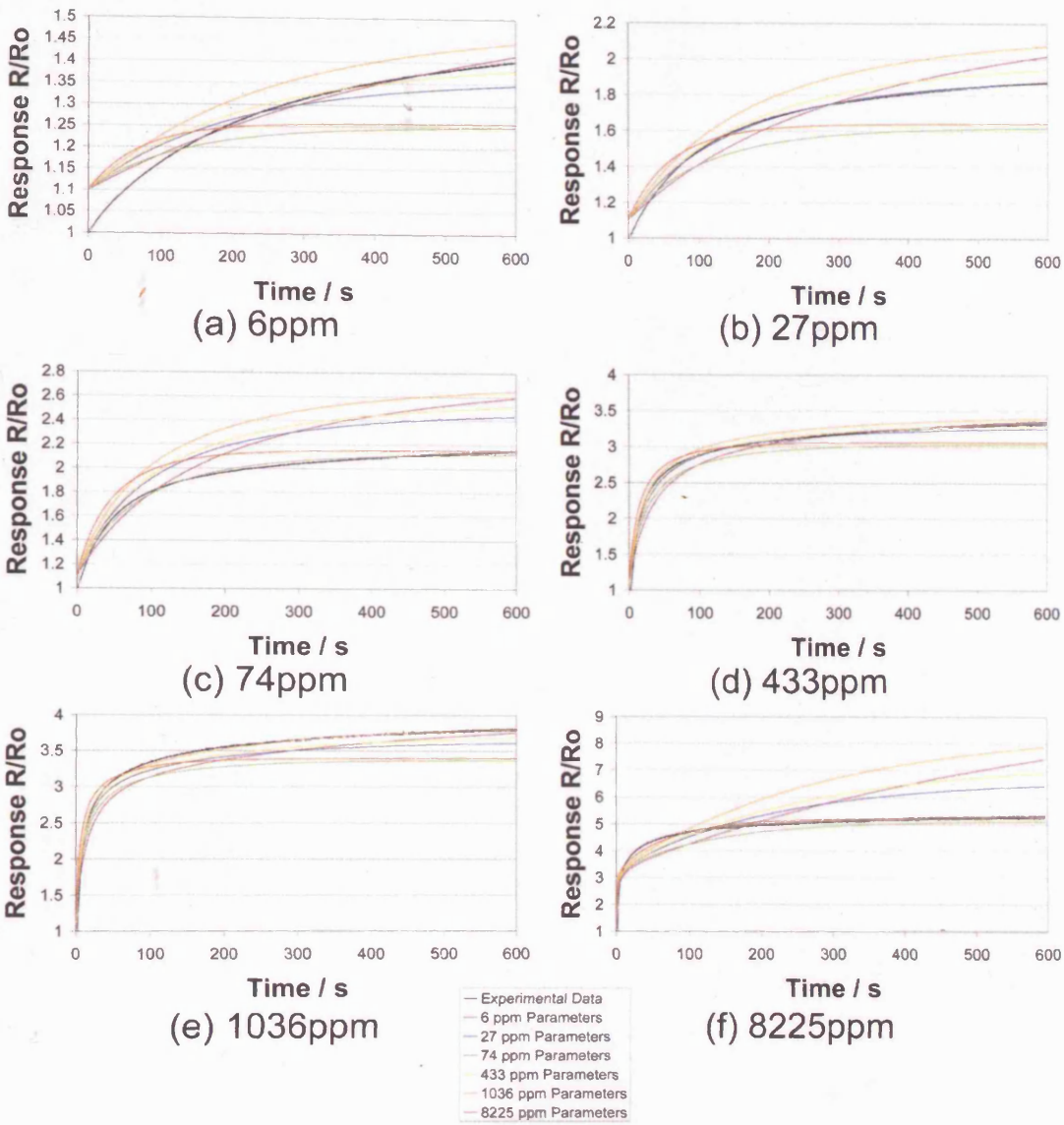

Figure 6.9 Fine chromia sensor, sintered at 775°C, operated at 350°C, sensor number 1, tested to CO. Chart (a) to (f) show the experimental response transient for the particular concentration indicated as the black lines and the simulated transients of the regression solutions of all concentrations as the coloured lines. The observations made from these data are: (1) Response of solutions at t=0 is not equal to 1 as it should be (this is because the steady state solution is slightly inaccurate); (2) The solution obtained for a particular concentration fits the experimental transient for that concentration very well; (3) In this case, for an experimental transient for a particular concentration the solutions obtained for other concentrations do NOT fit particularly well in general; (4) The degree of fit of solutions to other concentrations initially improves and then worsens with increasing gas concentration

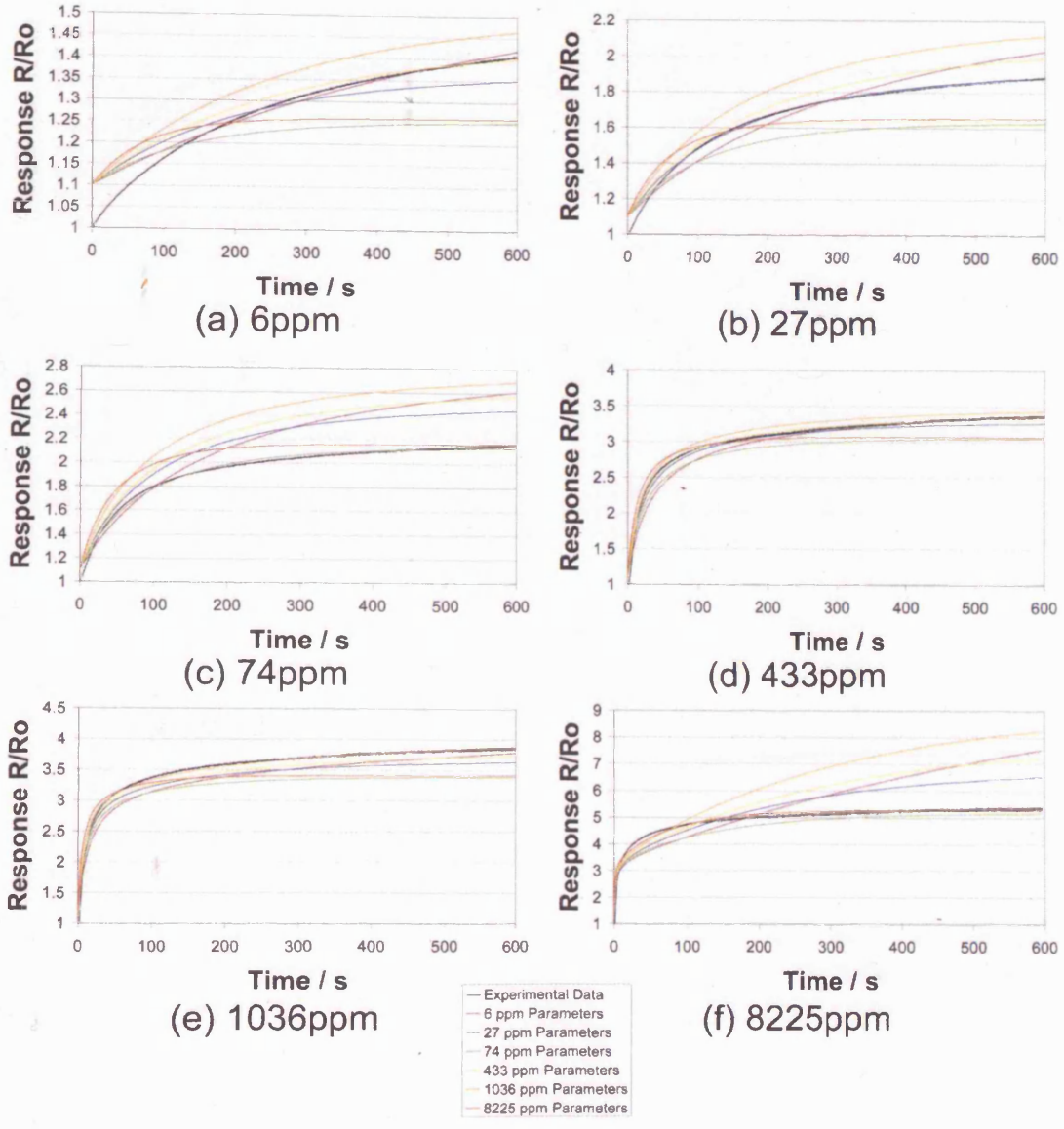

Figure 6.10 Fine chromia sensor, sintered at 775°C, operated at 350°C, sensor number 2, tested to CO. Chart (a) to (f) show the experimental response transient for the particular concentration indicated as the black lines and the simulated transients of the regression solutions of all concentrations as the coloured lines. The observations made from these data are: (1) Response of solutions at t=0 is not equal to 1 as it should be (this is because the steady state solution is slightly inaccurate); (2) The solution obtained for a particular concentration fits the experimental transient for that concentration very well; (3) In this case, for an experimental transient for a particular concentration the solutions obtained for other concentrations do NOT fit particularly well in general; (4) The degree of fit of solutions to other concentrations initially improves and then worsens with increasing gas concentration

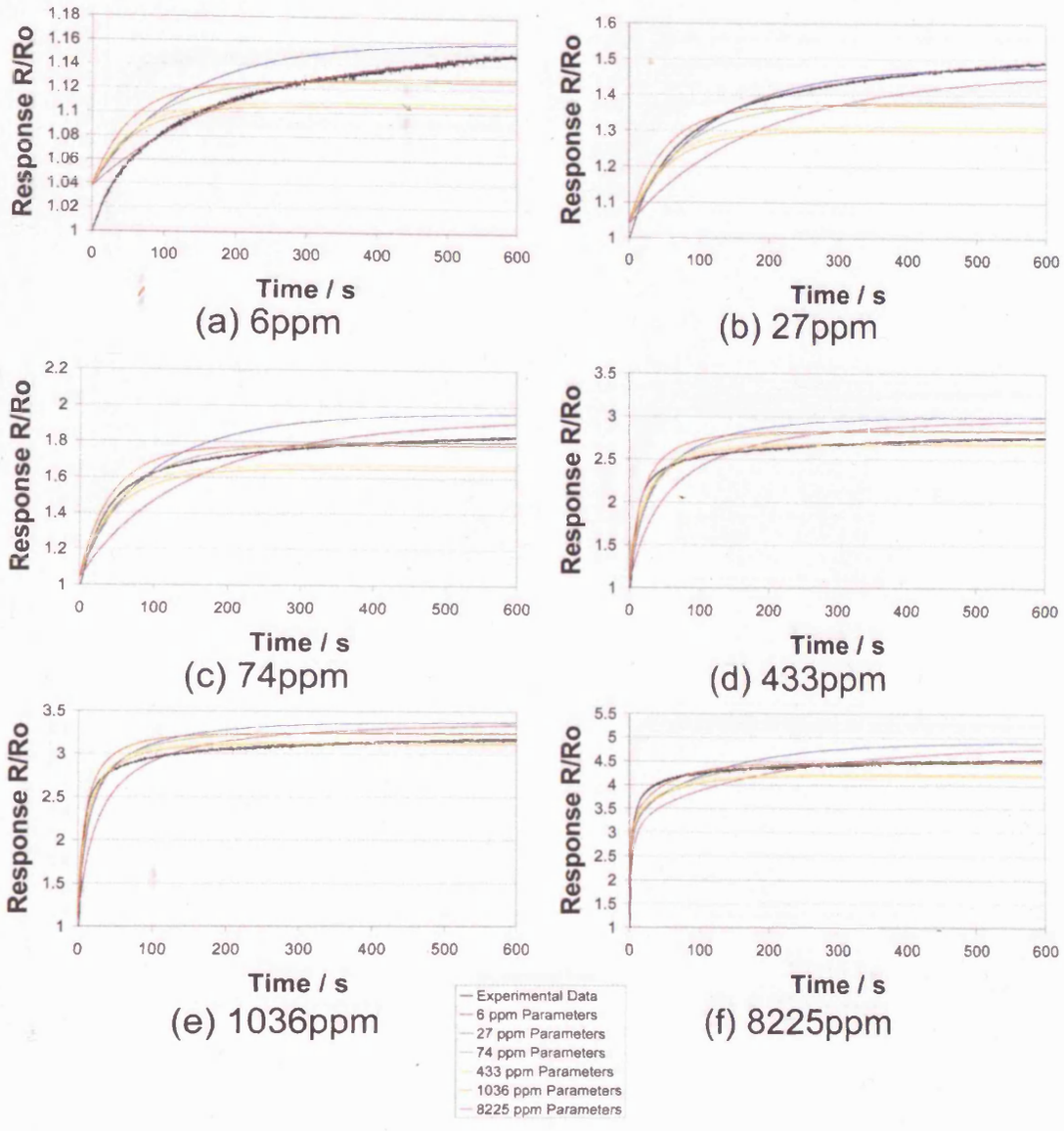

Figure 6.11 Fine chromia sensor, sintered at 775°C, operated at 400°C, sensor number 1, tested to CO. Chart (a) to (f) show the experimental response transient for the particular concentration indicated as the black lines and the simulated transients of the regression solutions of all concentrations as the coloured lines. The observations made from these data are: (1) Response of solutions at t=0 is not equal to 1 as it should be (this is because the steady state solution is slightly inaccurate); (2) The solution obtained for a particular concentration fits the experimental transient for that concentration very well; (3) In this case, for an experimental transient for a particular concentration the solutions obtained for other concentrations do NOT fit particularly well in general; (4) The degree of fit of solutions to other concentrations improves with increasing gas concentration

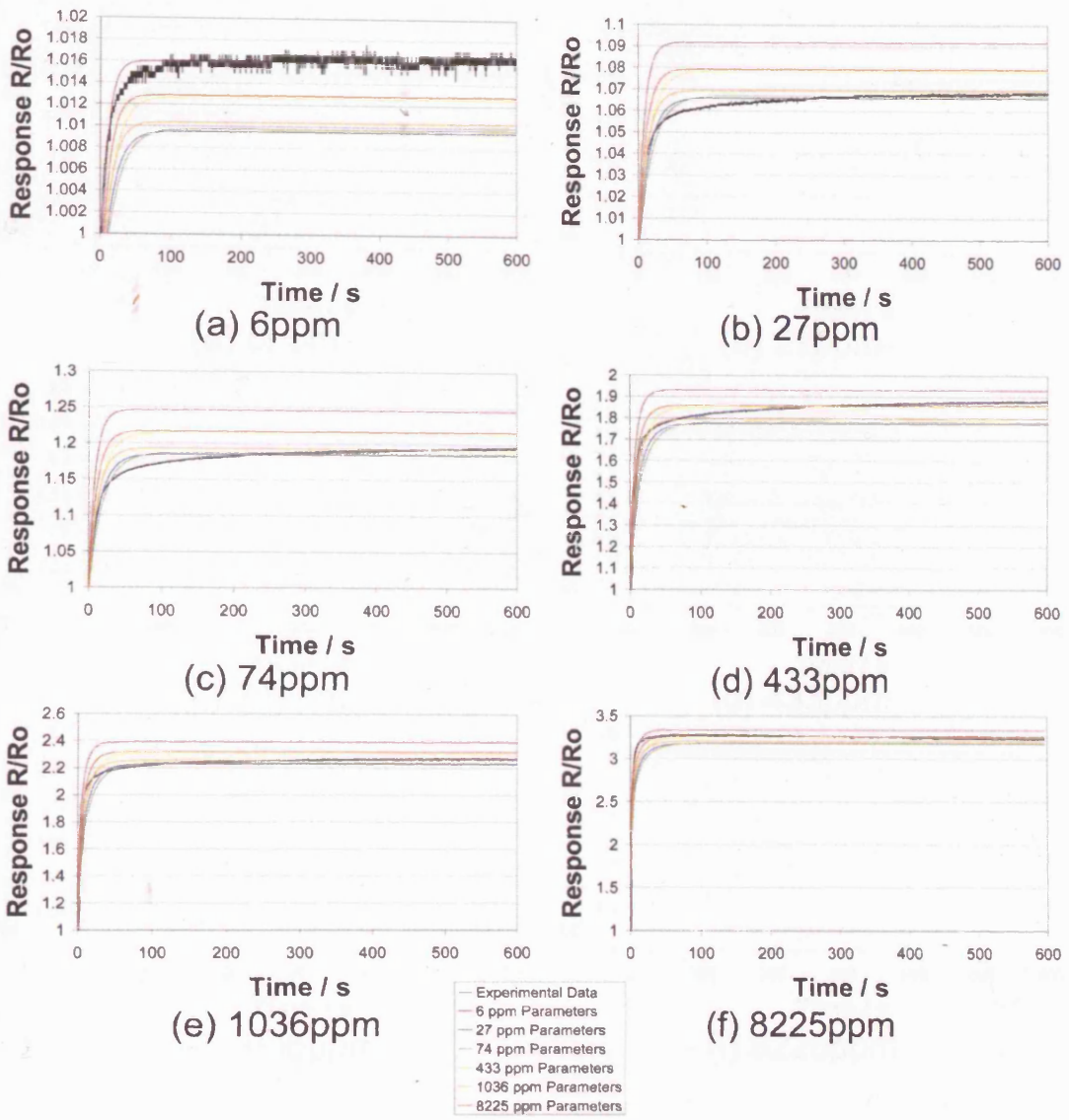

Figure 6.12 Fine chromia sensor, sintered at 775°C, operated at 450°C, sensor number 1, tested to CO. Chart (a) to (f) show the experimental response transient for the particular concentration indicated as the black lines and the simulated transients of the regression solutions of all concentrations as the coloured lines. The observations made from these data are: (1) Response of solutions at t=0 is not equal to 1 as it should be (this is because the steady state solution is slightly inaccurate); (2) The solution obtained for a particular concentration fits the experimental transient for that concentration very well; (3) In this case, for an experimental transient for a particular concentration the solutions obtained for other concentrations DO, generally, fit well; (4) The degree of fit of solutions to other concentrations improves substantially with increasing gas concentration

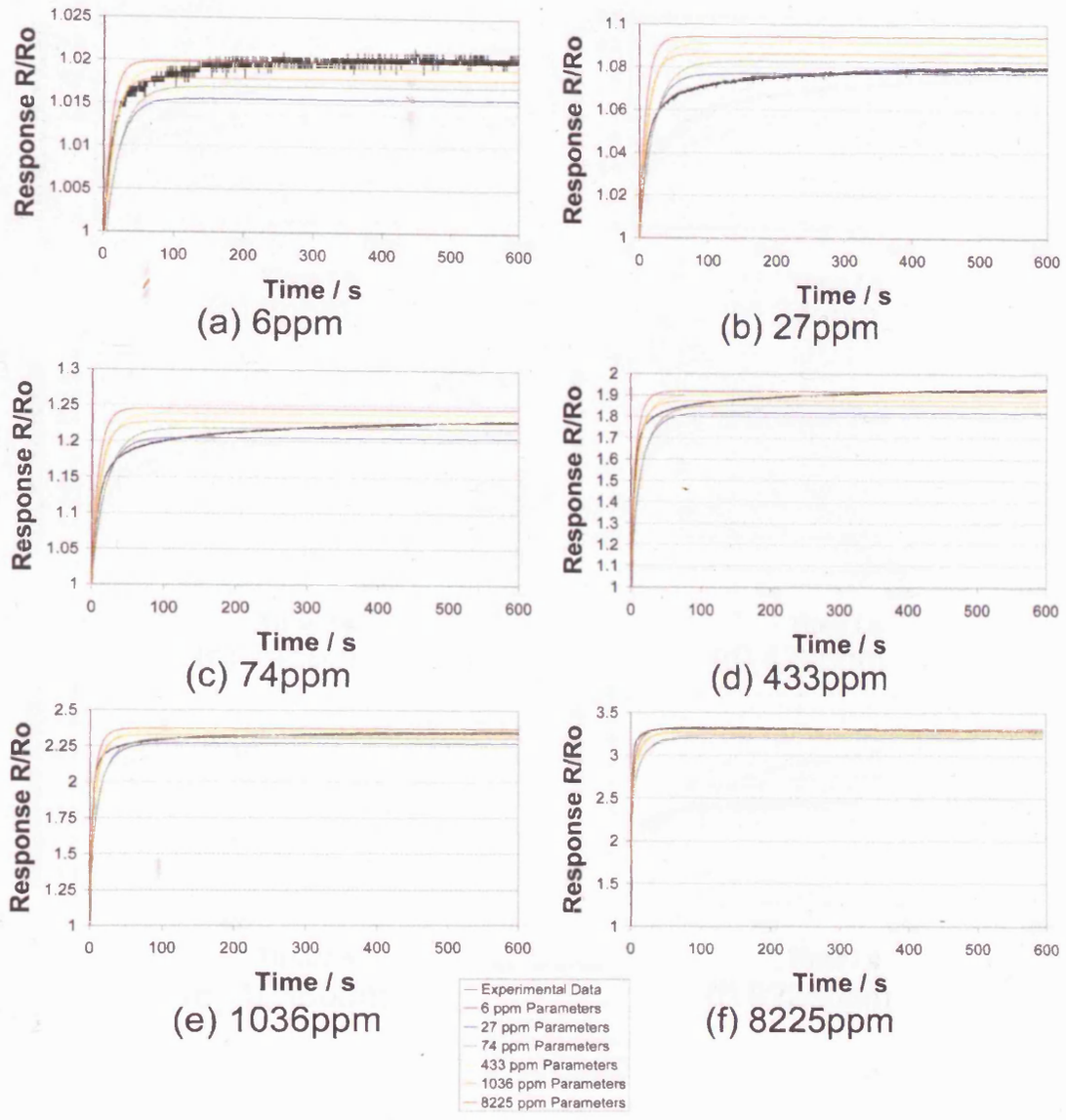

Figure 6.13 Fine chromia sensor, sintered at 775°C, operated at 450°C, sensor number 2, tested to CO. Chart (a) to (f) show the experimental response transient for the particular concentration indicated as the black lines and the simulated transients of the regression solutions of all concentrations as the coloured lines. The observations made from these data are: (1) Response of solutions at t=0 is not equal to 1 as it should be (this is because the steady state solution is slightly inaccurate); (2) The solution obtained for a particular concentration fits the experimental transient for that concentration very well; (3) In this case, for an experimental transient for a particular concentration the solutions obtained for other concentrations DO, generally, fit well; (4) The degree of fit of solutions to other concentrations improves substantially with increasing gas concentration

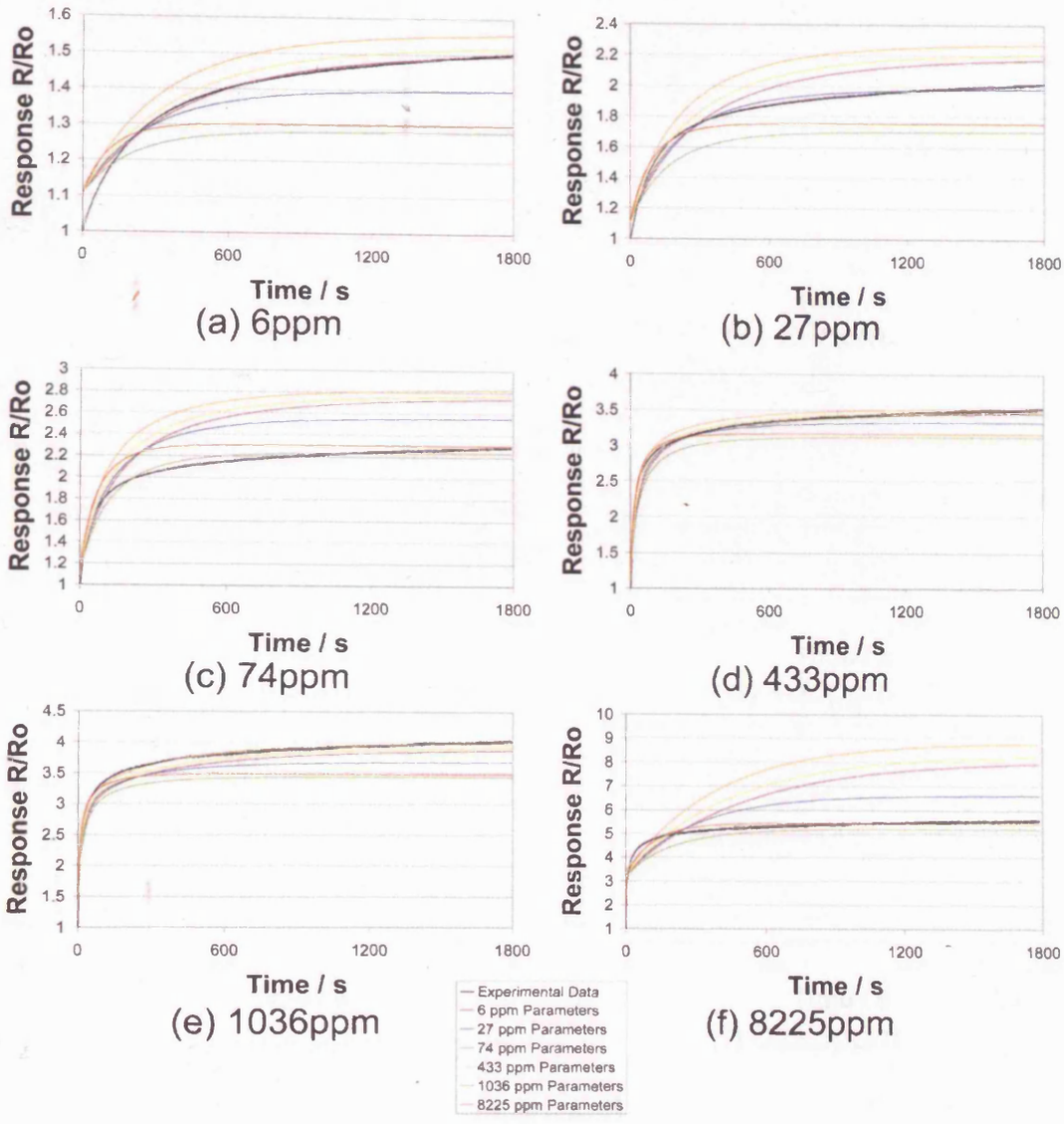

Figure 6.14 Response transients for each concentration tested on the first sensor made from fine chromia material sintered at 775°C and operated at 350°C. The experimental data obtained from each gas data is plotted versus time after the start of gas exposure up to 1800 seconds as the black line for each of the different concentrations of CO tested in a separate chart, (a) to (f). As described in the text, each transient of experimental data is subjected to regression to the microstructural model. For the solutions presented here the regression was performed on the data up to 1800 seconds. This produces a solution to the model for each gas concentration tested. These solutions vary somewhat between tests. The parameters obtained from each solution are used to generate transients that are plotted as the coloured lines in each chart. The solution obtained for the each particular transient fits that transient best, as would be expected. The solutions obtained for the transients at other concentrations are very poor fits for a transient for a particular concentration.

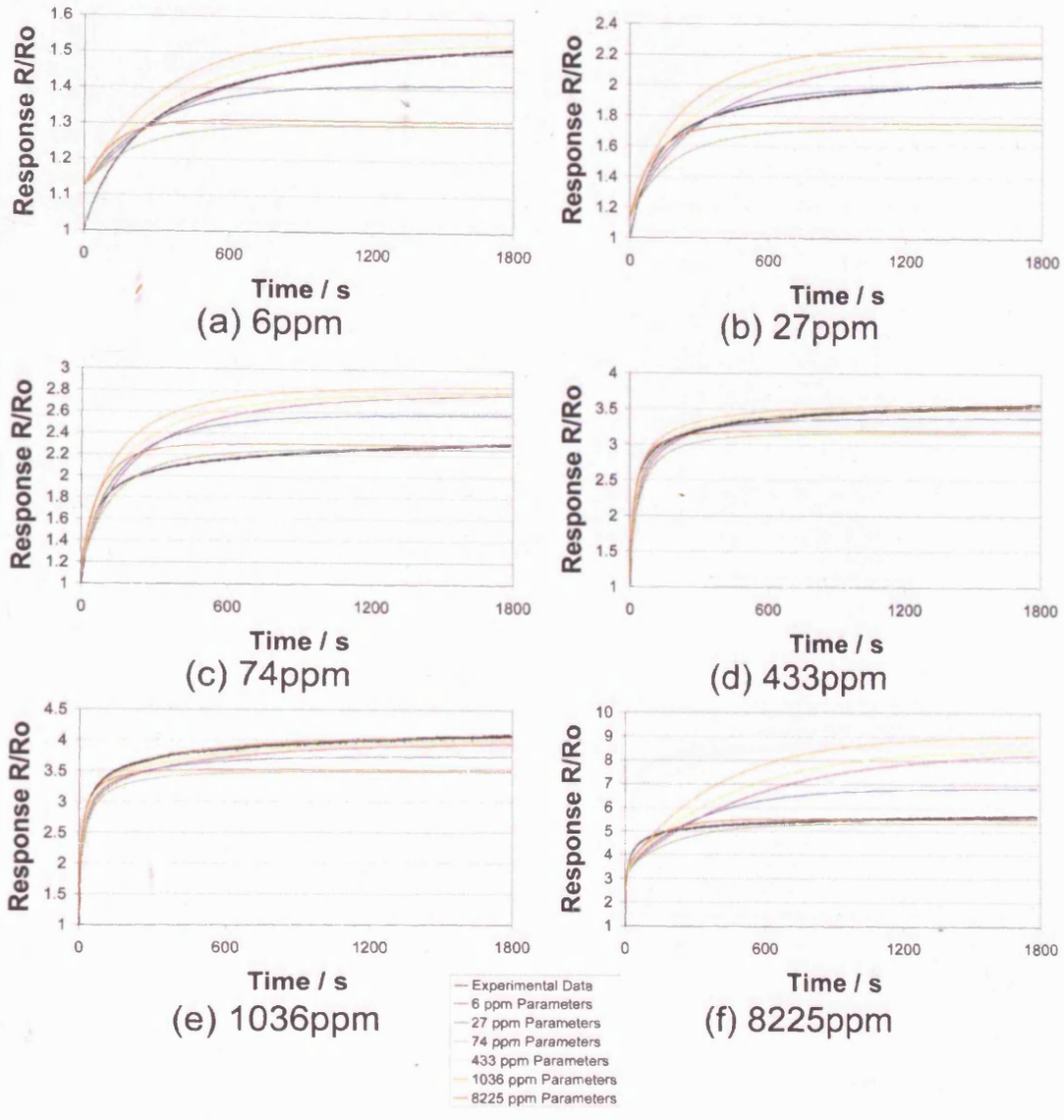

Figure 6.15 Response transients for each concentration tested on the second sensor made from fine chromia material sintered at 775°C and operated at 350°C. The experimental data obtained from each gas data is plotted versus time after the start of gas exposure up to 1800 seconds as the black line for each of the different concentrations of CO tested in a separate chart, (a) to (f). As described in the text, each transient of experimental data is subjected to regression to the microstructural model. For the solutions presented here the regression was performed on the data up to 1800 seconds. This produces a solution to the model for each gas concentration tested. These solutions vary somewhat between tests. The parameters obtained from each solution are used to generate transients that are plotted as the coloured lines in each chart. The solution obtained for the each particular transient fits that transient best, as would be expected. The solutions obtained for the transients at other concentrations are very poor fits for a transient for a particular concentration.

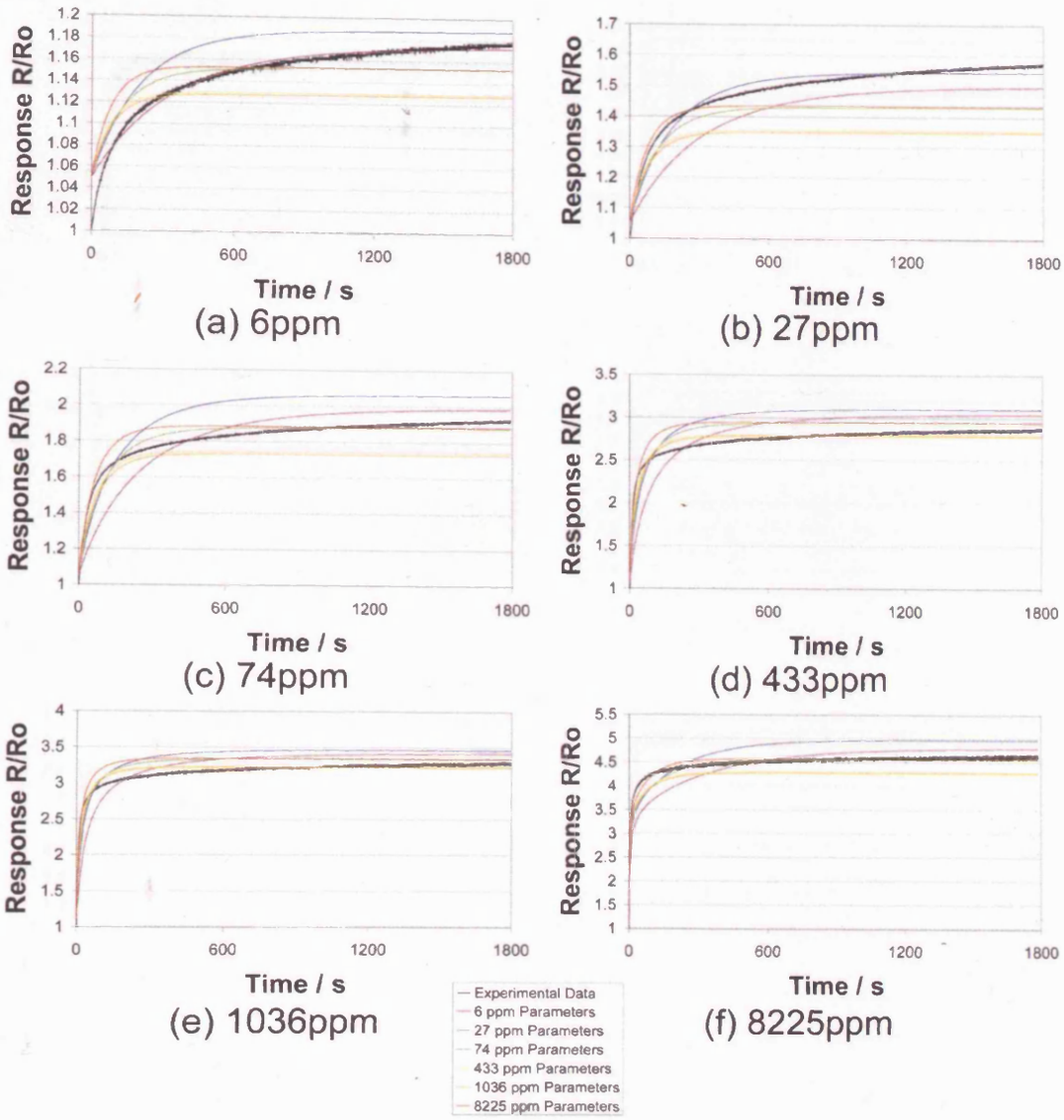

Figure 6.16 Response transients for each concentration tested on the only sensor made from fine chromia material sintered at 775°C and operated at 400°C. The experimental data obtained from each gas data is plotted versus time after the start of gas exposure up to 1800 seconds as the black line for each of the different concentrations of CO tested in a separate chart, (a) to (f). As described in the text, each transient of experimental data is subjected to regression to the microstructural model. For the solutions presented here the regression was performed on the data up to 1800 seconds. This produces a solution to the model for each gas concentration tested. These solutions vary somewhat between tests. The parameters obtained from each solution are used to generate transients that are plotted as the coloured lines in each chart. The solution obtained for the each particular transient fits that transient best, as would be expected. The solutions obtained for the transients at other concentrations are very poor fits for a transient for a particular concentration.

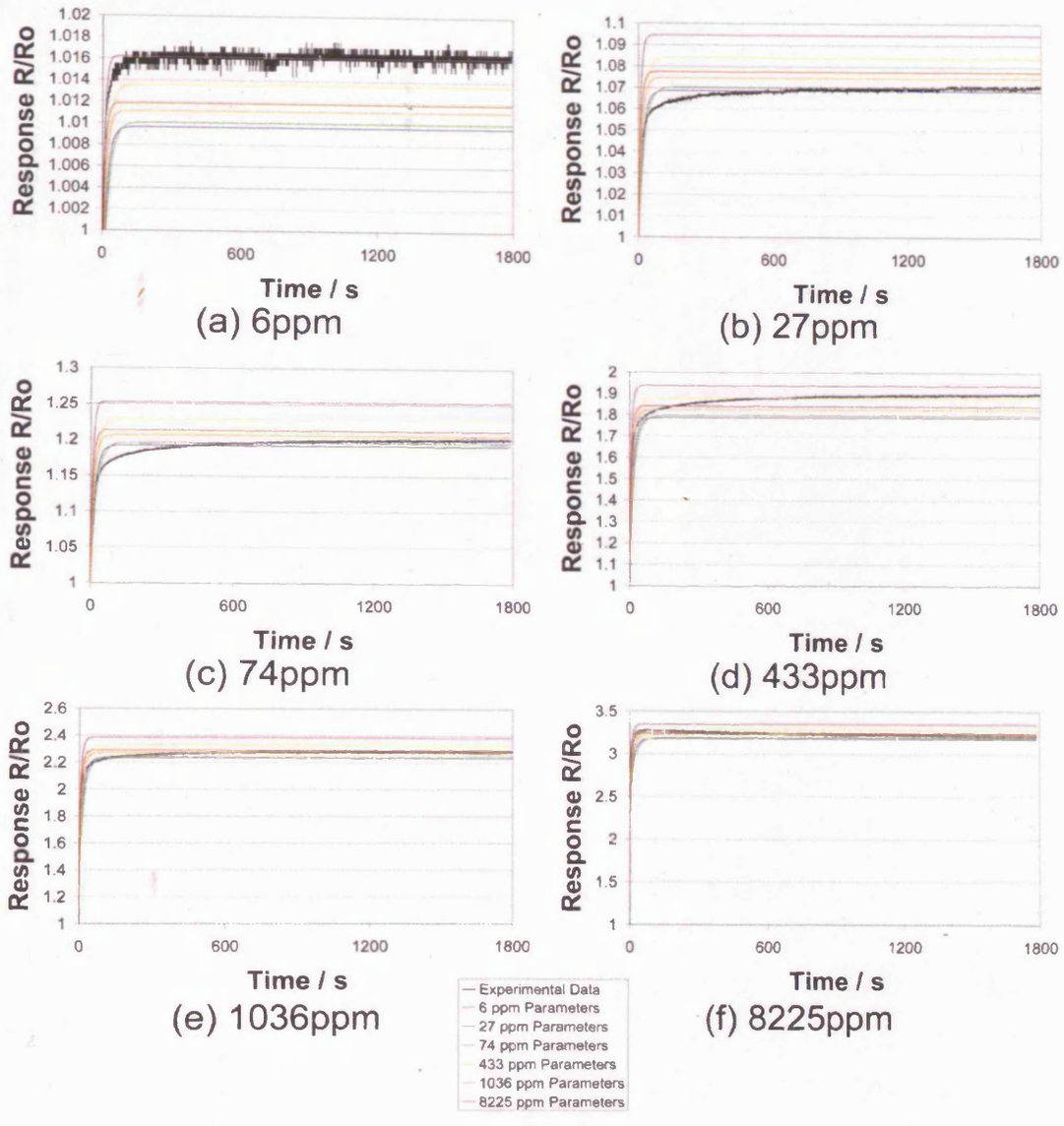

Figure 6.17 Response transients for each concentration tested on the first sensor made from fine chromia material sintered at 775°C and operated at 450°C. The experimental data obtained from each gas data is plotted versus time after the start of gas exposure up to 1800 seconds as the black line for each of the different concentrations of CO tested in a separate chart, (a) to (f). As described in the text, each transient of experimental data is subjected to regression to the microstructural model. For the solutions presented here the regression was performed on the data up to 1800 seconds. This produces a solution to the model for each gas concentration tested. These solutions vary somewhat between tests. The parameters obtained from each solution are used to generate transients that are plotted as the coloured lines in each chart. The solution obtained for the each particular transient fits that transient best, as would be expected. The solutions obtained for the transients at other concentrations are very poor fits for a transient for a particular concentration.

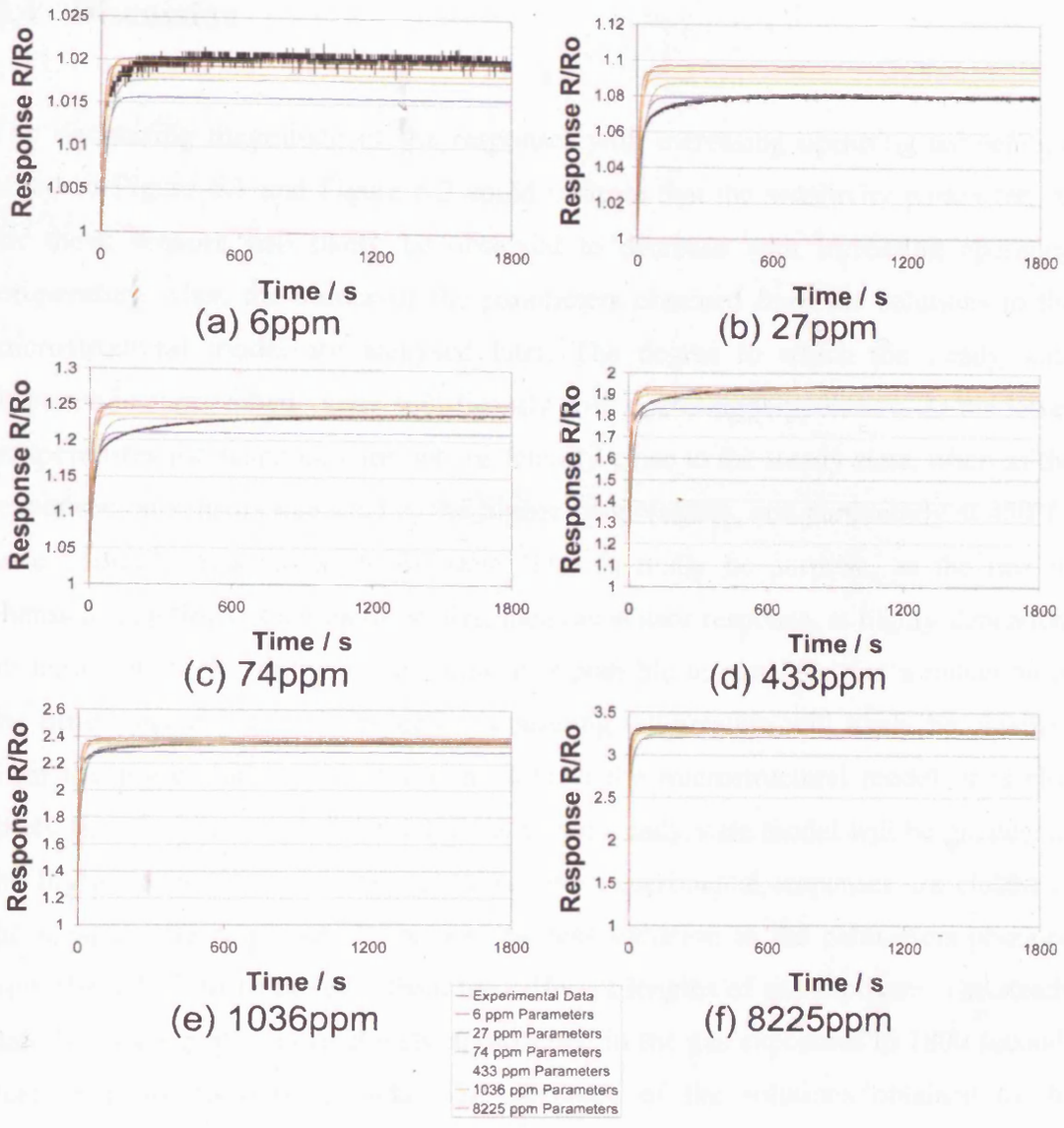

Figure 6.18 Response transients for each concentration tested on the second sensor made from fine chromia material sintered at 775°C and operated at 450°C. The experimental data obtained from each gas data is plotted versus time after the start of gas exposure up to 1800 seconds as the black line for each of the different concentrations of CO tested in a separate chart, (a) to (f). As described in the text, each transient of experimental data is subjected to regression to the microstructural model. For the solutions presented here the regression was performed on the data up to 1800 seconds. This produces a solution to the model for each gas concentration tested. These solutions vary somewhat between tests. The parameters obtained from each solution are used to generate transients that are plotted as the coloured lines in each chart. The solution obtained for the each particular transient fits that transient best, as would be expected. The solutions obtained for the transients at other concentrations are very poor fits for a transient for a particular concentration.

6.4 Discussion

The decreasing magnitude of the responses with increasing operating temperature noted in Figure 6.1 and Figure 6.2 could indicate that the sensitivity parameter, A, for these sensors will likely be observed to decrease with increasing operating temperature when the values of the parameters obtained from the solutions to the microstructural model are analysed later. The degree to which the steady state response is approached varies significantly with operating temperature. At the lower temperatures the responses are not particularly close to the steady state, whereas the responses on sensors operated at the higher temperatures, and particularly at 450°C, have virtually attained a steady state. This is really no surprise, as the rate of chemical reactions, such as those that mediate sensor response, is highly dependent on temperature. From this observation it is possible to conclude that a reduction in the time constant, τ, with increasing operating temperature will likely be obtained from the regressions of the transient data to the microstructural model. It is also likely that the accuracy of the solutions to the steady state model will be greater for the higher operating temperatures where the experimental responses are closest to the steady state response. There may be less variation in the parameters obtained from the solutions to the data from the different lengths of gas exposure. The steady state is only slightly more closely approached in the gas exposures to 1800 seconds than in those to 600 seconds. The accuracy of the solutions obtained to the microstructural model for the shorter exposures may be slightly diminished as a result.

The large difference between the response values obtained for the different exposure times in Figure 6.3 for the sensors operated at 350°C indicate how far these responses are from the steady state. By comparison, the responses from the different exposure times on sensors operated at higher temperatures are much closer, such that at 450 °C the responses are at identical values. This indicates the steady state is more closely approached in sensors operated at higher temperatures at shorter times. This is a result of the increased rate of reactions at higher temperatures, as discussed above. The solutions to the traditional square root model represent poor fits to the experimental data. In contrast, the solutions to the microstructural model represent a

much better fit to the experimental data over the entire range of conditions tested here. The degree of fit of the solutions to the microstructural model is best for the sensors operated at the highest operating temperature of 450 °C and diminishes at the lower operating temperatures. This change in the degree of fit of the solutions with operating temperature may be related to the change in the degree to which the steady state response is approached in the transients which was also noted to vary with operating temperature above. Using the steady state form of the model to fit the experimental response data means that if the response data is closer to the steady state the solution obtained is likely to be more accurate. If the solution is more accurate it is more likely to correctly account for the variations in response with concentration and the line representing the solution will therefore pass the experimental data points more closely. The solutions to the microstructural model for the different lengths of exposure are quite far apart for the sensors operated at the lower temperatures of 350 and 400°C, whilst at 450 °C they practically overlap. This is simply related to the fact that the responses used to obtain the solutions are practically identical at the higher temperature and they are further apart for the lower operating temperature.

The sensors used to provide these results are from the same batch as those used to produce the results in sections 5 and 5.2. They were also sintered at 775 °C. Therefore, the sensor operated at 400°C here may be compared with the sensors sintered at 775°C in the earlier sections. The plots of the parameters obtained from the solutions to the microstructural model versus operating temperature are shown in Figure 6.4. The results of CO testing on the earlier sensors sintered at 775 °C and operated at 400 °C are displayed in Figure 5.14 for comparison. The values of the microstructural parameters for the sensors operated here at 400 °C and those tested earlier are almost identical. Because the experimental techniques that have been used to create these sensors have been proved, at an industrial level, to produce repeatable sensors, the result of consistent values of the microstructural parameters for different sensors seem to indicate the model has some degree of validity in describing sensor response. Unfortunately for this argument, the value of the sensitivity parameter, A, obtained in these tests (~0.025) is somewhat higher than that obtained in the earlier tests (~0.012). However, this may not be such a problem for this argument as the value of this parameter is likely to be dependent on a great many experimental

details, some of which are not related to the preparation of the sensors. These include slight variations in operating temperature, ambient temperature, relative humidity, gas exposure history etc. The most important of these may be sensor history and sensitivity to the operating temperature, because this parameter is highly sensitive to operating temperature even a slight difference in this experimental detail could account for such a difference as has been noted here. The decreasing value of the sensitivity parameter with increasing operating temperature is consistent with the decreasing magnitude of response with increasing operating temperature observed in Figure 6.1, Figure 6.2 and Figure 6.3.

The fact that the values of the microstructural parameters are fairly constant with operating temperature indicates that contribution to resistance from the different microstructural regions does not change significantly with operating temperature. This is interesting because it means that, in this case at least, the processes that alter the resistance of the sensors appear to affect the different regions to the same degree with changing temperature. This need not necessarily be the case as the key processes that determine conductivity could be different at the different microstructural regions. For instance, in the case of the bulk the major determinant of conductivity will be the thermal excitation of electrons from the valence band to the acceptor levels. A similar process will occur at the particle boundaries and the surface. However, it could also be possible that the concentration of certain species at the surface and particle boundaries of the material are also sensitive to operating temperature and could also contribute to changes in conductivity at different rates to those for the thermal excitation of electrons. If this were the case the conductivity of these regions could change at a different rate to that of the bulk. The overall effect of a change in operating temperature would then be a change in the contribution to resistance made by the different regions and a resulting variation in the microstructural parameters with operating temperature.

The values of the sensitivity parameter, A, obtained from the transient regressions and the steady state data are very similar indicating the consistency between the two forms of the model. The values obtained for the steady state data for the 1800 second exposures were noted to be slightly higher than the values obtained from the 600 second exposures and this was not found to be the case for the transient values. The

strong decreasing trend of the value of the sensitivity parameter with increasing operating temperature was also noted for the steady state data and is consistent with the decreasing sensitivity to CO that is observed with increasing operating temperature. The fact that the value of the sensitivity parameter is not found to be dependent on concentration for the sensors operated at 400 and 450°C whilst it is for the sensors operated at 350°C is probably related to the offset in the baseline predicted from the steady state data being more important for the sensors operated at the lower temperatures. This is because the shape of the transients becomes more forgiving of this error as they become faster at the higher temperatures. The strong decreasing trend in the value of the time constant with increasing operating temperature is a clear indication that the effect of increased operating temperature is to speed up the response of the sensors. This is confirmed in the shape of the response transients being such that the steady state is most rapidly achieved in the sensors operated at the highest temperatures. The trends in the value of the time constant with concentration are probably a result of the variation in how the offset baseline predicted from the steady state microstructural parameters affects the regression process. The fact that similar values and trends are observed for these parameters obtained from the transient data for different lengths of exposure is an encouraging sign that the length of exposure may not significantly affect the steady state solutions enough to throw the transient regression process to far off. However, the fact that the values obtained for the sensitivity parameter remained relatively constant for the different lengths of exposure whilst the values obtained for the time constant increased going from 600 second exposures to 1800 second exposures at first appears contrary to what might be expected from what would essentially be a higher response (or sensitivity) in the longer exposures. However, it may be that the compensation is drawn from the decreasing effect of the offset baseline from the steady state microstructural parameters having less impact on the regression process for the longer exposure times.

6.5 Conclusions

The microstructural model has again been successfully applied to experimental response data to generate solutions which fit the experimental data far better than the

traditional square root model. The microstructural parameters obtained show no dependence on operating temperature. This indicates that the different microstructural regions show similar dependence of their conductivities on temperature. The changes in the sensitivity parameter, A, and the time constant, τ, that occur with operating temperature are entirely consistent with the character of the experimental data and how the reactions that mediate the sensor response can be expected to be affected by the temperature. The fact that the sensitivity parameter, A, varies with the exposure length in the steady state case but is constant in the transient case whilst the value of the time constant, τ, now varies means that the solutions fit the data differently with the different lengths of exposure. This is likely to be a result of differences in how well the steady state solutions fit the data and how accurate the microstructural parameters are. The similar values of the parameters obtained for the sensor operated at 400 °C here, and the sensors similarly operated at 400 °C and sintered at the same temperature of 775 °C in section 5.1.2 indicate that the sensors are repeatable, as expected, and the model can also be applied in a repeatable manner.

7 Conclusions

This work started with the hypothesis that sensors constructed from random arrangements of spherical particles could have their resistances modelled by a network of three resistors in the arrangement displayed in Figure 1.9, and that the sensor response could therefore be affected by microstructure. In this work, this simple hypothesis was combined with the hypothesis of how the different regions of microstructure are expected to be gas sensitive to form a model of sensor response. This model has been expressed in two different forms according to the data it is meant to represent: i.e. the steady state and transient forms. The main purpose for this work was to generate experimental data which could be used to test whether the model is a valid representation of how sensors respond. In this respect the study has had the following successes and failures:

- The trend in response data with gas concentration is very well accounted for by the microstructural model in every case and the solutions it provides fit the experimental data far better than those provided by the traditional square root model.
- The microstructural parameters obtained from sensors sintered at different temperatures display clear trends with the sintering temperature. These trends are very well accounted for by the changes that are observed in the microstructures of the sensors as observed in SEM.
- The top-down SEM micrographs obtained from the sensors made from raw materials having different particles size appeared to display significant differences between the groups of sensors. The microstructural parameters obtained do not show as much variation as may be expected from these SEM micrographs alone. The SEM micrographs of the FIB sections performed on the sensor constructed from the coarse material and sintered at the highest temperature show that there is a surface skin that appears to have undergone quite large degrees of sintering but that the underlying structure is much closer to the initial, finer structure that existed prior to sintering. This could account for the lack of variation noted for these microstructural parameters. There are also

likely to be other microstructural and compositional factors, such as porosity and titanium surface segregation, that have not been analysed in this study that could contribute to these results.

- The fact that the microstructural parameters are shown to have no dependence on operating temperature shows that all the material at the different regions is similarly affected by the change in temperature. This is likely to mean that the same sources of changes in conduction carriers are affected by the changes in temperature to the same extent at the different microstructural regions.
- The fact that the sensitivity parameter and time constant vary with sintering temperature when they are not expected to is probably a result of how well the pseudo steady state responses approximate the true steady state response and how accurate are the steady state solutions. The possibility of varying titanium surface segregation may also be a factor in this observation
- The variations in the sensitivity parameter and time constant with operating temperature are entirely consistent with the observed response data and how the reactions that mediate sensor response can be expected to be affected by the change in temperature.

8 Further Work

Overall, the study has been a resounding success. However, it does leave certain questions that may be answered by further investigations. The primary focus in this respect should be on developing more information about the sensor microstructures, particularly in terms of the porosity and surface area of the materials. These two characteristics of the sensing materials are of prime importance in gas sensors since they respectively determine the ability of gas to diffuse into the structure and the capacity of the structure to react with the gases in the atmosphere. The amount and distribution of porosity in the sensors could be determined by more extensive FIB milling of sensors and observation of the cross-sectional microstructures by SEM similar to that which has been demonstrated in this study in section 3.2.4. Ultimately, cross-sections through entire sensors, such as are obtained by conventional metallographic polishing techniques with metallic samples, would be desirable. Equipment such as the JEOL cross-section Polisher (SM-09010)[68] appears to be capable of producing such cross-sections and it would be most interesting to conduct a systematic study of the amount and distribution of porosity in sensors sintered at different temperatures using this technique along with the other features of sensor microstructure.

Information of the surface areas of the sensing materials by a technique such as the BET isotherm method would also be very useful in showing the variation of the capacity of the structures for gas reactions with sintering temperature or raw material particle size. Such a study would be complicated for the types of sensors produced in this study because the surface area would be affected to some degree by the presence of the alumina substrate and the gold and platinum structures on these substrates. However, pressed pellets of the CTO material could be produced and surface area measurements could be performed on these without such complications. Although the CTO materials used in this study have been very well characterised in previous studies, the uncertainties over material and phase composition in this study highlight the importance of characterisation using techniques such as XRD and XPS to determine bulk and surface composition as these factors are highly likely to affect

the sensitivity of the sensors. Further studies would benefit from a fuller characterisation of material composition than has been presented in this study. It would also be of interest to produce sensors having more extreme contrasts in microstructural features. Sensors having very fine features could be produced by a technique such as chemical vapour deposition to produce a thin film or sol-gel techniques to obtain materials of high purity and fine particle size. Alternatively, sensors having much larger particle sizes and varying porosity could be produced as alumina supported structure (as produced for this study) or pellets by varying raw material processing and/or sintering conditions.[59]

The form and method of implementation of the microstructural model to experimental response data would also benefit from further study. One of the major problems with the implementation used in this study is likely to be the fact that the responses at the start of the gas exposures predicted from the steady state solutions of the sensor responses to the microstructural model are not equal to 1 as they should be. The reason this occurs is that the several solutions to the microstructural model were obtained from the brute force search for solutions and the mean average of the values of the parameters of the model were taken as the final solution because the values of the parameters in the different solutions were deemed to be similar. Further studies should test whether removing this averaging procedure and making it a condition of the search for solutions that the response at the very start of the gas exposures predicted by a set of parameters must be equal to 1. It would also be of interest to study whether the transient data could be processed to obtain solutions of the response data to the model that better represent the responses of the sensors and their microstructures or whether more information about the type of gas reacting causing a response could be extracted from the transients using the solutions to the model obtained for particular sensors.

In a wider context, it would be of interest to study a wider variety and magnitude of parameters than has been studied here. As well as testing the model and the method of its implementation developed in this study to a wider range of p-type responding materials it would be of particular interest to attempt to apply the microstructural model to sensors which display n-type response. Such materials include the widely used tin dioxide (SnO_2) and tungsten trioxide (WO_3) materials. The particular form

of the model would have to be developed specifically for these materials to account for their differing signs of their responses. In this respect it may be better to formulate the model for conductance changes in response to reducing gases rather than resistance changes. Furthermore, it would also be highly interesting to test sensors to a much wider spectrum of gases than has been conducted in this study. In particular, oxidising gases have not been studied at all here. Along these lines, it would also be interesting to elucidate which parameters of the microstructural model are most affected by changes in oxygen partial pressure and humidity levels as changing the composition of oxygen surface states may change both the resistance and the sensitivity of the regions that are accessible to gas and therefore the values of the parameters of the model that represents the different regions and their sensitivity.

References

[1] The Concise Oxford Dictionary, Seventh Edition, Edited by J.B. Sykes, 1982, Oxford University Press, ISBN 0-19-861131-5

[2] City Technology Ltd., Walton Road, Portsmouth, PO6 1SZ, UK, Tel: +44 (0) 2392325511, http://www.citytech.com/

[3] Basic Solid State Chemistry, Second Edition, A.R. West, 1999, John Wiley & Sons, ISBN 0-471-98756

[4] "Semiconducting oxides as gas-sensitive resistors," D.E. Williams, Sensors and Actuators B, **57**, 1999, p1-16

[5] "A model for the operation of a thin-film SnO_x conductance-modulation carbon monoxide sensor," H. Windischmann and P. Mark, J. Electrochem. Soc., **126**, 4 (1979) 627-633

[6] "Fundamental and practical aspects in the design of nanoscaled SnO_2 gas sensors: a status report," N. Barsan, M. Schweizer-Berberich and W. Göpel, Fresenius J. Anal. Chem., **365**, 1999, p287-304

[7] "Conduction and gas response of semiconductor gas sensors," D.E. Williams in Solid State Gas Sensors, part of the Adam Hilger series on sensors, Edited by P.T. Moseley and B.C. Tofield, 1987, IOP Publishing, Bristol, ISBN 0-85274-514-1

[8] "Oxygen surface species on semiconducting oxides," by P.T. Moseley and D.E. Williams, in Techniques and Mechanisms in Gas Sensing, part of the Adam Hilger series on sensors, edited by P.T. Moseley, J.O.W. Noris and D.E. Williams, 1991, IOP Publishing, Bristol, ISBN 0-7503-0074-4

[9] "Sensitivity control of SnO_2 by morphology of thin film," Y. Nagasawa, K. Tabata and H. Ohnishi, Applied Surface Science, **121/122**, 1997, p327-330

[10] "Desenvolvimento de sensores para gás à base de SnO_2 nanoestruturado: influência da microestrutura no desempenho do sensor," translated as "Development of gas sensors based on nanostructured SnO_2: the influence of microstructure on sensor performance," I.T. Weber, E.R. Leite, E. Longo and J.A. Varela, Cerâmica, **46** (299), 2000, p156-159

[11] "A study of the $SnO_2.Nb_2O_5$ system for the ethanol vapour sensor: a correlation between microstructure and sensor performance," I.T. Weber, R. Andrade, E.R. Leite and E. Longo, Sensors and Actuators B, **72**, 2001, p180-183

[12] "Structural and dimensional effects in electrical conductivity of SnO_2 thin films used for gas sensors," A. Ivaschenko and I. Kerner, IEEE CAS99 International Semiconductor Conference, Volume 2, p499-502

[13] "Gas sensing properties of SnO_2 sputtered films deposited under different conditions," T. Yamazaki, T. Shimazaki, K. Tereyama, N. Nakatani and G.A. Mohamed, Journal of Materials Science Letters, **17**, 1998, p891-894

[14] "Enhancement os gas sensitivity by controlling microstructure of α-Fe_2O_3 ceramics," Y. Nakatami, M. Sakai and M. Matsuoka, Japanese Journal of Applied Physics, **22** (6), 1983, p912-916

[15] "Materials and processing issues in nanostructured semiconductor gas sensors," F. Cosandey, G. Skandan and A. Singhal, JOM-e, **52** (10), 2000

[16] "Effects of calcining temperature on lattice constants and gas-sensing properties of Nb_2O_5," Yu-De Wang, Lui-Fang Yang, Zhen-Lai Zhou, Yan-Feng Li and Xing-Hui Wu, Materials Letters, **49**, 2001, p277-281

[17] "Effect of variation of sintering temperature on the gas sensing characteristics of SnO_2:Cu (Cu=9wt%) system," P.S. More, Y.B. Khollam, S.B. Deshpande, S.K. Date, R.N. Karekar and R.C. Aiyer, Materials Letters, **58**, 2003, p205-210

[18] "New approaches for improving semiconductor gas sensors," N. Yamazoe, Sensors and Actuators B, **5**, 1991, p7-19

[19] "Preparation, development of microstructure, electrical and gas sensitive properties of pure and doped SnO_2 powders," W. Fliegel, G. Behr, J. Werner and G. Krabbes, Sensors and Actuators B, **18-19**, 1994, p474-477

[20] "The influence of morphology on the response of iron-oxide gas sensors," P. Althainz, L. Schuy, J. Goschnick and H.J. Ache, Sensors and Actuators B, **24-25**, 1995, p448-450

[21] "Microstructure and CO gas sensing properties of porous ZnO produced by starch addition," D.H. Yoon and G.M. Choi, Sensors and Actuators B, **45**, 1997, p251-257

[22] "Influence of tin oxide microstructure on the sensitivity to reductor gases," M.C. Horrillo, A. Serventi, D. Rickerby and J. Gutiérrez, Sensors and Actuators B, **58**, 1999, p474-477

[23] Comparison study of SnO_2 thin- and thick-film gas sensors," S.W. Lee, P.P. Tsai and H. Chen, Sensors and Actuators B, **67**, 2000, p122-127

[24] "Effect of particle size and dopant on properties of SnO_2-based gas sensors," G. Zhang and M. Liu, Sensors and Actuators B, **69**, 2000, p144-152

[25] "The properties of strongly pressed tin oxide-based gas sensors," Sensors and Actuators B, **79**, 2000, p28-32

[26] "Influence of the deposition method on the morphology and elemental composition of SnO_2 thin films for gas sensing: atomic force and X-ray photoemission spectroscopy analysis," C. Bittencourt, E. Llobet, M.A.P. Silva, R. Landers, L. Nieto, K.O. Vicaro, J.E. Sueiras, J. Calderer and X. Correig, Sensors and Actuators B, **92**, 2003, p67-72

[27] "Gas-sensing properties of indium-doped SnO2 thin films with variations in indium concentration," A. Salehi and M. Gholizade, Sensors and Actuators B, **89**, 2003, p173-179

[28] "Effect of processing on the properties of tin oxide-based thick-film gas sensors," A. Ahmad, J. Walsh and T.A. Wheat, Sensors and Actuators B, **93**, 2003, p538-545

[29] "Influence of the nanostructural characteristics on the gas sensing properties of pulsed laser deposited tin oxide thin films," R. Dolbec, M.A. El Khakani, A.M. Serventi and R.G. Saint-Jacques, Sensors and Actuators B, **93**, 2003, p566-571

[30] "Effect of poly ethylene glycol addition on the microstructure and sensor characteristics of SnO_2 thin films prepared by sol-gel method," M. Shoyama and N. Hashimoto, Sensors and Actuators B, **93**, 2003, p585-589

[31] "Microstructure and gas-sensing properties of thick film sensor using nanophase SnO_2 powder," Jae-Pyoung Ahn, Jung-Han Kim, Jong-Ku Park and Moo-Young Huh, Sensors and Actuators B, **99**, 2004, p18-24

[32] "Grain size effects on H_2 gas sensitivity of thick film resistor using SnO_2 nanoparticles," S.G. Ansari, P. Boroojerdian, S.R. Sainkar, R.N. Karekar, R.C. Aiyer and S.K. Kulkarni, Thin Solid Films, **295**, 1997, p271-276

[33] "Thickness and microstructure effects on alcohol sensing of tin oxide thin films," Sung-Soon Park and J.D. Mackenzie, Thin Solid Films, **274**, 1996, p154-159

[34] "Transmission electron microscopy investigation of the effect of deposition conditions and a platinum layer in gas-sensitive r.f.-sputtered SnO_2 films," A.M. Serventi, D.G. Rickerby, M.C. Horrillo and R.G. Saint-Jacques, Thin Solid Films, **445**, 2003, p38-47

[35] "The influence of film structure on In_2O_3 gas response," G. Korotcenkov, V. Brinzari, A. Cerneavschi, M. Ivanov, V. Golovanov, A. Cornet, J. Morante, A. Cabot and J. Arbiol, Thin Solid Films, **460**, 2004, p315-323

[36] "Microspheres of the gas sensor material $Cr_{2-x}Ti_xO_3$ prepared by the sol-emulsion-gel route," G. Chabanis, I.P. Parkin and D.E. Williams, Journal of Materials Chemistry, **11**, 2001, p1651-1655

[37] "Atmospheric pressure chemical vapour deposition of $Cr_{2-x}Ti_xO_3$ (CTO) thin films ($\leq 3\mu m$) on to gas sensing substrates," G.A. Shaw, I.P. Parkin and D.E. Williams, Journal of Materials Chemistry, **13**, 2003, p2957-2962

[38] "Microstructure effects on the response of gas-sensitive resistors based on semiconducting oxides," D.E. Williams and K.F.E. Pratt, Sensors and Actuators B, **70**, 2000, p214-221

[39] "A simple equivalent circuit model to represent microstructure effects on the response of semiconducting oxide-based gas sensors," G. Chabanis, I.P. Parkin and D.E. Williams, Measurement Science and Technology, **14**, 2003, p76-86

[40] "Engineered sensitivity of structured tin dioxide chemical sensors: opaline architectures with controlled necking," R.W.J. Scott, S.M. Yang, N. Coombs, G.A. Ozin and D.E. Williams, Advanced Functional Materials, **13**, 3, 2003, p225-231

[41] "Tin dioxide opals and inverted opals: near-ideal microstructures for gas sensors," R.W.J. Scott, S.M. Yang, G. Chabanis, N. Coombs, D.E. Williams and G.A. Ozin, Advanced Materials, **13**, 19, 2003, p1468-1472

[42] "Modelling the response of a tungsten oxide semiconductor gas sensor for the measurement of ozone," D.E. Williams, S.R. Aliwell, K.F.E. Pratt, D.J. Caruana, R.L. Jones, R.A. Cox, G.M. Hansford and J. Halsall, Measurement Science and Technology, **13**, 2002, p923-931

[43] "Ozone sensors based on WO_3: a model for sensor drift and a measurement correction method," S.R. Aliwell, J.F. Halsall, K.F.E. Pratt, J. O'Sullivan, R.L. Jones, R.A. Cox, S.R. Utembe, G.M. Hansford and D.E. Williams, Measurement Science and Technology, **12**, 2001, p684-690

[44] "Preparation, Morphology, and Gas-Sensing Behaviour of $Cr_{2-x}Ti_xO_{3+z}$ Thin Films on Standard Silicon Wafers," J. Wöllenstein, G. Plescher, G. Kühner, H. Böttner, D. Niemeyer and D.E. Williams, IEEE Sensors Journal, **2** (5), 2002, p403-408

[45] "Selectivity and Composition Dependence of Response of Gas-Sensitive Resistors. Part 2.- Hydrogen Sulfide Response of $Cr_{2-x}Ti_xO_{3+y}$," G.S. Henshaw, D.H. Dawson and D.E. Williams, Journal of Materials Chemistry, **5** (11), 1995, p1791-1800

[46] "Microspheres of the gas sensor material $Cr_{2-x}Ti_xO_3$ prepared by the sol-emulsion-gel route," G. Chabanis, I.P. Parkin and D.E. Williams, Journal of Materials Chemistry, **11**, 2001, p1651-1655

[47] "Experimental and computational study of the gas-sensor behaviour and surface chemistry of the solid-solution $Cr_{2-x}Ti_xO_3$ ($x \leq 0.5$)," D. Niemeyer, D.E. Williams, P. Smith, K.F.E. Pratt, B. Slater, C.R.A. Catlow and A.M. Stoneham, Journal of Materials Chemistry, **12**, 2002, p667-675

[48] "Atmospheric pressure chemical vapour deposition of $Cr_{2-x}Ti_XO_3$ (CTO) thin films ($\leq 3\mu m$) on to gas sensing substrates," G.A. Shaw, I.P. Parkin and D.E. Williams, Journal of Materials Chemistry, **13**, 2003, p2957-2962

[49] "Sol-Gel Synthesis of Sub-Micron Titanium Doped Chromia Powders for Gas Sensing," A.M. Nartowski and A. Atkinson, Journal of Sol-Gel Science and Technology, **26**, 2003, p793-797

[50] "Soft-chemical preparation and gas sensing properties of iron and manganese substituted $Cr_{1.8}Ti_{0.02}O_{3+\delta}$," V. Jayaraman, E. Prabhu, K.I. Gnanasekar, T. Gnanasekaran and G. Periaswami, Materials Chemistry and Physics, **86**, 2004, p165-175

[51] "Preparation and characterisation of $Cr_{2-x}Ti_XO_{3+\delta}$ and its sensor properties," V. Jayaraman, K.I. Gnanasekar, E. Prabhu, T. Gnanasekaran and G. Periaswami, Sensors and Actuators B, **55**, 1999, p175-179

[52] "A novel single chip thin film metal oxide array," J. Wöllenstein, J.A. Plaza, C. Cané, Y. Min, H. Böttner and H.L. Tuller, Sensors and Actuators B, **93**, 2003, p350-355

[53] "Description and characterization of a hydrogen sulphide gas sensor based on $Cr_{2-y}Ti_yO_{3+x}$," D.H. Dawson, G.S. Henshaw and D.E. Williams, Sensors and Actuators B, **26-27**, 1995, p76-80

[54] "Self diagnostic gas sensitive resistors in sour gas applications," K.F.E. Pratt and D.E. Williams, Sensors and Actuators B, **45**, 1997, p147-153

[55] "Low temperature sol-gel synthesis and humidty sensing properties of $Cr_{2-x}Ti_xO_3$," G. Neri, A. Bonavita, G. Rizzo and S. Galvagno, Journal of the European Ceramic Society, **24**, 2004, p1435-1438

[56] Phase Diagrams for Ceramists, Annual '91, A.E. McHale, The American Ceramic Society, Fig. 91-025; from H.D. Werner, Neues Jahrb. Mineral., Monatsh, No. 5, p218-234

[57] "Phase Relations in the System Fe_2O_3-Cr_2O_3-TiO_2 between 1000 and 1300°C and the Stability of $(Cr,Fe)_2T_{n-2}O_{2n-1}$ Crystallographic Shear Structure Compounds," M.I. Pownceby, M.J. Fisher-White and V. Swamy, Journal of Solid State Chemistry, **161**, 2001, p45-56

[58] "Electrical conductivity of Cr_2O_3 doped with TiO_2," A. Holt and P. Kofstad, Solid State Ionics, **117**, 1999, p21-25

[59] "Analytical transmission electron microscopy and surface spectroscopy of ceramics: The microstructural evolution in titanium-doped chromia polycrystals as a function of sintering conditions," S.P. McBride and R. Brydson, Journal of Materials Science, **39**, 2004, p6723-6734

[60] S. Somiya, H. Hirano and S. Kamiya, Journal of Solid State Chemistry, **25**, 1978, p273

[61] Procedures used were carried out by K. Lee of the Department of Electronic and Electrical Engineering, University College London, based on guidelines from the manufacturer Carl Zeiss SMT AG, Oberkochen, Germany

[62] "Application of the new CrossBeam® Technology to extend Accuracy in Site Specific Cross Sectioning and TEM Sample Preparation," Peter Gnauck, LEO Elektronenmikroskopie GmbH, D-73446 Oberkochen, Germany

[63] "Triple Potentiostat Unit," designed by K.F.E. Pratt, built by J.D. Stewart, April 1996, booklet produced by electronics support staff at the Department of Chemsitry, University College London,

[64] "Op Amps for Everyone", Design Reference, Ron Mancini, Editor in chief, Texas Instruments, Dallas, Texas, page 16-37

[65] XL Statistics, version 5, Rodney Carr, http://www.deakin.edu.au/~rodneyc

[66] Engineering Ceramics, M. Bengisu, 2001, Springer-Verlag Berlin Heidelberg, ISBN 3-540-67687-2

[67] "SEMDEC – Investigation into Reverse Concentration Gradient," D.P. Mann and K.F.E. Pratt, 2001, internal report on project 2036-E, Capteur Sensors and Analysers Ltd. (now part of City Technology Ltd.)

[68] JEOL USA, Inc., 11 Dearborn Road, Peabody, MA 01960, USA, Tel: +1 (978) 535-5900, http://www.jeol.com/spe/speprods/cross_section.html

[69] Carl Zeiss NTS GmbH, Carl Zeiss-Str. 56, 73447 Oberkochen, Germany, Tel: +49 07364 20-44 88, http://www.smt.zeiss.com/

[70] London Centre for Nanotechnology, Temporary Contact Address, Brook House, 2-16 Torrington Place, London, WC1E 7HN, UK, Tel: +44(0)20 7679 0997, http://www.london-nano.ucl.ac.uk

Appendix – cfUnit1.cpp Programme Code Written by K.F.E. Pratt

Appendix – cfUnit1.cpp Programme Code Written by K.F.E. Pratt

Appendix – cfUnit1.cpp Programme Code Written by K.F.E. Pratt

Appendix – cfUnit1.cpp Programme Code Written by K.F.E. Pratt

Appendix – cfUnit1.cpp Programme Code Written by K.F.E. Pratt

Appendix – cfUnit1.cpp Programme Code Written by K.F.E. Pratt

Appendix – cfUnit1.cpp Programme Code Written by K.F.E. Pratt

Appendix – cfUnit1.cpp Programme Code Written by K.F.E. Pratt

Appendix – cfUnit1.cpp Programme Code Written by K.F.E. Pratt

Appendix – cfUnit1.cpp Programme Code Written by K.F.E. Pratt

Appendix – cfUnit1.cpp Programme Code Written by K.F.E. Pratt

Appendix – cfUnit1.cpp Programme Code Written by K.F.E. Pratt

Appendix – cfUnit1.cpp Programme Code Written by K.F.E. Pratt

Appendix – cfUnit1.cpp Programme Code Written by K.F.E. Pratt

Appendix – cfUnit1.cpp Programme Code Written by K.F.E. Pratt

Appendix – cfUnit1.cpp Programme Code Written by K.F.E. Pratt

Appendix – cfUnit1.cpp Programme Code Written by K.F.E. Pratt